SAND-74-0130
Unlimited Release

Mars Penetrator:
Subsurface Science Mission

Sandia Laboratories

SF 2900 Q(7-73)

SAND-74-0130
Unlimited Release
Printed August 1974

MARS PENETRATOR:
SUBSURFACE SCIENCE MISSION

Sandia Laboratories
Albuquerque, New Mexico 87115

ABSTRACT

This report describes a penetrator system designed by Sandia
Laboratories to emplace subsurface science on the planet Mars.
The need for subsurface science is discussed, and the technologies
for achieving successful atmospheric entry, Mars penetration, and
data retrieval are presented.

SUMMARY

The Mars penetrator designed by Sandia Laboratories is a Mars entry, landing, and subsurface emplacement system. The design calls for the penetrator system to enter the Martian atmosphere in a high-drag configuration programmed so that the penetrator arrives at the surface in an attitude and with a velocity which will result in subsurface emplacement of the onboard science. As the main vehicle containing the principal science and electronics penetrates below the surface, a separable afterbody containing the antenna and a transmitter and command receiver is left behind on the surface. This afterbody remains connected to the penetrator with a multiconnector umbilical which is payed out from the aft section of the penetrator during the penetration. A sequence of science experiments is then conducted, and the data are stored in an onboard memory until they can be transmitted to the orbiter for relay to earth. This penetrator has several unique features for science objectives:

- 4 penetrators (4 landing sites) per orbiter

- 400 day operational lifetime for each penetrator

- subsurface emplacement of science

- capable of operation in polar regions

- compatible with broad range of landing sites

- tolerant of uncertainties about atmosphere, terrain, and terrain relief

The Mars penetrator makes possible major subsurface science in the following areas:

- heat flow

- geochemistry

- seismology

- thermal conductivity

- quantitative water assay

- vertical profile physical geology

A baseline science package incorporating experiments in geochemistry, seismology, and vertical profile physical geology is used for the systems design. These experiments are well matched to the Mars penetrator, but many others are equally compatible.

TABLE OF CONTENTS

LIST OF TABLES

LIST OF ILLUSTRATIONS

APPENDICES

MARS PENETRATOR:
SUBSURFACE SCIENCE MISSION

Introduction

The problem of landing scientific instruments on Mars can be solved in several ways. One approach is to make a soft landing by reducing the descent velocity to essentially zero just as the vehicle touches down on the surface. This requires a precision determination of the vehicle's altitude above the surface during descent coupled with an active retro-propulsion system to control the rate of descent.

Another approach is to slow the vehicle passively during its entry through the Martian atmosphere and then to make a hard landing at the terminal velocity so that the vehicle stops abruptly at the surface. In this approach, the scientific payload must tolerate extremely large decelerations. In hard landing, the magnitude and duration of the landing shock depends on many parameters such as the terminal velocity, the impact site material properties, shock mitigating structures in the vehicle, etc., but is typically $\geq 20,000$ Earth g's for all passive descent systems, i.e., those which do not flare the descent velocity just prior to touchdown.

A third approach, intermediate to soft and hard landings, allows the vehicle to impact the surface with appreciable velocity but, instead of stopping abruptly at the surface, spreads the deceleration over some significant time--and distance--by designing the vehicle to penetrate the surface before coming to rest. Again, many parameters, such as weight-to-frontal area of the penetrator, terminal velocity, impact site material properties, etc., influence the depth of penetration and hence the landing shock; however, a good rule of thumb is that the decelerations experienced in this type of landing are an order of magnitude less than for a hard lander. The third approach has been selected for the Mars penetrator mission.

However, the answers to two pivotal questions determine the feasibility of such a Mars penetrator mission:

1. Are there significant objectives for subsurface science and, if so, what are the proper instruments and can they be made compatible with the penetrator and the penetrator-induced environment?

2. Is a passive Mars entry and subsurface emplacement system feasible and, if so, what are its physical characteristics and science limitations?

The answer to the first part of both of these questions is unequivocally "yes": important science is uniquely possible through subsurface emplacements, and entry and subsurface penetration can be achieved. The answers to the second part of both questions are more involved because they encompass all aspects of the mission system design.

This report discusses subsurface science objectives and presents a detailed systems design for an elegantly simple lander of the third type, i.e., for a Mars penetrator. Stripped of all inessential details, the design calls for the penetrator to enter the Martian atmosphere in a high-drag configuration programmed so that the vehicle arrives at the surface in an attitude and with a velocity which will result in penetration to a sufficient depth to limit the deceleration to a safe level for the onboard science and electronics. As the main vehicle containing the principal science and electronics penetrates below the surface, a separable afterbody containing the antenna and a transmitter and command receiver is left behind on the surface. This afterbody remains connected to the penetrator with a multiconnector umbilical which is payed out from the aft section of the penetrator during the penetration. A sequence of science experiments is then conducted either by command from the orbiter or under the control of a preprogrammed sequence, and the data are stored in an onboard memory until they can be transmitted to the orbiter for relay to earth.

Major Scientific Questions About Mars

Many of the scientific questions concerning elemental and mineralogical composition, geological history, modifying forces, geomorphology, etc. of Mars are also questions relevant to the Earth, to the Moon, and indeed to any body in the solar system. Mars, however, is perhaps the only nonterrestrial body in the solar system which invites questions about the existence of life, either contemporaneous or historical--witness the dedication of the 1975 Viking mission to this question. The following paragraphs outline some of the vital, non-biological issues about Mars to guide an appraisal of possible subsurface science. Biological questions are not considered here because they seem best pursued on the surface or near the surface; furthermore, Viking should answer most of the specific biological questions which could be posed at this time, because only the data returned from the successful landing and operation of Viking can provide a new basis for additional biological questions.

One of the most exciting results from the close look at Mars given by Mariner 9 is the geo-logical variety exhibited. At least a dozen distinct geological regimes, such as chaotic terrain, volcanic shields, extensive collapse pits or slumping, aeolian mantles and dunes, impact craters, knobby terrain, fractured plains and faulted block structures, dendritic features, and sedimentation plains, are well represented. This geological variety, in turn, suggests that the planet was shaped by a corresponding variety of forces such as ballistic modification by meteor impact, volcanism, aeolian erosion, tectonic shifting and faulting, subsurface sapping of volatiles deposits, fluid erosion, and quakes. The determination of these forces, the periods when the shaping took place, and, perhaps most important of all, the contemporary processes of modification are clearly questions which must be addressed by future Mars missions. The quest for answers to these questions leads immediately to the search for and measurement of H_2O and CO_2; the seismological investigation of the planet--both passive listening and active probing; measurements of wind erosion and materials transport; studies of polar cap dynamics; and observations of surface and subsurface petrology and

mineralogy. Furthermore, this quest is especially intriguing because the thin atmosphere and the scarcity, if not absence, of liquid water makes Mars a geological museum, presumably contemporaneous in formation with Earth, in which processes obscured on Earth by millions of years of accelerated erosion have been preserved.

The Surveyor remote geochemistry and later the laboratory analyses of lunar rock and soil samples revealed interesting variations between the elemental and mineralogical composition of the Earth and the moon. For example, as compared with those of Earth, lunar materials have been found to be deficient in lower temperature volatile materials. These discrepancies have forced a revision of some hypotheses about the moon's formation, but primarily they have focused attention on the vital data required for an understanding of the processes, timing, etc. of the formation of the solar system to be gained by learning of the physical and chemical composition of Mars. The primary questions of course are how the bodies of the solar system were formed and what their primordial compositions were. For example, the earth has a crust and mantle overlaying a molten iron core. The seismic investigation of the moon has shown it to also have a crust and mantle; however, deep-going seismic waves suggest the absence of a contemporary molten core. If Mars was formed by accretion from the same solar-system raw stock as Earth, the absence of a differentiated crustal structure (for example, a uniform distribution of radionuclides in the planet rather than a preferential occurrence in the crust) or a verification of the existence of a crust-mantle-core structure would give vital additional information for the modeling of planetary formation processes and hence for an understanding of the solar system. Whether the Earth's structure is simply an artifact of the inhomogeneity of the solar-system raw stock or whether it reflects a dependence between the time of formation of the planetary bodies and an evolving elemental composition of the primordial solar system may be resolved by answering such questions on Mars. The hope that Mars can aid in answering questions such as these is heightened by several apparently paradoxical facts. For example, Mars geodesy shows that the planet is pear shaped with a pronounced lowering of mean elevation (≈ 2 to 3 km) in a girdle at near 65°N latitude and a corresponding raising of mean elevation in the southern hemisphere which could be explained by continental plate drift[1] similar to that on Earth. This hypothesis is contradicted by the fact that although the Mariner 9 photos reveal vertical movement of the crust, i.e., faulting, etc., the volcanoes, as may be deduced from their size and relative placement with respect to major fault zones,[2] must have remained fixed with respect to their underlying sources of heat. Nix Olympica towers 24 km above the surrounding plains, and the volcanoes of the North Spot, Middle Spot, and South Spot, although their elevation above the Tharsis Ridge on which they are sited is less impressive, have approximately the same mean lip elevations. Therefore, the lava pools for each must have been very deep inside the planet to generate the necessary hydrostatic forces. This observation, together with the sheer magnitude of the volcanic cones, indicates that the crust was not mobile in the period when a molten interior certainly existed.

Another fundamental planetary question, which overlaps the previous two in science implications and for which the information available at this time also appears to be paradoxical, is the quantitative assay of volatiles for Mars. By volatiles is meant only H_2O and CO_2, in that the only known components of the atmosphere are water vapor, ozone, and CO_2 and its dissociation products, CO, O_2, O. The Russian measurements showing ≈ 15 percent argon would not influence volatiles dynamics in any event. In that water is vital to life processes and is currently the most logical formation agent for some of the gross geological features seen on Mars (dendritic patterns, typical canyonland erosion, surface slumping, etc.), the existence or absence of water in significant (geologically) quantities on Mars is of prime importance.

On the one hand, the rates of dissociation of water vapor, escape of hydrogen to space, and recombination of the oxygen with surface materials are inconsistent with the expected outgassing of the planet; on the other hand, the low partial pressure of precipitable water vapor in the atmosphere would require large surface or subsurface entrapment in reservoirs.

The rate at which Mars can be expected to expire water because of the decay of rocks under pressure, heat, and radioactive processes can be estimated if the planetary processes are assumed to be similar to those postulated by Rubey[3, 4] and Kulp[5] for the Earth.

The surface area of Mars, computed with the mean equatorial radius of 3393.4±4 km, is 1.45×10^{18} cm^2. Mars has a mass of 0.1065 Earth mass. Hence, if the production of volatiles by the decay of rocks is assumed to be proportional to the planetary mass and if Rubey's estimate[3, 4] of 10^{11} to 10^{12} grams of water expired per day for the Earth is used, Mars should expire between 10^{10} and 10^{11} grams of water per day. This might appear to be an excessive figure in view of the measured 20 to 30 microns[6, 7] of precipitable water in the Martian atmosphere; however, this figure can be reconciled with observations. If the partial pressure of water is 30 microns, the atmosphere must contain a total of 5×10^{15} grams of water[7] so that the annual (Martian) replenishment represents only 0.14 percent of the total. If the Martian water balance is assumed to be stable, this replenishment must be accounted for by loss processes such as dissociation of the water and loss of the gases, chemical bonding at newly exposed exfoliated rock surfaces, etc., and stable entrapment in regions whose mean temperature is lower than -90°C (subsurface and polar caps), which corresponds to the equilibrium temperature of ice for a vapor pressure of 30 microns. The quantitative measurement of the efficiency of these competing processes is a volatiles inventory which is clearly crucial to an understanding not only of the history of outgassing of the planet but also of the most active of the probable surface modification processes. In turn, knowledge of the release of volatiles is essential to tracing the history of internal heating, volcanism, and surface and near-surface geochemistry. This knowledge could even be the key to understanding the evolution of the Martian atmosphere, if it can be assumed that the atmosphere has not always been as tenuous as at present or as dry as is suggested by many of the major erosional features revealed by Mariner 9. Crucial to understanding major atmospheric or climatic changes is the determination of whether or not large volatiles reservoirs exist. If not, major changes are unlikely unless the planet, by some mechanism not currently active, lost an earlier dense atmosphere.

The discussion thus far has highlighted major scientific questions about Mars with special emphasis on those evoked by the data received from Mariner 9. The next section will consider which of these science questions can best be explored subsurface by penetrators primarily designed for such investigations.

Science - Subsurface

Two categories of subsurface science are addressed in this section: that which is uniquely possible by virtue of the subsurface emplacement of the appropriate instruments and that which is enhanced by subsurface emplacement although the experiment could possibly be conducted with the instrument on the surface.

The first category includes the following:

1. Crustal heat flow

2. Borehole or vertical profile physical geology

3. Variation with depth of physical parameters

    a. Temperature

    b. Volatiles

    c. Particle sizes and/or porosity

    d. Stratigraphy

    e. Geochemistry - crust and polar cap

4. Existence of subsurface permafrost - H_2O or CO_2

5. Thickness of

    a. Aeolian mantle or dunes

    b. Polar ice cap

    c. Sedimentary layers

    d. Crust and/or mantle (if present)

In the second category we have:

1. Seismological studies

    a. Passive (multisite installation)

    b. Active

2. Bulk physical properties

    a. Thermal conductivity

    b. Specific heat

    c. Compressibility and bearing strength

    d. Density

3. Geochemistry

The one-to-one relationship between the major questions discussed earlier and several of these science objectives is clear, such as a measurement of the polar ice cap thickness and its bearing on the planetary volatiles inventory. Others require some discussion. For example, a geochemical analysis of near-surface rocks capable of identifying low-temperature hydrates and carbonates or clays would give an indication of the geological history of the volatiles inventory. This is important information for deciding whether Mars has experienced a major change in its atmosphere or whether liquid water has existed on the surface in the past.

Langseth and Wechsler fielded lunar heat flow experiments in Apollo 15 and 17 which showed a flux of approximately half that on Earth. A similar measurement on Mars would deserve extremely high priority because it would give direct information about the differentiation of radioactive materials in the planet and their abundance in the crust and hence about the thermal evolution of the planet. Comparative heat flow measurements in the region of high volcanism and elsewhere on the planet could indicate the existence of magma cells or recent (geologically speaking) volcanic activity.

Two basic types of seismic experiments are to be considered: passive and active. The passive experiment requires, for a very meaningful interpretation of the data, at least two and preferably three sites from which a common event can be observed. These sites should have roughly 90-degree arc separation on the surface with an absolute time tie-together of better than 0.1 sec. Ideally, each site should have 3-axis sensing with a long-period instrument with sufficient sensitivity for monitoring remote seismic events. The key point, however, is the need for multiple station siting. With such an array, the questions about the existence of a crust, mantle, and core could be answered in exactly the same way as was done on Earth and on the Moon; current tectonic activity could also be determined.

The active seismic experiment is analogous to well-logging shots where a linear array of geophones picks up the returned signals from a subsurface detonation of a high-explosive charge. Lehner and Kovatch have developed and tested a dual to this in which a single high-frequency sensor (geophone) picks up the signals from the successive detonations of a series of surface high-explosive charges. The depth probed is comparable to the charge-sensor spacing and the resolution is a function of the frequency response of the sensors. As would be expected, this is a precision shallow mapping technique well suited for polar cap exploration or for use in areas with prominent stratification such as an aeolian mantle overlying lava or bed rock.

Clearly, the penetrator method of subsurface exploration does impose certain limitations on the science which may eliminate some of these desirable subsurface experiments and render questionable the validity of others. To facilitate an evaluation of the effect of these limitations, summaries of relevant penetrator and environmental characteristics are presented in Tables I and II.

TABLE I

Penetrator Limitations on Science and Electronics

Dimensions	Cylinder: 7.6 cm diameter by 102 cm long
Weight	7.3 kg
Power	300 mW
Memory	50,000 bits
Transmission window (once per Martian day)	6.4 minutes at 200 bits/sec, max

TABLE II

Penetrator Induced Environment

Deceleration:[*] forebody	Max average $\leq$ 1200 g for 15-20 ms (see Appendix C) Max peak $\leq$ 1800 g for 5 ms (see Appendix C)
afterbody	Max peak $\leq$ 18,000 g for 2-3 ms (see Appendix C)
Thermal exhaust	20 watts (see Appendix D)
Radiation	$\approx 10^5$ neutrons/sec (see Appendix D)
Placement depth	Uncontrolled 1 - 15 meters
Attitude	$\leq 15^{\circ}$ displacement from vertical
Physical	Comminution and fracture of surrounding solid media

[*]Earth g

Of the experiments listed earlier as particularly suitable for subsurface emplacement, some are compatible with the penetrator-imposed limitations, and some are less so.

The penetrator carries a high-frequency accelerometer whose output is doubly integrated to give the depth at which the forebody comes to rest. This deceleration record itself provides a direct measurement of the penetrability and stratification, over the depth of the penetrator emplacement, of the Martian surface. These data, when compared with similar data taken in analog Earth materials, will provide insight into the structure of the Martian subsurface. In addition, other data will aid in interpreting the accelerometer data. For example, in that Doppler-shift measurements on the 400-MHz carrier of the penetrator transmitter (made at the orbiter) can locate the penetrator to an accuracy of ≈ 50 meters, the geology of the impact site can be determined by using the Mariner 9 photogeology survey. Furthermore, if a chemistry experiment is conducted, knowing the light element composition of the material surrounding the penetrator could aid in its petrological and mineralogical characterization supplemented by the deceleration record. Similarly, measurements of thermal properties or a determination of water content would aid in analyzing the "borehole or vertical profile physical geology" over the depth of the penetrator emplacement.

1

Passive seismological studies are eminently suited to the penetrator mission. The penetrator can accommodate appropriate three-axis seismic instruments of two types: the Viking seismometer and the geophone (see Appendix F). The fact that the penetrator mission provides four penetrator locations automatically provides a seismic net. Dispersion of the seismic sites will be achieved by deploying the penetrators at different times as the orbit precesses around the planet. The master clock in the orbiter will be compared with the clocks in the penetrators to provide a 0.1-second time tie-together for the seismic data from all four penetrators. Additionally, the subsurface placement of the penetrator provides a superior coupling of seismic instruments to the surrounding soil.

Thermal conductivity can be measured or inferred from three different sets of measurements. First, the rate at which the vehicle cools after coming to rest is related to the thermal diffusivity of the surrounding material so that a vehicle cooling-time history can give thermal conductivity. Second, because the preferential heat path from the accurately known RTG heat source is through the nose of the penetrator, the equilibrium temperature distribution along the vehicle is a function of the vehicle parameters and of the thermal conductivity of the material around the vehicle. The thermal parameters can be empirically determined before launch. Finally, a precisely determined electrical source of heat can be applied locally, and the resulting temperature can be measured. These techniques are completely compatible with the penetrator environment, and at least the first two would probably be used in all penetrators for corroboration of the measurements.

Two remote chemical analysis techniques used on the moon are candidates for a penetrator mission: alpha-backscatter analysis and neutron activation analysis. As discussed in Appendix F, there is little doubt that the alpha-backscatter instrument can tolerate the penetration-induced environment; therefore, it is classified among the most compatible science instruments. The neutron activation instrument as it exists at present uses a thallium-loaded sodium iodide monocrystal in a scintillation detector in conjunction with a photomultiplier. Both of these components are very susceptible to shock damage; therefore, a development program would be required to adapt the neutron activation chemistry instrument to a penetrator, although the extended range of elements which it would assay would appear to justify such an effort. Incidentally, both techniques can infer the total quantity of H_2O and CO_2 from indirect measurements of C, H, etc., which make them very valuable adjuncts to a direct volatiles analysis which would only ascertain loosely (thermal release at moderate temperatures) bound H_2O and CO_2.

Because of their adaptability to the penetrator mission, the following experiments have been included in the baseline design presented in this document: in the forebody, geochemistry, temperature, deceleration, and seismic instruments; in the afterbody, temperature and deceleration instruments.

An aspect of the penetrator mission which can aid the determination of these more difficult soil characteristics is that information returned from a fairly inexpensive penetrator mission can be used to help choose desirable locations for a future sample-return mission.

Penetrator Delivery and Emplacement

Delivery and emplacement of the penetrators and their science payloads for subsurface exploration of Mars involves the combination of mechanical design, aerodynamics, and terradynamics. This task is accomplished in three steps: (1) transport to a Martian orbit, (2) entry through the Martian atmosphere, and (3) emplacement into the Martian surface. Each part of the delivery sequence imposes demands, often competing, on the penetrator and entry system designs. For instance, compatibility with the spacecraft dictates a compact package, while atmospheric entry and deceleration require a large drag area. Also, successful penetration of a broad range of surface materials requires a slender, rather heavy vehicle, while launch vehicle and spacecraft capabilities dictate that the weight be kept as low as possible. Furthermore, accomplishment of scientific objectives requires subsurface emplacement of the payload, while communications of data to the orbiter requires that the antenna be at the surface.

A design concept, which accomplishes the delivery of the penetrator to the surface and satisfies the competing demands of the spacecraft, atmospheric entry, and surface penetration, is illustrated in Figure 1. This concept is based on existing technology. The penetrator and its terminal deceleration system are packaged in a cylindrical canister which is in turn carried in the spacecraft launch tube. The canister provides a clean interface with the spacecraft launch tube and the deorbit rocket motor. In addition, the canister provides a biobarrier which minimizes the impact on the mission of a prelaunch failure of the primary biobarrier, the launch tube. Upon ejection from the launch tube, the canister is pneumatically extended to twice its original length to provide a high-drag first-stage decelerator and heatshield for atmospheric entry. At the appropriate time, the cylinder is removed, and a large parachute is deployed. This large parachute further decelerates the penetrator and orients it to near vertical. After the proper attitude has been achieved, the large parachute is released and a cluster of three small parachutes is deployed for terminal velocity control.

The penetrator employs the detachable afterbody design concept illustrated in Figure 2. In this sequence, the afterbody remains at the surface as the forebody penetrates the subsurface material. The probe is designed to penetrate sufficiently deep in a broad range of surface materials to limit the deceleration experienced by the onboard science and electronics to tolerable levels. The penetrator containing the science and electronics payload is shown in Figure 3.

Atmospheric Entry

The atmospheric entry and deceleration system must provide surface impact conditions compatible with penetrator technology and instrumentation. The impact angle must be within 15 degrees of vertical so that the seismic instrument will operate properly and so that the antenna orientation will be favorable for data transmission to the orbiting spacecraft; the impact velocity must be between 140 and 170 meters per second in order to insure satisfactory terradynamics performance. Furthermore, Martian topographical variations in the expected impact zones require that the rather narrow range of impact conditions be achieved at surface elevations ranging from 0 to 4 kilometers. The atmospheric entry and deceleration system must provide these
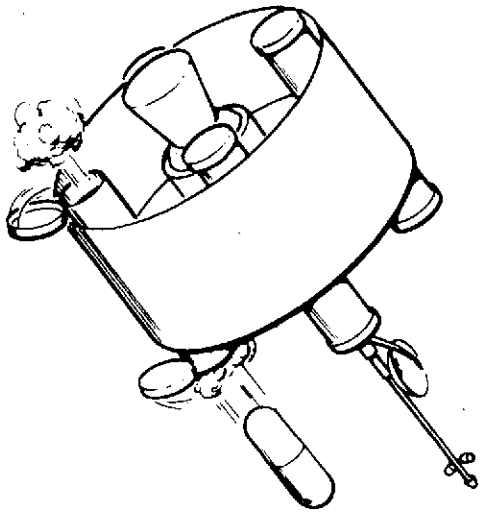
Canister Ejection
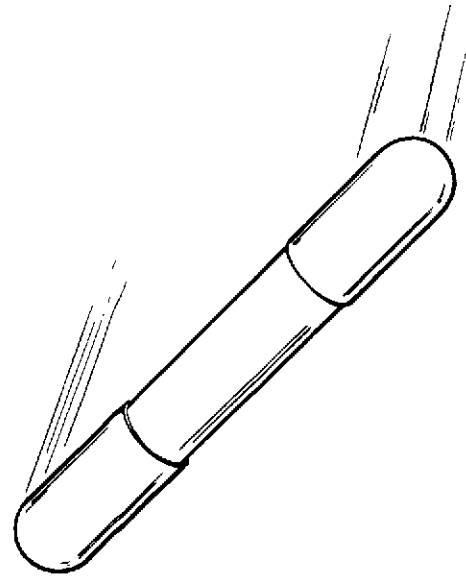
First-Stage Deceleration
(Canister Extended)
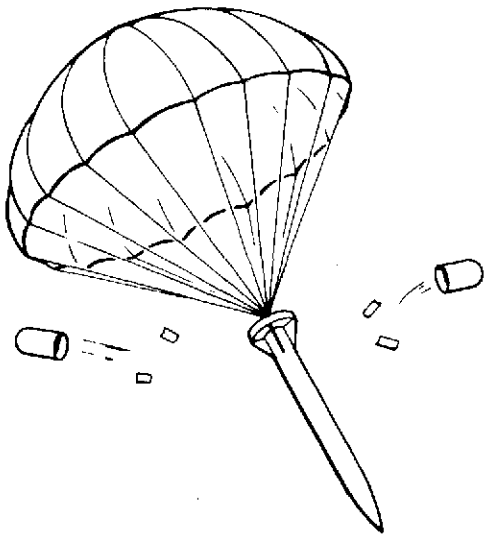
Second-Stage Deceleration
(Turnover Phase)

Third-Stage Deceleration
(Terminal Velocity Control)

Figure 1.   Atmospheric Entry and Deceleration Concept

Figure 2. Implant Sequence

required impact conditions for initial entry angles ranging from -12.5 to -22.5 degrees with an initial entry velocity of 4730 meters per second. In addition, the entry system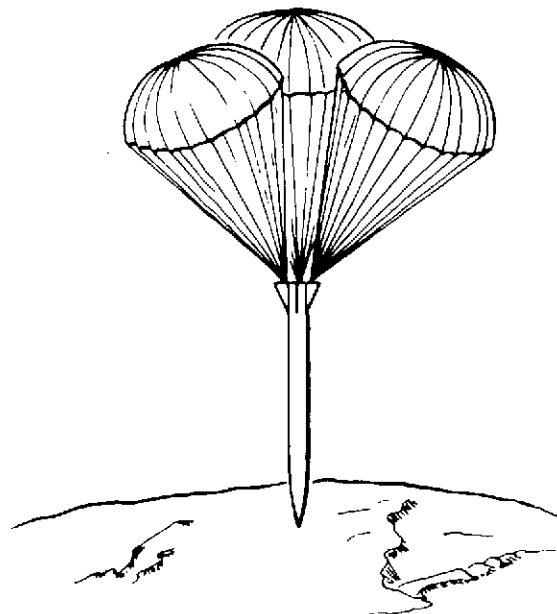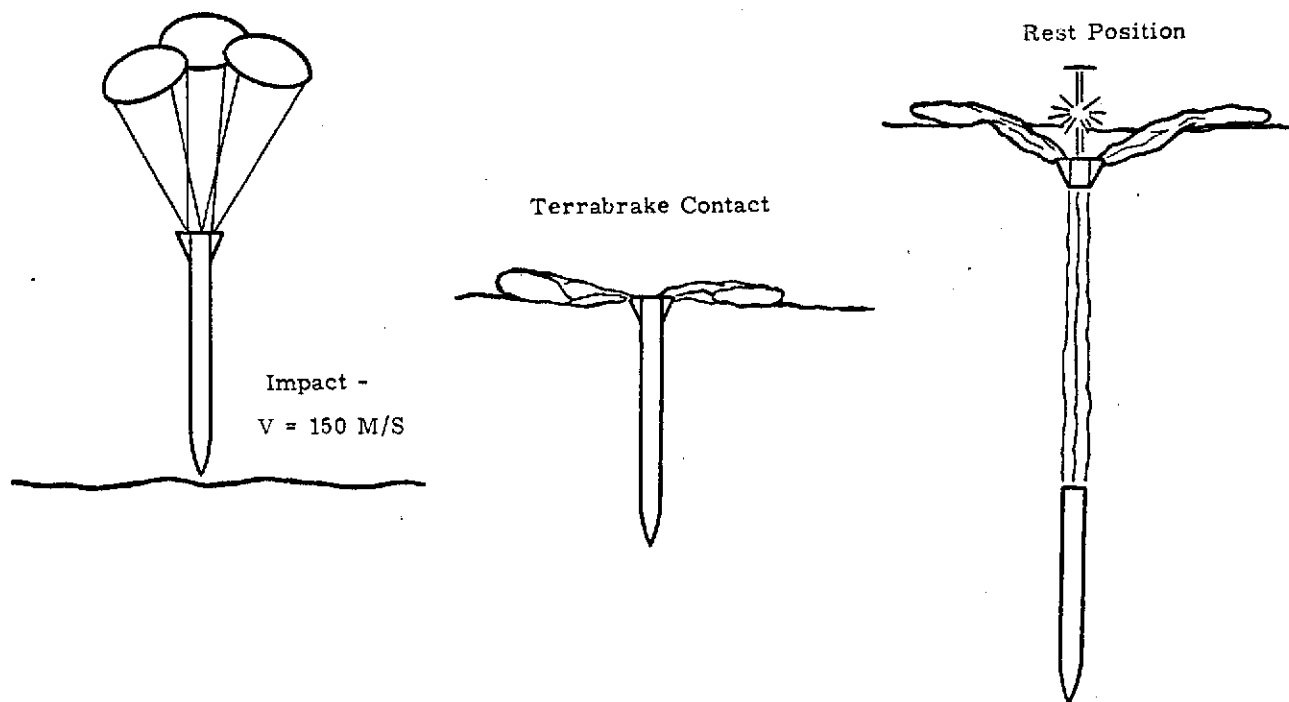 must withstand the aerodynamic heating environment and thermally protect the penetrator and its payload. Finally, the entry system must have the ability to change from an initial compact configuration compatible with storage in the spacecraft to a high-drag configuration required for descent through the Martian atmosphere.

The entry and deceleration system chosen for the Mars penetrator employs, as shown in Figure 1, a telescoping canister first stage which provides thermal protection and initial deceleration and a multistage parachute system which provides the required impact conditions. The detailed analysis which resulted in the selection of this entry and deceleration system is presented in Appendix A. The following discussion summarizes the key points of the analysis.

Two overriding considerations influenced the selection of the entry and deceleration system: the system had to be fundamentally simple and had to employ existing technology wherever possible. The use of a single-stage system was investigated first. A point-mass trajectory computer code was used to perform a parametric study. The results of the study indicated that a single-stage system could not provide the necessary impact conditions over the range of initial atmospheric entry conditions and surface elevations required. The study firmly established the requirement for a multistage system.

Radioisotopic Thermal
Generator (2 required)

Battery

3-Axis Seismometer

Accelerometer

Alpha-Proton Backscatter Assembly
(3 required 120° apart)

Electronics

Temperature
Sensor

Umbilical Storage

Accelerometer-Temperature
Sensor-Electronics

Transmitter

Receiver

Antenna

Weight - 31 kg
Length - 140 cm
Principal Diameter - 9 cm
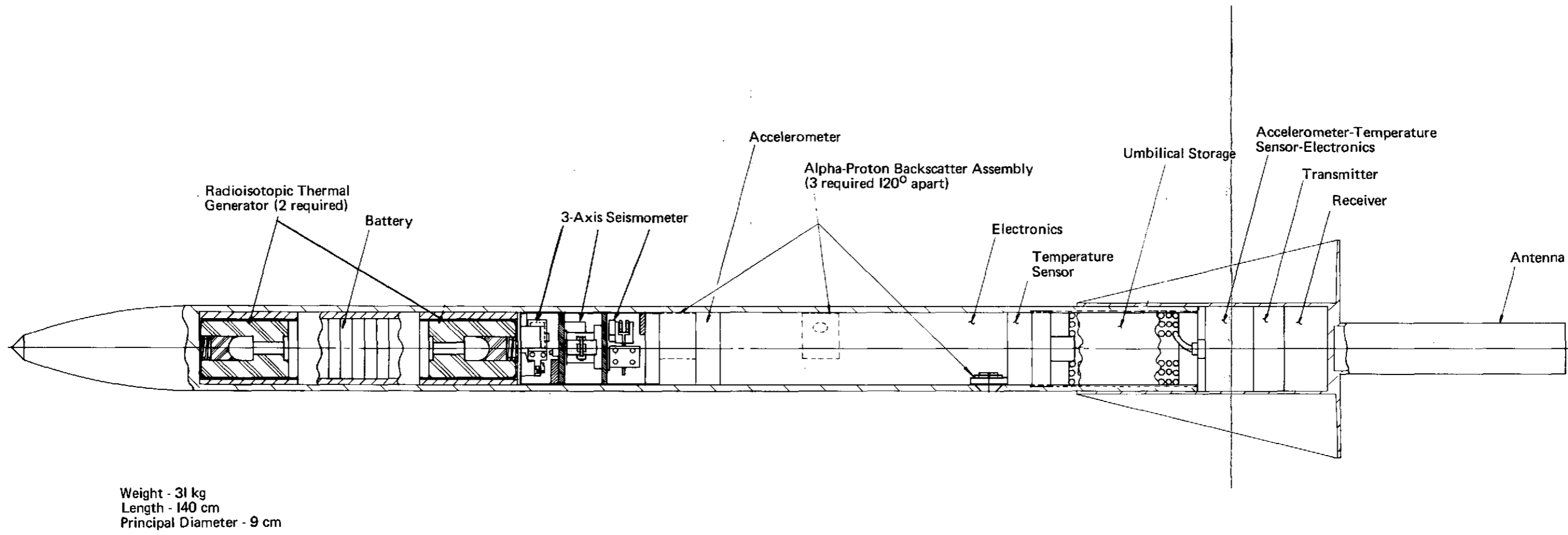
Figure 3. Mars Penetrator

FOLDOUT FRAME 1

FOLDOUT FRAME 2

Further trajectory calculations indicated that a two-stage system might be possible and that a three-stage system would provide the required impact conditions over the entire range of initial entry conditions and surface elevations. Parachutes were chosen for the final-stage (or stages) deceleration devices because of their simplicity of operation and because existing technology could be used. Three first-stage deceleration devices which would provide flight conditions compatible with parachute deployment were considered: a deployable attached decelerator, decelerator flaps, and a telescoping canister. An analysis of each of the three first-stage systems addressed the mechanical operation, flight dynamics, and aerodynamic heating of each system. The results of the analyses show that the telescoping canister is a viable first-stage deceleration system whose development is within existing technology. The decelerator flap system is a possible option; but further study of the aerodynamic heating and flight dynamics problems is required. Viability of the deployable attached decelerator has not been established, and development of a thermal protection system sufficient to withstand the high (near stagnation) local heating rate appears formidable. Furthermore, the flight dynamic effects associated with the flexible body system involve many attendant motion problems. Therefore, the telescoping canister has been chosen for the first-stage deceleration device for the Mars penetrator. This technique, which has been used extensively for the recovery of sounding rocket payloads, will be employed, with parachutes, to recover the Space Shuttle boosters.

The basic design of the telescoping canister (Figure 4) features a thin-walled, thermally protected beryllium cylinder with two telescoping sections at each end of a central fixed penetrator compartment. The force to telescope the sections is provided by low-pressure gas stored in a two-piece toroidal tank positioned around the penetrator. When the canister is ejected from the space-craft, explosive valves open the line from the supply tanks to the molded Dacron-Viton inflatable boots at each end of the penetrator compartment. Upon inflation, the boots extend and lock the telescoping section into position.

As the canister enters the Martian atmosphere, the aerodynamic forces act to rapidly stabilize the longitudinal axis of canister normal to the velocity vector; in this way, maximum drag is achieved. A g-threshold-ΔV fuze, which has proven effective for reentry vehicles in the past, is used to initiate removal of the canister and deployment of the second-stage decelerator. Trajectory analyses show that the fuzing criteria of 20-Mars-g threshold and 3637-meters-per-second velocity change provide conditions (altitude and Mach number) compatible with second-stage decelerator deployment for the complete range of initial entry angle. The canister is removed by a network of hexanitrostilbene flexible linear shaped charge. A circumferential cut at each end and four longitudinal cuts are made to allow the penetrator to be released and the second-stage decelerator to be deployed. The second-stage decelerator is a 6.1-meter-diameter disk-gap-band parachute (a scaled-down version of the Viking parachute). This large parachute rapidly stabilizes and decelerates the penetrator and orients it to near vertical. After this turnover phase has been completed (22 seconds after the large parachute is deployed), a cluster of three 1.0-meter-diameter ribbon parachutes is deployed for terminal velocity control. This cluster of parachutes remains with the penetrator until surface impact. At impact, the parachutes are automatically disconnected from the penetrator. A cluster of three small parachutes was chosen instead of a single, larger

Penetrator

Penetrator Antenna (Stored)

Turnover Parachute Deployment Mortar & Squib

Detonator Assembly

Telescoping Sections

Low Pressure Supply Tank

Inflatable Boot

Circumferential Shaped Charge

Turnover Parachute

Longitudinal Shaped Charge (2 plcs)

Heat Path & Support Structure

Deployment Sequencer

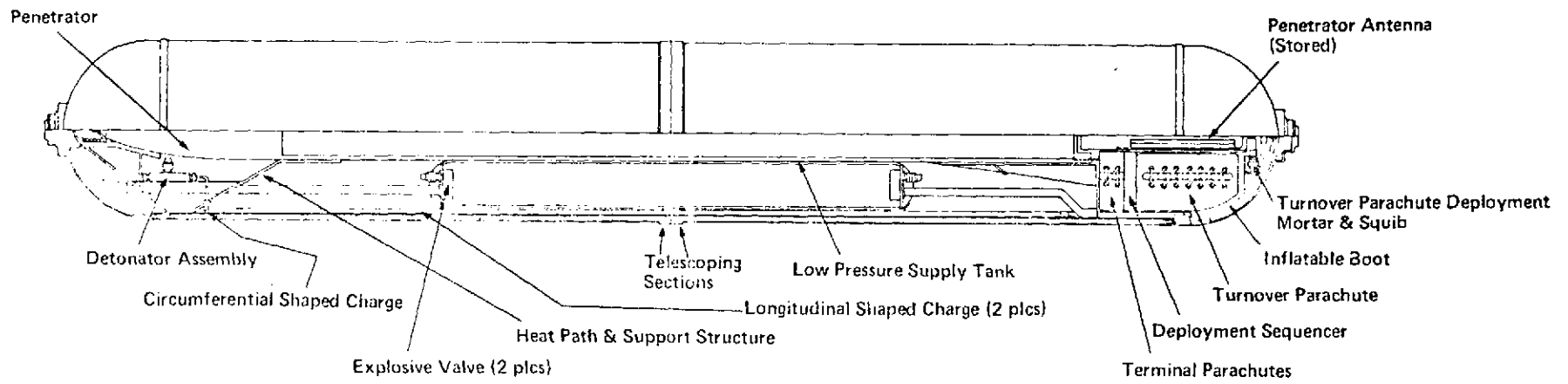Explosive Valve (2 plcs)

Terminal Parachutes

Figure 4. Telescoping Canister

parachute because past experience with Earth penetrators has shown that small parachutes do not interfere with antenna erection (Figure 2).

Subsurface Penetrator

After the penetrator reaches the surface, it must penetrate to its subsurface rest position without exceeding the deceleration limits of the onboard science and electronics. In that the precise impact point cannot be predetermined, the penetrator must be capable of emplacing the science experiments as deep as possible in the broadest range of surface materials.

The penetrator design (Figure 3) which meets these performance requirements employs the detachable afterbody design concept discussed in Appendix B. In this concept (Figure 2), the antenna is left on the surface as the main body continues to penetrate.

In the Mars penetrator (Figure 3), the antenna, transmitter, and receiver are located in the afterbody. The principal scientific payload, power supply, and data handling electronics are all located in the forebody probe. The probe is fabricated of HY180 steel which combines high yield strength and superior fracture toughness. The afterbody is constructed of 7075 T7351 alumimun for minimum weight and adequate strength.

The physical characteristics of the Mars penetrator are shown in Table III.

TABLE III

Physical Characteristics of Mars Penetrator

Complete Penetrator

Weight	31 kg
Principal diameter	9.0 cm
Frontal area	63.6 cm^2
Sectional density	0.49 kg/cm^2
Length	140 cm

Forebody Probe

Weight	28.7 kg
Principal diameter	9.0 cm
Frontal area	63.6 cm^2
Sectional density	0.45 kg/cm^2
Length	123 cm

Detachable Afterbody

Weight	2.3 kg
Principal diameter	23.0 cm
Frontal area	348 cm^2
Sectional density	0.007 kg/cm^2
Length	28 cm

As designed, for a nominal impact velocity of 150 m/s, the penetrator performs as follows:

1. Penetrates to a depth of 1 meter in a basaltic lava with a 2500 N/cm^2 unconfined compressive strength, a bulk density of 2 gm/cm^3, and a porosity of 30 percent.

2. The forebody probe penetrates to a maximum depth of 15 meters.

3. The payload experiences maximum average decelerations of 1200 Earth g's for 15 to 20 msec and maximum peak decelerations of 1800 Earth g's for 5 msec.

4. The detachable afterbody experiences peak decelerations of 18,000 Earth g's for 2 to 3 msec.

The detailed systems analysis which led to the penetrator configuration is presented in Appendix C. As in the case of the atmospheric and entry systems analysis, the key points of the penetrator design analysis are summarized here.

The empirically developed penetration prediction equation (B-2) of Appendix B,

$$D = 0.0117 \text{ SNK } (W/A)^{1/2} (V - 30.5),$$

where

D = depth, meters

S = material penetrability, dimensionless

N = nose coefficient, dimensionless

K = mass scale factor, dimensionless

W = weight, kg

A = sectional area, cm^2

V = velocity, m/s,

was used to determine the values of the design parameters N, W/A, and V which would give the desired depth of implantation over the broadest range of penetrability of surface materials.

A tangent ogive nose with a length-to-diameter ratio of 2.4 was chosen because test experience has shown this nose shape to have satisfactory performance characteristics over a wide range of surface materials. The nose shape has a nose coefficient value of 1.0.

The impact velocity and sectional density were determined by

1. Requiring a minimum penetration of one meter in the hardest anticipated material: S = 1.0,

2. Restricting the maximum allowable payload deceleration to 1800 Earth g's or less.

The analysis resulted in a sectional density (W/A) of 0.49 kg/cm^2 and an impact velocity of 150 m/s being chosen for the Mars penetrator.

The penetrator diameter and the weight were determined by the payload diameter and the penetrator case wall thickness. A payload diameter of 7.6 cm and a case wall thickness of 0.70 cm were selected as being consistent with the science and structural requirements of the Mars penetrator. The resulting principal diameter of the penetrator is 9 cm, and penetrator weight is 31 kg.

The forebody probe length is determined by the payload volume. The nominal design has a payload volume of 4500 cm^3; therefore, the resulting payload length is 102 cm. When the nose length is added, the length of the probe becomes 123 cm. The weight of the probe is 21.4 kg, exclusive of the payload. The payload is estimated to weigh 7.3 kg, which brings the total probe weight to 28.7 kg. The detachable afterbody is estimated to weigh 2.3 kg including aluminum structure, antenna, transmitter, and receiver.

Surface Materials -- Four surface materials have been considered for Mars: rock, lag gravel, dune sand, and loess (Reference 8). A range of expected penetrability values has been estimated for these models on the basis of experience with similar Earth materials. Table IV gives typical penetrability values for some natural Earth materials.

TABLE IV

Typical Penetrability Values for Natural Earth Materials

Soil Constants	Materials
0.2 - 1	Massive medium- to high-strength rock, with few fractures. Concrete, 2000 to 5000 psi, reinforced.
1 - 2	Frozen silt or clay, saturated, very hard. Rock, weathered, low strength, fractured. Sea or fresh-water ice more than 10 feet thick. Basaltic lava flows.
2 - 3	Massive gypsite deposits. Well-cemented coarse sand and gravel. Caliche, dry. Frozen moist silt or clay.
4 - 6	Sea or fresh-water ice from 1 to 3 feet thick. Medium dense, medium to coarse sand, no cementation, wet or dry. Hard, dry dense silt or clay. Desert alluvium.
8 - 12	Very loose fine sand, excluding topsoil. Moist stiff clay or silt, medium dense, less than about 50 percent sand.
10 - 15	Moist topsoil, loose with some clay or silt. Moist medium stiff clay, medium dense, with some sand.
20 - 30	Loose moist topsoil with humus material, mostly sand and silt. Moist to wet clay, soft, low shear strength.
40 - 50	Very loose dry sandy topsoil (Eglin AFB). Saturated very soft clay and silts, with very low shear strengths and high plasticity (Great Salt Lake Desert and bay mud at Skaggs Island). Wet lateritic clays.
> 50	Massive sediments.

The rock is expected to have a penetrability ranging from S = 0.2 to S = 1.5. The Mars penetrator is designed to satisfactorily implant in fairly porous (porosity ≥ 30 percent) lava rock which, from previous test data, has a penetrability of 1.0. A penetrator capable of penetrating in a massive, very hard rock formation would be too heavy for the Pioneer/Mars mission, and the payload would experience excessive decelerations. Reference 8 states that a surface of hard rock "... seems improbable."

Lag gravel is defined by Reference 8 as being "... coarse particulate materials too large to be removed by wind." The effect of such blocks on penetrator performance is dependent on block size and the probability of hitting a block large enough to adversely affect penetrator performance. A block diameter of the order of 5 times the penetrator diameter is considered tolerable. Data from Surveyor sites, shown in Reference 8, indicate that the cumulative frequency of blocks per square meter larger than 0.5 meter in diameter is of the order of 10^{-2} and that the cumulative fraction of the area covered by blocks larger than 0.5 meter is also of the order of 10^{-2}. Consequently, it is assumed that the lag gravel will have no effect on the penetrator performance, and no penetrability value has been assigned for this case.

Dune sand and loess are wind-deposited materials differing primarily in grain size; loess is the finer grained material. Experience with similar Earth materials indicates that the penetrability of dune sand should range between S = 10 and S = 12 and that the penetrability of loess should range between S = 10 and S = 15.

Performance -- The penetration performance of the Mars penetrator has been estimated from Equation (B-2) of Appendix B. In that the surface penetrability of Mars is unknown, the performance has been estimated as a function of surface penetrability (S). The depth and average deceleration of the afterbody are shown as functions of surface penetrability in Figure 5. The deceleration curve is terminated at a penetrability value of 2.0. For penetrability values less than 2.0, separation does not occur, and the afterbody experiences the same deceleration as the probe. The probe deceleration and depth are shown in Figure 6.
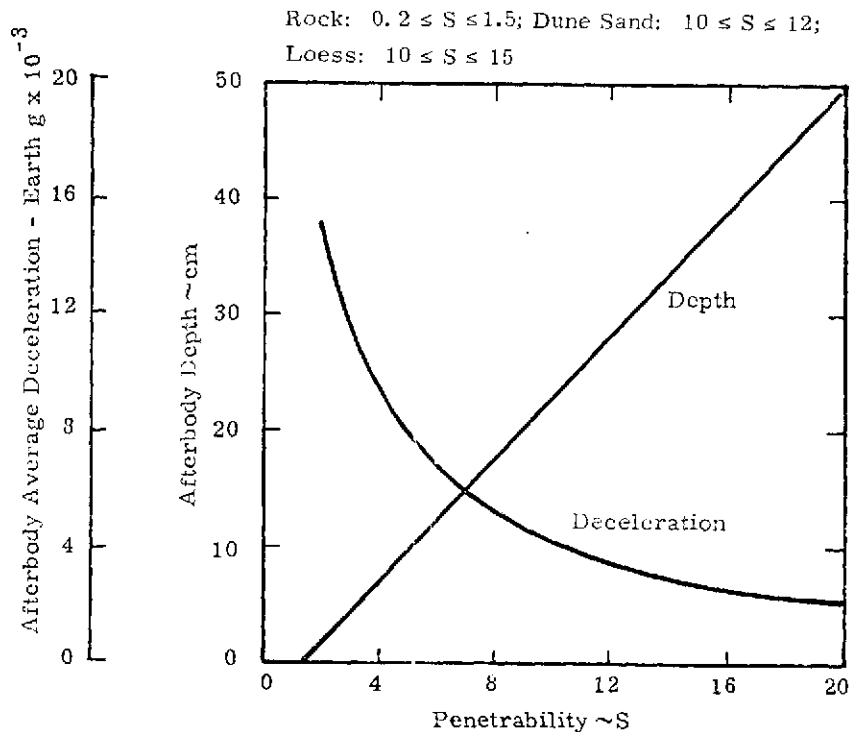

Figure 5. Afterbody Performance

Rock: $0.2 \le S \le 1.5$; Dune Sand: $10 \le S \le 12$;
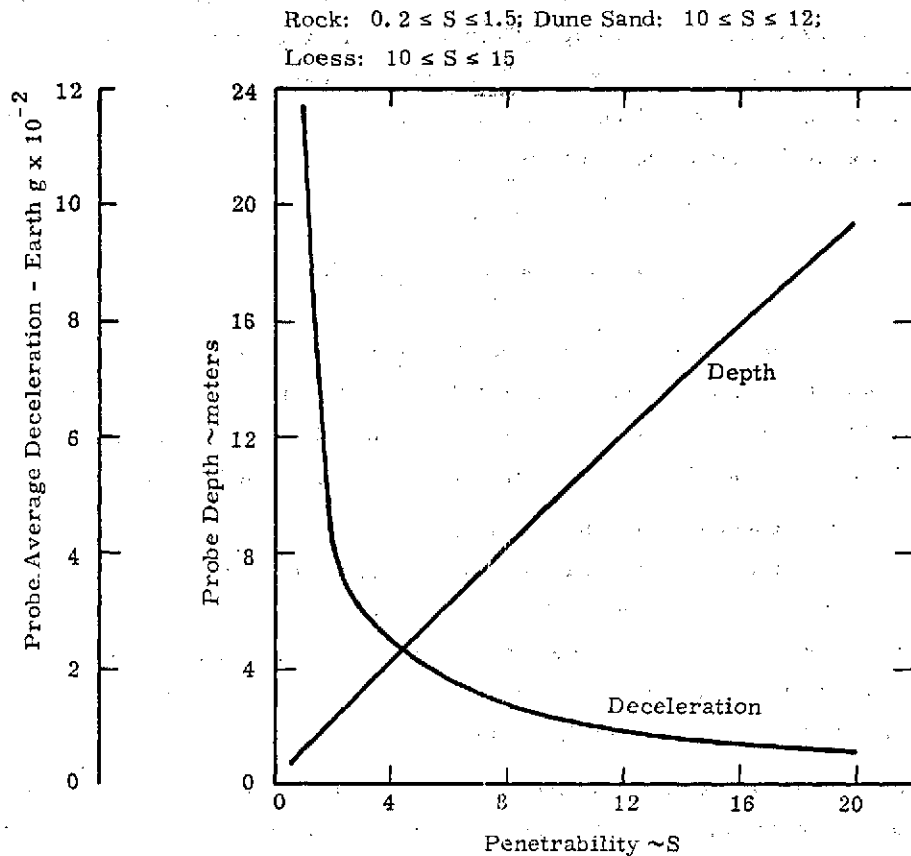Loess: $10 \le S \le 15$

Figure 6. Probe Performance

Wind Effects -- Surface winds affect penetrator performance. In the presence of a surface wind, the velocity vector of the penetrator with respect to the ground is not aligned with the longitudinal axis of the penetrator at impact. As the penetrator enters the surface, lateral forces are experienced as the longitudinal axis of the penetrator aligns itself with the resultant velocity vector. The magnitude of the resulting lateral forces is a function of the ratio of the wind velocity to the impact velocity and of the penetrability of the material: the larger the velocity ratio and the harder the surface material, the greater the lateral forces. The effect of lateral forces ranges from slight changes in penetrator rest angle, with respect to the local vertical, to failure to implant. However, to date, the effects of winds on penetration performance have not been predictable. Experience has led to an empirical rule: for all soils (not rock), a velocity ratio of

$$\frac{\text{wind velocity}}{\text{impact velocity}} \le 0.2$$

is tolerable. For the Mars penetrator, this corresponds to a wind velocity of 30 m/s. Probability distributions for near-surface winds for both north and south latitudes are given in Reference 8 and are summarized in Appendix G. These data indicate that tolerable wind conditions can be expected in the north 95 percent of the time; in the south, the probability drops to 80 percent.

It should not be concluded that a penetrator necessarily fails if the wind exceeds 30 m/s at impact. In cases where the material impacted is fairly penetrable (such as loess), the result of somewhat higher winds would be larger rest angles (with respect to the local vertical) than anticipated. In such cases, only that science, such as the nonrighting seismometer, dependent on close alignment with the local vertical would be affected.

Postemplacement Operations

As presented in the mission concept, when the penetrator enters the Martian surface, the afterbody separates from the forebody and is emplaced at the surface to provide antenna support. The abrupt deceleration of the afterbody triggers a deceleration-sensing mechanism which releases the parachutes so that they will not interfere with antenna deployment.

As the forebody descends below the surface, the accelerometer generates a signal proportional to the deceleration. This signal is digitized and stored in the random access memory in the electronics package. After the forebody finally comes to rest and the deceleration signal has been safely stored in the memory, the penetrator command and control electronics issues the command to erect the antenna. Antenna erection must be accomplished immediately after the penetration to prevent the extreme cold from hindering the movement of the mechanical parts.

The most notable characteristic of the electronics designed for use in the Mars penetrator is the technique of maximizing the usefulness of the limited random access memory (RAM) available (50 kbits). This maximizing is accomplished by use of three features: (1) the analytical abilities of the command and control logic, (2) the wide variety of the sequences stored in the read only memory (ROM), and (3) the control of operations through the command receiver. As an example, if the seismic level on Mars is lower than has been anticipated, a command to the appropriate set of instructions in the ROM could lower the threshold above which seismic events are recorded. Analyses such as spectral analysis could be performed so that the amount of data to be stored and transmitted could be reduced. Moreover, if a portion of the random access memory should fail, the appropriate ROM instruction could be initiated to bypass the failed portion so that the remainder of the random access memory could continue to function.

After the antenna is erected, various measurements such as those of temperature in the forebody, temperature in the afterbody, and of battery voltage are made. In that the penetrator actually strikes the Martian surface in front of the orbiter, the penetrator transmits to the orbiter on the same orbit during which the penetrator has been deployed. This first transmission is automatically initiated by the command and control electronics, and the available data (the deceleration pulse and the measurements mentioned above) are transmitted repeatedly to the orbiter, either until the orbiter commands a cessation of the transmission or until a preset time has passed.

As the orbiter passes over and receives the initial transmission, the Doppler shift in the transmission from the penetrator is analyzed so that the actual location of the penetrator is determined. Knowledge of the location of the penetrator is important for three reasons: first, the location of the penetrator should be known so that a correlation with photographic data can be made to allow a determination of the type of terrain the penetrator has landed in; second, the location of all the penetrators which form a seismic net must be known so that seismic data can be properly interpreted; third, the location of the penetrator must be known by the orbiter so that the best times for transmission from the penetrator can be determined. Transmission from the penetrator to the orbiter only at the best times is crucial for extending the mission lifetime. If transmission at other than optimal times is performed, the transmission must be for longer periods. The longer periods of transmission use the battery energy at a greater rate and thereby lessen the total mission lifetime. However, a fail-safe mode of operation has been designed into the penetrator. If the command link from the orbiter does not work for some reason, the penetrator clock is used to control transmission times, and the instructions stored in the read only memory are used automatically to sequence the penetrator operation through at least some experiments. Thus, the failure of the command link does not mean a failure of the whole mission, because provisions have been made to continue the mission with a lessened capability.

During the first pass, the orbiter also commands the penetrator to perform the alpha-backscatte experiment calibration. After reception of any command, the penetrator retransmits what it received back to the orbiter. The penetrator operations then pause to allow time for any necessary correction from the orbiter. If no correction is received, the penetrator operations proceed. The alpha-back-scatter calibration is performed while the orbiter is out of transmission range; therefore, the calibration results must be stored for transmission to the orbiter when the orbiter comes back within range. If something has gone wrong with the calibration, it is repeated under command from the orbiter. If the calibration has gone well, the penetrator is commanded to perform the alpha-back-scatter experiment.

In that the experiment is performed while the orbiter is again out of transmission range on the next orbit, the results of the experiment are stored for later transmission to the orbiter. Each transmission will normally include data from the temperature and light (day/night) sensors. If desirable, the alpha-backscatter experiment, as well as any other, can be repeated.

Because each alpha-backscatter measurement involves counting as many as 4096 events (representable by 12 bits) in each of 256 different energy slots for both the alpha and proton detectors, each measurement produces 12 x 256 x 2 = 6144 bits of data. During the calibration portion of the experiment, which occurs during the first orbit, three measurements are performed: the accumulation of background data, the actual pulser calibration, and the standard sample and local atmosphere measurements. Therefore, the calibration produces 3 x 6144 = 18,432 bits, a number of bits well within the ability of the penetrator electronics to store and transmit. The actual experiment, which is normally performed during the second orbit, produces 2 x 6144 = 12,288 bits, because the Mars sample measurement is immediately followed by another pulser calibration.

The mechanism for opening the door to allow illumination of the Mars sample by the alpha source is shown in Figure 7. The penetrator command and control logic operates the pyrotechnic pin puller which allows the spring door to retract.
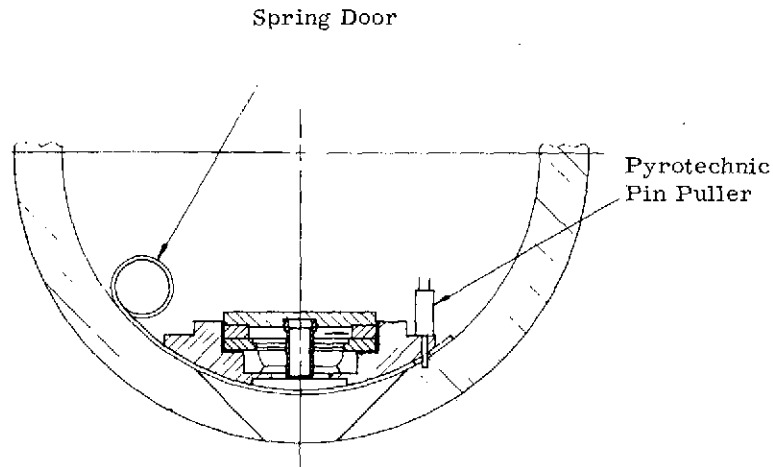
Spring Door

Figure 7. Alpha-Proton Backscatter Door

Three separate alpha-backscatter detector assemblies, each looking at a different Martian sample, are used; therefore, the total alpha-backscatter sequence (alternating calibration and Mars sample measurements for each of the three assemblies) normally takes 6 days.

After the first alpha-backscatter series of experiments, the penetrator mission is primarily devoted to seismic measurements. Because considerable analytical ability is built into the command and control logic, the logic on the penetrator can make decisions about seismic thresholds. Thresholds determined on the basis of seismic information which has already been received can also be set from Earth by the experimenters via the command link. Battery energy sufficient to transmit an average of about 37 kilobits per day for 400 days is available. These 37 kilobits are enough to define 17 "interesting" seismic events. Each such seismic event, which is limited to one minute, is defined on the basis of a data compression scheme which samples the envelope of the signal once per second, produces an 8-bit sample, counts up to 10 zero crossings per second, and produces a 4-bit zero-crossing word. Therefore, 12 bits are produced each second or 720 bits per minute per channel. With three seismic channels, there are 2160 bits per minute, plus a 20-bit time word, for a total of 2180 bits per interesting event. For a total of 17 interesting events per day, there are 17 x 2180 = 37,060 bits per day. Of course, this is only an average, and it is possible to transmit more bits on some particular day at the expense of fewer bits on some subsequent day, because the total number of bits to be transmitted is limited by a fixed amount of battery energy.

The 20-bit time word is necessary for the seismic experiment, because 0.1-second time resolution is important for seismic data. For proper time correlation of all the sensors in the seismic net, the electronic package in the orbiter reads the clocks in all the penetrators, determines their differences from the orbiter master clock, and adjusts the timing of the received seismic data accordingly.

The total data bit output for the whole mission is determined by the battery energy. With the 72-watt-hr lithium battery in the penetrator, a total of 20×10^6 bits can be transmitted. Most of the data thus transmitted are seismic data. A rough division of the total data output is as follows:

Synchronization codes, 3 percent;

Housekeeping and low-data-rate data (temperature, light), 5 percent;

Alpha-backscatter experiment, 2 percent;

Accelerometer, less than 1 percent;

Seismic data, 89 percent.

After the initial experiments are completed, the penetrators continue to fulfill their mission on Mars: measuring seismic activity and temperature and responding to commands from Earth. These commands can initiate such things as an adjustment of criteria for recording seismic events or the reperformance of the alpha-backscatter experiments. The penetrator mission thus provides a long-term assessment of Martian seismic activity and performs other measurements over an extended period of time.

REFERENCES

1. Exploration of Mars After 1976, NASA Preliminary Report, April 1974.

2. J. F. McCauley, "Preliminary Mariner 9 Report on the Geology of Mars," Icarus, Vol. 17, No. 2, 1974, pp. 289-327.

3. William W. Rubey, "Development of the Hydrosphere and Atmosphere, with Special Reference to Probable Composition of the Early Atmosphere," Crust of the Earth, edited by Arie Poldervaart, pp. 631-650; also, The Geological Society of America Special Paper 62, Geological Society of America, New York, 1955.

4. William W. Rubey, "Geological History of Seawater: An Attempt to State the Problem," Geological Society of America, Bulletin, Vol. 62, 1951, pp. 1111-1147.

5. J. L. Kulp, "Origin of the Hydrosphere," Geological Society of America, Bulletin, Vol. 62, 1951, pp. 326-329.

6. F. P. Fanale and W. A. Cannon, Exchange of Adsorbed H_2O and CO_2 Between the Regolith and Atmosphere of Mars Caused by Changes in Surface Insolation, JPL Preprint, January 30, 1974.

7. R. A. Schorn, C. B. Farmer, and S. J. Little, "High-Dispersion Spectroscopic Studies of Mars. III. Preliminary Results of 1968-69 Water-Vapor Studies," Icarus, Vol. 11 (3), 1969, pp. 283-288.

8. Mars Engineering Model, prepared by the National Aeronautics and Space Administration, Langley Research Center, Viking Project Office, Hampton, Virginia, M75-125-3, January 1974.

APPENDIX A

ATMOSPHERIC ENTRY AND DECELERATION SYSTEMS ANALYSES

Introduction

The use of penetrators for subsurface exploration of the planet Mars requires successful delivery of the penetrators to the planet surface within a range of prescribed impact conditions. These conditions, imposed by penetrator technology and instrumentation limitations, must be provided for a range of initial entry conditions compatible with mission requirements and goals. The mission constraints are defined as follows: entry velocity at an altitude of 100 km (328 kft) of 4730 m/s (15,518 fps), entry angles from -12 to -22.5 degrees; impact velocities from 137 to 168 m/s (450 to 550 fps), impact angles of 15 degrees or less from the vertical, and desired impact conditions (velocity and angle) to be provided over an altitude range from 0 to 4 km (0 to 13 kft).

This appendix discusses the design and analysis of three entry systems potentially capable of meeting these requirements.

Summary

The major results of this atmospheric entry and deceleration systems analysis, performed in support of the proposed subsurface exploration of Mars by use of penetrators, are summarized as follows:

1. A single-stage system (fixed β) is not capable of providing the desired impact conditions (velocity and angle) for the range of imposed mission constraints. A multistage system is required.

2. A common multistage deceleration system (parachutes) used in conjunction with any one of the three first-stage decelerator designs presented will provide the desired impact conditions for the range of imposed mission requirements.

3. A telescoping cylinder is a viable first-stage deceleration system capable of significantly reducing entry speeds. Furthermore, its development is within existing technology, and no major problems are foreseen.

4. A flap decelerator is a possible first-stage option but requires further study to satisfactorily address the shock interference problem and to establish the shell structural stability. Extensive development may be required to solve the flight dynamic resonance problems.

5. Viability of a deployable attached decelerator as a first-stage decelerator has not been established. Development of a thermal protection system to withstand the high (near stagnation) local heating rates appears formidable. The flight dynamic effects associated with the flexible body system involve many attendant motion problems; moreover, potential weight/packing problems are implied.

6. Results of analyses are preliminary. Optimum designs (weight and size) have not been achieved in the limited study presented herein.

Entry Systems Conceptual Designs

A design feature common to all three entry systems is the ability to change from the initial configuration, which is compatible with storage in the spacecraft, to a low ballistic coefficient (β) configuration after ejection from the spacecraft but prior to entry into the Martian atmosphere. The initial low-β configuration is desired to provide flight conditions compatible with parachute deployment at appropriate altitudes and to reduce the overall aerodynamic heating environment. To achieve this goal, three conceptual designs, a telescoping cylinder, a deployable attached decelerator, and decelerator flaps have been considered.

Telescoping Cylinder

The basic features of the telescoping cylinder are shown in the drawing presented in Figure A-1. This design is a thin-walled, thermally protected beryllium cylinder with two telescoping sections at each end of a central fixed penetrator compartment; these sections are capable of expanding not more than 2.5 times the original length of 190 cm (6.2 ft).

The force required to telescope the sections is provided by low-pressure gas stored at 43.2×10^4 N/m^2 (0.9 lbs/ft^2) in a two-piece toroidal tank $\left[0.014 \text{ m}^3 \text{ (0.50 ft}^3\text{) each}\right]$ positioned around the penetrator probe.

When the cylinder is ejected from the spacecraft, explosive valves open the line from the supply tanks to the molded Dacron-Viton inflatable boots at each end of the penetrator compartment. This extends the cylinder in such a way that the penetrator remains at the center.

The pressure system is sized to provide 7.2×10^4 N/m^2 (0.15 lb/ft^2) in a fully inflated boot; this establishes a force of 2700 N to expand and lock the telescoping sections together. A locking taper and a detent system (not shown) will ensure that the sections will stay fully extended.

At the appropriate time, the cylinder will be removed from around the penetrator by a network of hexanitrostilbene (HNS) flexible linear shaped charges. A circumferential cut at each end and four longitudinal cuts will separate the cylinder into segments and allow release of the penetrator.

The turnover parachute will be deployed by the mortar assembly (Figure A-1). A mechanical/explosive mechanism which deploys the terminal chute and releases the turnover chute is provided. Terminal chute release and antenna deployment will be initiated at surface impact.
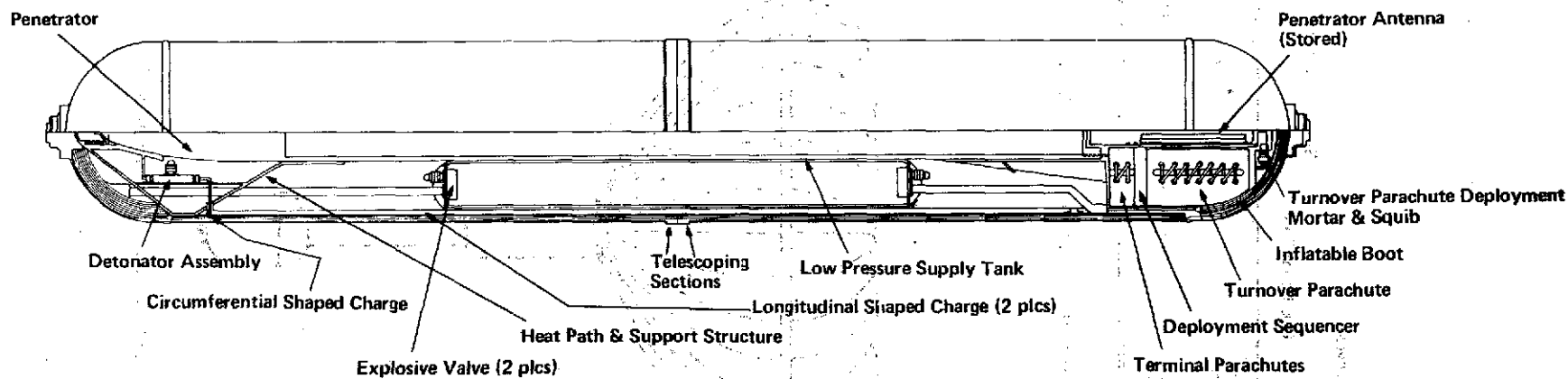
Penetrator

Penetrator Antenna (Stored)

Detonator Assembly

Circumferential Shaped Charge

Explosive Valve (2 plcs)

Heat Path & Support Structure

Telescoping Sections

Low Pressure Supply Tank

Longitudinal Shaped Charge (2 plcs)

Turnover Parachute Deployment Mortar & Squib

Inflatable Boot

Turnover Parachute

Deployment Sequencer

Terminal Parachutes

Figure A-1. Telescoping Cylinder

Parachute Deployment Mortar

Canister Release Device

Penetrometer Canister

Parachute Container

Regulator

Gas-Foam Tank

Sabot

DAD

Mars Orbiter Storage Tube
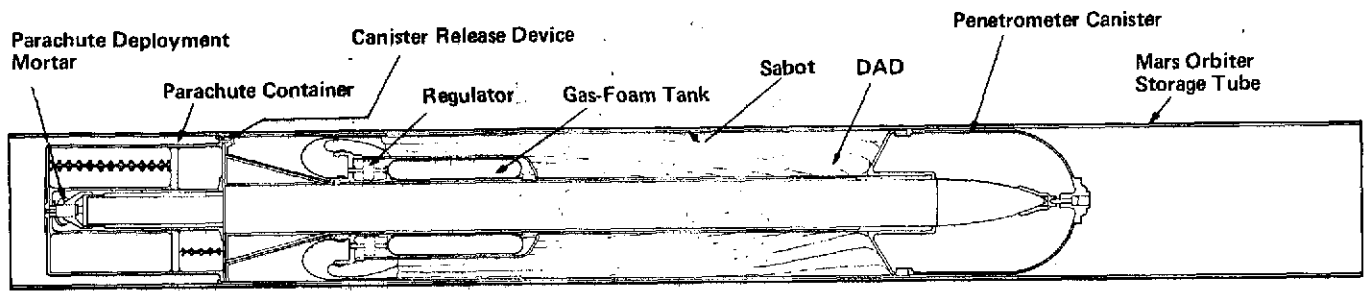
Figure A-2a. Deployable Attached Decelerator (DAD) Entry Design (Stored)
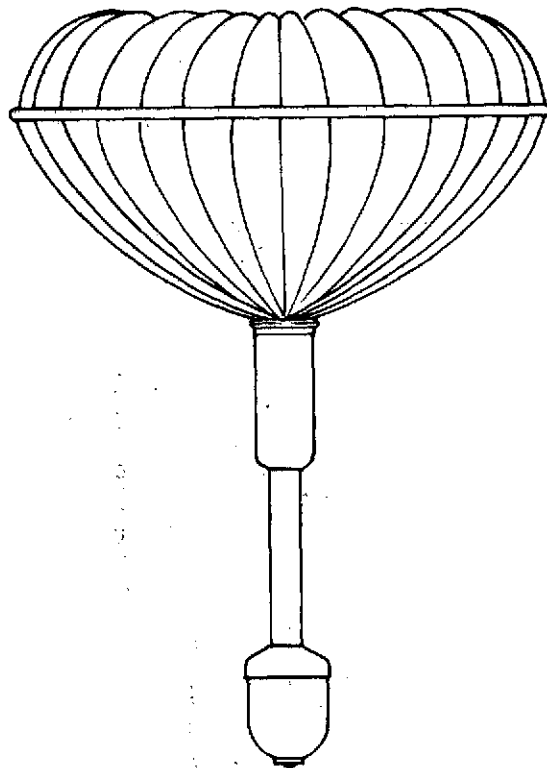
Figure A-2b. DAD Deployed

Telescoping Cylinder Weight Statement --

Penetrator	31.0 kg	(68.3 lbs$_m$)
Parachutes and release mechanism	8.0	(17.6)
Penetrator antenna	1.0	(2.2)
Low-pressure supply tank	1.5	(3.3)
Telescoping cylinder	10.0	(22.0)
Telescoping cylinder thermal protection	8.0	(17.6)
Structural foam and stiffeners Plumbing Explosive/electrical circuits Inflatable boots	2.5	(5.5)
Total	62.0 kg	(136.5 lbs$_m$)

Deployable Attached Decelerator (DAD)

The second concept for the entry system is a deployable attached decelerator (DAD). The decelerator (Figure A-2) would be deployed and inflated from an onboard pressure supply after the penetrator is ejected from the spacecraft. This assures that the decelerator is available to stabilize and begin to decelerate the vehicle as soon as the sensible atmosphere is encountered. Self contained filling also avoids possible problems arising from ram-air inflation, i.e., decelerator flagging, extreme heating concentration at the ram-air inlets, and the necessity to protect the decelerator inside from high-temperature ram-air.

The decelerator provides the proper conditions for deployment of the parachute system. The system ballistic coefficient is 34.3 kg/m^2 (2.6 lb/ft^2).[*] At the proper time, the turnover parachute is mortar deployed. The inflation load of this parachute actuates a mechanism which releases the forward heatshield, decelerator, and decelerator pressurization system. The forward end falls away and assumes a different trajectory because the ballistic coefficient of the decelerator is about three times greater than that of the penetrator/parachute system. The remainder of the parachute system sequence is described in a later section of this appendix.

[*]Based on Martian gravitational constant.

Deployable Attached Decelerator Weight Statement --

Parachute system	7.3 kg	(16 lbs)	
DAD	7.3 to 15.9	(16 to 35)	
Penetrator	31	(69)	
Chute container	1.8	(4)	(Fiberglass)
Mortar assembly	0.9	(2)	(Aluminum)
Canister, forward section	0.7	(1.5)	(Beryllium)
Canister, mid-section	2.9	(6.5)	(Beryllium)
Canister - nose	3.4	(7.5)	(Beryllium)
Tank - gas	0.9	(2.0)	(Beryllium)
Regulator	0.7	(1.5)	(Beryllium)
Total	57.2 to 65.8 kg	(126 to 145.00 lbs)	

Decelerator Flap System

This decelerator system uses a series of curved panels as aerodynamic drag brakes. These flaps serve a double function: their initial function is to form the canister which houses the penetrator package before flap deployment. This would be accomplished by segmenting each of two closely fitting concentric cylinders into four equal circumferential sections (see Figure A-3), a total of eight flaps when deployed. The flaps would be hinged from a tubular lightweight pedestal behind the penetrator. Deployment would take place by releasing two snap rings (top and bottom), allowing the shells to segment freely. Segmenting would proceed at a prescribed rate; this is accomplished by spring-loaded base hinges which have a known viscous damping rate. Once the flaps have attained their correct angular attitude, the hinge would be locked. Decelerator Flap Weight Statement will be furnished at a later date.
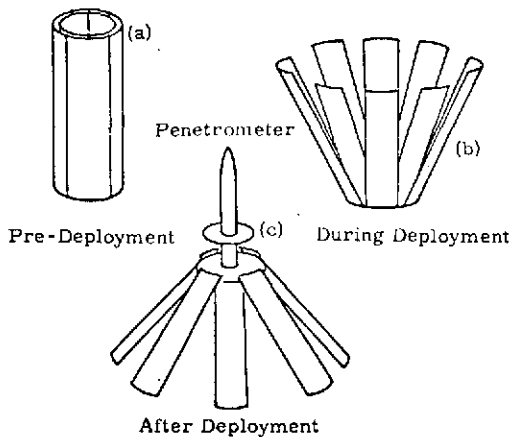
Decelerator Flap Weight Statement

	Large Flaps		Small Flaps	
Penetrator	31.0 kg	(69 lbs)	31.0 kg	(69 lbs)
Parachute	6.0	(13.2)	8.0	(17.6)
Hinge mechanism	2.7	(6.0)	2.7	(6.0)
Flaps	11.8	(26.0)	6.0	(13.2)
Flap thermal protection	9.2	(20.3)	4.6	(10.1)
Flap release system	1.0	(2.2)	1.0	(2.2)
End caps	2.0	(4.4)	2.0	(4.4)
	63.7 kg	(141.1 lbs	55.3 kg	(122.5 lbs)

Figure A-3. Concentric Cylinder Flap Concept

Trajectory Parametric Study

A parametric study of trajectories in the Martian atmosphere was conducted with ballistic coefficient (β) and entry angle (γ_I) as parameters. The purpose of this study was twofold: (1) to determine whether a single-stage vehicle (C_D variation with Mach and Reynolds number only) could provide the required impact conditions described earlier and (2) to suggest initial configuration β's that would provide acceptable chute deployment conditions at later trajectory times when deceleration staging becomes necessary. The trajectories were computed by assuming a point mass entry body with drag coefficients for a cylinder in crossflow input as a function of Mach number and Reynolds number. The ballistic coefficient (β) identified in the parametric study was based on conditions at 22.9-km (75 kft) altitude and Mach 20. The Martian "Mean Equatorial Atmosphere," gravitational constant, and planet diameter were used in the trajectory computations. Plots of velocity, Mach number, dynamic pressure, and flight-path angle as functions of altitude with ballistic coefficient and entry angle as parameters are presented in Figures A-4 through A-23. The study indicates that the required impact conditions $\left[\gamma_I \geq 75°\text{ and }V_I = 137\text{ to }168\text{ m/s (450 to }550\text{ fps) at altitudes between 0 and 4 km (0 and 13 kft)}\right]$ cannot be achieved within mission constraints by a single-stage vehicle. Either the impact velocity or impact angle can be achieved separately, but simultaneous attainment of both impact conditions cannot be achieved. The study clearly indicates that a multistage system is required to achieve the desired impact conditions.
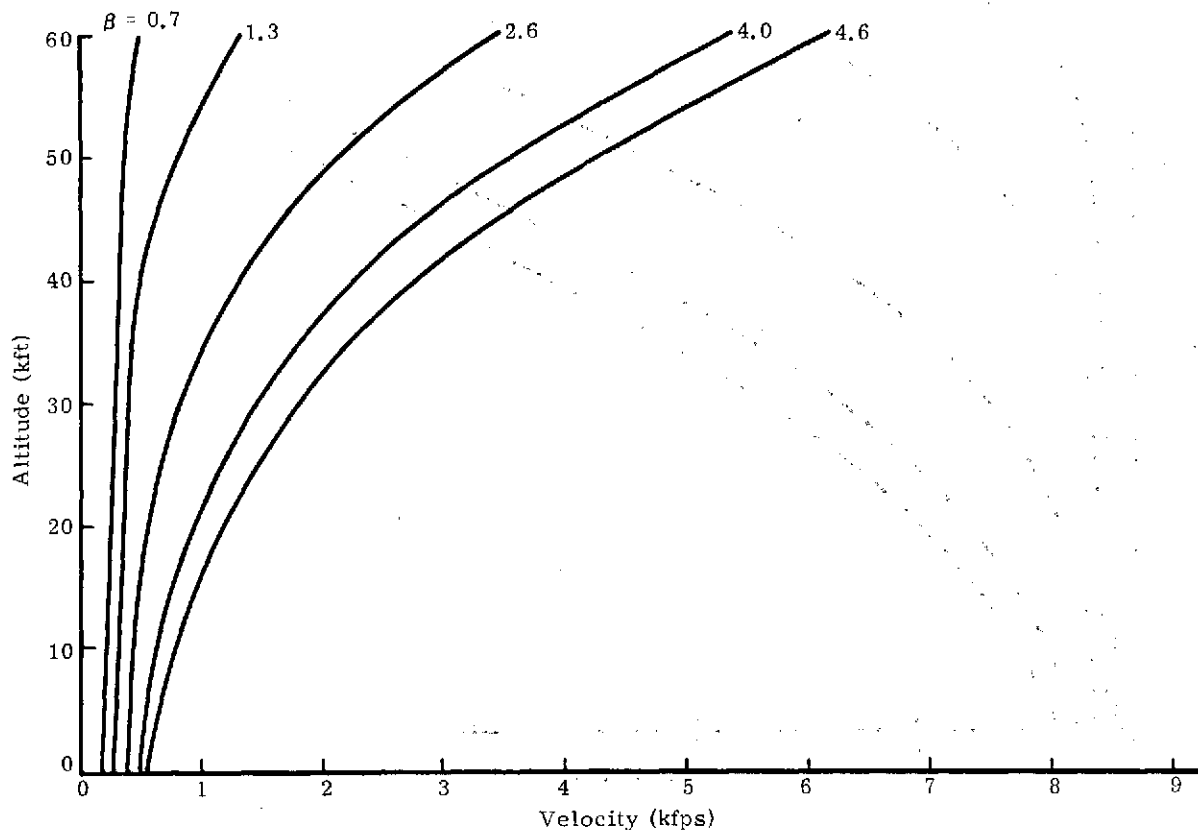

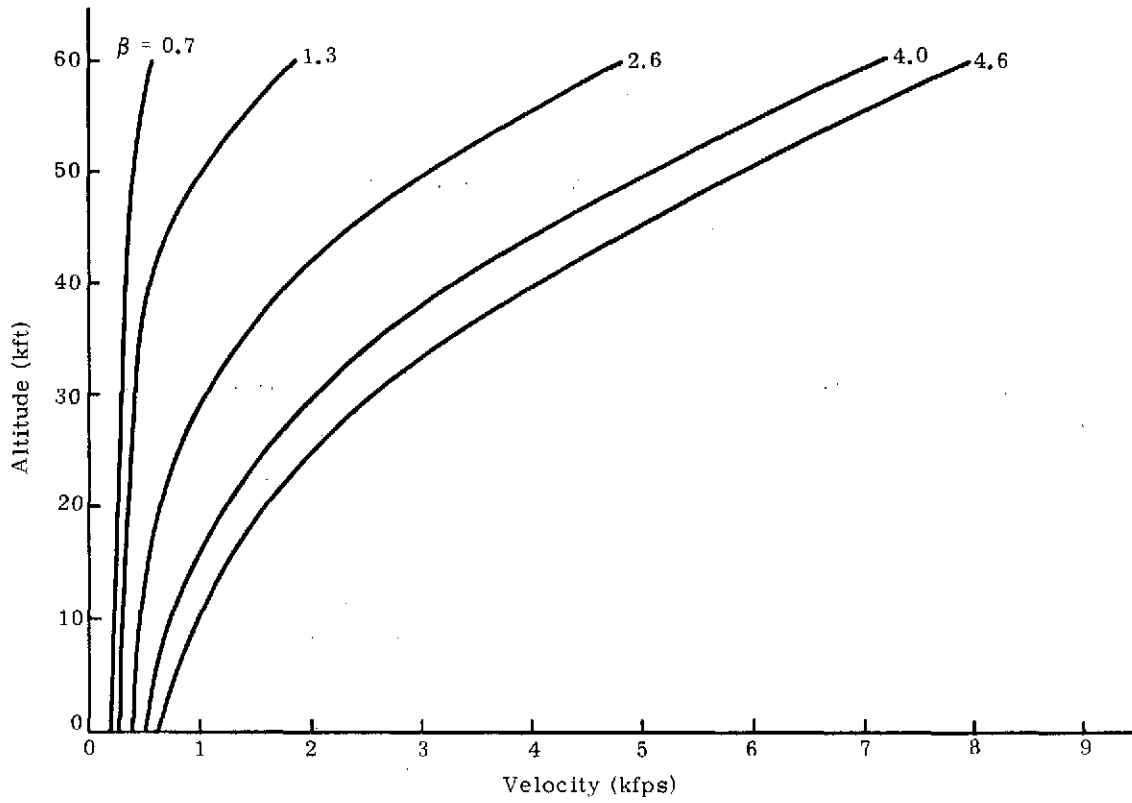
Figure A-4. Mars Penetrator Trajectory ($\gamma_I = -12°$)
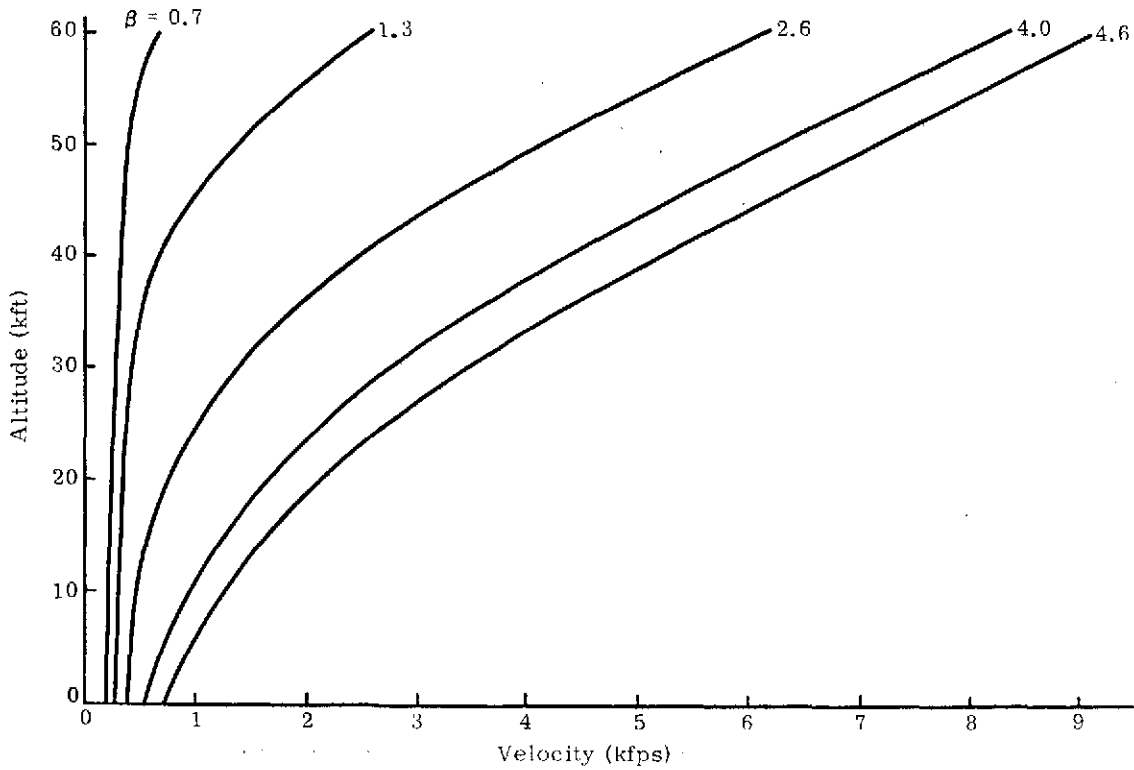
Figure A-5. Mars Penetrator Trajectory ($\gamma_I = -15°$)
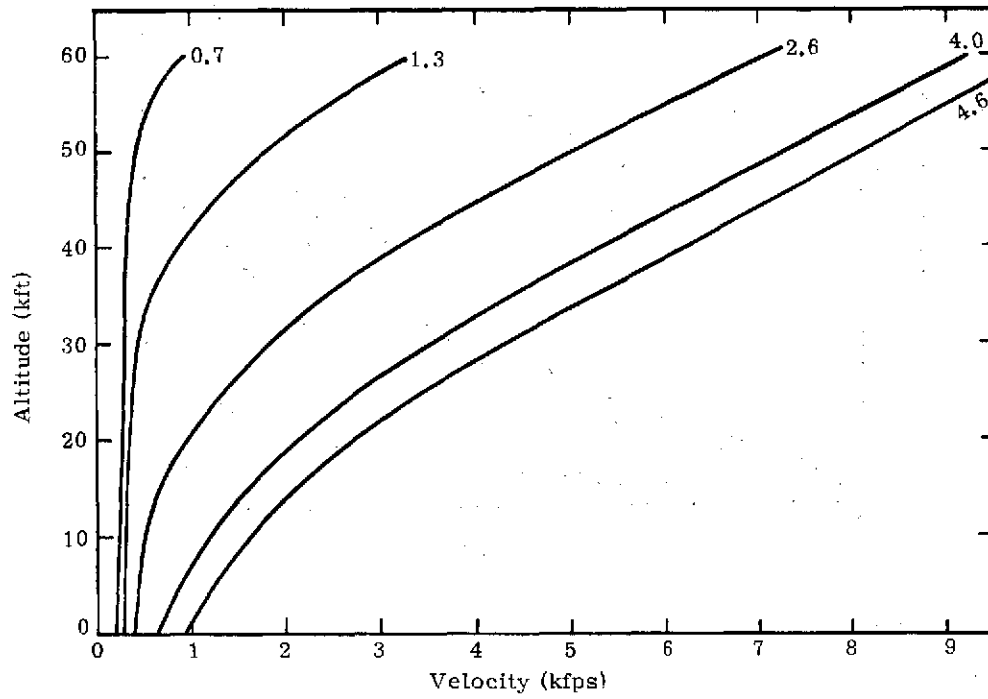

Figure A-6. Mars Penetrator Trajectory ($\gamma_I = -18°$)
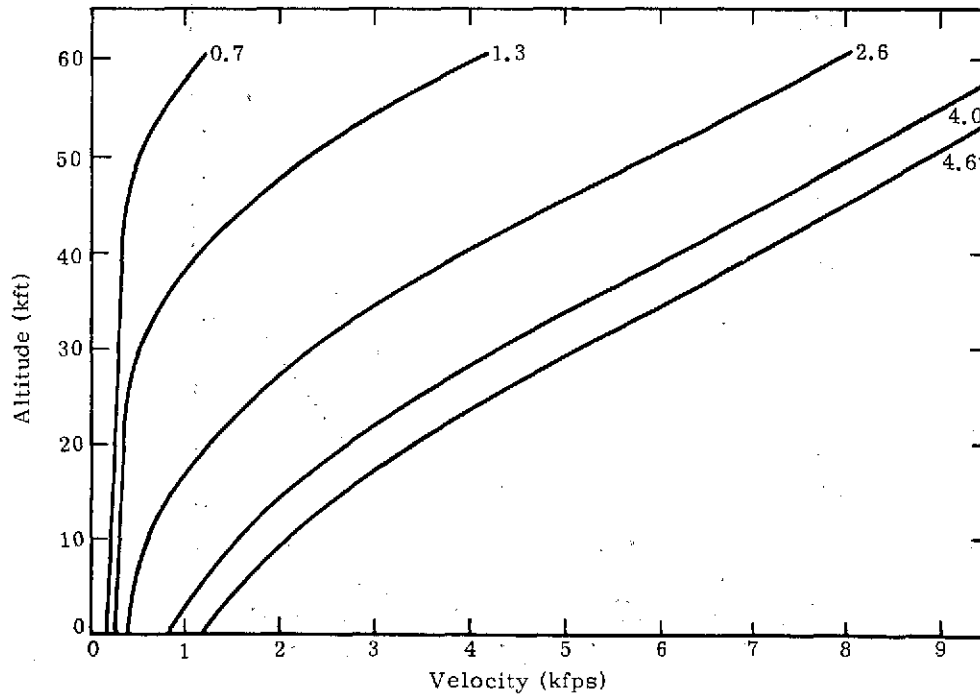
Figure A-7. Mars Penetrator Trajectory ($\gamma_I = -21°$)
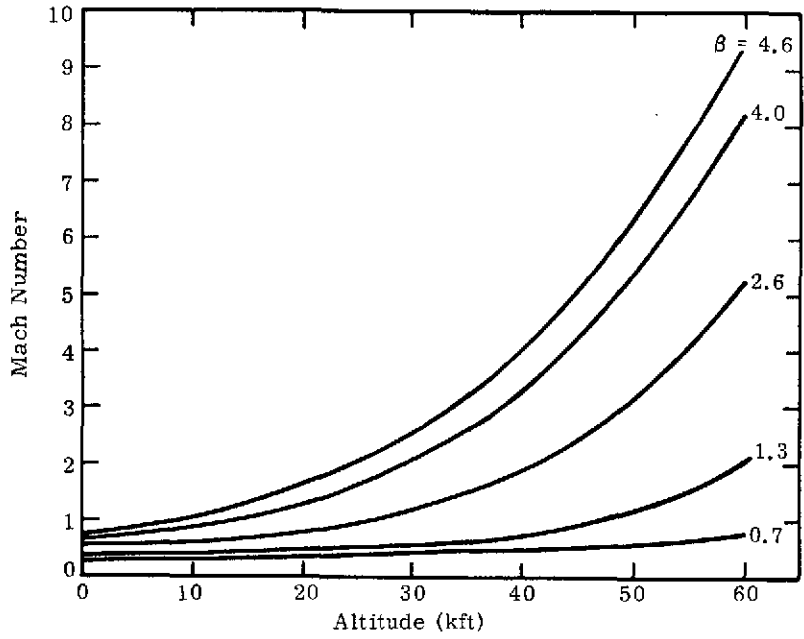

Figure A-8. Mars Penetrator Trajectory ($\gamma_I = -24°$)

Figure A-9. Mach Number as a Function of Altitude ($\gamma_I = -12°$)

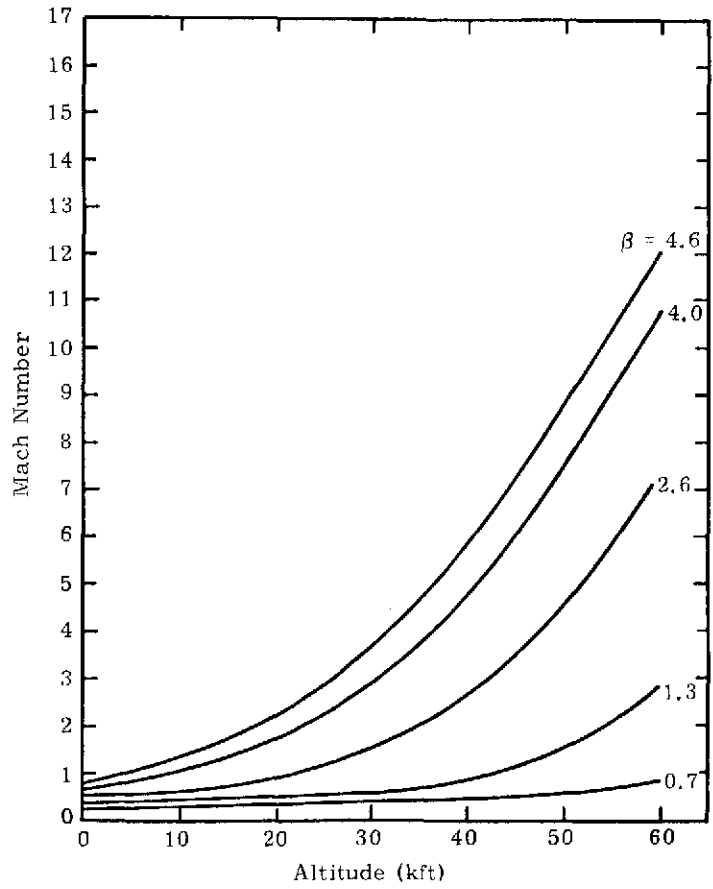Figure 10. Mach Number as a Function of Altitude ($\gamma_I = -15°$)

Figure A-11. Mach Number as a
Function of Altitude
$(\gamma_I = -18°)$
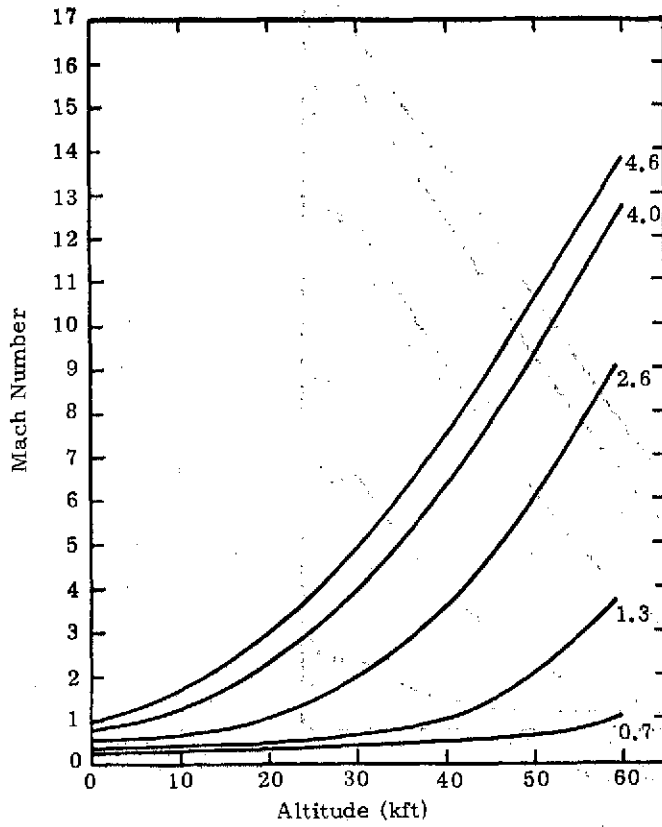
Figure A-12. Mach Number as a
Function of Altitude
$(\gamma_I = -21°)$
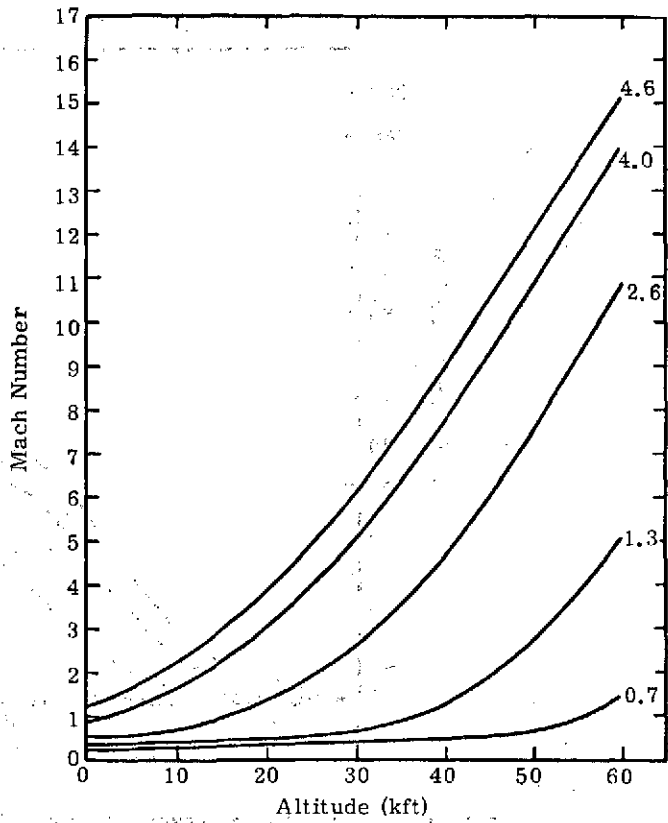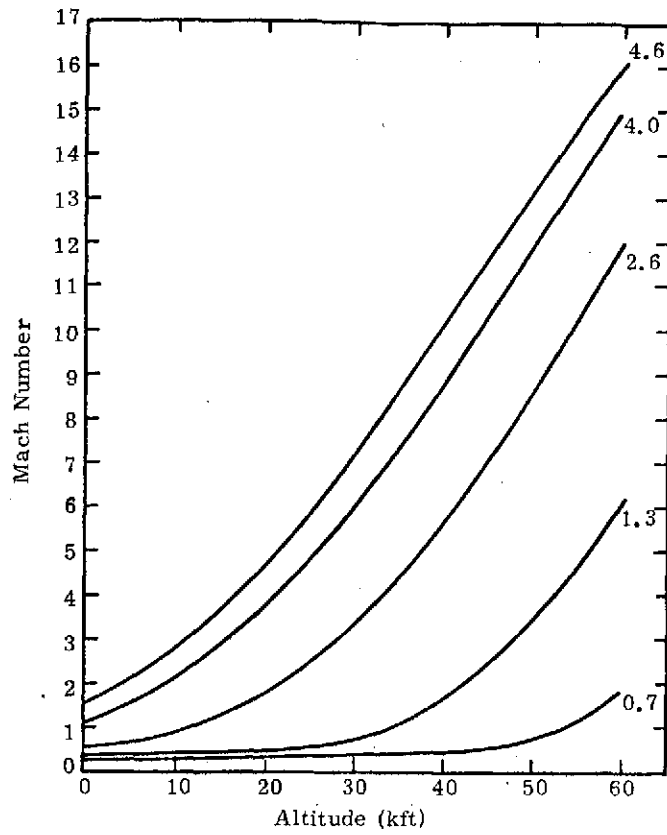
Figure A-13. Mach Number as a Function of Altitude ($\gamma_I = -24°$)
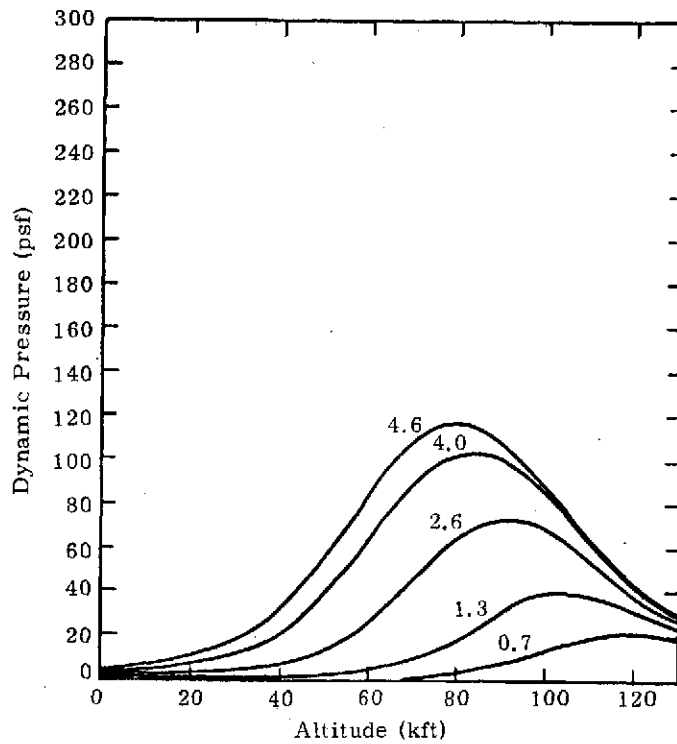
Figure A-14. Dynamic Pressure (Q) as a Function of Altitude ($\gamma_I = -12°$)
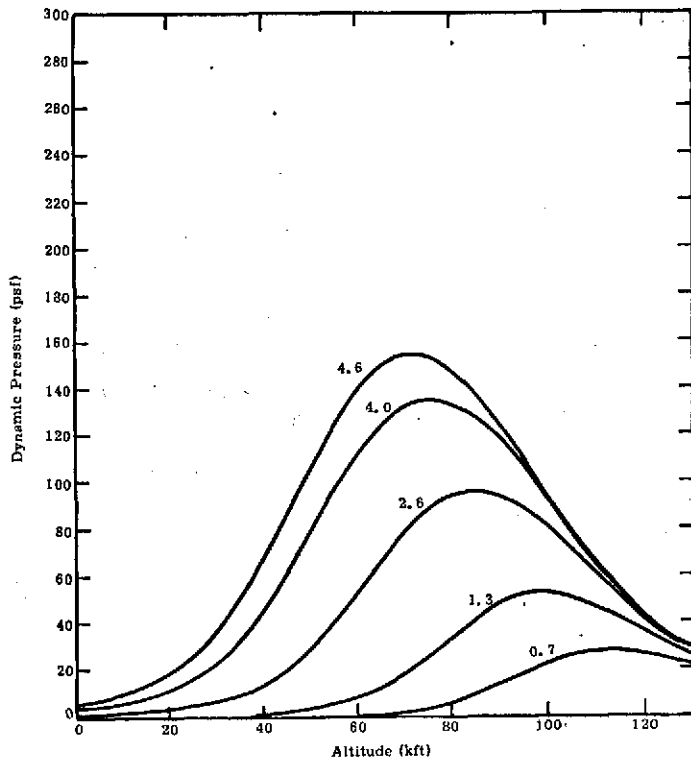
Figure A-15

Dynamic Pressure (Q) as a Function of Altitude ($\gamma_I = -15°$)

Figure A-16

Dynamic Pressure (Q) as a Function of Altitude ($\gamma_I = -18°$)
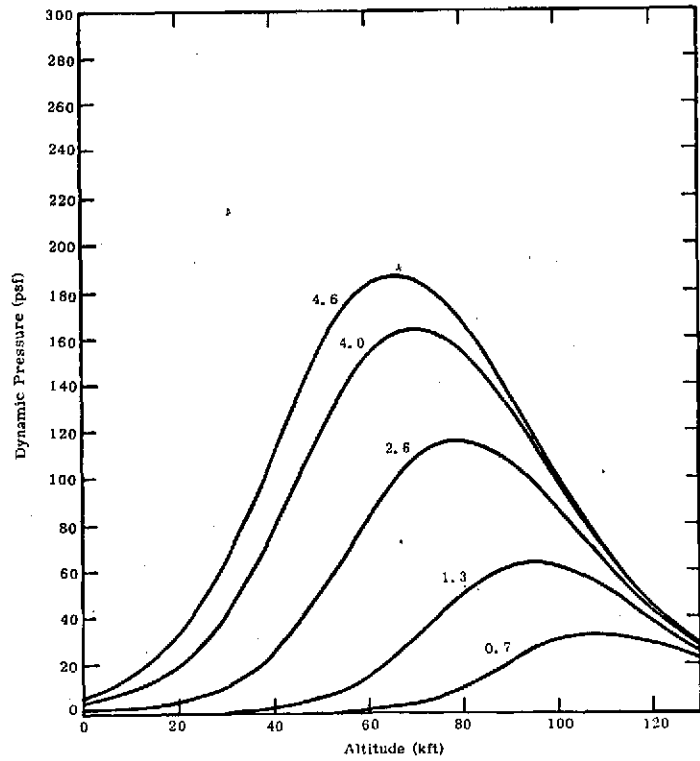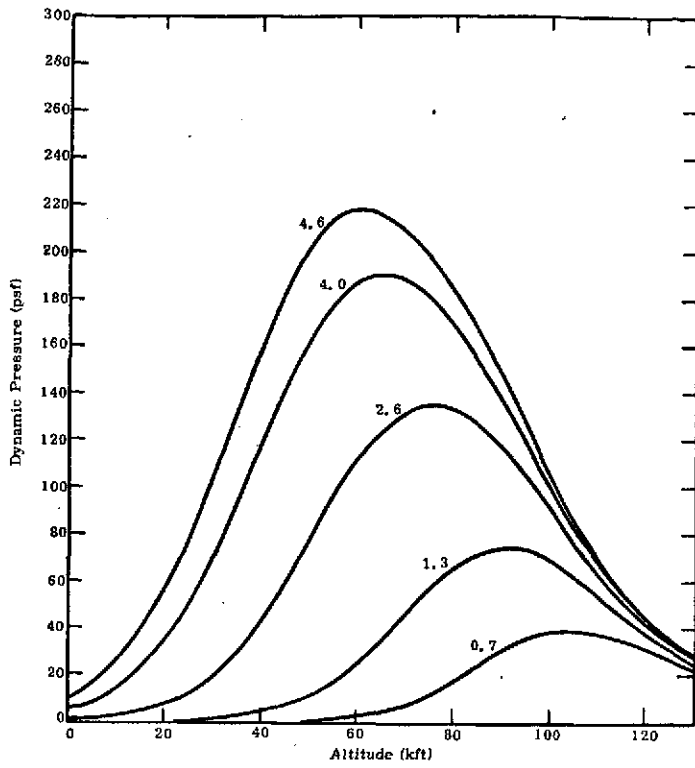
Figure A-17

Dynamic Pressure (Q) as a Function of Altitude ($\gamma_I = -21°$)

Figure A-18

Dynamic Pressure (Q) as a Function of Altitude ($\gamma_I = -24°$)
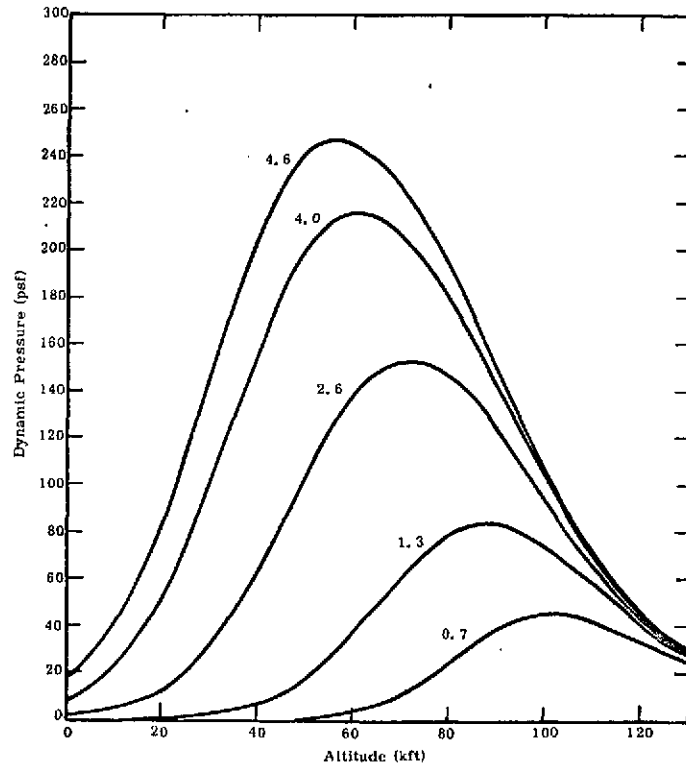
Figure A-19

Flight Path Angle as a Function
of Altitude ($\gamma_I = -12°$)

Figure A-20

Flight Path Angle as a Function
of Altitude ($\gamma_I = -15°$)

Figure A-21

Flight Path Angle as a Function
of Altitude ($\gamma_I = -18°$)

Figure A-22

Flight Path Angle as a Function
of Altitude ($\gamma_I = -21°$)

Figure A-23. Flight Path Angle as a Function
of Altitude ($\gamma_I = -24°$)

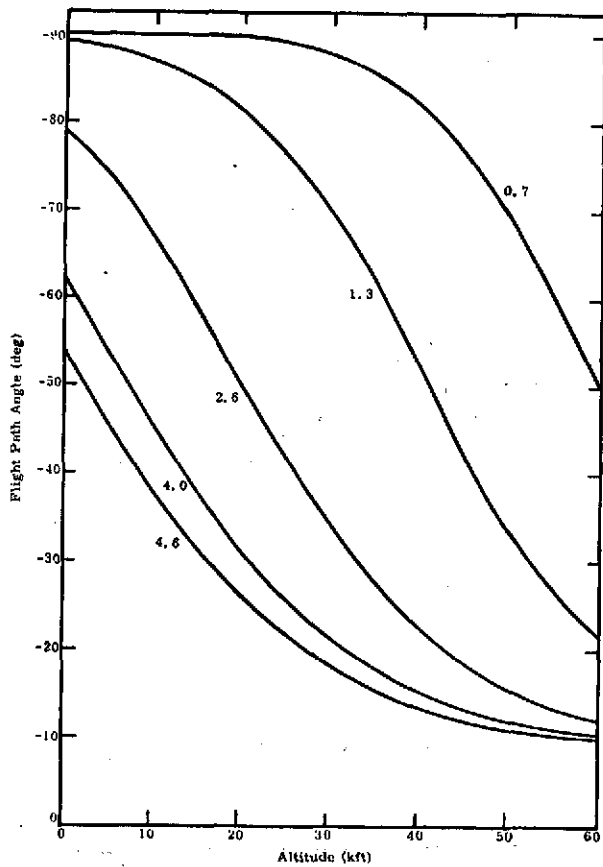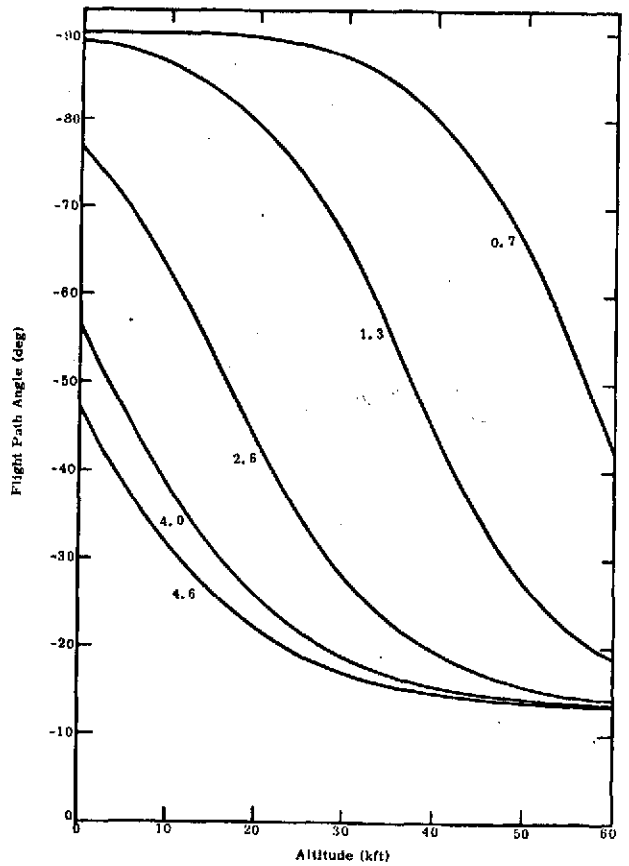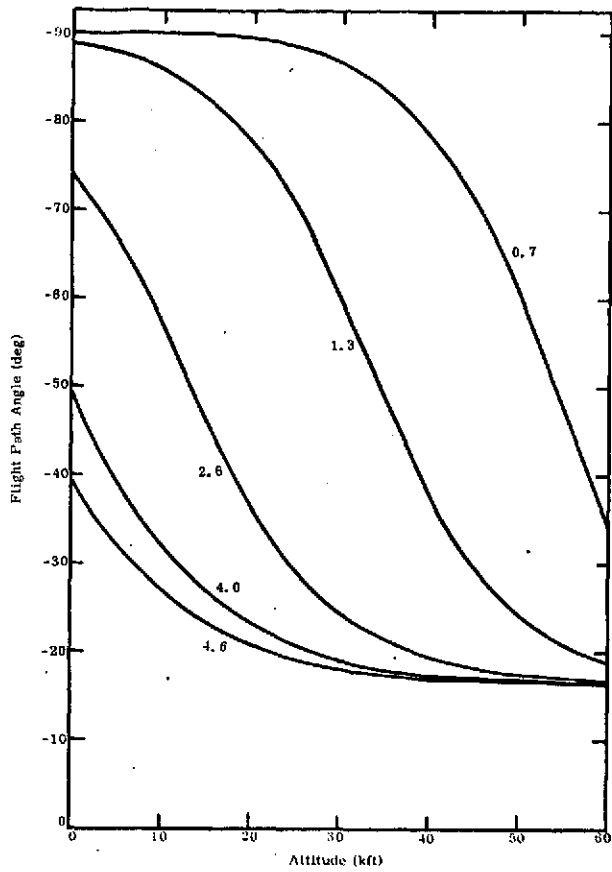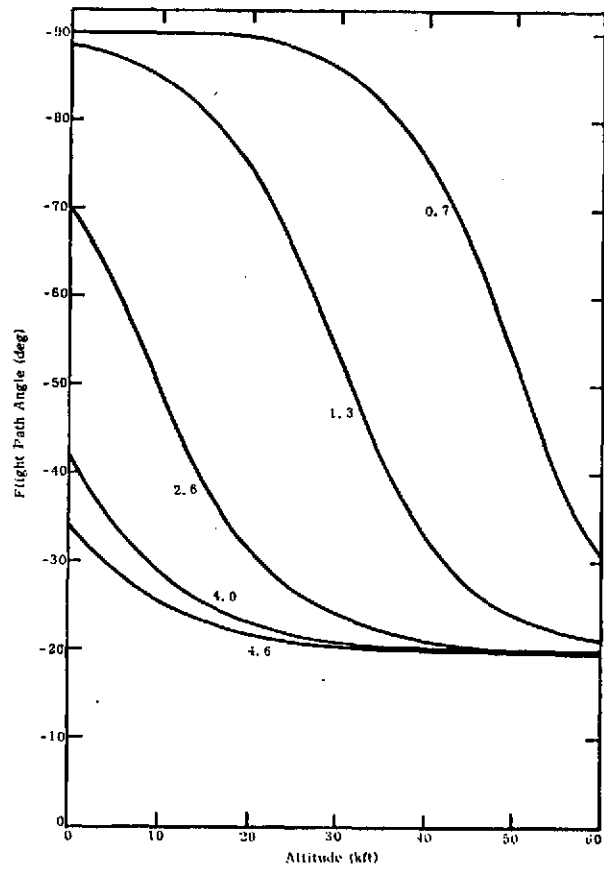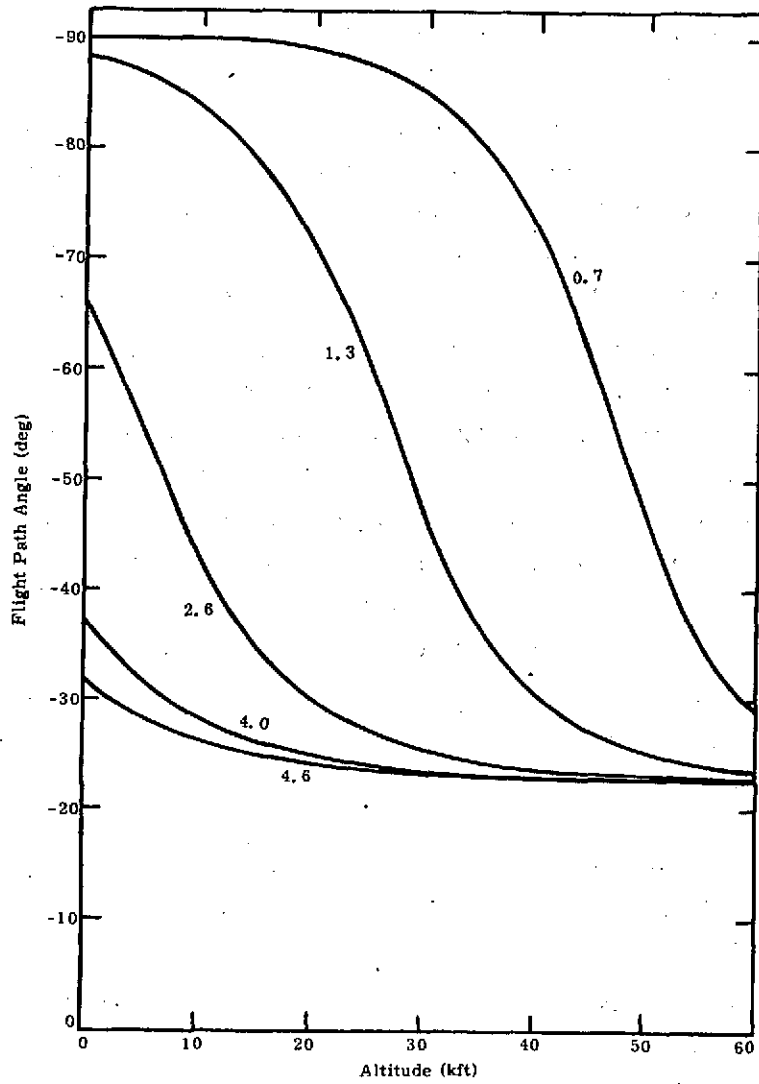## Six-Degree-of-Freedom Trajectory
and Dynamics Analysis for the Telescoping Cylinder

To reduce the ballistic coefficient of the entry canister to an acceptable value, an extendable body is considered. The telescoped configuration consists of a right circular cylinder with hemispherical end caps. When this body is so extended that the length is twice the canister length, the ballistic coefficient becomes 43.9 kg/m^2 (3.4 lbs/ft^2).

In parametric studies of the complete 6-degree-of-freedom motion, the trajectory computer code specifies the telescoping phase as an instantaneous process that occurs immediately prior to entry. Although the dynamic effect of extending the body serves to decrease the body initial tumbling rate (2 rpm), the angular momentum remains unaffected. Fluid dynamic forces that develop during entry destroy the residual tumbling in the altitude interval above 61 km (200 kft).

At 30.5-km (100-kft) altitude, the angle-of-attack excursions decay to less than 0.1 radian; the longitudinal body axis is stabilized normal to the velocity vector and is essentially fixed in inertial space, spinning at 98 percent of the initial value (20 rpm). At 21.3 km (70 kft), the deceleration load attains maximum magnitude, 40 g's (Mars) in the case of the nominal entry (γ_I - -15 degrees).

At 9.1-km (30-kft) altitude, the velocity decreases to 1/10 of the entry speed 4.73 km/s (15.5 kft/sec); the corresponding Mach number is 2.2, and it becomes twice that amount in the steepest entry (-22.5 degrees). In all trajectories, the flight path maintains an approximately straight-line course, with angular deflections no more than 13 degrees from the initial entry.

The detailed trajectory characteristics of the nominal case are summarized in Figures A-24 through A-30. Figures A-30 through A-36 describe the extreme mass asymmetry flight in which the longitudinal center-of-mass position is offset from the geometric center by 1 percent of the body length. The results indicate that the Mach number at 9.1-km (30-kft) altitude (the approximate parachute deployment point) increases a small amount from the nominal value ($\Delta M = 0.3$), and the body attitude stabilizes 17 degrees from the broadside position. The center of mass may be passively maintained to approximately 0.1 percent of body length so that mass asymmetry effects are essentially eliminated.

Several factors concerning the sensitivity of speed and range at parachute deployment to variations in configuration and environment have been determined. The results are summarized in Table A-I. Atmospheric winds and initial entry velocity have little effect on the terminal conditions. Atmospheric density, vehicle mass, and entry angle are important parameters, especially entry angle.

Fluid Dynamic Forces Acting on Cylindrical Bodies

The theoretical development of the forces that act on a yawed cylinder with hemispherical end caps is given in Reference A1. The results are based on Newtonian impact theory which, when modified to account for centrifugal effects, adequately describes the flow about blunt bodies at all angles of attack. Additional studies and experiments at intermediate speeds complete the description of the fluid forces (References A2 through A28). With the fluid dynamic forces defined for the entry configuration in a generalized manner, a parametric trajectory study of spinning and tumbling bodies can be made.
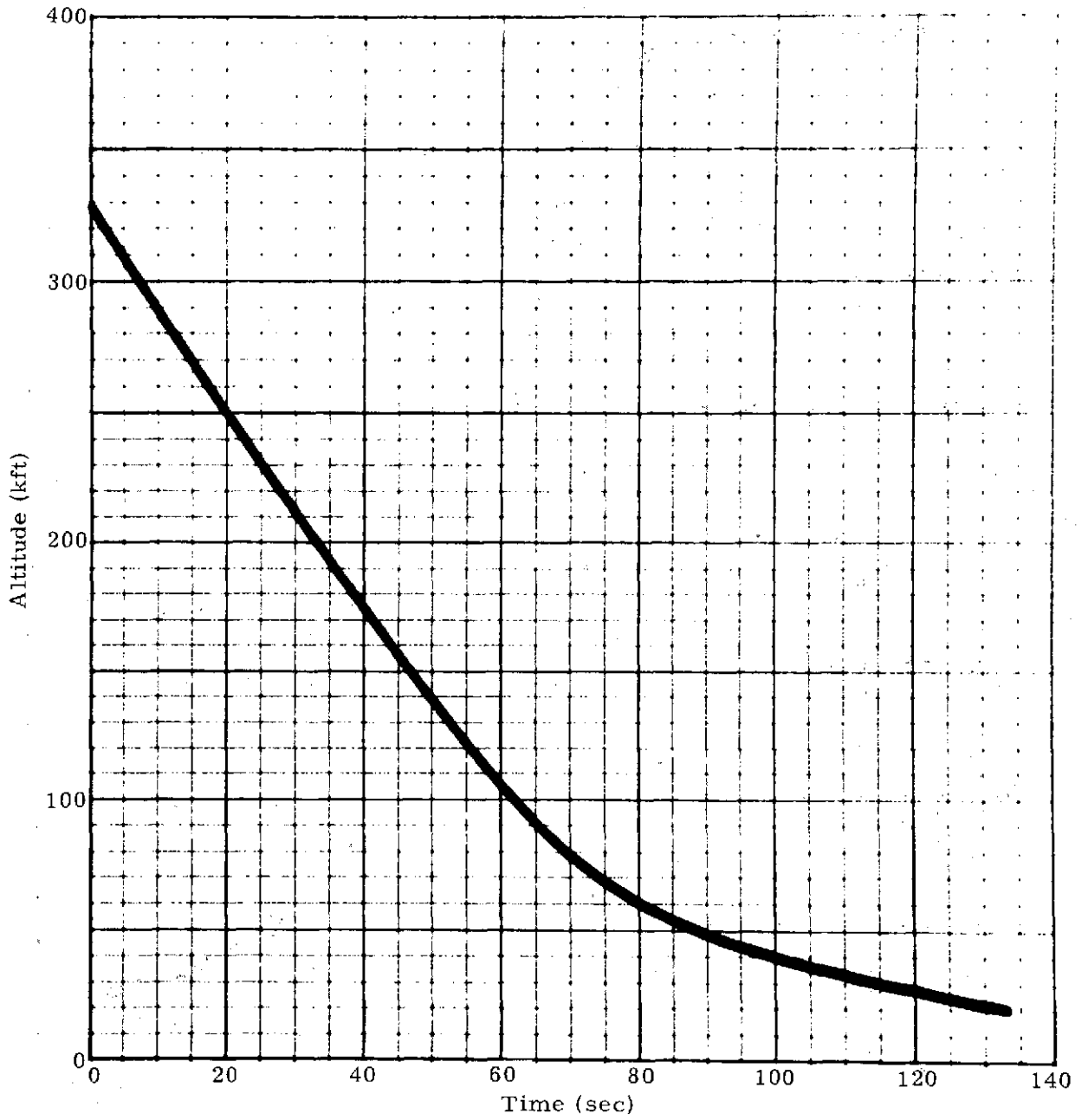
Figure A-24. Altitude versus Time (Nominal Trajectory)
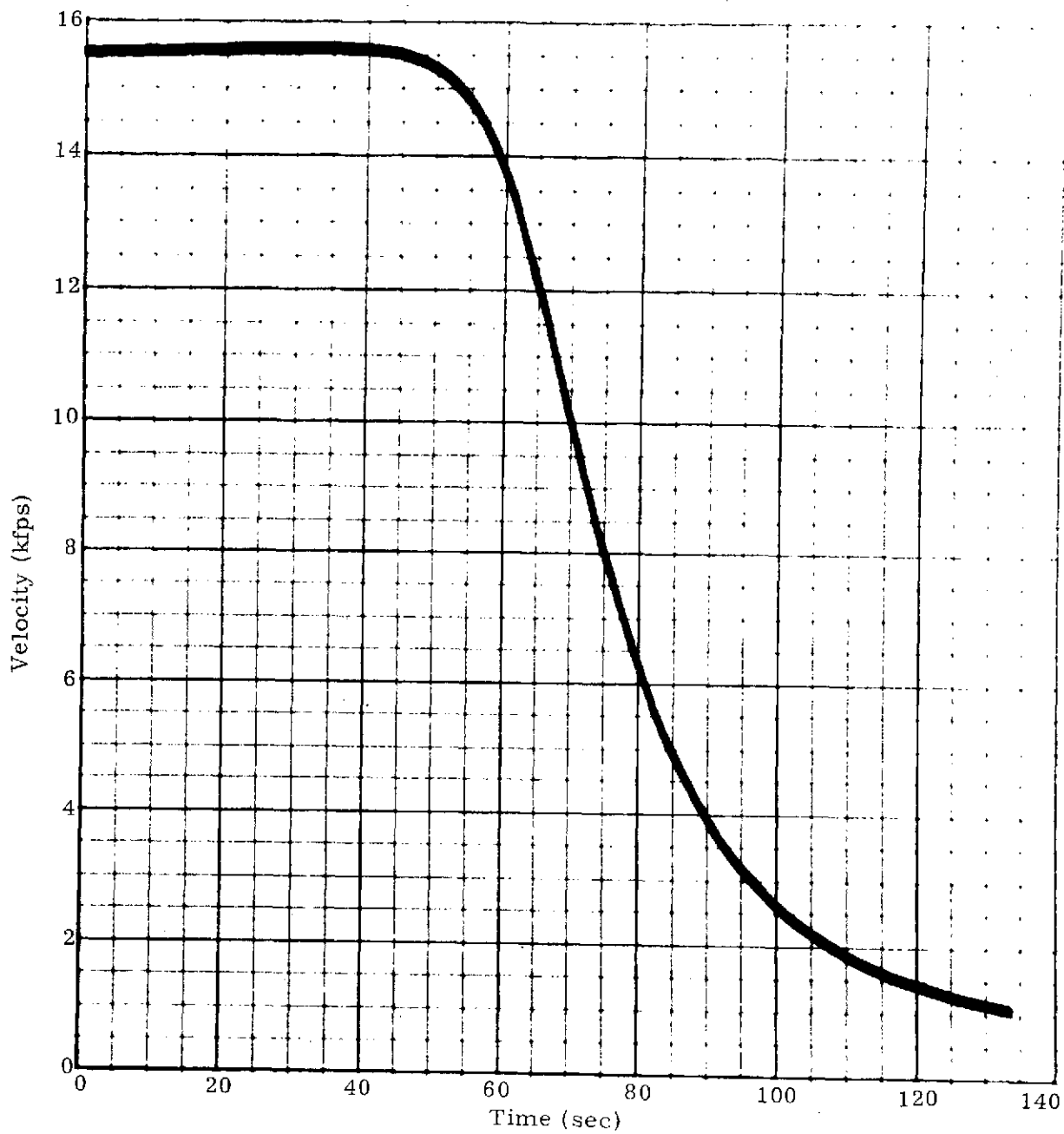
Figure A-25. Velocity versus Time (Nominal Trajectory)
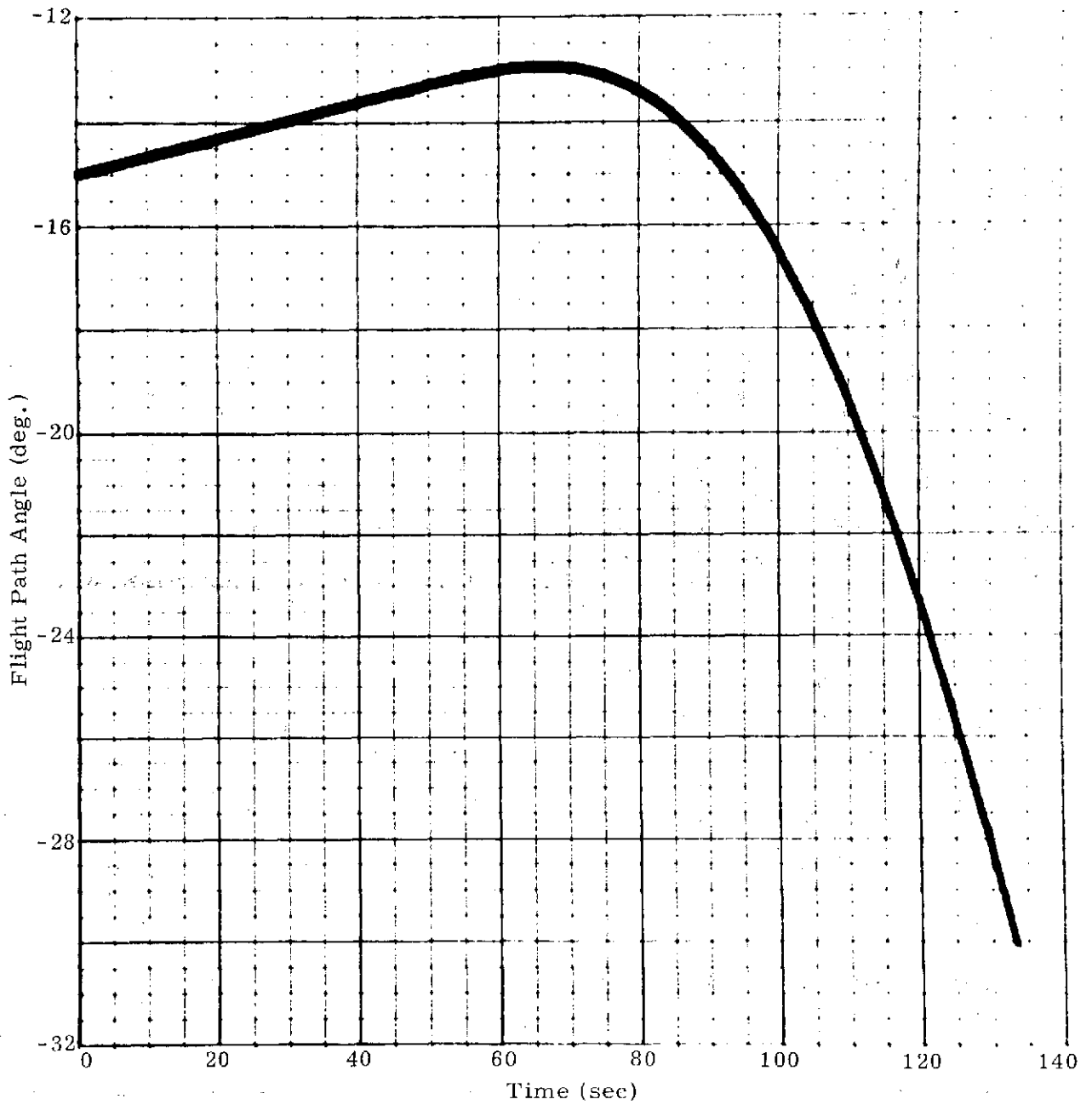
Figure A-26. Flight Path Angle versus Time (Nominal Trajectory)
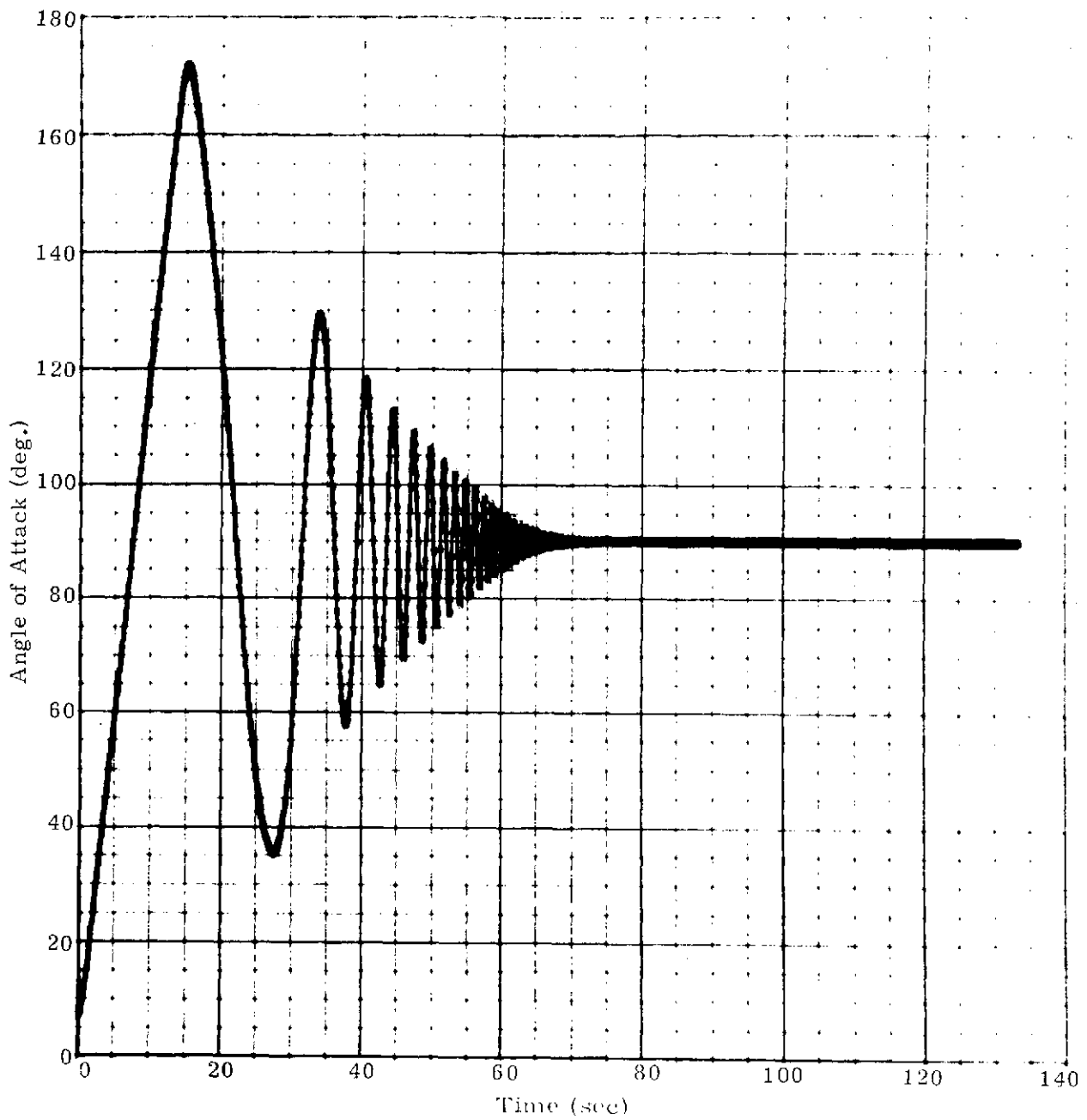
Figure A-27. Angle of Attack versus Time (Nominal Trajectory)
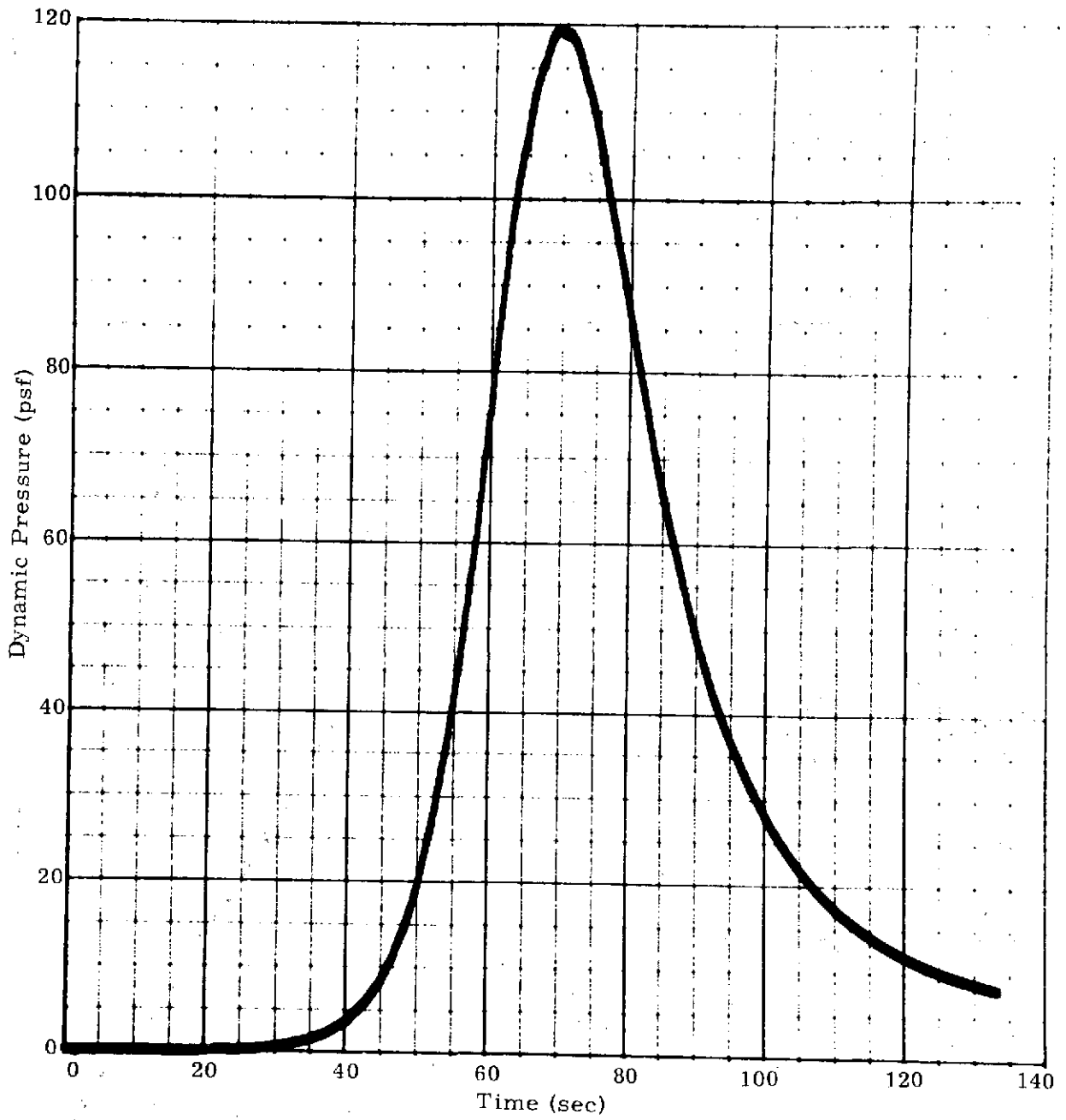
Figure A-28. Dynamic Pressure versus Time (Nominal Trajectory)
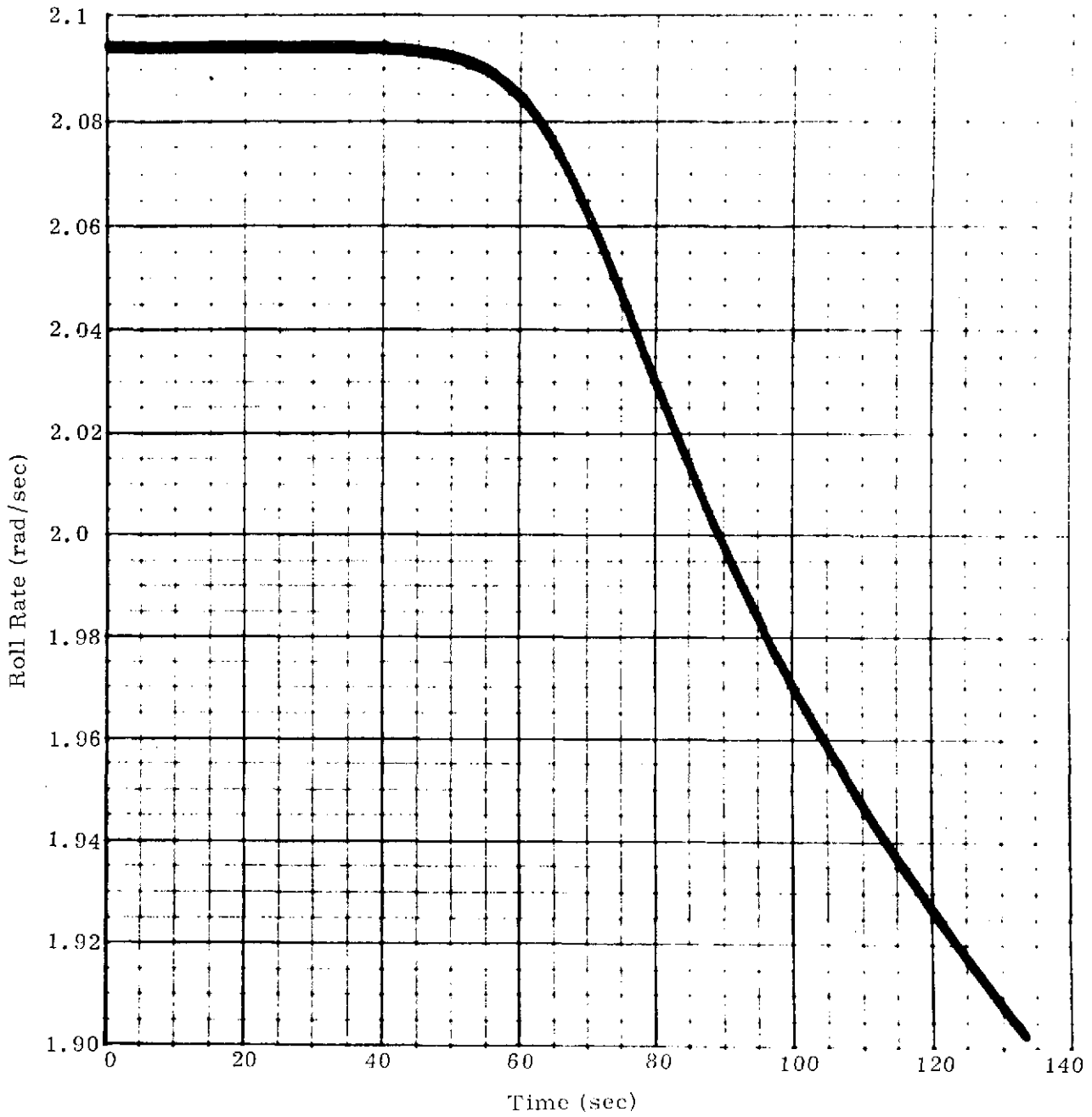
Figure A-29. Roll Rate versus Time (Nominal Trajectory)
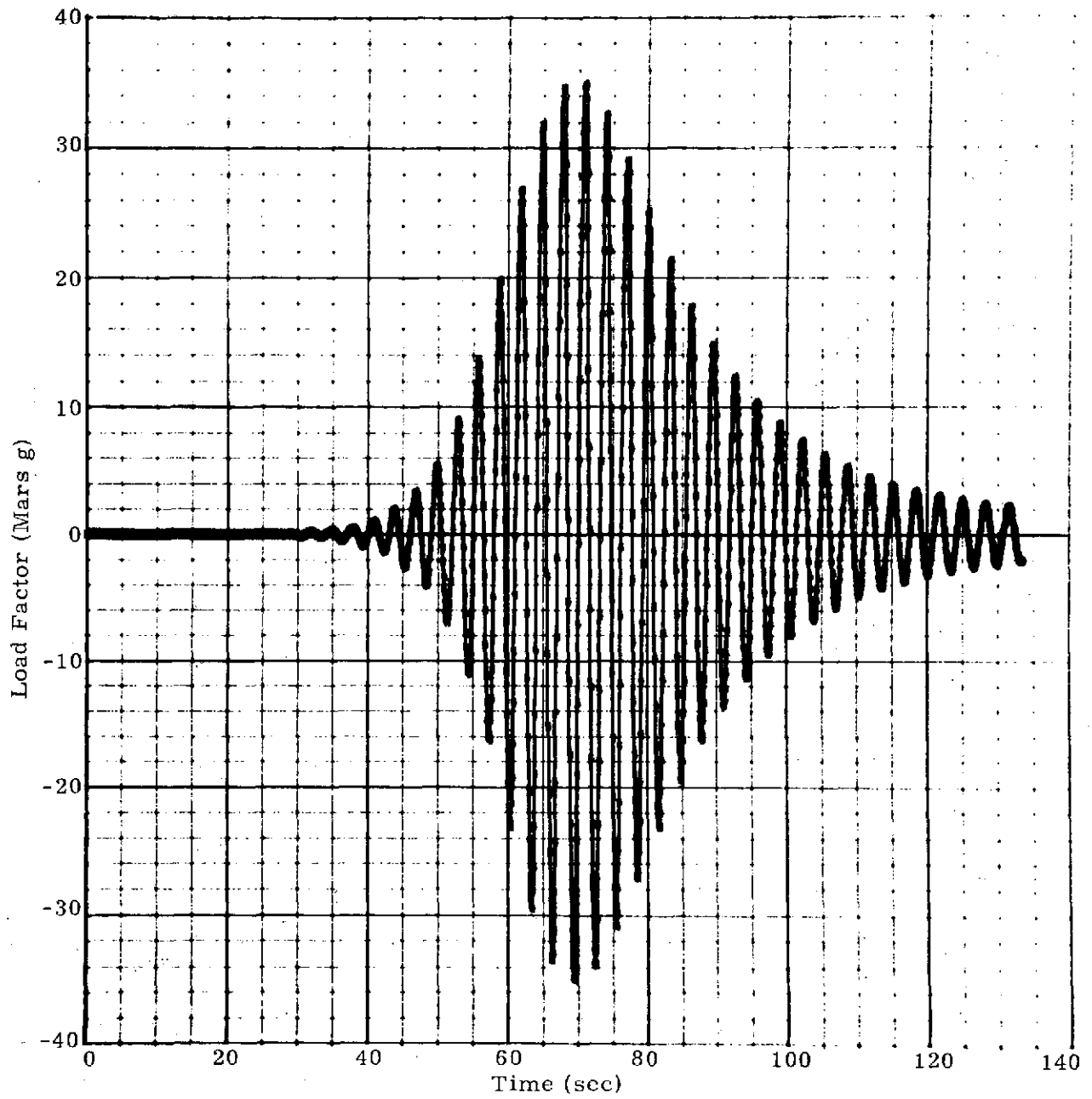
Figure A-30. Body-Fixed Load Factor (Normal to Cylinder Axis) versus Time (Nominal Trajectory)
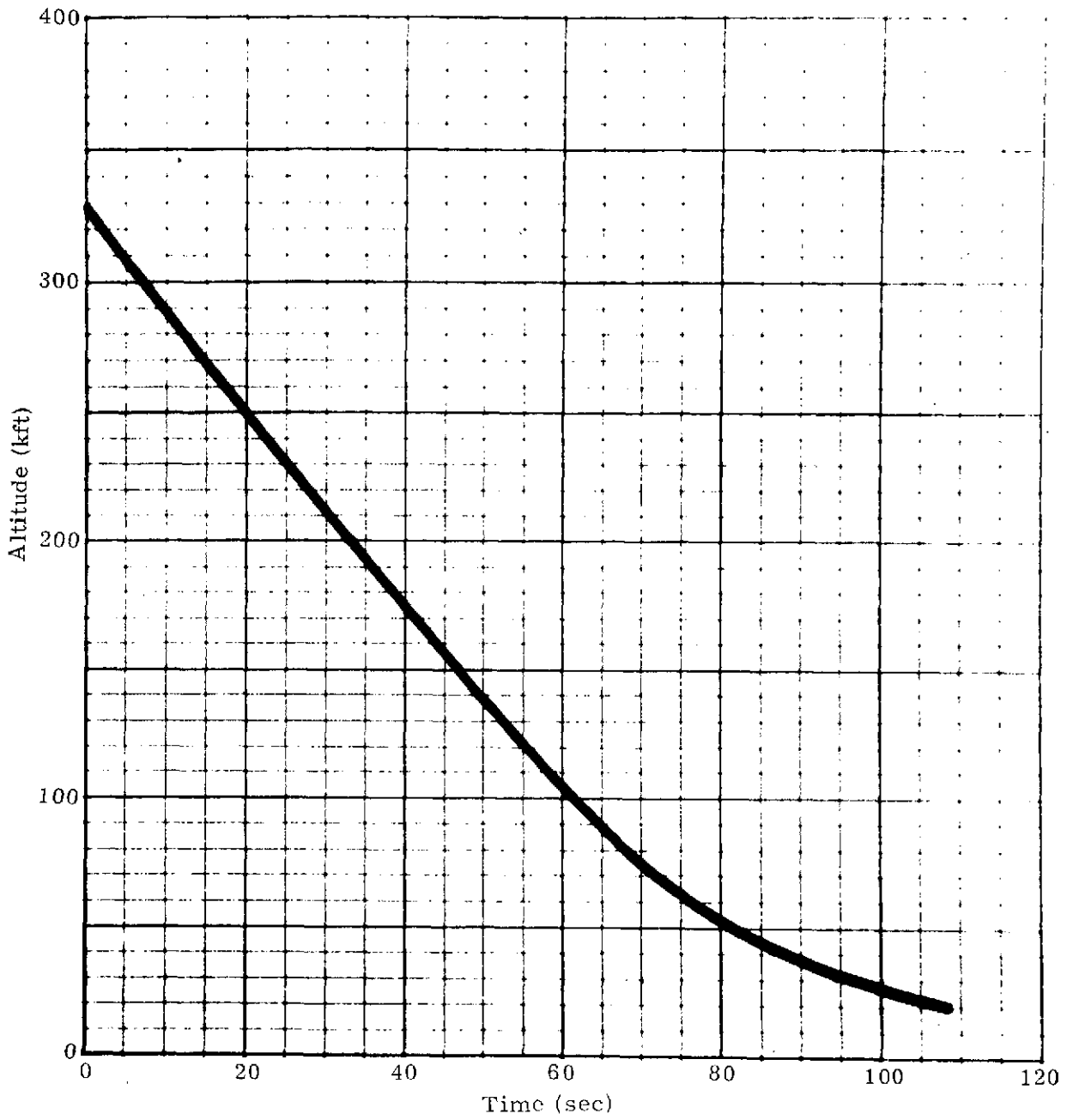
Figure A-31. Altitude versus Time (Mass Asymmetry Trajectory, $\Delta x_{cm}/L = 0.01$)
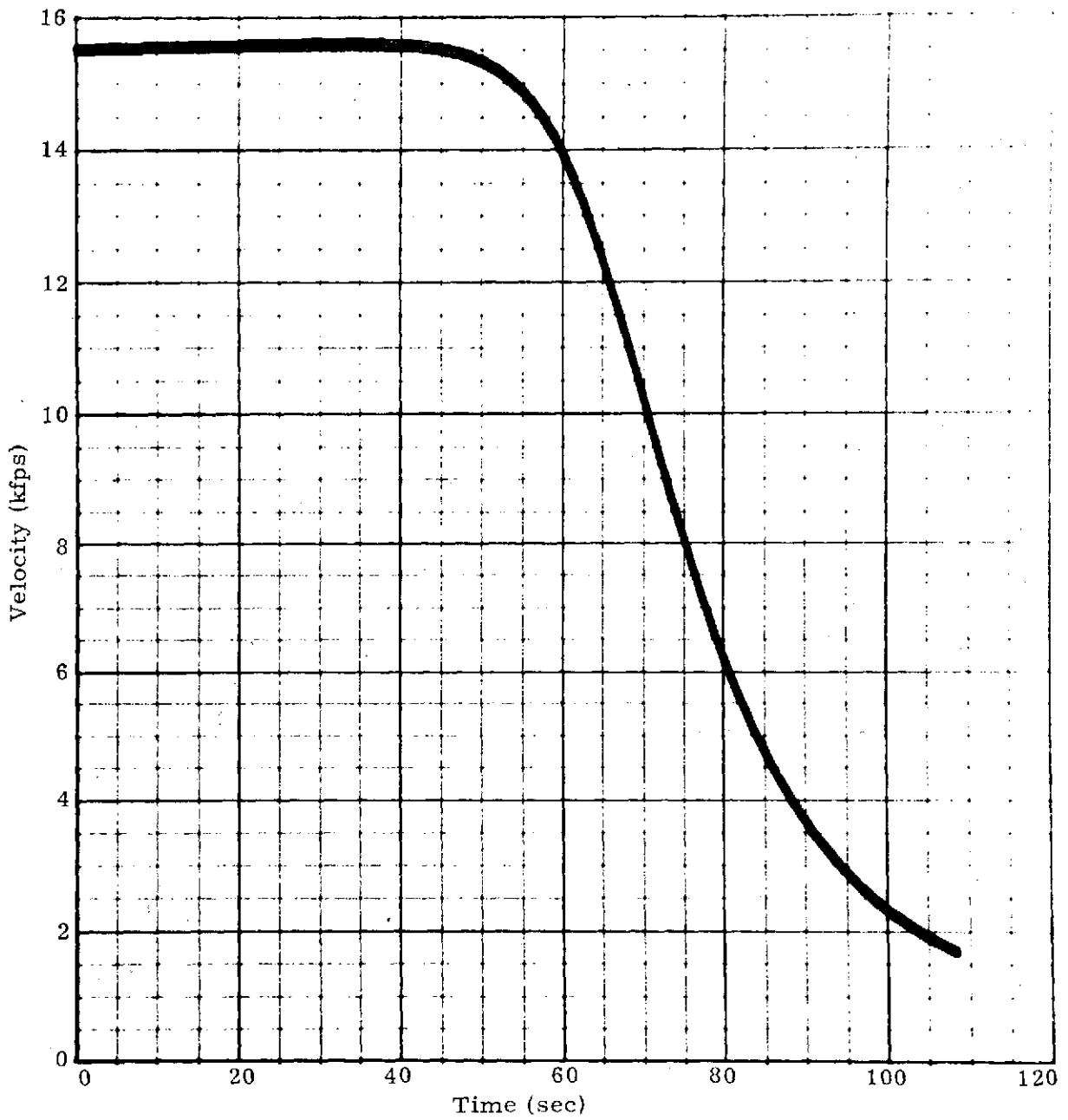
Figure A-32. Velocity versus Time (Mass Asymmetry Trajectory, $\Delta x_{cm}/L - 0.01$)
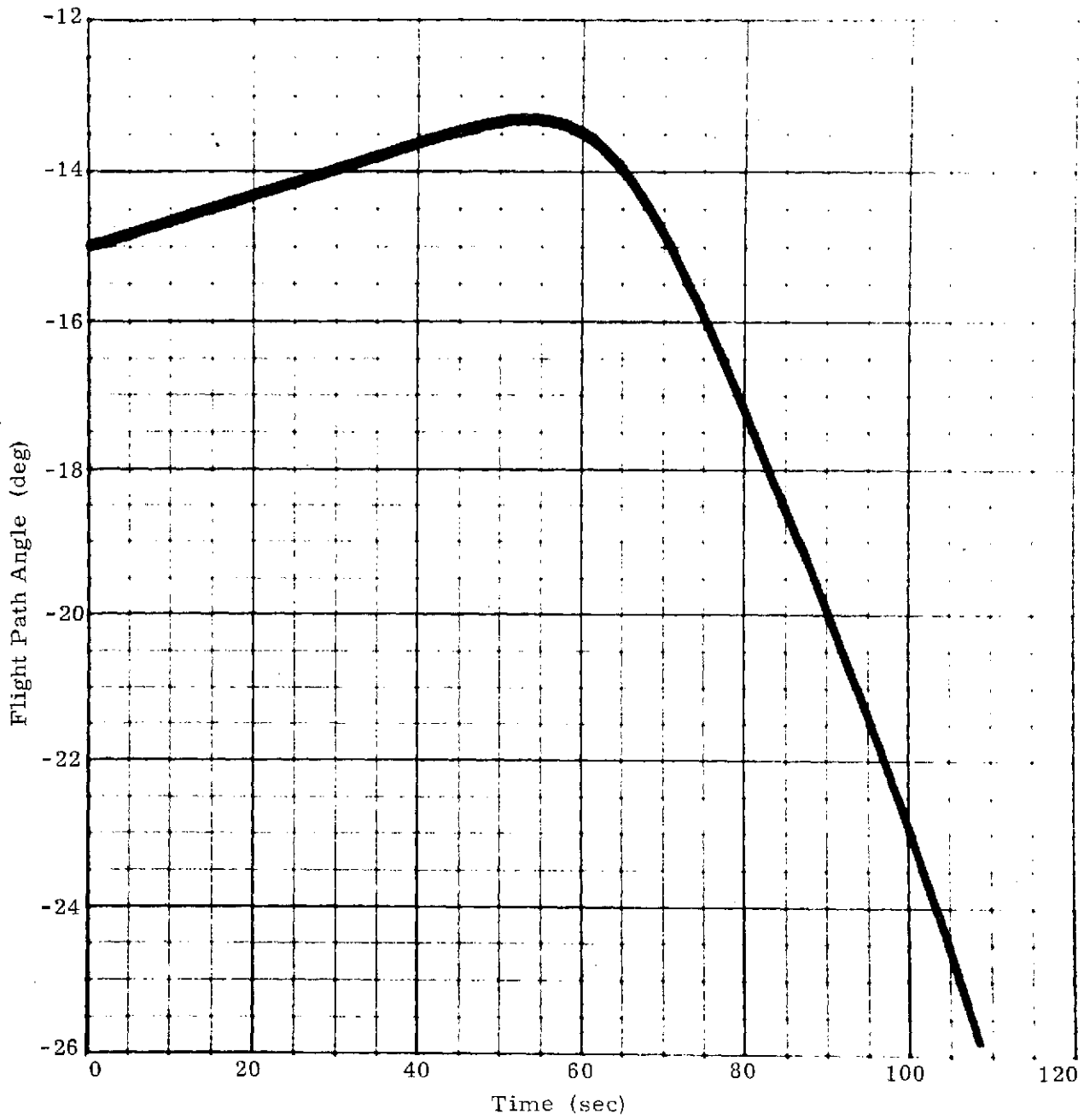
Figure A-33. Flight Path Angle versus Time (Mass Asymmetry Trajectory, $\Delta x_{cm}/L = 0.01$)
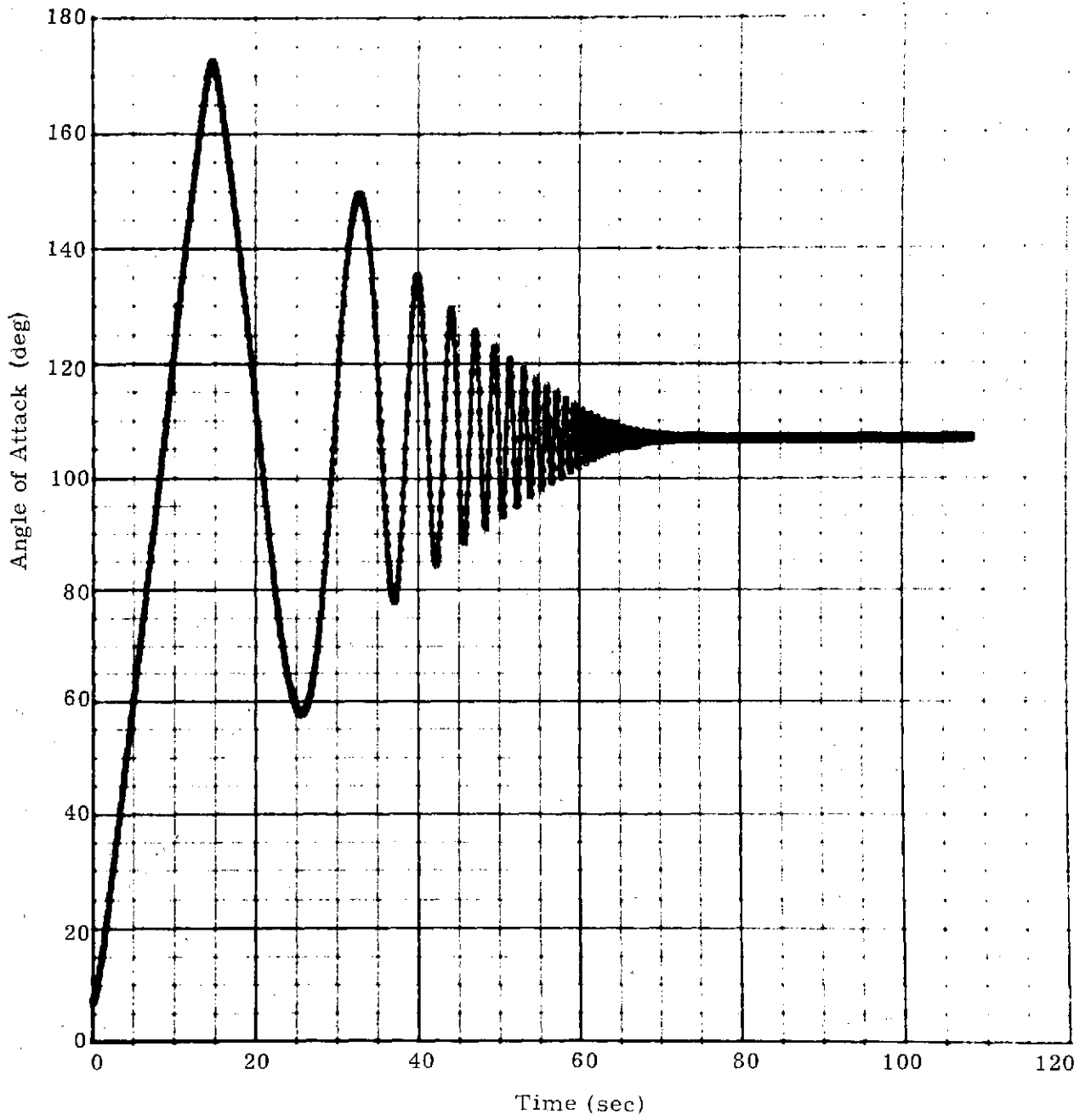
Figure A-34. Angle of Attack versus Time (Mass Asymmetry Trajectory, $\Delta x_{cm}/L = 0.01$)
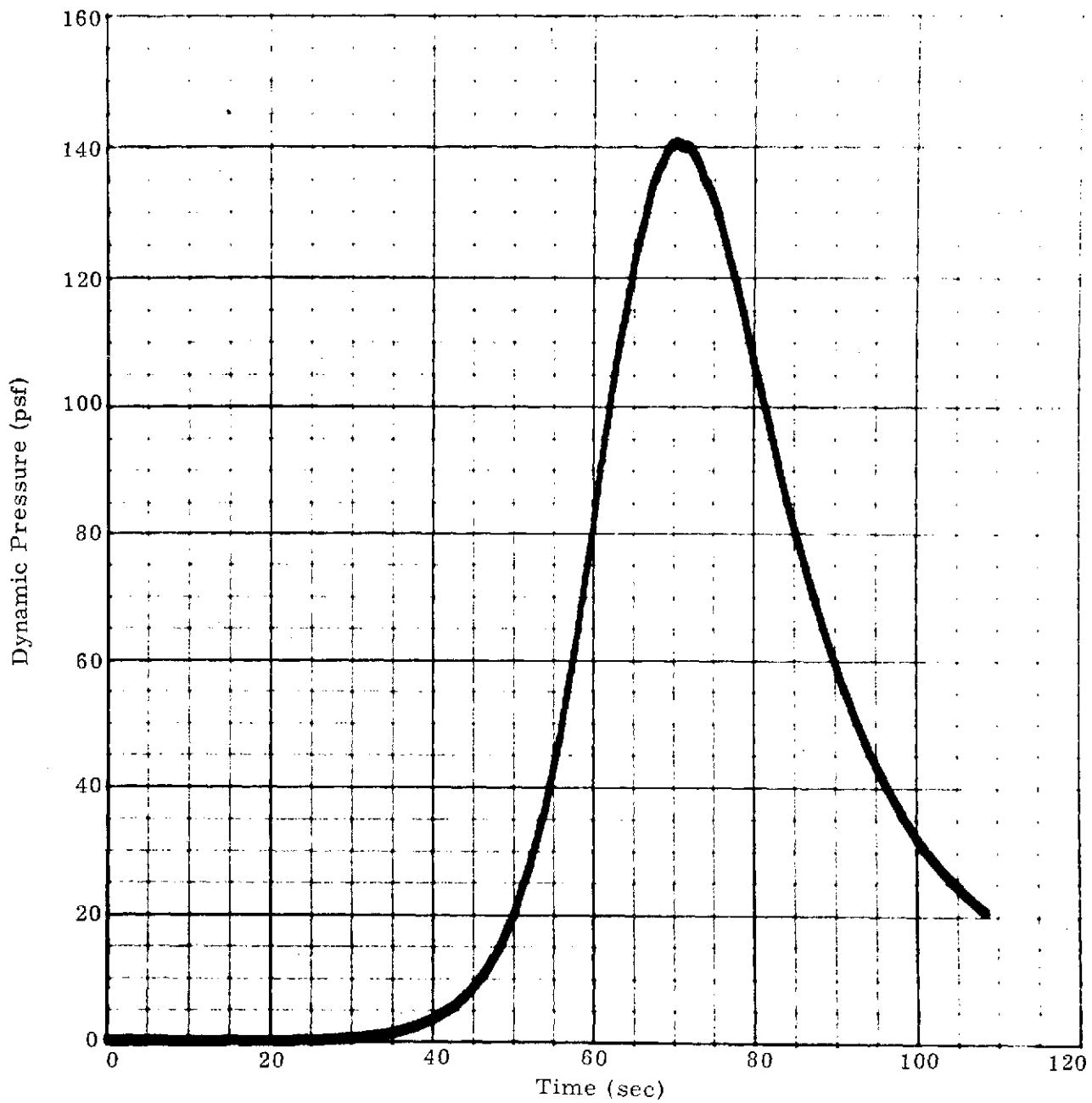
Figure A-35. Dynamic Pressure versus Time (Mass Asymmetry Trajectory, $\Delta x_{cm}/L = 0.01$)
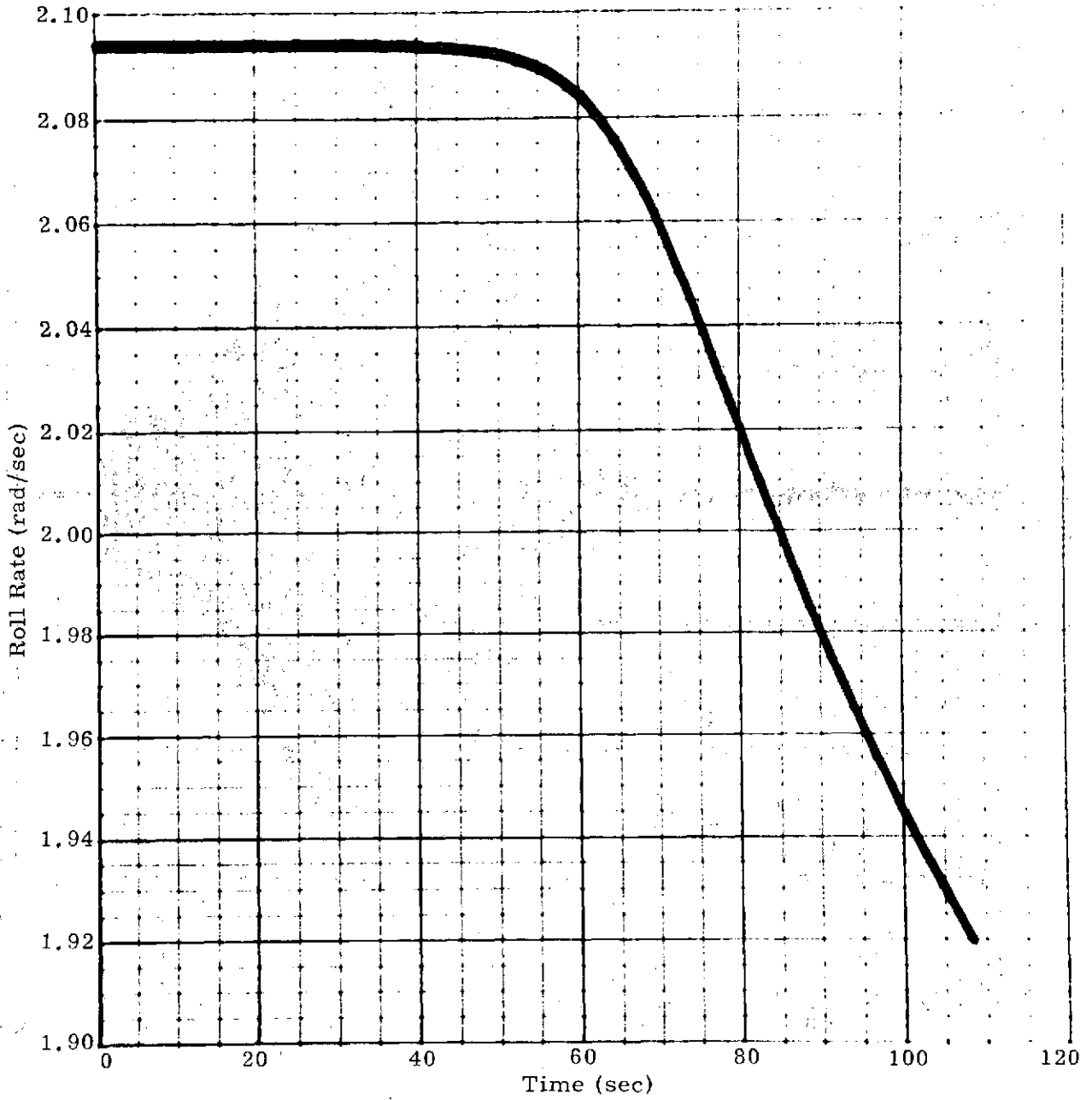
Figure A-36. Roll Rate versus Time (Mass Asymmetry Trajectory, $\Delta x_{cm}/I = 0.01$)
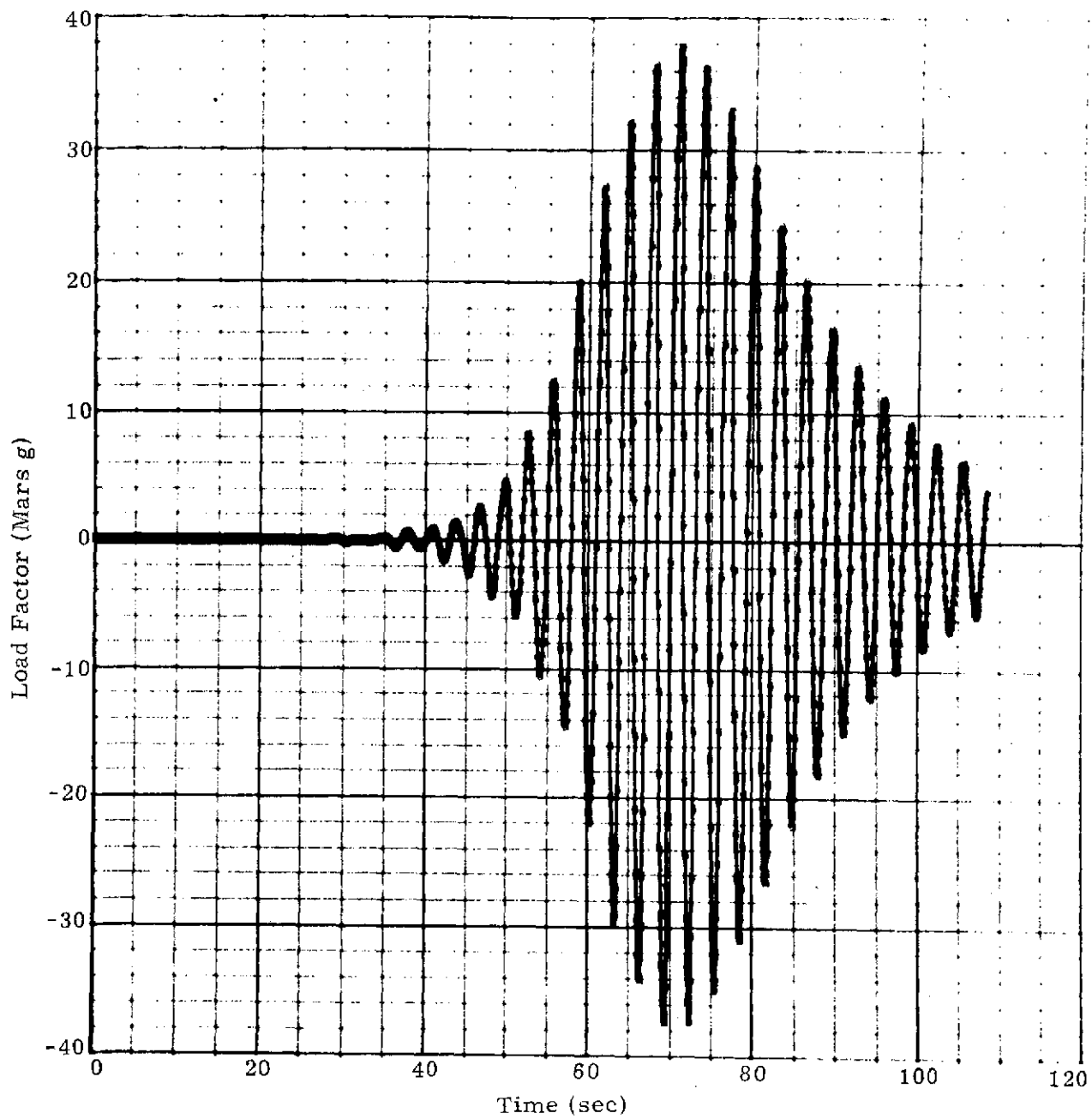
Figure A-37. Body-Fixed Load Factor (Normal to Cylinder Axis) versus Time
(Mass Asymmetry Trajectory, $\Delta x_{cm}/L = 0.01$)

Trajectory Sensitivity Factors
(Telescoping Cylinder Entry Body)

1. Entry velocity sensitivity

$$\frac{\partial R}{\partial \left(\frac{\Delta V_I}{V_I} \right)} \Bigg]_{\substack{h = 30 \text{ kft} \\ \gamma_I = -20°}} = 20.2 \text{ nautical miles}$$

$$\frac{\partial M_\infty}{\partial \left(\frac{\Delta V_I}{V} \right)} \Bigg]_{\substack{h = 30 \text{ kft} \\ \gamma_I = -20°}} = 1.86$$

2. Entry angle sensitivity

$$\frac{\partial R}{\partial \left(\frac{\Delta \gamma_I}{\gamma_I} \right)} \Bigg]_{\substack{h = 30 \text{ kft} \\ \gamma_I = -20°}} = -142 \text{ nautical miles}$$

$$\frac{\partial M_\infty}{\partial \left(\frac{\Delta \gamma_I}{\gamma_I} \right)} \Bigg]_{\substack{h = 30 \text{ kft} \\ \gamma_I = -20°}} = 7.2$$

3. Atmospheric density sensitivity

$$\frac{\partial R}{\partial \left(\frac{\Delta \rho_\infty}{\rho_\infty} \right)} \Bigg]_{\substack{h = 30 \text{ kft} \\ \gamma_I = -20°}} = -4.0 \text{ nautical miles}$$

$$\frac{\partial M_\infty}{\partial \left(\frac{\Delta \rho_\infty}{\rho_\infty} \right)} \Bigg]_{\substack{h = 30 \text{ kft} \\ \gamma_I = -20°}} = -7.0$$

4. Atmospheric wind sensitivity

$$\frac{\partial R}{\partial \left(\dfrac{V_w}{V_I}\right)} \Bigg]_{\substack{h = 30 \text{ kft} \\ \gamma_I = -20°}} = -21.9 \text{ nautical miles}$$

$$\frac{\partial M_\infty}{\partial \left(\dfrac{V_w}{V_I}\right)} \Bigg]_{\substack{h = 30 \text{ kft} \\ \gamma_I = -20°}} = -0.76$$

5. Configuration mass asymmetry sensitivity

$$\frac{\partial R}{\partial \left|\dfrac{\Delta x_{am}}{L}\right|} \Bigg]_{\substack{h = 30 \text{ kft} \\ \gamma_I = -20°}} = 250 \text{ nautical miles}$$

$$\frac{\partial M_\infty}{\partial \left|\dfrac{\Delta x_{am}}{L}\right|} \Bigg]_{\substack{h = 30 \text{ kft} \\ \gamma_I = -20°}} = 30.0$$

6. Mass sensitivity

$$\frac{\partial R}{\partial \left(\dfrac{\Delta m_I}{m_I}\right)} \Bigg]_{\substack{h = 30 \text{ kft} \\ \gamma_I = -20°}} = 2.4 \text{ nautical miles}$$

$$\frac{\partial M_\infty}{\partial \left(\dfrac{\Delta m_I}{m_I}\right)} \Bigg]_{\substack{h = 30 \text{ kft} \\ \gamma_I = -20°}} = 5.5$$

7. Cylinder diameter sensitivity

$$\left. \frac{\partial R}{\partial\left(\frac{\Delta d}{d}\right)} \right]_{\substack{h = 30 \text{ kft} \\ \gamma_I = -20°}} = -2.2 \text{ nautical miles}$$

$$\left. \frac{\partial M_\infty}{\partial\left(\frac{\Delta d}{d}\right)} \right]_{\substack{h = 30 \text{ kft} \\ \gamma_I = -20°}} = -5.7$$

8. Cylinder length sensitivity

$$\left. \frac{\partial R}{\partial\left(\frac{\Delta \ell}{\ell}\right)} \right]_{\substack{h = 30 \text{ kft} \\ \gamma_I = -20°}} = -3.2 \text{ nautical miles}$$

$$\left. \frac{\partial M_\infty}{\partial\left(\frac{\Delta \ell}{\ell}\right)} \right]_{\substack{h = 30 \text{ kft} \\ \gamma_I = -20°}} = -5.1$$

Parametric Trajectory Studies of Cylindrical Bodies

A generalized six-degree-of-freedom flight-path study of cylindrical bodies with hemispherical end caps was used to define the pertinent design parameters and to determine the detailed behavior of the telescoping entry configuration. The trajectory computer code (1) utilizes a rotating planet to account for spherical ablateness on altitude as well as gravity and (2) includes atmospheric variations such as 3-dimensional winds. The code has provision for asymmetry effects in the vehicle physical characteristics; the forcing functions have no restrictions concerning small angles of motion.

The results of the study are summarized in Figures A-38 through A-40. Extending the entry body to twice its original length ($\eta = 2$) is obviously an effective means of significantly reducing the speed in the altitude range 6 to 12 km (20 to 40 kft). In that terminal flight conditions have not been attained at altitudes of concern for parachute deployment, additional telescoping beyond a factor of 2, if structurally feasible, will provide still further proportional speed reduction.
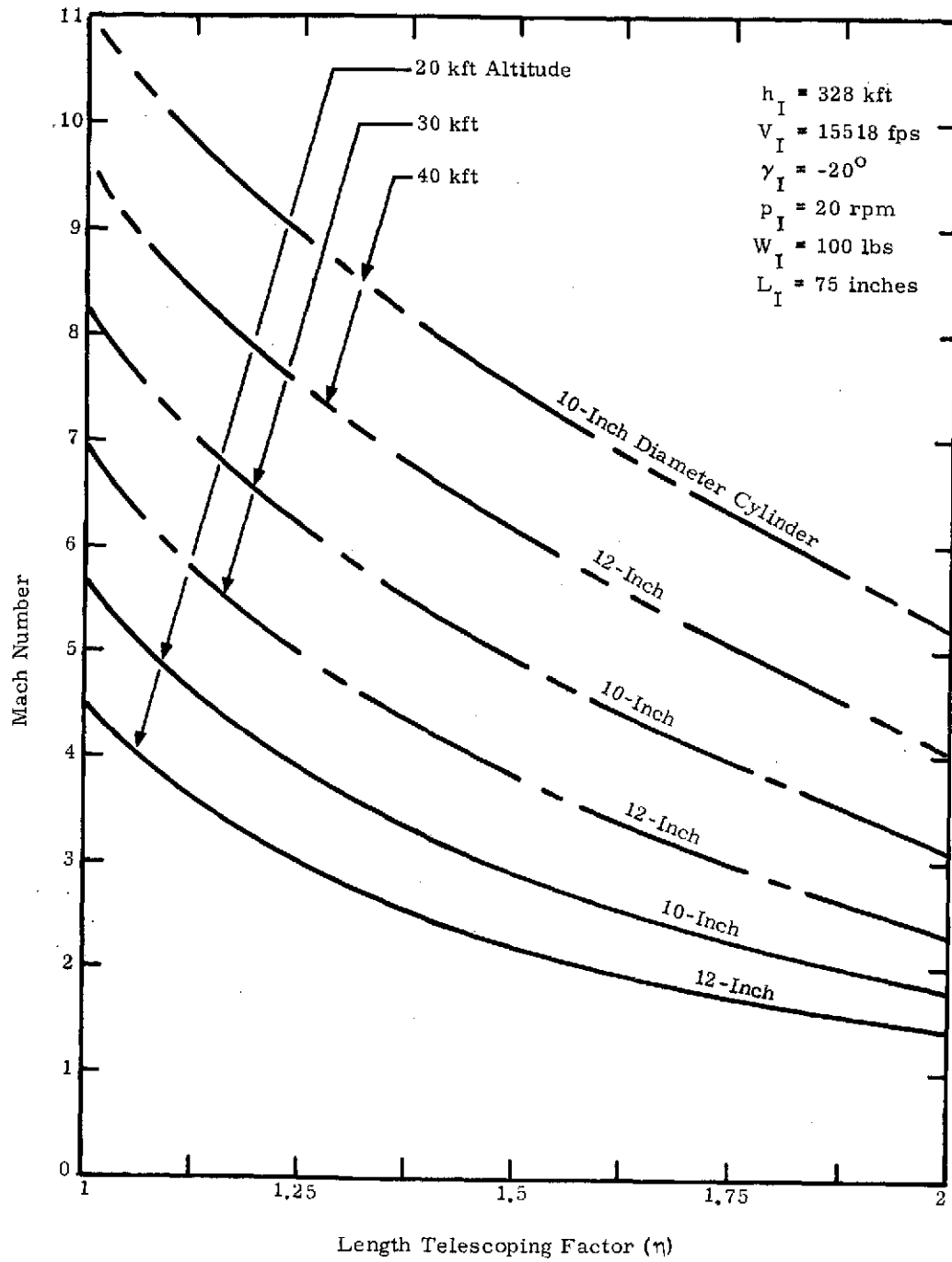
Figure A-38. Mach Number at Typical Parachute Deployment Altitudes
Showing Effects of Cylinder Length and Diameter
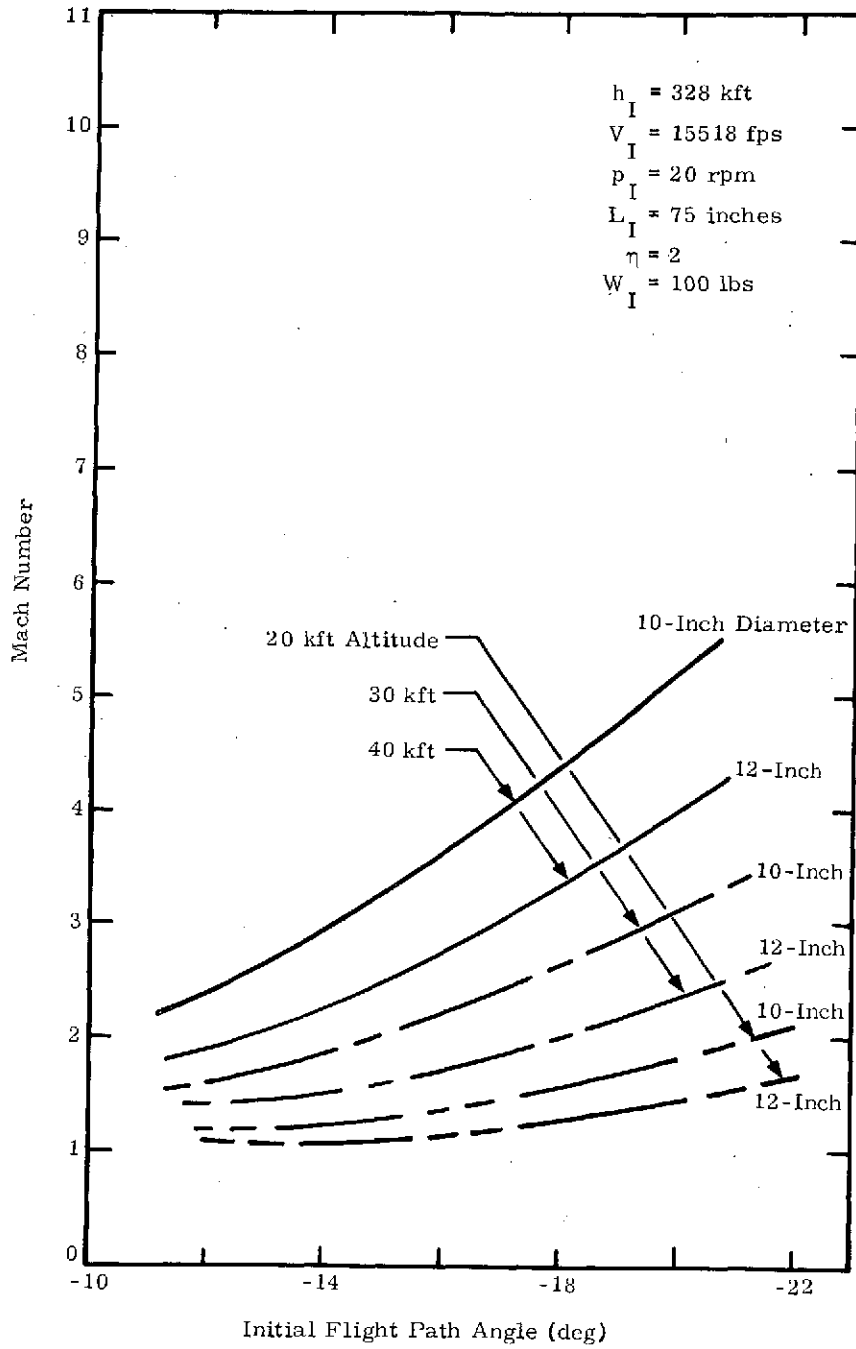
Figure A-39. Mach Number at Typical Parachute Deployment
Altitudes Showing Effects of Initial Flight Path Angle
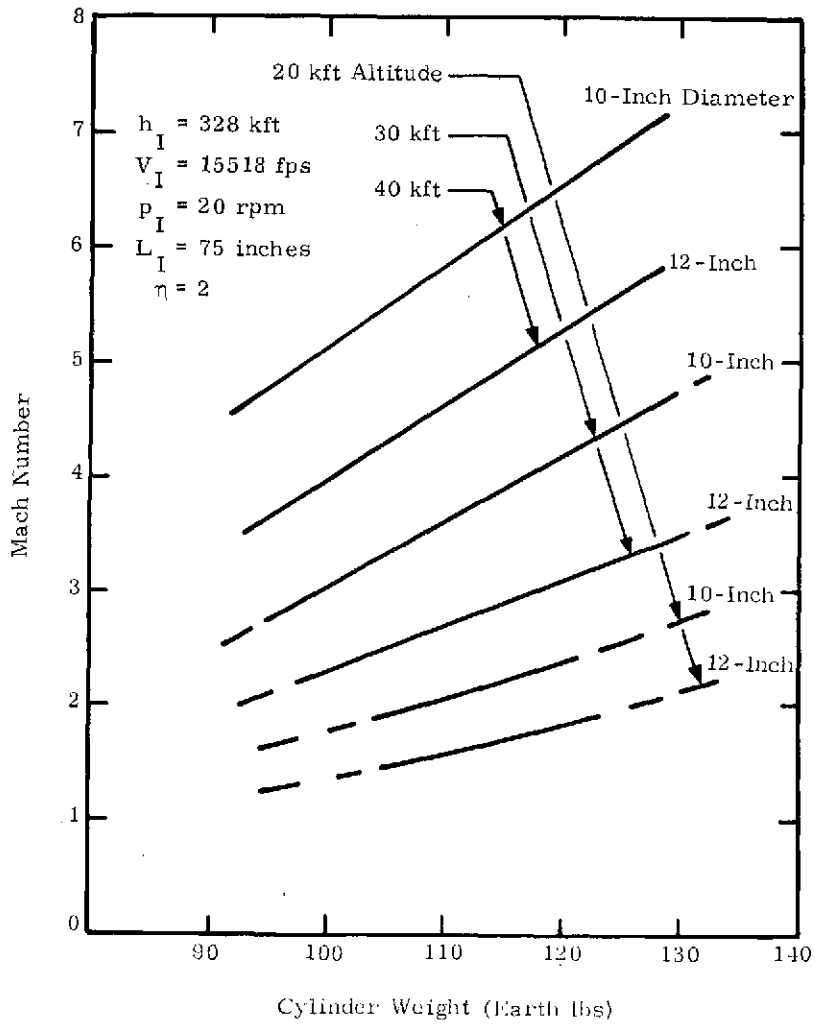
Figure A-40. Mach Number at Typical Parachute Deployment Altitudes
Showing Effects of Cylinder Mass and Diameter

Because of the relatively large bluntness of all the reentry configurations considered, it was assumed that a normal shock with an isentropic expansion to local pressures would adequately model the environment. The ACE[A29] chemical equilibrium computer code was used to generate real gas normal shock solutions in an atmosphere consisting of CO_2, CO, O_2, and O molecular species. The boundary-layer aeroheating analysis was accomplished with the BLIMP[A30] code. The assumptions were that the boundary layer remained laminar and that it consisted of the above species in chemical equilibrium. The CMA[A31] code was used with a heat-of-ablation model (or nonablating for the heat-sink designs) to determine the thermal response of the various candidate heatshields. While this type of thermal analysis does not model the pyrolysis and charring capabilities of some of the heatshields, it is felt to be a conservative analysis (pyrolysis decomposition and charring would tend to lower backface temperatures). Thus, while a predicted inadequacy by this method does not necessarily imply failure of a heatshield concept, predicted adequacy should imply success. It is felt that future more complex analyses including these mechanisms could only tend to lighten and optimize the heatshield design.

Cylindrical Entry Canister

The cylindrical canister concept was analyzed for two different cylindrical configurations.

Eight-Inch Cylinder -- A 20.3-cm (8-inch) diameter nontelescoping canister was analyzed in parallel with the dynamics analysis which culminated in elimination of this canister from consideration. The results of this thermal analysis are, nevertheless, of interest because the environment and heatshield requirements were more severe than for the present candidate 27.9-cm (11-inch) telescoping cylinder. The cylinder considered had the following properties:

External radius	10.2 cm (4 inches)
Length	215 cm (75 inches)
Total weight of penetrator, parachute, and canister	43 kg (95 pounds)

The reentry velocity and angle at 100 km (328 kft) were 4730 m/s (15,518 fps) and -15 degrees, respectively. The TRANCE[A32] computer program was used to compute a point-mass trajectory through a Martian atmosphere with the mean summer density. The cylinder orientation was side-on, and the drag coefficients (C_D) were synthesized from data found in References A33 and A34.

The hot-wall stagnation-line heating and also the average laminar heating around a spinning cylinder are shown in Figure A-41. The cross sections, material properties, and significant results for each of the heatshields considered are presented in Table A-II. The ablator thicknesses vary inversely with the densities in order to maintain a constant canister weight. With the stagnation-line heating, excessive temperatures or recession were computed for all the heatshields. The results of this analysis with average heating on a spinning cylinder indicated that the following heatshield would provide adequate thermal protection for the penetrator during Martian entry:
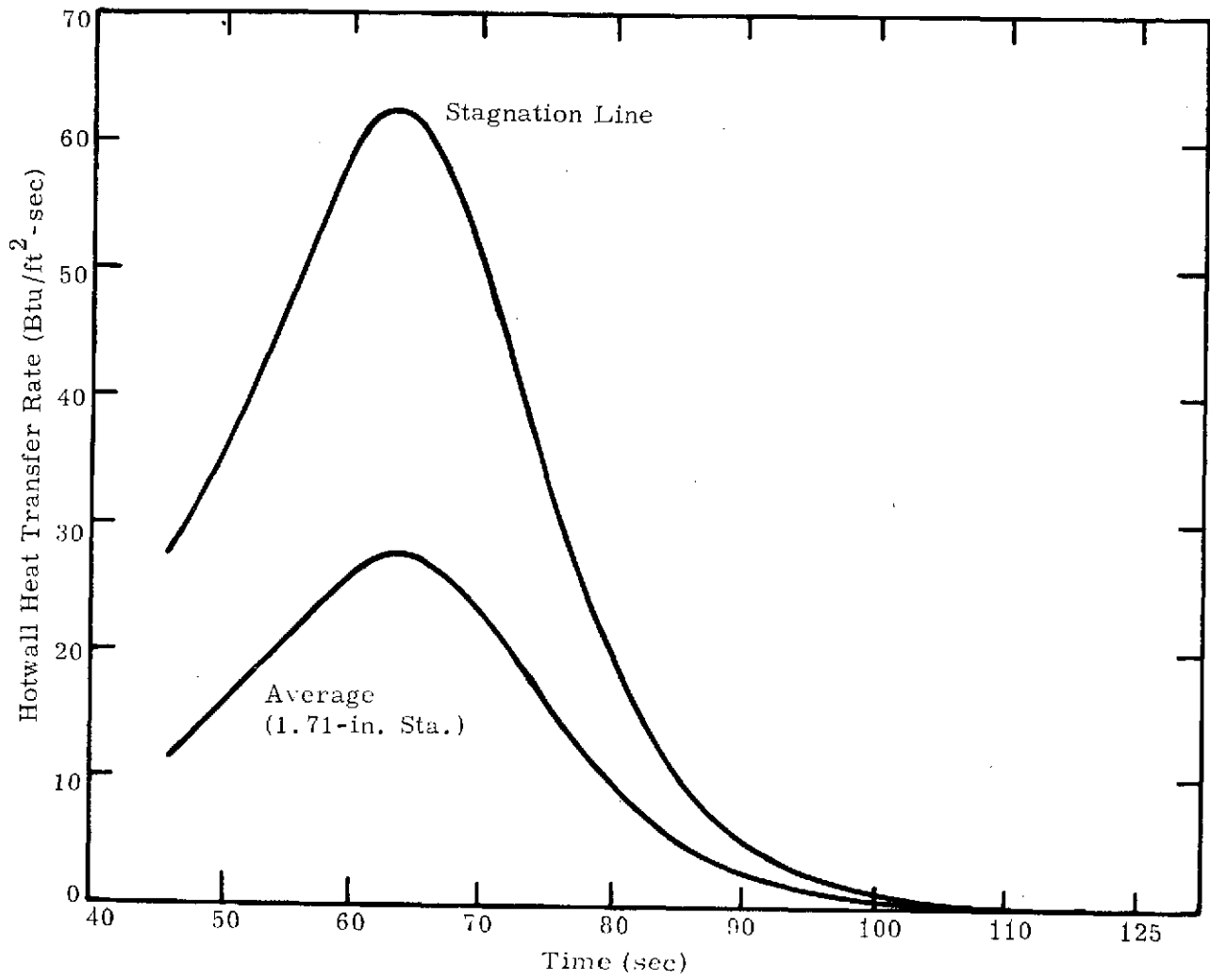
Figure A-41.   Hotwall Heating, 8-Inch Cylinder

Dow Corning 325 Silicone Rubber		0.254 cm (0.10 inch)	
Beryllium		0.152 cm (0.06 inch)	
Radiation Shield		Minimize	

The surface and indepth temperatures for this heatshield as functions of time are plotted in Figure A-42. The data shown in Figures A-43 and A-44 indicate that at the maximum computed temperature of 1150°R (640°K) the ultimate tensile strength of the beryllium would be 66 percent of the strength at room temperature on 8.8 kN/m^2 (26,400 psi).

TABLE A-II

Results of Preliminary 8-Inch-Diameter Mars Canister Analysis
(Substructure was 0.06-inch beryllium in all heatshields)

Ablator Cross Section (in.)	Density (lb/ft^3)	Q* (Btu/lb)	Ablation Temp. ($^{\circ}$R)	Stagnation Line		Average on Spinning Cylinder (1.7.-in. Sta)	
				Total Recession (in.)	Max. Be Temp. ($^{\circ}$R)	Total Recession (in.)	Max. Be Temp. ($^{\circ}$R)
0.100 Dow Corning 325 Silicone Rubber	54.3	24,750^{A35}	3080^{A35}	0.008	1380	0.0	1137
0.070 Thermolag	78.0	5,600	2000	0.034	1627	0.008	1385
0.065 Beryllium	115.4	560	2760	0.0	2400	0.0	1530
0.050 Quartz Phenolic	105.	4,840	3100	0.0	2136	0.0	1630
0.080 Dow Corning 092 Silicone Rubber	68.9	2,000	1560	0.080 at 67 sec		0.040	1120
0.080 Sparesyl	70.0	960	1860	0.080 at 60 sec		0.060	1200
0.040 Teflon	136.	900	1000	0.040 at 57 sec		0.040 at 68 sec	

Eleven-Inch Cylinder -- The 11-inch-diameter, 150-inch-long cylindrical canister was analyzed in the same manner as the 8-inch cylinder. Trajectories for this vehicle assumed a reentry velocity of 4730 m/s (15,518 fps) at -12 and -24 degree entry angles at an altitude of 100 km (328 kft. Cold-wall heating and pressure histories for these trajectories are shown in Figures A-45 and A-46. The significant results are shown in Table A-III. The silicone elastomer coating recommended for the 8-inch cylinder could not be used because of the telescoping requirement. It is presently felt that the initial rubbery consistency of that material might impede the sliding telescope action. This deficiency could conceivably be overcome by a thin low friction coating or different guide surfaces. If so, the silicone elastomer would again emerge as a viable alternative. Design constraints of 6.7 kN/m^2 (20,000 psi) tensile strength required in the substructure and a maximum heatshield and substructure weight of 18.1 kg (40 pounds) eliminate all but the 0.32-cm (0.125-in.) beryllium heat sink and the silica-phenolic composite as alternatives out of those analyzed. While the beryllium heat sink is approximately 4.5 kg (10 pounds) heavier, it has the considerable advantage of simplicity. A real choice between these two (or any other such as the silicone elastomer, emerging from a more exhaustive study) must be left to future more detailed and better optimized analyses.
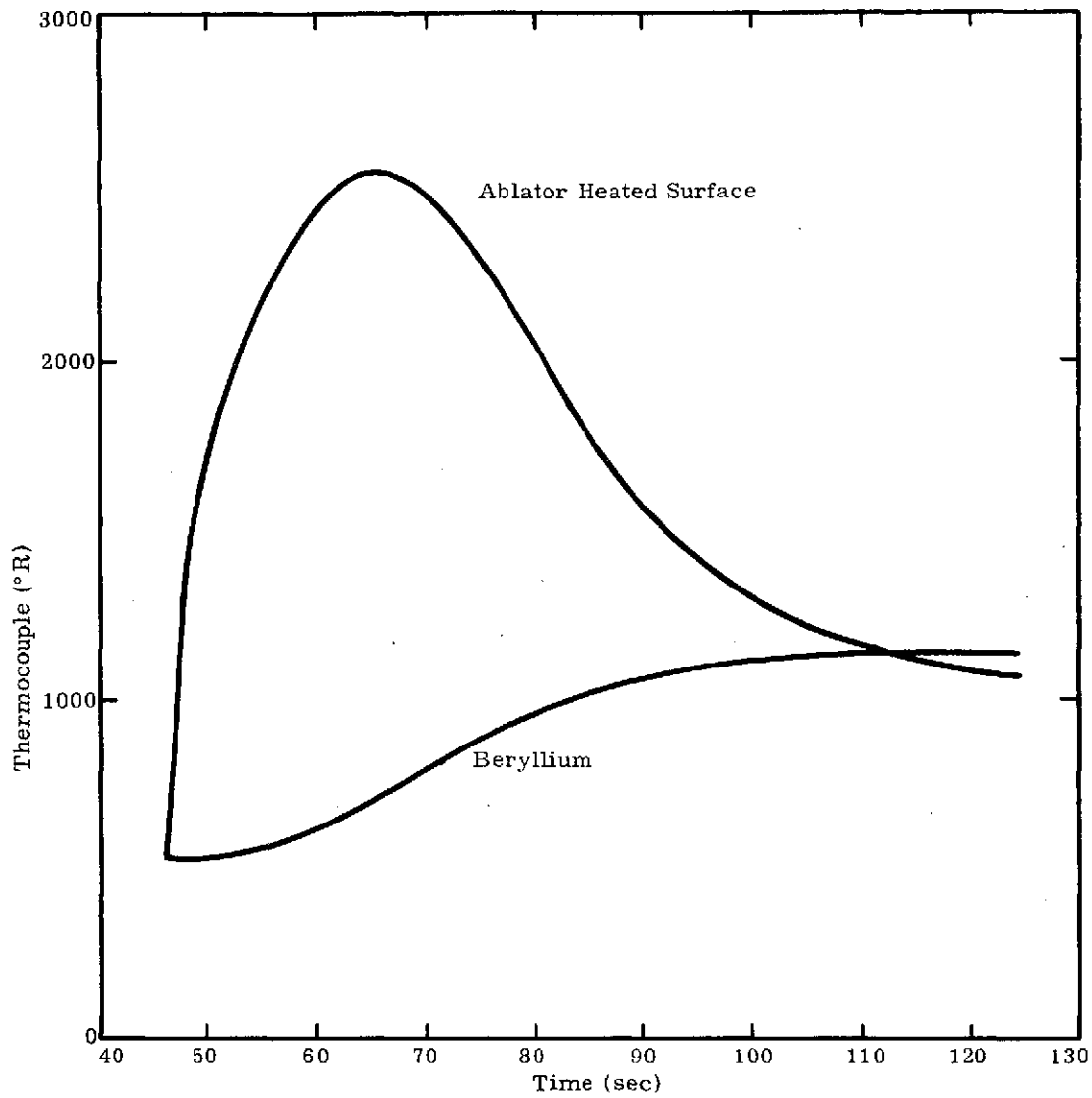
Figure A-42. Dow Corning 325 Heat Shield Temperatures
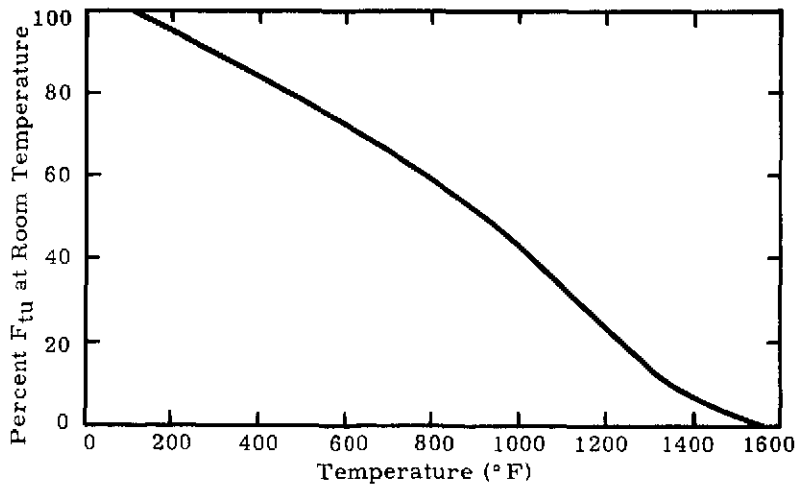
Figure A-43. Effect of Temperature on the Ultimate Tensile Strength ($_{tu}$) of Vacuum Hot-Pressed Beryllium (bars, rods, and shapes)

Specification	MIL-B-21531A			
Form	Bars, rods, and shapes			
Condition	As hot pressed			
Pressing size, lb.	<500		>500	
Basis	A	B	A	B
Mechanical properties:				
F_{tu}, ksi				
L^a	40	44	38	42
LT	40^b	47	40	44
F_{ty}, ksi	27	32	26	29
F_{cy}, ksi	27	32	26	29
F_{su}, ksi	33	36	....	....
F_{bru}, ksi:				
(e/D = 1.5)	88	100	....	....
(e/D = 2.0)	110	125	....	....
F_{bry}, ksi:				
(e/D = 1.5)	....	....	....	....
(e/D = 2.0)	....	....	....	....
e, percent:				
In 2 in.	....	....	....	....
In 4 D	1	....	1	....
E, 10^3 ksi	42.5			
E_c, 10^3 ksi	42.5			
G, 10^3 ksi	20			
μ	$\approx 0.025 \pm 0.005$			
Physical properties:				
ω, lb/in.^{3}	0.066 (min.)			
C, Btu/(lb)(F)	0.445 (at 77 F)			
K, Btu/[(hr)(ft^2)(F)/ft]	104 (at 77 F)			
α, 10^{-6} in./in./F	6.4 (77 F to 212 F)			

[a]Grain direction: L — Parallel to pressing direction.
LT — Normal to pressing direction.

[b]Since the computed A value of 43 ksi for F_{tu} LT is greater than the specification S value of 40 ksi the latter value is shown in the table per Section 9.2.14.

Figure A-44. Design Mechanical and Physical Properties of
Vacuum Hot Pressed Beryllium Shapes
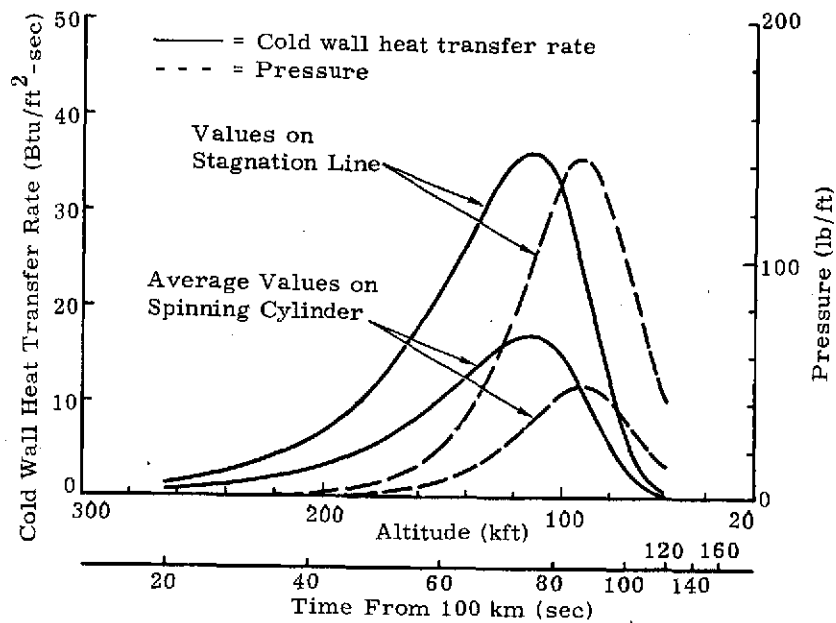
Figure A-45. Heat Transfer Rate and Pressure Histories for 11-Inch Diameter Times 150-Inch Long Cylinder. $\beta = 2.6$ psf, $\gamma = -12°$
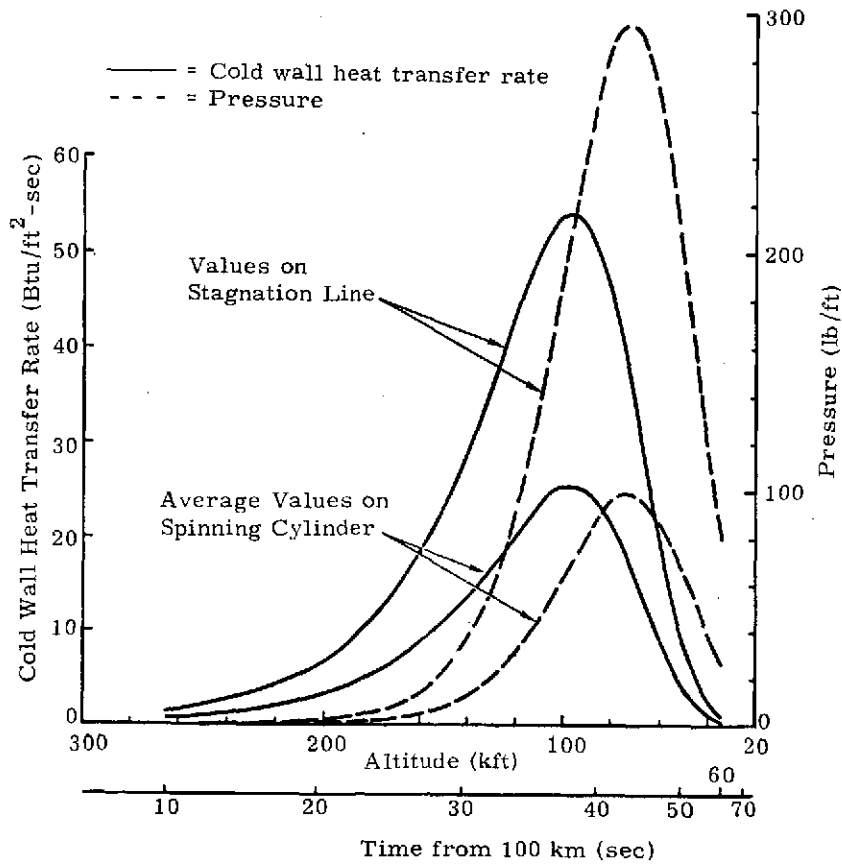
Figure A-46. Heat Transfer Rate and Pressure Histories for 11-Inch Diameter times 150-Inch Long Cylinder. $\beta = 2.6$ psf, $\gamma = -24°$

TABLE A-III

Results of Reentry Canister Thermal Analysis

(β = 2.6 psf, Diameter = 11 Inches, Extended Length = 150 Inches)

Cross Section (in.)	Density (lb/ft^3)	Component Weight (lbs)	Total Weight (lbs)	$\gamma = -12°$			$\gamma = -24°$		
				Max Temp (°R)	% RT Ultimate Strength	Ult. Ten. Strength at Temp (psi)	Max Temp (°R)	% RT Ultimate Strength	Ult. Ten. Strength at Temp (psi)
0.060 Beryllium	115	20.7	20.7	1910	5	2,000	1610	28	11,200
0.125 Beryllium	115	43.1	43.1	1360	51	20,400	1150	66	26,400
0.060 Aluminum (2024T3)	175	31.5	31.5	2170	0	0	1860	0	0
0.125 Aluminum	175	65.6	65.6	1600	0	0	1370	0	0
0.040 Ti-6 Aℓ-4V	276	33.1	33.1	2590	0	0	2520	0	0
0.125 Ti-6 Aℓ-4V	276	103.0	103.0	1850	0	0	1550	50	67,500
0.050 Silica Phenolic ⎫ 0.050 Fiber Frax ⎬ 0.040 Beryllium ⎭	105 20 115	15.8 3.0 13.8	32.6	1234	61	24,400	915	80	32,000

Thermal Analysis of the Deployable Attached Decelerator (DAD)

The maximum aerodynamic heating on the Deployable Attached Decelerator (DAD) was evaluated from data presented by Holden, Nestler, and Elfstrom.[A36,A37,A38] Wedge-induced laminar separation and reattachment were shown to produce heating rates in the reattachment area in the range of 16 to 80 times the undisturbed cylinder values. These techniques, when applied to the DAD, produced maximum heating rates, which approximate the cylinder stagnation line values.

Two heatshield concepts were considered for the forward surface of the DAD: (1) a multilayered system consisting of 0.16-cm (0.0625-inch) carbon (fiber) cloth, 0.16 cm (0.0625-inch) silica cloth, and 0.64-cm (0.25-inch) fiberfrax, and (2) silicone elastomers such as Dow-Corning 325. The external surface and indepth temperature computed for the multilayered heatshield are shown in Figure A-47. The temperature of the Kevlar at the parachute deployment altitude of approximately 10.7 km (35,000 feet) is $1060^{\circ}R$ which is significantly greater than the maximum allowable Kevlar temperature of $810^{\circ}R$. These results indicate that considerable developmental effort would be required to make this concept a viable thermal protection system.

In that pyrolysis and charring are two of the basic attributes of silicone elastomer heatshields, the heat-of-ablation analysis described previously proves too conservative to adequately model the problem. Thermal analyses of the silicone elastomer heatshield will be performed.

Decelerator Flaps System Analysis

In the decelerator flap system analysis, two reentry conditions (β = 1.3 and 2.6 lbs/ft^2, γ = -24.0°) have been considered. The first condition (β = 1.3, γ = -24) provides the most severe structural requirements; the second condition (β = 2.6, γ = -24) results in the most severe heating. The analyses presented are for the first stage of deceleration only.

Flap Drag -- In determining the drag of the deceleration flaps, it has been assumed that the pressure on the flap is given by modified Newtonian theory, and that this pressure is uniform over the entire area of the flap.[*] The results of this calculation are shown in Figure A-47, where the axial force coefficient, $C_A \equiv F_{axial}/q_{\infty}S_{flap}$, is plotted against flap deflection angle for Mach numbers of 5 and 20. As may be seen, the drag coefficient decreases rapidly for deflections less than 50 degrees, and it is not a strong function of Mach number.

For reasons which will be discussed later, a flap deflection of 60 degrees was selected. From the flap deflection selected, the areas required and the forces to be expected (see Table A-IV) can be computed.

TABLE A-IV

Flap Axial Forces

β	Flap Area (ft^2)	Maximum Axial Force (lbs)
1.3	22.6	2300
2.6	11.3	2100

---

[*]There is experimental evidence that this is a reasonable approximation on a sphere-cone-cylinder configuration with long, narrow flaps at M = 4.5.
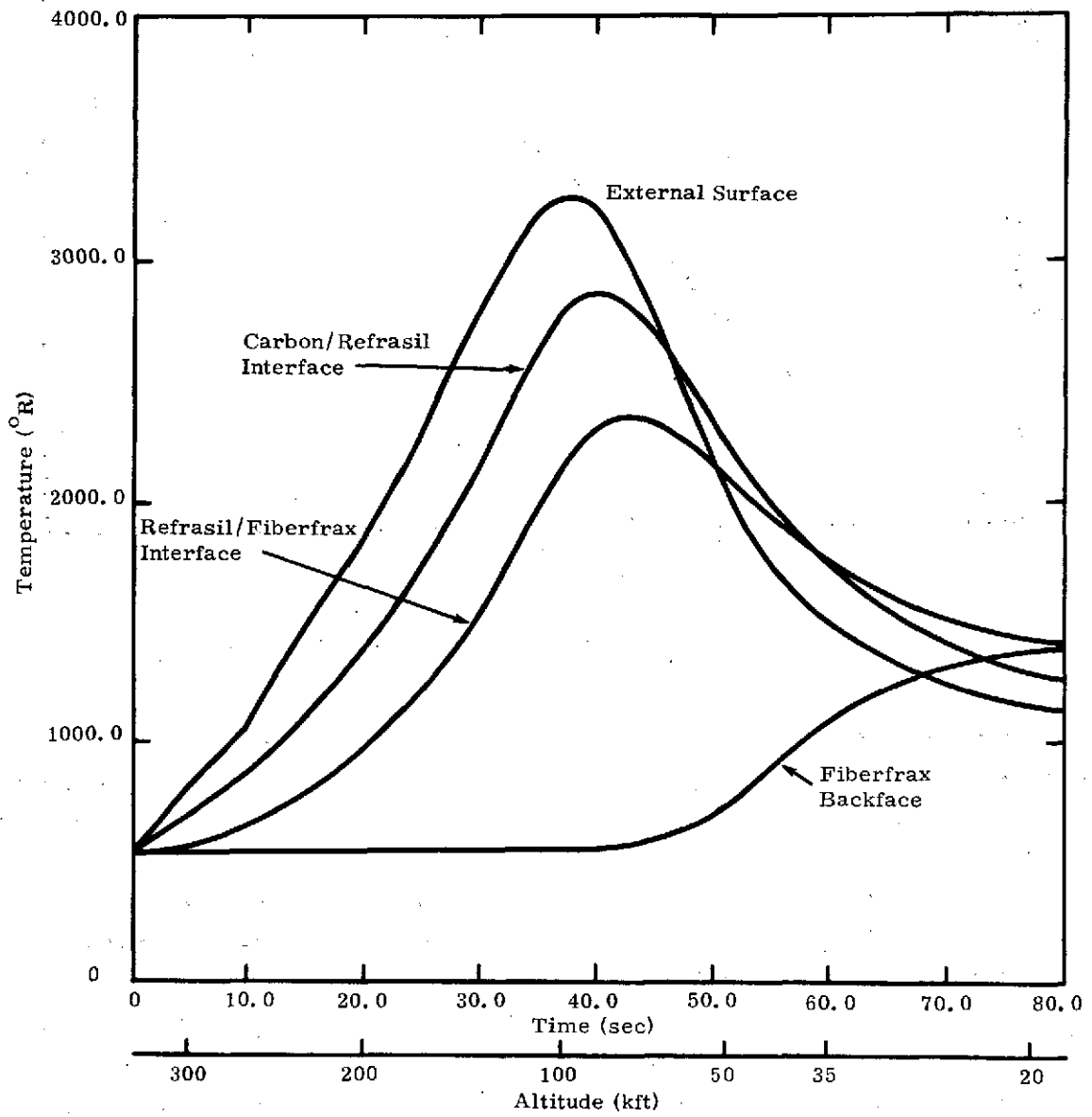
Figure A-47. DAD Heatshield Temperaures for β = 2.6 psf and γ = -24° with Cross Section of 0.0625-Inch Carbon (Fiber) Cloth, 0.0625-Inch Refrasil and 0.25-Inch Fiberfrax
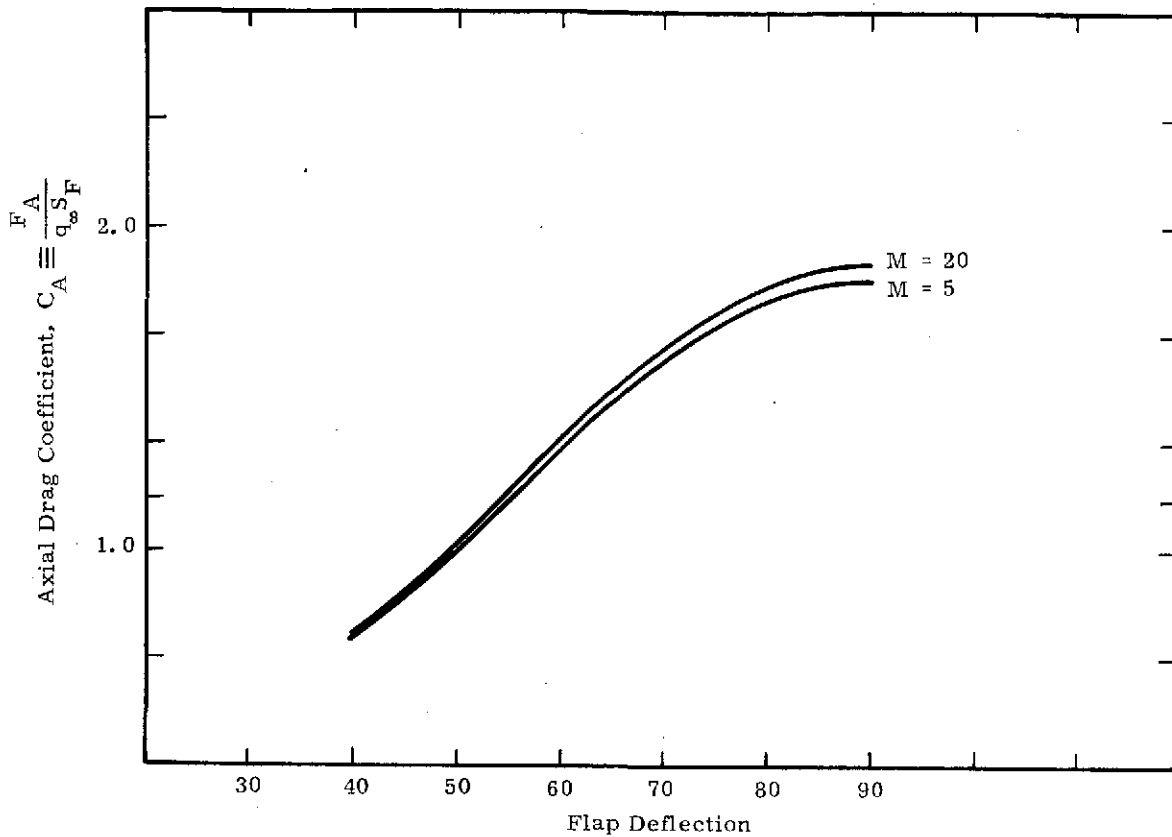
Figure A-48. Newtonian Drag Coefficient versus Flap Deflection

As discussed later, the flaps will be formed from two concentric cylinders which are sectioned into quarters and pivoted at the aft end of the vehicle (the inner cylinder is rotated 45 degrees before deployment). Each flap is thus formed from the inner surface of a portion of a cylindrical shell. The width of each section is approximately 19. 8 cm (7. 8 inches), which leads to flap lengths of 1. 3 and 0. 7 meters (4. 4 and 2. 2 feet), respectively, for the two β's. It must be stressed that these lengths are based upon the assumption of Newtonian pressures, and therefore they should be regarded as first approximations to the actual lengths.

Flap Heating -- In assessing the severity of flap heating, two cases need to be considered:
(1) the basic heating to be experienced in the absence of any interference effects, and (2) the increase in heating associated with houndary-layer separation and reattachment and shock interference.

Figure A-49 presents the flap heating as a function of time for the two reentry conditions. These results were obtained by adjusting the solutions for a 20. 3-cm (8-inch) diameter cylinder with no sweep through the relation[A39]

$$\frac{Q_{\Lambda = 30}}{Q_{\Lambda = 0}} = \cos^{1.1} \Lambda .$$

The justification for using the cylindrical heating rate for a flat plate geometry is based upon earlier work on flat-faced fins,[A40] where it was found that, if the length were large compared to the width,
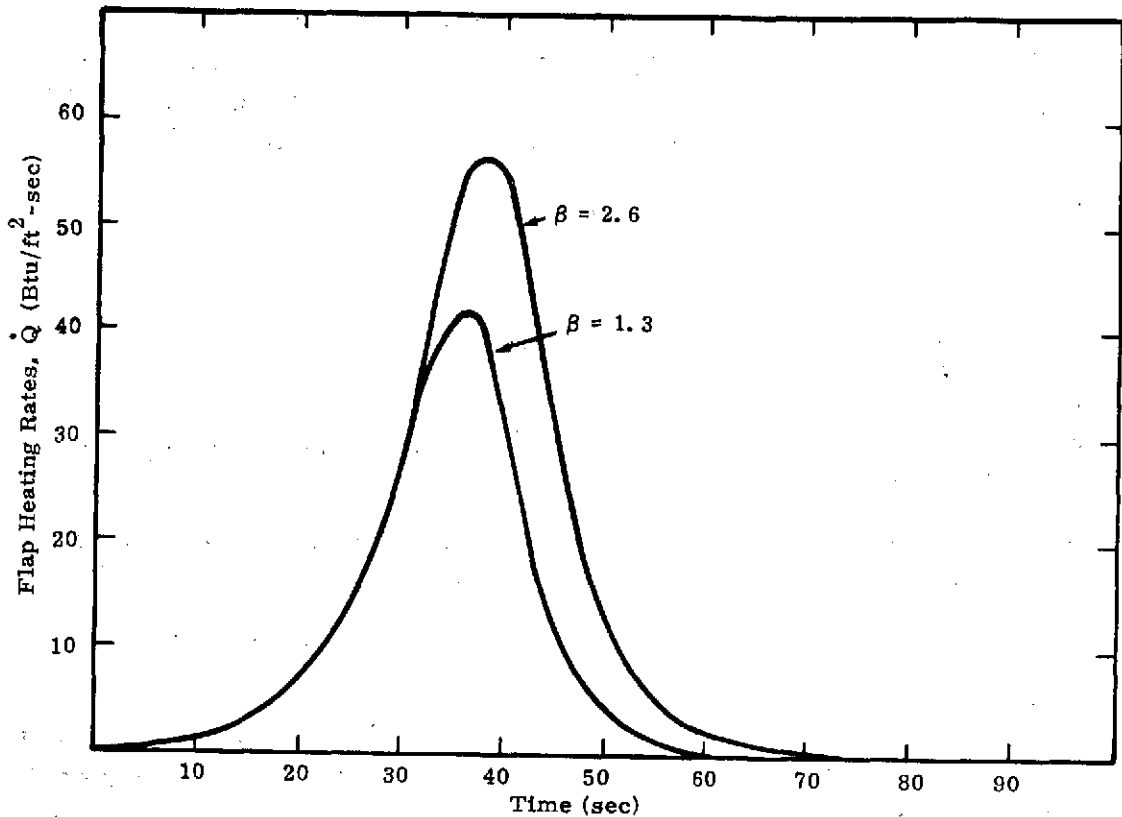
Figure A-49. Flap Aerodynamic Heating

the heating rates were approximately equal to those for fins with cylindrical leading edges of a diameter equal to the flat width. As expected, the most severe heating occurs for the β = 2.6 case, in which a peak heating rate of approximately 56 Btu/ft^2-sec is obtained at 39 seconds.

In determining how this basic heating is altered by boundary-layer separation and reattachment, it is necessary to determine the separation geometry.[*] The approach taken here is based upon correlations[A41] of wind-tunnel data which provide estimates of the plateau pressure in the separated region, the length of separation, and the peak heating in the reattachment region. To use these correlations, it is necessary to determine the boundary-layer edge Mach and Reynolds numbers at the flap hinge line. These quantities were obtained with the computer code described in Reference A42 (the forebody was assumed to be a spherically blunted cylinder). Given the Mach and Reynolds numbers, the plateau pressure and separation length are determined from

$$C_{p,\ plateau} = 1.6 \left(Re_{x_{H.L.}} \right)^{-1/4} \left(M_e^2 - 1 \right)^{-1/4}$$

$$\frac{\ell_{sep}}{\delta_{H.L.}} = \frac{35}{M_e^3} \left[\left(\frac{P_f - P_{pl}}{P_e} \right) Re_{x_{H.L}}^{1/4} \right]^{0.98} .$$

[*]Laminar boundary layers typically separate for flap deflections of only a few degrees.

where the various quantities appearing in these expressions are defined in the nomenclature. When the plateau pressure is known, the separation angle may be determined, and this angle, together with the separation length, determines the reattachment point. If the reattachment point is known, the peak pressure at reattachment may be computed; the peak heating is given by

$$\frac{\dot{q}_{pk}}{\dot{q}_{cyl}} = \left(\frac{p_{pk}}{p_e}\right)^{1.3}$$

where $\dot{q}_{cyl}$ is determined from Reference A42.

By utilizing the conditions obtained at the maximum heating condition in the $\beta = 2.6$ trajectory, the following results were obtained:

1. Separation occurred near the spherical nose, and reattachment occurred on the flap approximately 25.4 cm (10 inches) from the hinge line.

2. The peak reattachment heating was 55 Btu/ft^2 sec, which is comparable to the stagnation-point value.

It should be noted that the above analysis has assumed that there is no boundary-layer flow through the hingeline. For laminar boundary layers, it has been observed[A43] that a very small amount of boundary-layer bleed will eliminate separation entirely. This approach should be investigated experimentally for the present configuration.

The second type of interference heating which is of concern is that induced by bow shock impingement on the flap. Estimates[A44] of the bow shock shape at M = 15 for the present configuration (assuming a spherically blunted cylinder with boundary-layer separation) indicate that shock impingement will occur for flaps approximately 30 inches long. In the absence of separation, this distance would be less. Because the flap lengths are known, shock impingement must be regarded as a possibility for both β's.

For flap deflections in the range 50 to 90 degrees, two types of shock interference (Types IV and V) are possible.[A45, A46] Both types are illustrated in Figures A-50 and A-51. Type IV, which results from the interaction of an impinging oblique shock with a strong shock (i.e., one behind which the flow is subsonic), leads to the formation of a supersonic jet which subsequently impinges on the flap. At the impingement point on the flap, very severe localized pressures and heat transfer rates are experienced. The exact level depends upon the strength of the impinging shock; levels an order of magnitude above the undisturbed values are not uncommon. This type of interference may be avoided by decreasing the flap deflection to ensure that the flap shock is a weak oblique shock, which was the reason that a 60-degree flap was selected.

When an impinging shock intersects a weak oblique shock of the same family, Type V interference occurs (see Figure A-51). This interference results in a supersonic jet, a shear layer, and a transmitted shock, all of which may impinge on the flap and cause increased heating. Of the three mechanisms, the transmitted shock leads to the most severe increases in pressure and heating.

Flap Shock

Flap

Bow Shock

Region of High
Heating Pressure

Supersonic
Jet
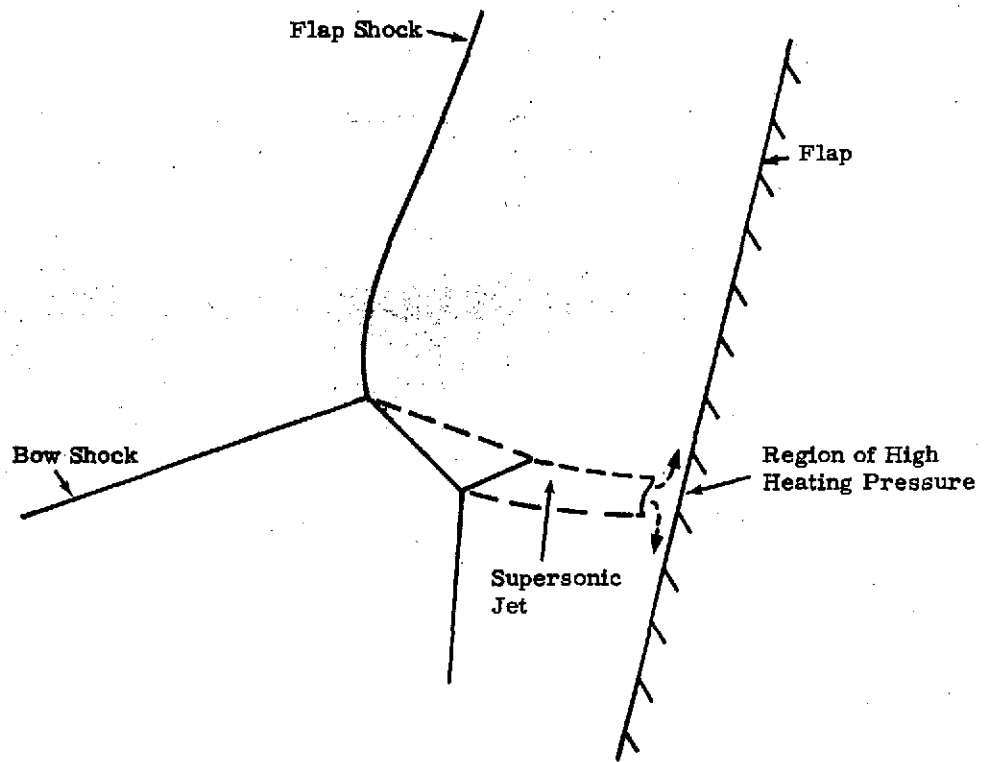
Figure A-50. Type IV Shock Interference

Flap Shock

Supersonic
Jet

Flap

Shear
Layer

Bow Shock

Reflected Shock

Increased Pressure
and Heating

Transmitted
Shock
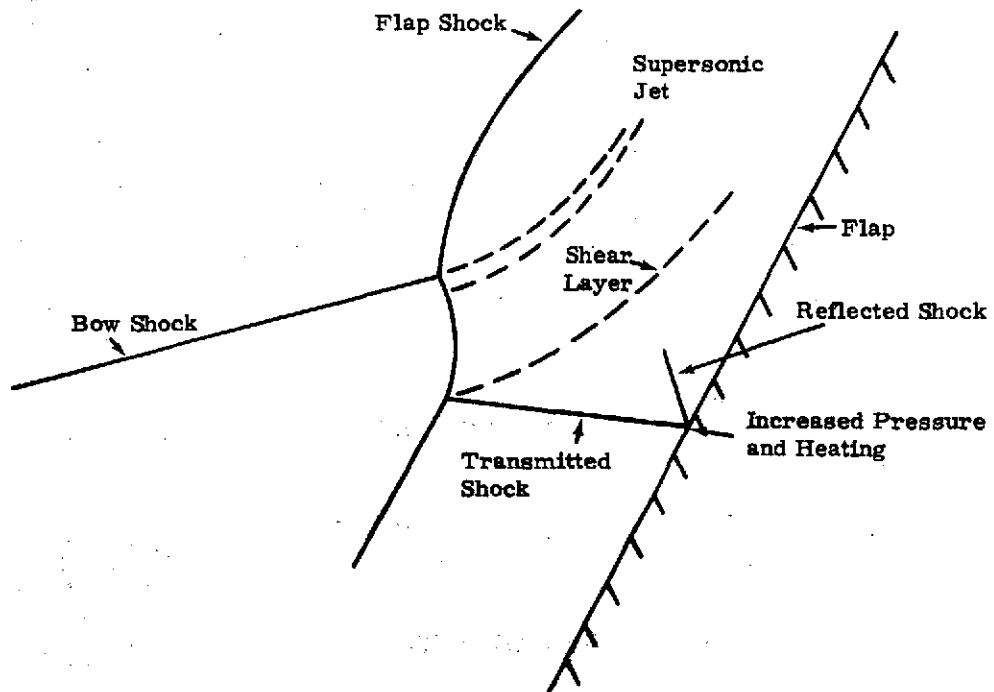
Figure A-51. Type V Interference

Although the increases are less severe than for Type IV, for the present configurations, increases in heating of a factor of four or five may be anticipated.[A50]

It should be noted that, for both Type IV and Type V interference, it is not possible to calculate the location of increased heating because of the uncertainty in location of the impinging shock and the nature of the two interference patterns.

Thermal Protection of Decelerator Flaps

The heatshield and structure cross section considered for the decelerator flaps was 0.25-cm (0.10-inch) silica phenolic, 0.25 to 1.0-cm (0.1 to 0.40-inch) Fiberfrax, and 0.13 cm (0.05-inch) aluminum. The computed external surface and indepth temperatures of the heatshield are shown in Figure A-52. These results indicate that a Fiberfrax thickness of 0.51 cm (0.20 inch) would be adequate.
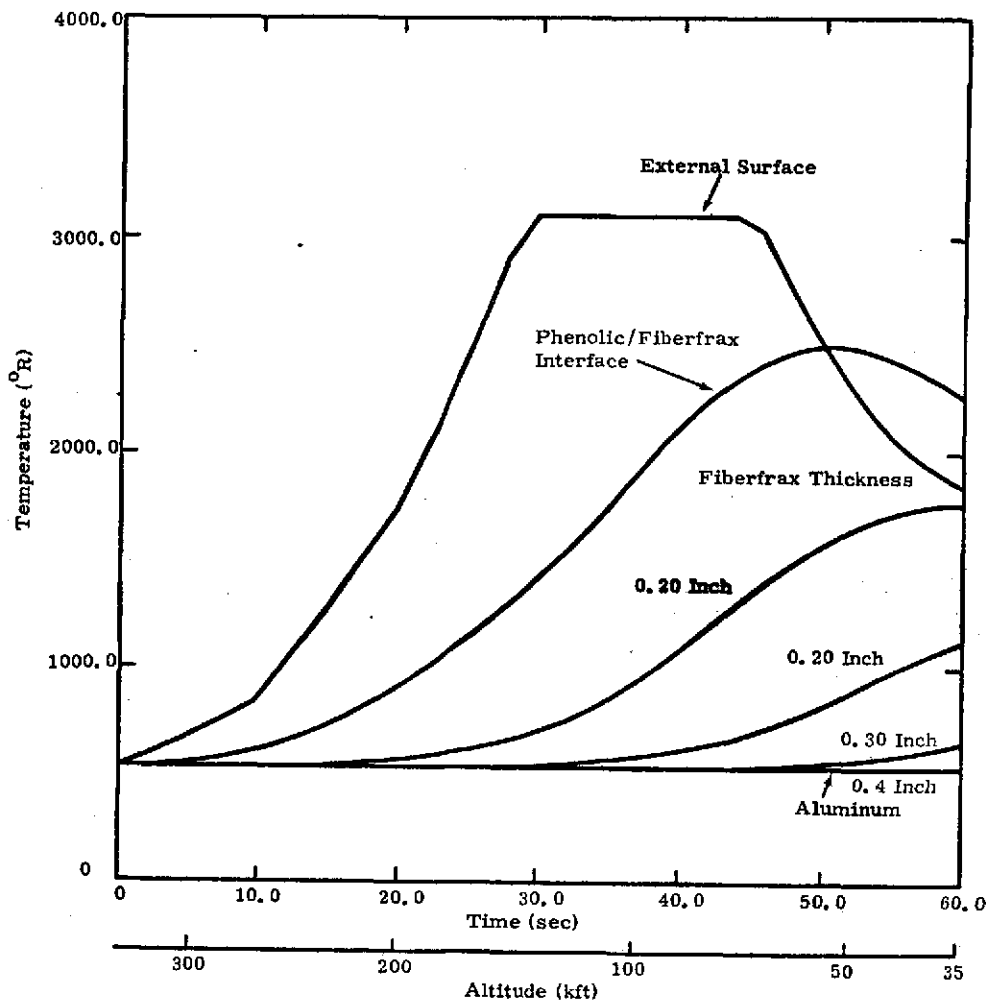
Figure A-52. Decelerator Flap Heatshield Temperatures for β = 2.6 psf and γ = -24° with Cross Section of 0.10-Inch Silica Phenolic, 0.10-0.40-Inch Fiberfrax and 0.05-Inch Aluminum

Decelerator Flap Structural Analysis

The launching, packaging, aerodynamic, and trajectory requirements place the following constraints on the proposed flap deceleration system:

1. The flaps must be easily and remotely deployable;

2. The penetrator plus the deceleration system must be housed in an 11-inch-diameter, 1.5- to 1.83-meter-long (5 - 6-foot long) canister in the predeployment configuration.

3. For the worst "structural" trajectory, a maximum total surface area of 1.86 to 2.32 m^2 (20 to 25 ft^2) is required;

4. Maximum weight of the total flap deceleration system is 9.1 to 11.3 kg (20 to 25 pounds);

5. A net force opposing the direction of flight of 10.2 kN (2300 pounds) is required;

6. The flaps should be dployed at an angle of approximately 60 degrees with respect to the trajectory path; and

7. A variable projected area should be attainable.

Basic Geometry -- The proposed deceleration scheme would have the flaps perform the function of forming the predeployment canister. This would be accomplished by segmenting each of two closely fitting concentric cylinders into four equal circumferential sections (see Figure A-53), making a total of eight flaps when deployed. The flaps would be hinged from a tubular lightweight pedestal below the penetrator as in Figure A-54. Such a system of eight flaps, which are each 1.5 meters (5 feet) long and have a radius of 13.97 cm (5.5 inches), would have a total projected area normal to conical flap envelope of 2.4 cm^2 (25.6 ft^2). This scheme adheres to the first three constraints mentioned above.

(a)
Predeployment

Penetrometer

(b)
During Deployment

(c)
After Deployment
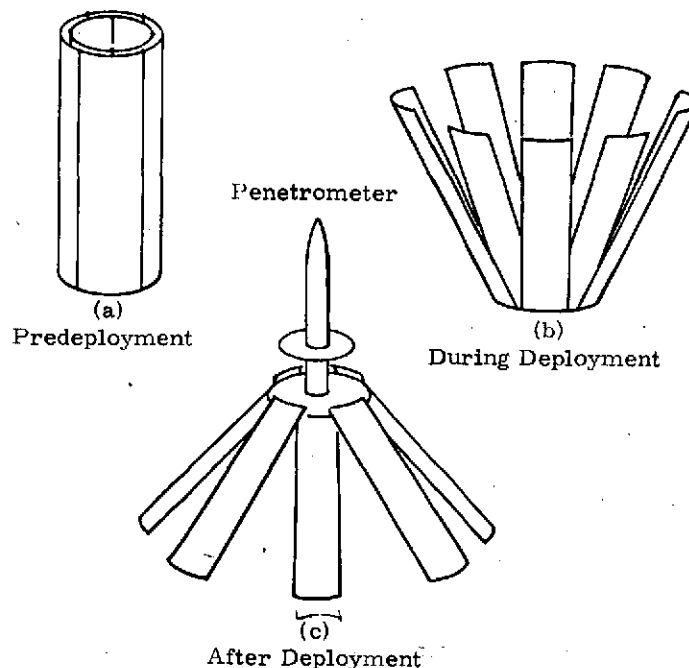
Figure A-53. Concentric Cylinder Flap Concept
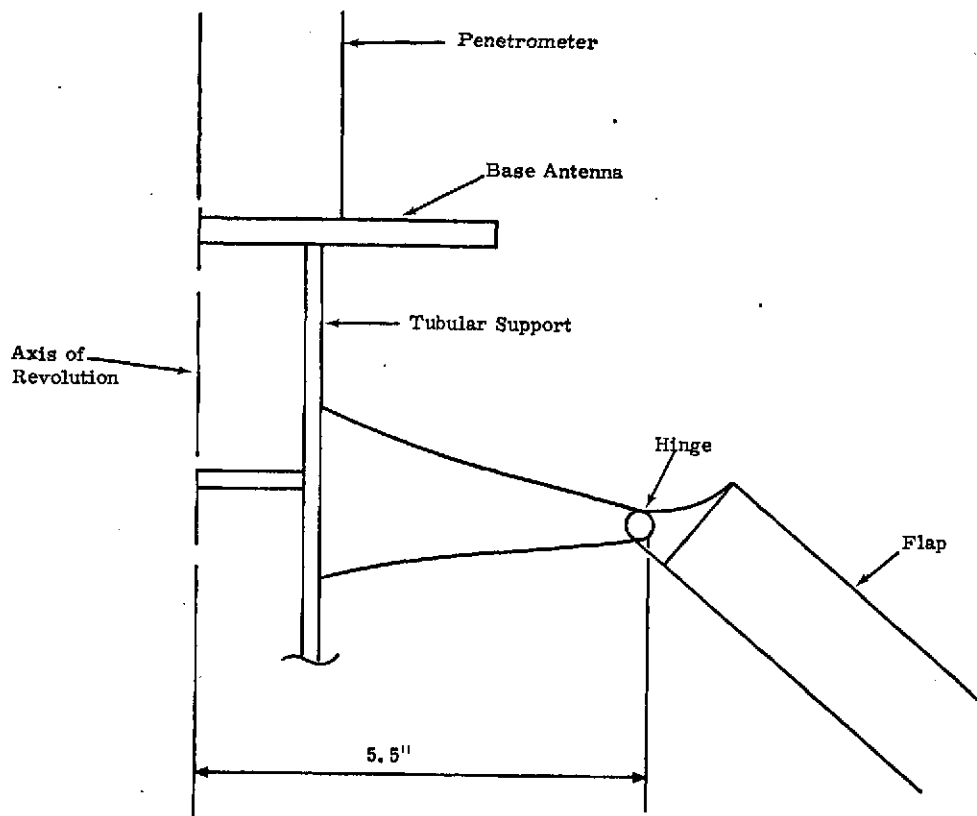
Figure A-54. Hinge Concept

Because of the packaging requirements and the concentric cylinder predeployment configuration, each shell flap must carry its load in the plane of the shell[*] and not rely on additional structural elements. It has been assumed that the basic shell plus any stiffening ribs will be no thicker than 0.64 cm (0.25 inch).[**] It is assumed that the shell will be made of high-strength aluminum with a density of 0.271 gm/cm^3 (0.098 $lb/in.^3$). In addition, the weight requirements for the flap system dictate the approximate mass per unit circumferential distance. If a total weight for the flaps is chosen to be 9.1 kg (20 pounds) 1.1 kg (2.5 lbs per flap), the average thickness of the shell should be 0.13 cm (0.051 inch). Because of machinability problems, the thickness of the shell skin should not be less than 0.076 cm (0.030 inch).

Thus the shell or skin thickness, t_s, is 0.076 cm (0.030 in. $< t_s$ 0.31 cm (0.051 in.) and the total thickness, t_t, with stiffeners, $t_t < 0.64$ cm (0.250 in.).

In that the thickness of the shell, even with stiffeners, is small compared with the radius, the gross bending and shear stresses may be determined by assuming the shell to be a thin-wall beam element of nominal thickness t = 0.13 cm (0.05 in.) with an area A and moment-of-inertia I (see Figure A-55) of

$$A = 2.79 \text{ cm}^2 \text{ (0.432 in.}^2)$$

$$I = 32.34 = 4.20 \text{ cm}^4 \text{ (0.101 in.}^4)$$

---

[*]The exception to this will be to consider a single support cable or strut for each flap.
[**]The inner shell will thus have a diameter $\sim$ 1.27 cm (0.5 inch) less than the outer shell.
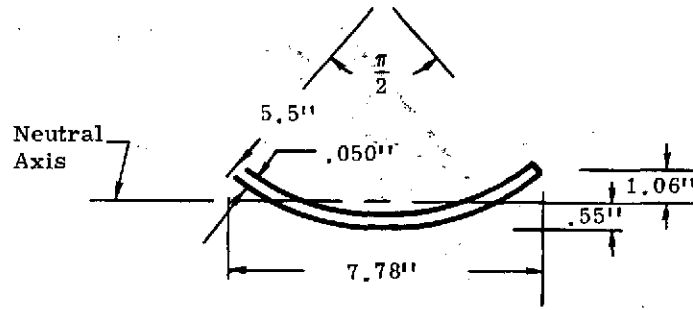
Circumferential Length = 8.64"

Figure A-55. Flap Cross Section Dimensions

Loads -- The required maximum aerodynamic load is 10.2 kN (2300 pounds) in the axial direction which is developed from total pressure load of 11.8 kN (2656 pounds) normal to the envelope of the flaps which form an angle of 60 degrees with the axis (see Figure A-56). It is assumed that pressure is uniform over the flap with a resultant load per unit length normal to the flap of 5.53 lbs/in. Three different strut support schemes based on these loads were investigated (Figure 57).

The beam model peak bending moments, M, shear load, V, and axial load, P, along with the respective stresses corresponding to bending, σ_{NB}, shear, σ_S, and axial normal, σ_{NP}, stress are shown in Table A-V.

TABLE A-V

Maximum Loads and Stresses Corresponding to Support Schemes I, II, and II (Figure A-57)

Scheme	M (in-lbs)	V (lbs)	P (lbs)	Compressive σ_{NB} (psi)	Tension σ_S (psi)	σ_S (psi)	σ_{NP} (psi)
I	9954	332	0	54204	105000	1300	0
II	852	235	0	8950	8950	924	0
III	852	235	457	8950	8950	924	1058

W = 5.53 lbs/in

Flap 60'' long

Possible Cable
Support
Length = 68.2''

27.2°

Possible strut support
Length = 73''

60°

36''

84.8''
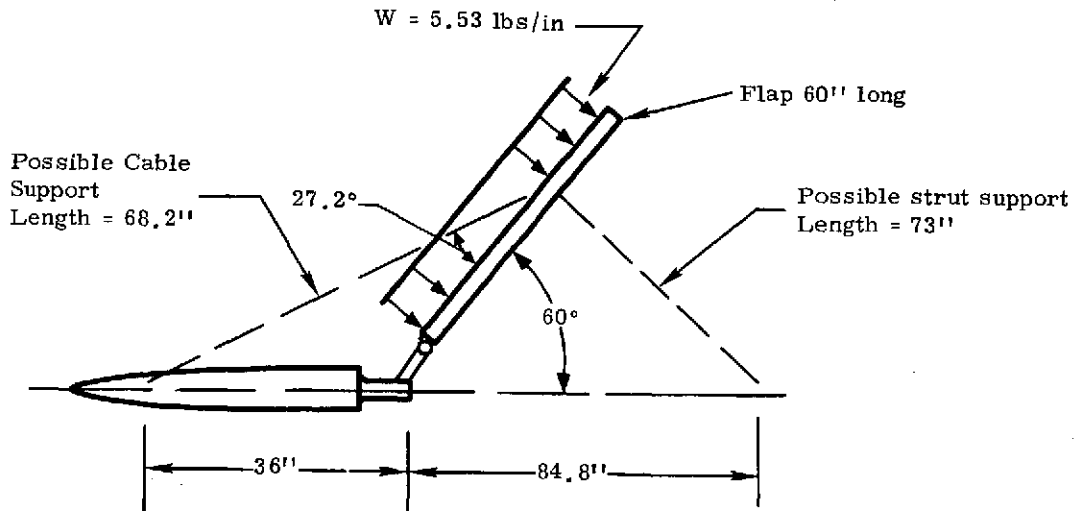
Figure A-56. Geometry and Applied Loads on a Typical Flap

Scheme

W = 5.53 lbs/in

I

60''

W = 5.53 lbs/in

II

42.4''

17.6''

Strut
Support

Cable Support

W = 5.53 lbs/in

III

Note: These
Dimensions
Correspond to
Minimum Bending Moments
in Beam

42.4''

17.6''
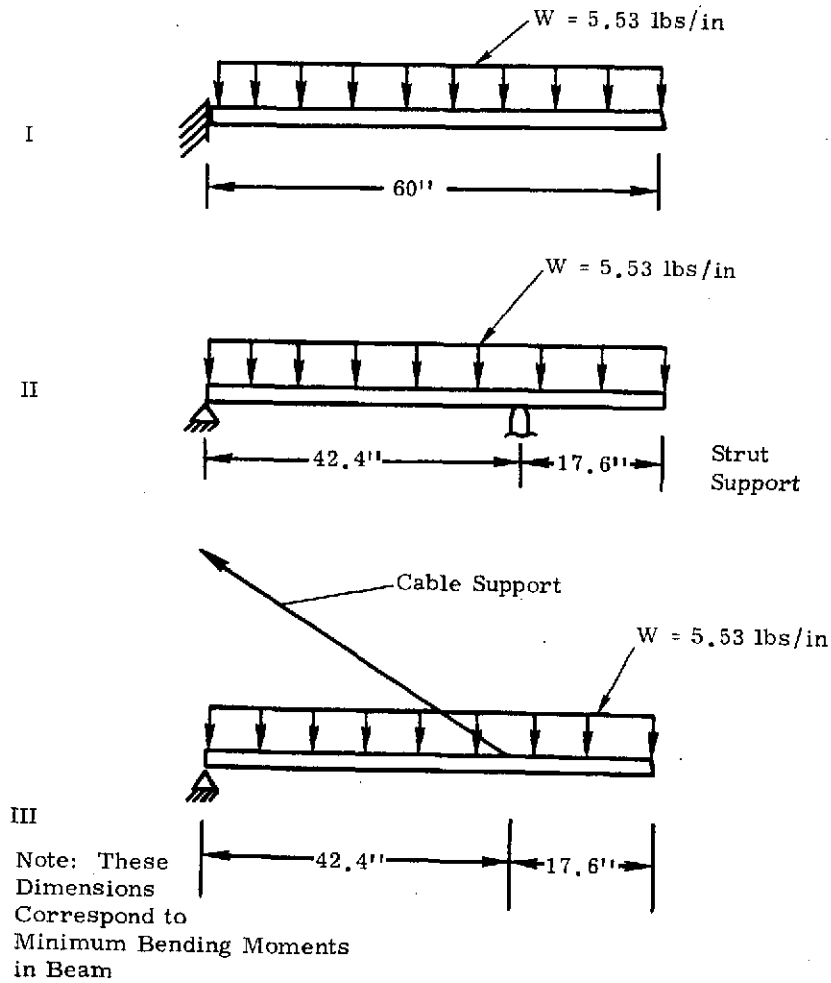
Figure A-57. Support Schemes

In that high-strength aluminum has a yield stress of 25 kN/m^2 (75,000 psi), yielding is not a problem except for Scheme I. Even here, local thickening of the shell will greatly reduce the stresses. Buckling and the detailed design of the shell skin and stiffeners will be investigated.

The three modes of buckling considered when sizing the shell skin stiffener design are Mode (a) beam mode (Euler Column) type buckling of the flap, Mode (b) local skin buckling, and Mode (c) gross panel buckling in which the stiffeners buckle in a localized area. Mode (a) will be caused only by the net axial thrust on the beam, but the bending stresses may precipitate either buckling types (b) or (c).

In addition, if the net axial thrust on the shell element is large enough, it may precipitate any of the three modes. Because this load produces a uniform stress state in the shell, any stiffening designed to prevent failure must be uniform in the shell. On the other hand, in that the bending loads produce no net axial thrust and produce axial stress states in localized areas, only local stiffening can often be designed to preclude localized buckling.

The critical axial stresses $(\sigma_{cr})_a$, $(\sigma_{cr})_b$ corresponding to buckling Modes (a) and (b) found are given by the formulas

$$(\sigma_{cr})_a = \frac{\pi^2 EI}{AL^2} = 4.3 \text{ kN/m}^2 \text{ (12,838 psi)} ,$$

$$(\sigma_{cr})_b = \frac{K_s \pi^2 E}{12(1 - \nu^2)} \left(\frac{t_s}{b_s}\right) = 72,000 \text{ psi} \dagger.$$

K_s, t_s and b_s are defined in Reference A48. ν is Poisson's Ratio. E is Young's modulus (3333 kN/m^2) (10^7 psi), and t is the equivalent thickness of a solid plate having the same flexural rigidity as a plate with the skin stiffener configuration shown in Figure A-58. The skin stiffener configuration shown in Figure A-58 is a design arrived at after several iterations maximizing I_ℓ and keeping the area-per-unit length of circumference at 0.323 (0.050 in.^{2}).

No precise value for the buckling of an axially compressed curved panel with free sides is available. One estimate of the buckling stress was obtained by approximating the curved panel by a long slender flanged element with equal flange lengths corresponding to half the circumference of the panel. By this approximation,

$$(\sigma_{cr})_c = 0.388 \, E \left(\frac{\bar{t}}{b}\right)^2 = 5.408 \times 10^3 \text{ psi} ,$$

where b is the flange length.

A different approximation for the same mode can be made by letting

$$(\sigma_{cr})_c = R \, \sigma_{EPL} ,$$

where σ_{EP1} is the Euler critical stress for a flat plate or

---

$\dagger$In this analysis, units in some equations are not converted because of constants in the author's choice of equation.

$$\sigma_{EP1} = \frac{2EI_\ell L}{AL^2} = 364 \text{ psi}$$

and R is the ratio of the critical stress corresponding to buckling of an axially compressed curved panel with simply supported sides to the critical buckling stress of the flat plate with simply supported sides (all other dimensions of the two plates are the same). From Reference A49,

$$R = 0.395 \left(\frac{r}{t}\right) = 13.6 \quad .$$

Thus,

$$(\sigma_{cr})_c = 13.6 \times 364 = 4950 \text{ psi.}$$
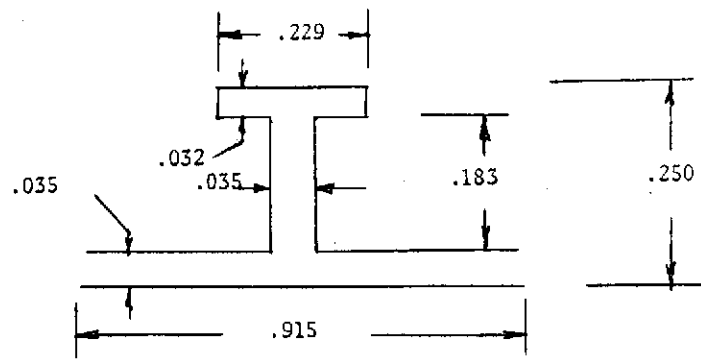
Note: I_ℓ = Moment of inertia/unit length of skin plus stiffeners

$\bar{t}$ = effective thicknerers

$\bar{t} = (12 I_\ell)^{1/3} = .162$

$I_\ell = 3.58 \times 10^{-4}$

Figure A-58. Shell Skin Stiffener Design

It should be noted that Mode (c) will precipitate at the outer edge of the cylinder and that just a small amount of constraint keeping the flap from expanding in the region of high stress will greatly increase the critical stress level.

By comparing the calculated critical stresses with the reaction-produced stresses, the following generalizations can be made: Mode (a) will not occur, Mode (b) will not occur unless the modulus is lowered significantly by heating [25 percent for support Scheme I and 80 percent for Schemes II

and III)], Mode (c) buckling is uncertain* in each design but can probably be circumvented for support of Schemes II and III by low-weight-penalty circumferential stiffening of each shell in the regions of maximum axial stress. Additional axial stiffening near the support may alleviate the problem in Scheme I.

Shown in Table A-VI is a breakdown of the estimated weight penalties for each support scheme.

TABLE A-VI

Additional Weights (20-Pound Flaps)

Support Scheme	Hinge Support (lbs)	Cables* (lbs)	Struts[†] (lbs)	Circumferential** Stiffening (lbs)	Additional Stiffening (lbs)	Total (lbs)	Comments
I	2.0	0	0	0.7	4.0 (?)	26.7	Marginal
II	1.5	0	8	0.7	0	30.5	Possible if aero-heating is below tolerable limits. Also struts may not be deployable.
III	1.5	1.34	0	0.7	0	23.5	Possible if aero-heating is below tolerable limits.

* Steel cable (wire) with a density of 0.04 lb/ft and 0.125-inch diameter, 69 inches long.
[†] Struts assumed 0.5-inch diameter and were designed to critical Euler load, L = 73.
** Six circumferential supports of type used in the axial direction for each of the eight flaps imposes a total weight penalty of 0.7 pound.

Summary -- With local structural stiffening, support schemes II and III can be made to withstand the imposed structural loads. If the thermal degradation is not too severe, Scheme II is not as weight competitive as Scheme III, and the struts may not be deployable. Scheme III appears feasible. Testing and analysis of local stiffening should be done to resolve panel buckling uncertainties (Mode c).

---

* There is an apparent lack of data and analysis for this mode applicable to curved panels with free edges. The effective low circumferential flexural rigidity may significantly reduce the critical loads which were calculated. On the other hand, it can be argued that the calculated critical loads for $(\sigma_{cr})_c$ will be extremely conservative because the stress state is localized and the assumed effective, unsupported length and width are too long.

Deceleration System

The deceleration system must perform in such a way that, after the entry phase, the trajectory of the penetrator is within the conditions of $-90° \leq \gamma \leq -75°$ and 450 fps $\leq V \leq$ 550 fps for all of the impact altitude range, $0 < h < 13123$ feet (4 km). Furthermore, it must do this for all initial entry conditions, $-22.5° \leq \gamma_I \leq -12.5°$ with $V_o = 15518$ fps (4.73 km/sec) and $h_I = 328084$ feet (100 km). A further constraint is the limiting of parachute deployment to $M \leq 4$.

From the parametric trajectory study, it was seen that both the velocity and angle requirements cannot be met with a single-stage system (i.e., the same drag area from entry to impact). The parametric trajectory study does suggest the possibility of a two-stage system with an entry ballistic coefficient of $\beta_{Mars} \sim 1.3$ lb_f/ft^2 (16.8 kg/m^2) and staging to a terminal β_{Mars} of ~ 2.6 lb_f/ft^2 (33.6 kg/m^2) at approximately 9- to 10-km altitude. However, the weight and size of such a system would probably be prohibitive.

An early system which was investigated was a three-phase/two-stage system where the entry phase and terminal phase used the same deployable attached decelerator (DAD) and a parachute was used in addition to the DAD for turnover in the second phase. The problems encountered in this system were (1) the turnover parachute was getting too large because of the additional mass of the DAD and (2) the acceleration to the necessary impact velocity after turnover with the DAD attached was too slow.

The final system analysed was a four-phase/three-plus stage system. In this system, any of the previously discussed first-stage deceleration devices may be used. At deployment of the turnover parachute, the first-stage deceleration system is shed. After the turnover phase, the terminal parachutes (a cluster of three) are deployed in a reefed state for acceleration (Phase 3) to the terminal velocity; at this time, they are disreefed for full open terminal descent (Phase 4). The weight of the smaller turnover parachute plus the cluster of terminal parachutes is less than what would be required for the turnover parachute alone for the three-phase/two-stage system. Furthermore, the reefed terminal parachutes provide higher acceleration for the penetrator after turnover.

Nominal deployment conditions for the turnover parachute are Mach 4 and a dynamic pressure of 2.4 kN/m^2 (50 lb/ft^2). Development tests in this range were run during the preparatory stages of the Viking decelerator system design. Several of these tests were successfully run at high altitude in the Mach 3.4 to 3.9 range. These results along with other applicable data are reported in References A50 through A57.

Early in the study, the ground rules specified that the impact velocity and angle requirements be maintained for an impact altitude range of 0 to 6 km. For that condition, the deceleration system employing a first-stage ballistic coefficient of 2.6 has been analyzed. This system is described in Table A-VII.

TABLE A-VII

Summary of Mass and Drag Devices Assumed for Trajectory Analysis of a Four-Phase/Three-Stage
System Designed for a 6-km Impact Altitude Range

Phase / Stage	Drag Device	Diameter	C_D	Drag Area $(C_D S)$	Total Mass	Ballistic Coefficient	Function
$\frac{1}{1}$	DAD	6 ft (1.8 m)	0.6 (M>4)	17.09 ft^2 (1.59 m^2)	120 lb$_m$ (54.4 kg)	2.65 lb$_f$/ft^2 (Mars)	Entry: used to an altitude of 35,376 ft (10.78/km)*
$\frac{2}{2}$	Disk-gap-band Parachute	20 ft (6.1 m)	0.53 (M<1.4)	166.5 ft^2 (15.47 m^2)	94.6 lb$_m$ (42.9 kg)	0.214 lb$_f$/ft^2 (Mars) (2.78 kg/m^2)	Turnover: used for 22 sec
$\frac{3}{3}$	Cluster of three ribbon parachutes (reefed to 25 percent of full open drag area)	3.4 ft (1.0 m)	0.45 unreefed (including cluster effects)	3.07 ft^2 (0.285 m^2)	78.5 lb$_m$ (35.6 kg)	9.66 lb$_f$/ft^2 (Mars) (125 kg/m^2)	Acceleration: used for 26 sec
$\frac{4}{3+}$	Cluster of three ribbon parachutes, full open			12.27 ft^2 (1.14 m^2		2.41 lb$_f$/ft^2 (Mars) (31.2 kg/m^2)	Terminal: used until impact

*M = 4 for γ_I = -22.5° entry trajectory

A trajectory study, performed for this system, included variation of γ_I from -22.5 degrees to -12.5 degrees, deployment altitude variation of ±10 percent and staging-time variations of ±10 percent. Figure A-59 and A-60 show plots of γ and V, respectively, versus altitude for γ_I = -22.5 degrees and -12.5 degrees for nominal conditions. Figure A-61 shows the effect of Phase 2 initial altitude (deployment altitude) variation on terminal velocity for a γ_I = -22.5-degree trajectory.

In Figure A-59, the turnover in the trajectory is accomplished in both Phase 2 and Phase 3. The corresponding velocities (Figure A-60) at the altitudes of rapid turnover are at a minimum, because it is necessary for the velocity to be low for a rapid change in γ caused by gravity. Thus, the turnover parachute was selected to rapidly bring the penetrator to low velocity, nearly the terminal velocity for the turnover parachute. This also makes the initial velocity of Phase 3 nearly independent of the initial velocity of Phase 2 (Figure A-60). Therefore, for a constant altitude deployment of the turnover parachute for the entire range of γ_I , the altitude is set by the altitude where the steepest-initial-entry-angle trajectory passes through the maximum allowable velocity (or Mach number) for deployment of the turnover parachute.

The perturbations of time for Phase 2 and Phase 3 indicated that the trajectories are relatively insensitive to the time variation in Phase 3 (accelerate) and vary only slightly in γ (approximately ±1.5 degrees for the γ_I = -22.50 trajectory) for a ±10-percent variation in Phase 2 (turnover) time. The altitude perturbations showed that, for a low initial altitude for Phase 2 [h = 9.7 km (31,838 ft)], the velocity was slightly below 450 fps at the 6-km altitude but was within the velocity range well before the 4-km altitude. The velocity was within range for all cases with the high initial Phase 2 altitude [11.9 km (h = 38,914 ft)].

The altitude for M = 4 for a 54.4-kg (120-lb$_m$) expanding cylinder entering at γ_I = 22.5° is 8.5 km (27,931 ft). For the same Phase 2, 3, and 4 systems as for the DAD systems, a trajectory for γ_I = -22.5° resulted in γ and V versus altitude which are plotted in Figures A-62 and A-63, respectively. The trajectory does meet the required V and γ for the 0- to 4-km impact altitude range. Deployment of the turnover parachute for this trajectory represents the maximum deployment condition with dynamic pressure of 47 psf (2250 N/m^2) and a load factor of 29.5 g (earth g) on the penetrator.

Parachute Deployment Fuze

The fuze concept proposed to deploy the parachute is a g-threshold-ΔV fuze. This type fuze has proven effective for conventional reentry vehicles in the past. The fuze will be body fixed and will sense accelerations normal to the axis of the spinning cylindrical vehicle. Figure A-64. The acceleration sensed will vary sinusoidally because of the spinning vehicle (see Figure A-65). The envelope of the acceleration will be the drag acceleration on the vehicle after the initial tumbling motion has decayed.

A threshold of 20 Mars-g will be below the maximum accelerations experienced for all reentry angles (-22-1/2, -20, -15, and -12 degrees) examined, and the amplitude of the tumbling motion will have decayed below ±12 degrees from nominal.

The velocity change of the vehicle between a 20-Mars-g threshold and the desired fuzing height of 8.5 km (27,931 ft) (Mach 4) for the -22-1/2-degree trajectory is 3.64 km/s (11,928 fps) from the 6-DOF computer calculation. Using the 20-Mars-g threshold and the 3.64-km/s (11,928-fps) velocity
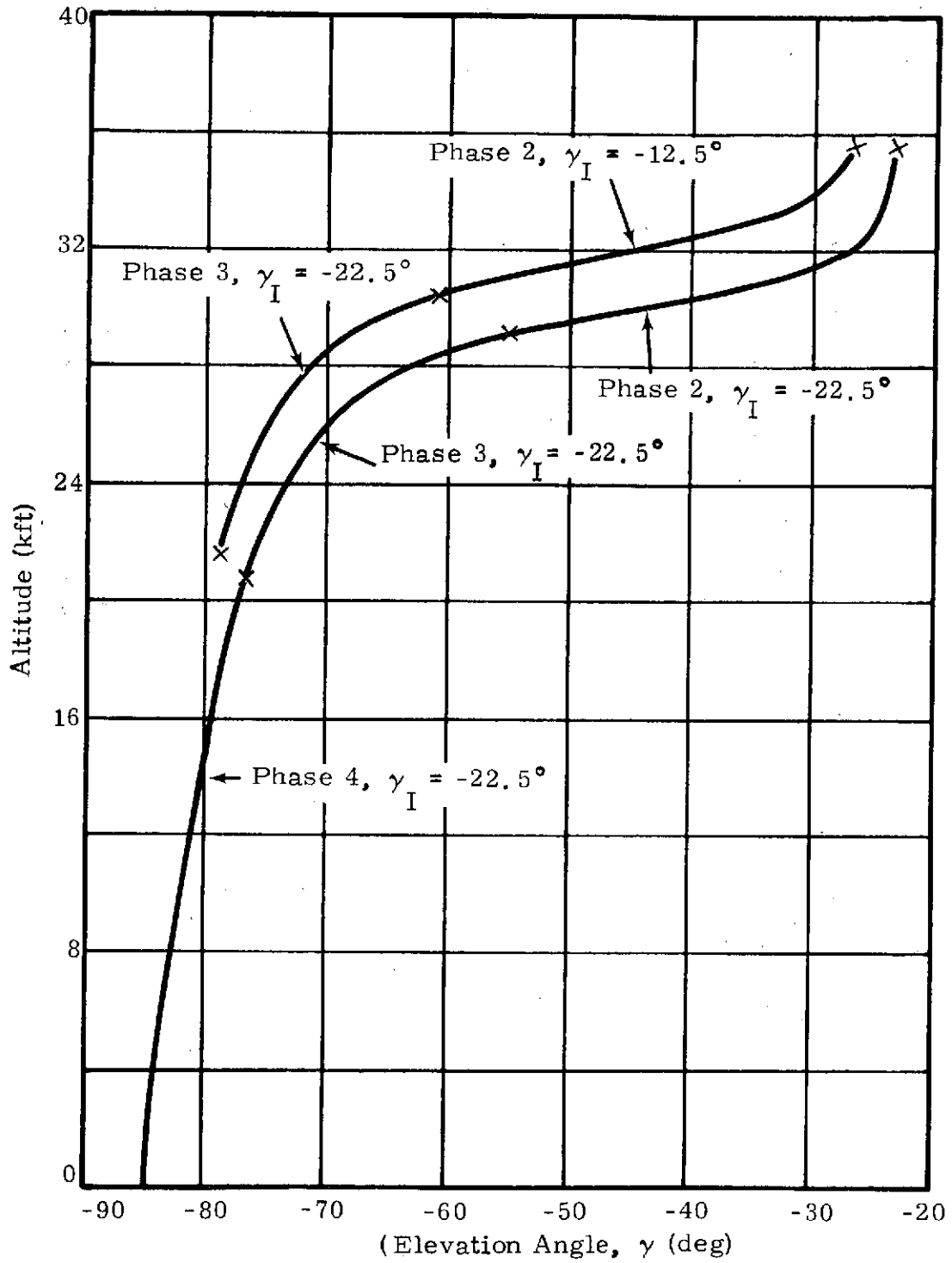
Figure A-59.   Elevation Angle versus Altitude for
$\gamma_I = -22.5^O$ and -12.5^O Trajectories
of DAD Concept

Figure A-60. Velocity versus Altitude for γ_I = -22.5 and -12.5°
Trajectories of DAD Concept
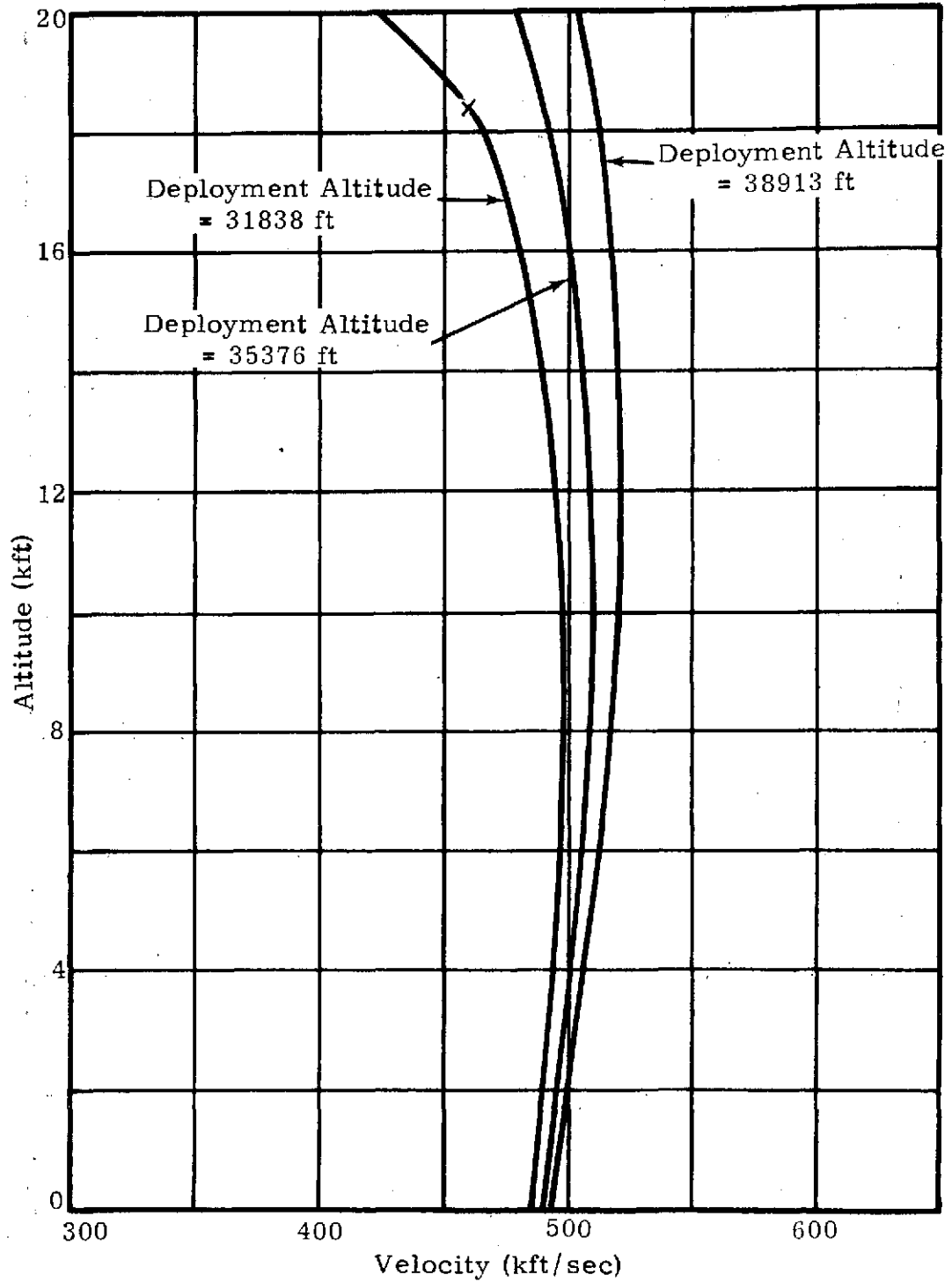
Figure A-61. Terminal Velocity versus Altitude for $\gamma_I = -22.5^\circ$ Trajectory for DAD Concept for Three Turnover Chute Deployment Altitudes
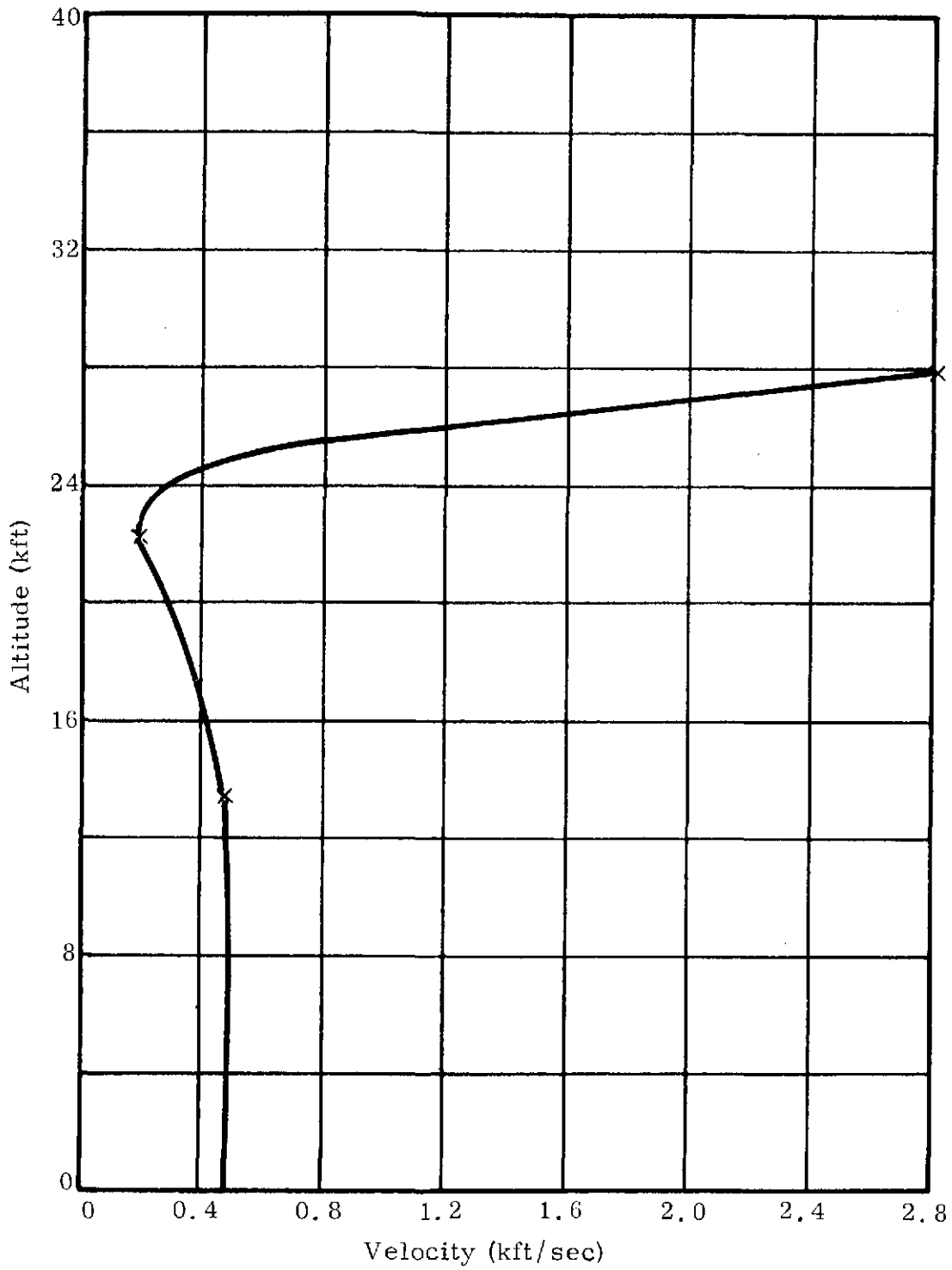
Figure A-62. Velocity versus Altitude for $\gamma_I = -22.5^O$
Trajectory of 120 lb_m Cylinder Concept
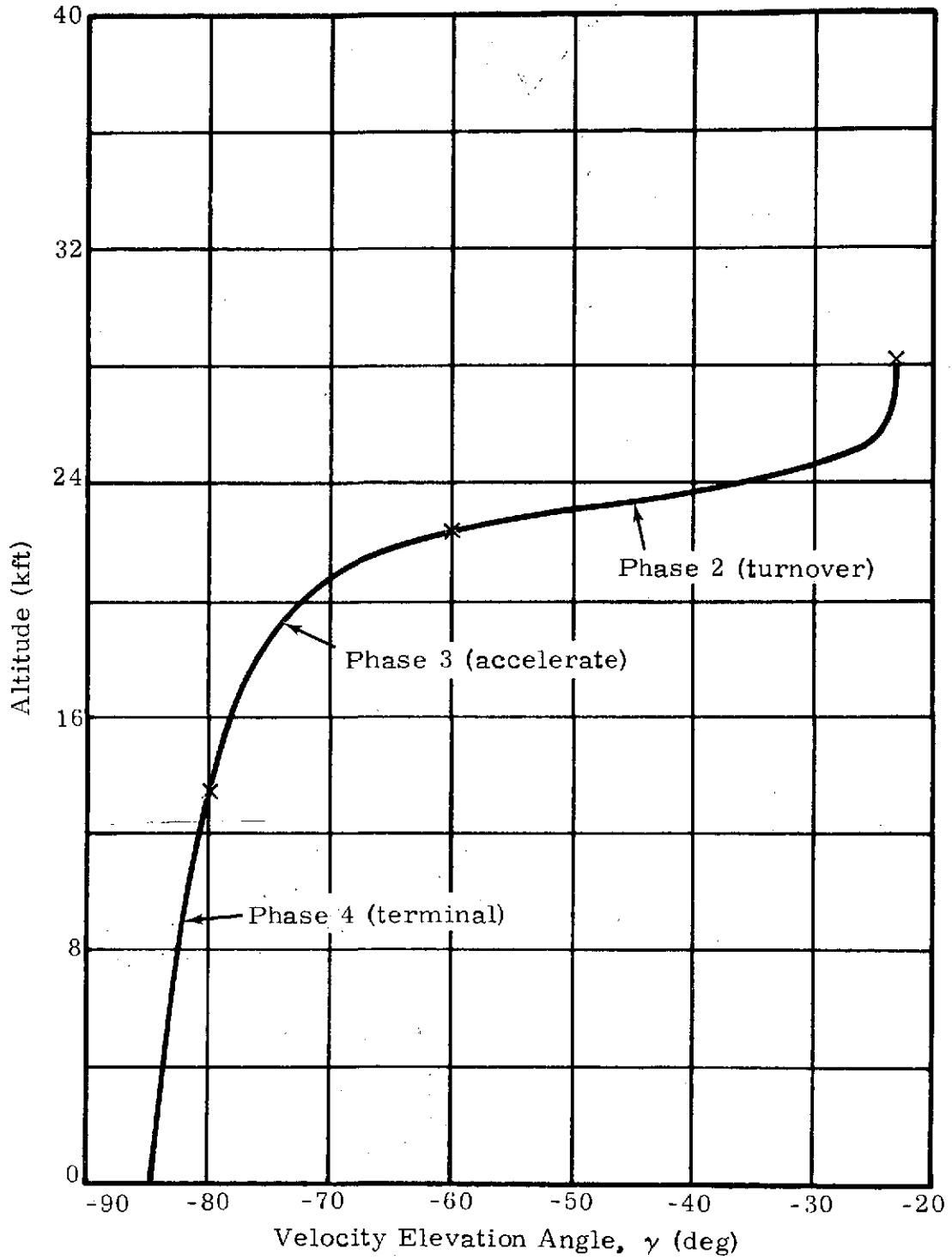
Figure A-63.   Elevation Angle versus Altitude for $\gamma_I = -22.5^O$
Trajectory of 120 lb$_m$ Cylinder Concept
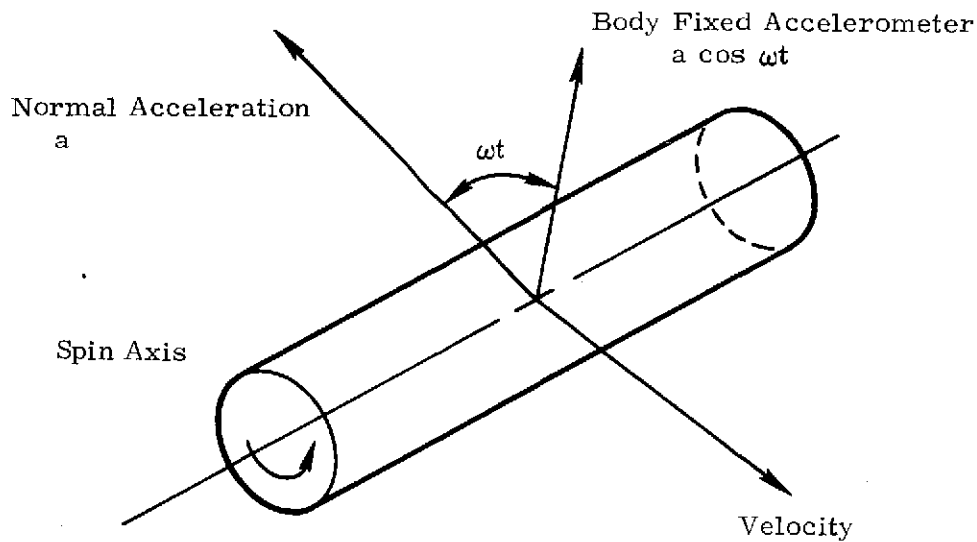
Figure A-64.   Configuration
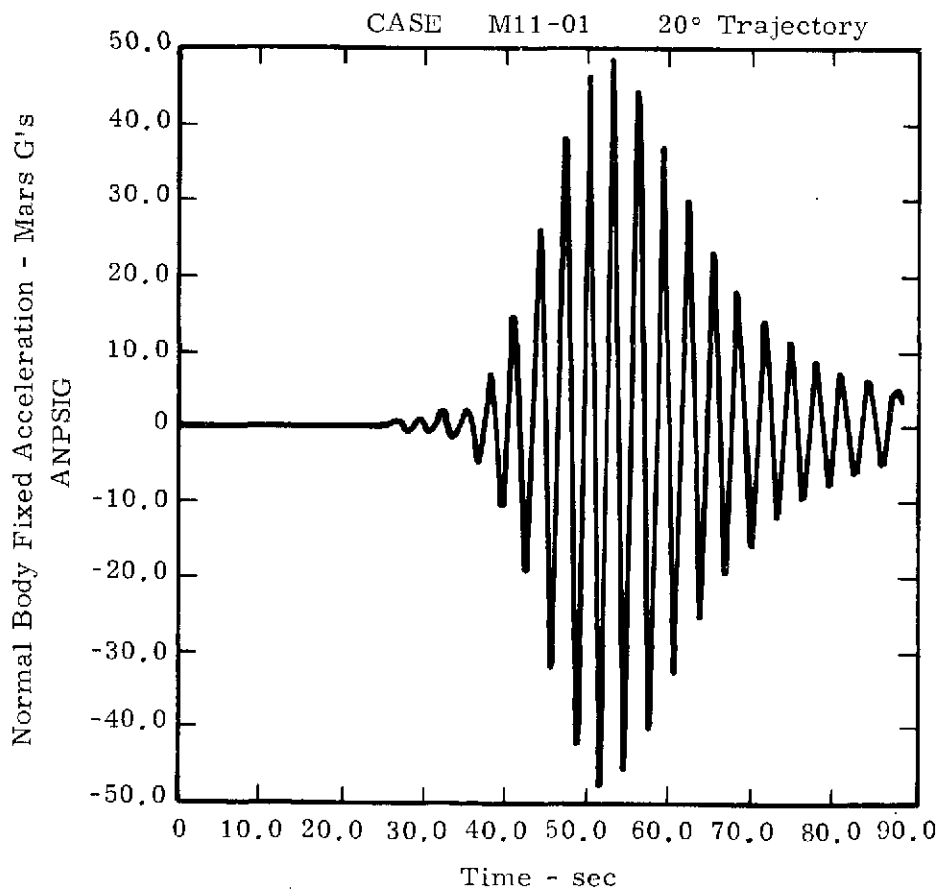
Figure A-65.   Spinning Cylinder - Normal Acceleration

change as the fuzing criteria gives nominal fuzing altitudes of 8.5 km (27,931 ft) at -22-1/2-degree reentry angle, 9.6 km (31,650 ft) at -20 degrees, 11.4 km (37,305 ft) at -15 degrees, and 9.7 km (31,868 ft) at -12 degrees without requiring presetting for the specific reentry angle. Table A-VIII shows the fuzing data for the four trajectories. The deployment altitudes for γ_I = -20, -15, and -12 degrees, which are essentially within the altitude range of the altitude perturbation study will give the correct V and γ for a 0- to 6-km impact altitude.

TABLE A-VIII

Fuzing Data
(g-Threshold = 20 Mars g, ΔV = 11,928 fps)

	-22-1/2°	-20°	-15°	-12°
$t_{20\,g}$, sec	38.0	41.4	57.2	76.6
$V_{20\,g}$, fps	14,771	14,678	14,185	13,258
$(V_{20\,g}, -11,928)$ fps	2,843	2,750	2,256	1,330
Fuze Mach	4	3.90	3.24	1.89
Fuze Time, sec	65.6	74.4	104.5	157.1
Fuze Altitude, ft	27,931	31,650	37,305	31,868

Figure A-66 is a block diagram of the proposed fuze.
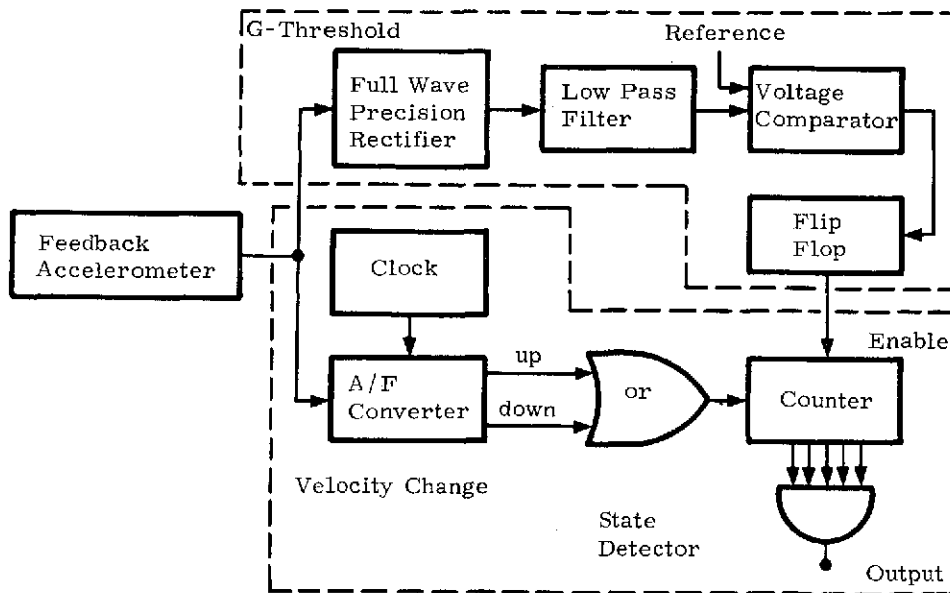
Figure A-66. Fuze Block Diagram

Most of the individual components including the feedback accelerometer (FBA) and analog-to-frequency (A/F) converter have been flight tested by Sandia. However, they are combined in a new configuration in this concept. Sensitivity studies of both the trajectories and the components will be used to predict fuzing accuracy for this application. Very preliminary indications are that to

keep altitude variations from nominal below ±10 percent will require fuze errors of ±2 percent. If a settable fuze for each trajectory is allowed, the nominal altitudes can be matched with the proposed fuze. Also other fuze concepts might be acceptable with settings for each trajectory.

It is concluded that the same parachute system can be used for either the DAD or cylinder first-stage concept. Further, the ballistic coefficient of the DAD first-stage can be increased to that of the cylinder first stage with the 4-km (13-kft) impact altitude range.

Parachute Thermal Analysis

One of the parachute system design concerns is heating of the turnover parachute when it is first deployed. A similar problem in which a thermally induced parachute failure was encountered is addressed in Reference A57. The analysis developed therein was modified and applied to the present 20-foot-diameter disk-gap-band turnover parachute over a range of deployment Mach numbers in the Martian atmosphere.

The aerodynamic heating rate computed for the stagnation-line region in the canopy was equated to the surface reradiation heat transfer rate. This equation was then solved to determine a surface equilibrium temperature. The analysis neglects the thermal capacity of the canopy material. Thus, the results yield an upper limit on the canopy temperature.

The results are shown in Figure A-67. Surface equilibrium temperature is plotted as a function of deployment Mach numbers from 6 to 3. Also shown by solid symbols along the right-hand scale of the figure is the temperature-strength characteristic of Kevlar 29, a new high-strength parachute material. At the equilibrium temperatures resulting from a Mach 4 deployment, about 50 percent of the material strength remains and, at Mach 5, about 25 percent of the strength remains. (The extra strength required to accommodate the thermal degradation up to at least Mach 4 is available from Kevlar for the same weight and volume as a nylon or dacron parachute). For Mach 5 deployments, some small increment of thermal protection such as a thin layer of silicone rubber may be required.

The analysis by which equilibrium surface temperatures were computed does not include transient effects. Figure A-68 shows that the Mach number decreases from 4 to 3 in about 0.75 second. The finite thermal capacity of the canopy and the rapid decay of the heat pulse will tend to result in actual temperatures lower than shown in Figure A-67.
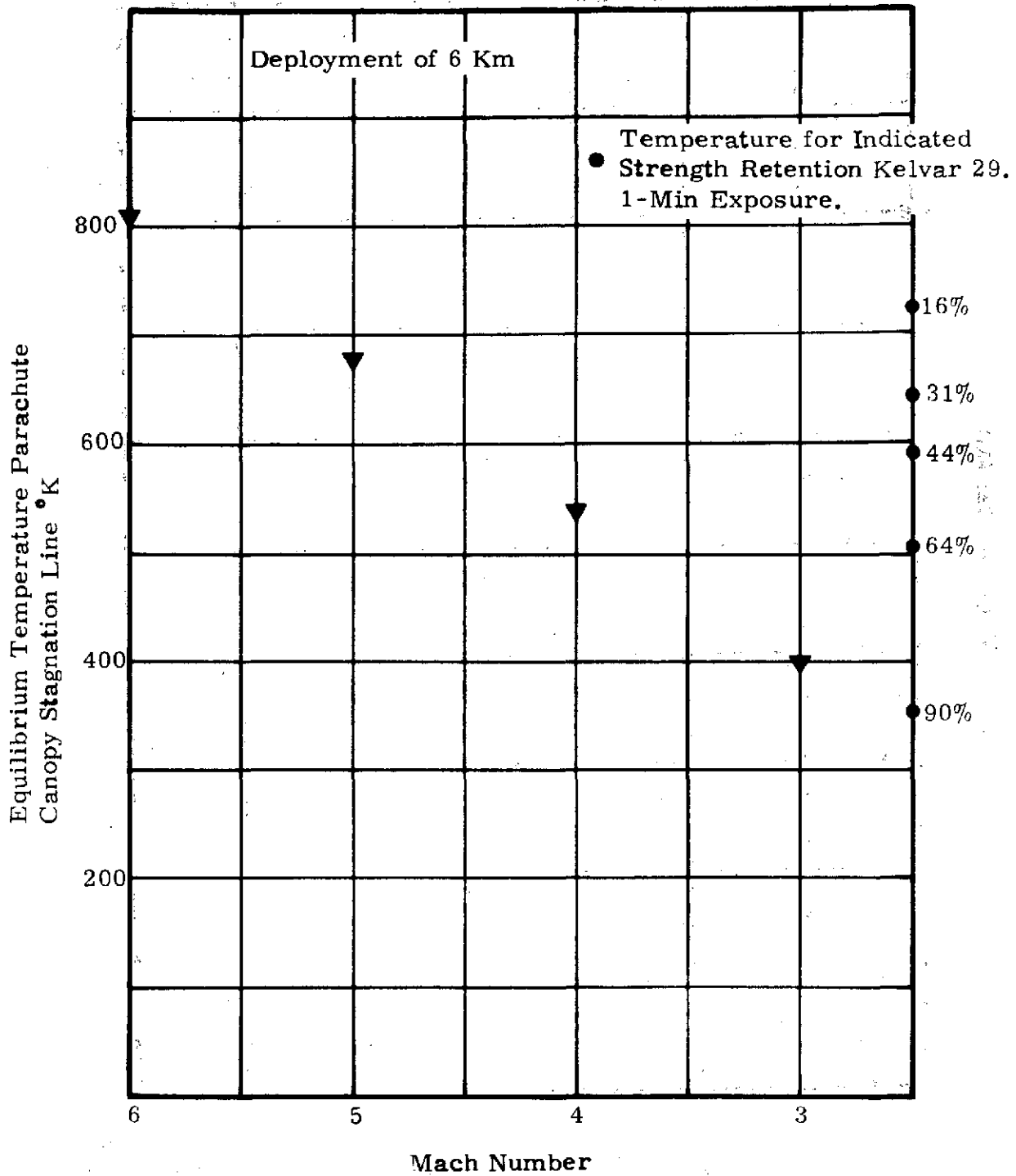
Figure A-67. Canopy Stagnation Line Equilibrium Temperature
as a Function of Mach Number
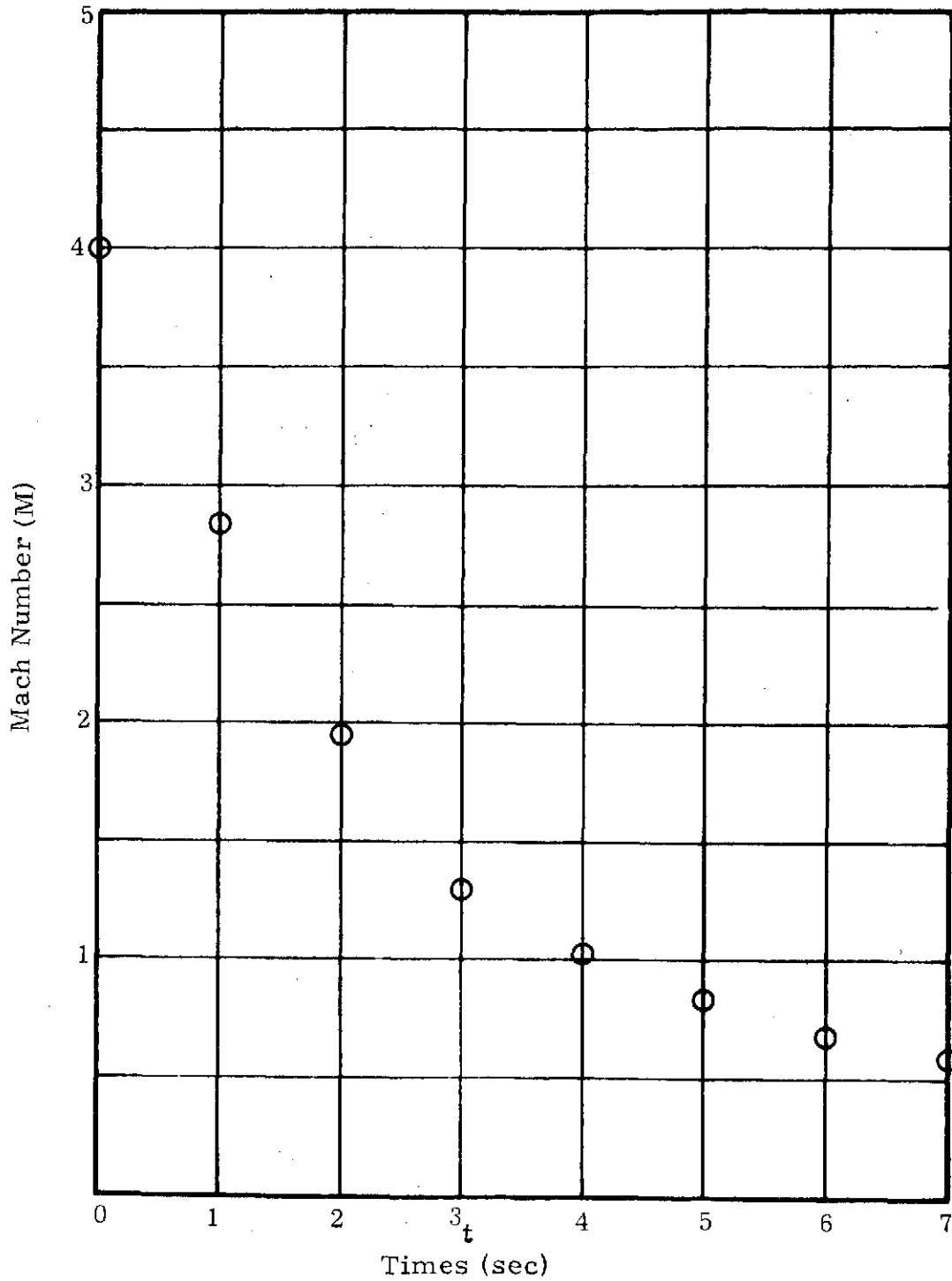
Figure A-68.   Mach Number as a Function of Time
From Deployment of Turnover Parachute

LIST OF REFERENCES

A1. D. H. Johnson, Investigation of the Motion of Two Configurations Reentering the Atmosphere, Sandia Laboratories, Albuquerque, N. M., SC-TM-66-393, September 1966.

A2. G. Grimminger, E. P. Williams, and G. B. W. Young, "Lift on Inclined Bodies of Revolution in Hypersonic Flow," Journal of Aeronautical Sciences, Vol. 17, November 1960, p. 675.

A3. Raymond and Garber, On the Stability of a Circular Cylinder at Hypersonic Speeds, RAND-P-723, January 9, 1956.

A4. Donald M. Kuehn, Experimental and Theoretical Pressures on Blunt Cylinders for Equilibrium and Nonequilibrium Air at Hypersonic Speeds, NASA-TN-D-1979.

A5. William J. Bursnall and Lawrence K. Loftin, Jr., Experimental Investigation of the Pressure Distribution About a Yawed Circular Cylinder in the Critical Reynolds Number Range, NACA-TN-2463, September 1951.

A6. J. A. Penland, Aerodynamic Characteristics of a Circular Cylinder at Mach Number 6.86 and Angles of Attack up to 90°, NACA-TN-3861, January 1957.

A7. Duane E. Randall, A Method for Estimating the Drag Coefficient of a Tumbling Circular Cylinder, Sandia Laboratories, Albuquerque, N. M., SC-TM-64-528, May 1954.

A8. O. K. Tewfik and A. H. Gredt, Heat Transfer Recovery Factor and Pressure Distributions Around a Cylinder Normal to a Supersonic Rarefied Air Stream. Part I, Experimental Data, HE-150-162, January 30, 1959.

A9. O. K. Tewfik, Heat Transfer, Recovery Factor and Pressure Distributions Around a Circular Cylinder Normal to a Supersonic Rarefied Air Stream. Part II, Comparison of Experiments With Theory, HE-150-189, May 15, 1959.

A10. Stephen Shien-Pu Tang, Cylinder Drag in the Hypersonic Free Jets of a Rarefied Air Stream, UC-AS-64-3, January 30, 1964.

A11. G. J. Masloch, Supplementary Cylinder Drag Data for Transition Flow Conditions, AS-63-3, July 1, 1963.

A12. A. K. Sreekanth, Drag Measurements on Circular Cylinders and Spheres in the Transition Regime at a Mach Number of 2, UTIA-74, April 1961.

A13. F. E. Gowen and E. W. Perkins, Drag of Circular Cylinders for a Wide Range of Reynolds Numbers and Mach Numbers, NACA-TN-2960, June 1953.

A14. Clement J. Welsh, The Drag of Finite-Length Cylinders Determined from Flight Tests at High Reynolds Numbers for a Mach Number Range from 0.5 to 1.3, NACA-TN-2941, June 1953.

A15. G. Goodwin, M. O. Creager, and E. L. Winkler, Investigation of Local Heat Transfer and Pressure Drag Characteristics of a Yawed Circular Cylinder at Supersonic Speeds, NACA-RM-A5SH31, January 24, 1956.

A16. J. E. Long, Supersonic Drag Coefficients of Circular Cylinders up to Mach Number 8, Aero-Ballistic Research Report 353, NAVORD-4382, October 26, 1956.

A17. W. F. Lindsey, Drag of Cylinders of Simple Shapes, NACA-619, 1938.

LIST OF REFERENCES (Cont)

A18. C. C. Horotman, The Flow Over a Cylinder with Various Nose Shapes at Zero Angle of Attack at Hypersonic Speeds, PR-7629-63-14, January 1963.

A19. P. B. Burbank and R. L. Stallings, Jr., Heat-Transfer and Pressure Measurements on a Flat-Face Cylinder at a Mach Number Range of 2.49 to 4.44, NASA-TM-X-19, August 1959.

A20. H. Strassl, Three Component Measurements of Short Cylinders at Supersonic Speeds, ZWB/UM-3003, November 9, 1948.

A21. W. T. Davey and C. E. Brigsby, Stability Characteristics of Cones and Cylinders at Large Angles of Attack at Mach Number 2.87, AERON-U-540.

A22. J. L. Potter, N. M. Shapiro, and W. D. Murphree, Normal Force Distributions of Right Circular Cylinders in Subsonic and Supersonic Flows, RA-2R4F, December 2, 1954.

A23. O. Walchner, Systematic Wind-Tunnel Measurements on Missiles, NACA-TM-1122, March 1947.

A24. C. C. Horstman, Pressure and Heat-Transfer Measurements Over a Circular Cylinder at Angles of Attack Up to 15° at M = 11, PR-7629-63-8, May 1963.

A25. G. M. Gregorek and K. D. Korhan, "An Experimental Observation of the Mach Number and Reynolds Number Independence of Cylinders in Hypersonic Flow," AIAA Journal, Vol. 1, No. 1, p. 210.

A26. J. L. Potter, W. D. Murphree, and N. M. Shapiro, "Normal Force and Center of Pressure on Right Circular Cylinders," Journal of the Aeronautical Sciences, March 1955, p. 214.

A27. I. M. Hall, "Experiments on Supersonic Flow Over Flat-Nosed Circular Cylinders at Yaw," Philosophical Magazine, Vol. 45, Seven Series 362, March 1954.

A28. J. A. Darling, Handbook of Blunt-Body Aerodynamics, Vol. 1, Naval Ordnance Laboratory, December 1973.

A29. C. A. Powars and R. M. Kendall, User's Manual, Aerotherm Chemical Equilibrium (ACE) Computer Program, Aerotherm Corporation, Palo Alto, California, May 1969.

A30. R. M. Kendall and E. P. Bartlett, "Nonsimilar Solution of the Multicomponent Laminar Boundary Layer by an Integral-Matrix Method," AIAA Journal, Vol. 6, June 1968, pp. 1089-1097.

A31. B. F. Blackwell and P. C. Kaestner, Operation Instructions for Charring Material Ablation Code, Sandia Laboratories, Albuquerque, N. M., SC-DR-70 140 (U), March 1970.

A32. E. L. Clark, "TRANCE – A Point Mass Trajectory Analysis Program," Personal Communication, Sandia Laboratories, Albuquerque, N. M., July 1974.

A33. II. Schlichting, Boundary-Layer Theory, McGraw-Hill Book Company, New York, 1968.

A34. S. F. Hoerner, Fluid-Dynamic Drag, published by the author, Midland Park, New Jersey, 1958.

A35. Dow-Corning Bulletin 61-051b, October 1973.

A36. M. S. Holden, Shock Wave-Turbulent Boundary Layer Interaction in Hypersonic Flow, Cornell Aeronautical Laboratory, AIAA Paper No. 72-74, AIAA 10th Aerospace Sciences Meeting, January 1972.

LIST OF REFERENCES (Cont)

A37.   D. E. Nestler, An Engineering Analysis of Reattaching Shear Layer Heat Transfer, General Electric Company, AIAA Paper No. 72-717, AIAA 5th Fluids and Plasma Dynamics Conference, June 1972.

A38.   G. M. Elfstrom, "Turbulent Hypersonic Flow at a Wedge-Compression Corner," Department of Aerenautics, Imperial College, London; J. Fluid Mechanics, Vol. 53, Part 1, 1972, pp. 113-127.

A39.   I. E. Beckwith and J. J. Gallagher, Local Heat Transfer and Recovery Temperatures on a Yawed Cylinder at a Mach Number of 4.15 and High Reynolds Numbers, NASA TR-R-104, 1961.

A40.   E. C. Lemmon and H. W. Coleman, Turbulent Heat Transfer to a Fin Leading Edge-- Flight Test Results, Sandia Laboratories, Livermore, California, SCL-DC-72-0329, October 1972.

A41.   C. F. Markarian, Heat Transfer in Shock Wave-Boundary Layer Interaction Regions, Naval Weapons Center, China Lake, California, NWC-TP-4485, November 1968.

A42.   F. R. DeJarnette, Calculations of Heat Transfer on Shuttle Type-Configurations Including the Effects of Variables Entropy at Boundary Layer Edge, North Carolina State University, Raleigh, North Carolina, NASA CR-1121810, October 1972.

A43.   K. O. W. Ball and R. H. Korkegi, "An Investigation of the Effect of Suction on Hypersonic Laminar Boundary-Layer Separation," AIAA Journal, Vol. 6, No. 2, February 1968.

A44.   F. S. Billig, "Shock-Wave Shapes Around Spherical- and Cylindrical-Nosed Bodies," J. Spacecraft and Rockets, Vol. 4, No. 6, June 1967.

A45.   B. E. Edney, Anomalous Heat Transfer and Pressure Distributions on Blunt Bodies at Hypersonic Speeds in the Presence of an Impinging Shock, FFA, Stockholm, Sweden, Report 115, February 1968.

A46.   B. E. Edney, T. T. Bramlette, J. Ives, F. D. Hains, and J. W. Keys, Theoretical and Experimental Studies of Shock Interference Heating, Bell Aerospace, Buffalo, New York, Report No. 9500-920-195, October 1970.

A47.   J. W. Keyes and F. D. Hains, Analytical and Experimental Studies of Shock Interference Heating in Hypersonic Flows, NASA TN D-7139, May 1973.

A48.   E. F. Bruhn, Analysis and Design of Flight Vehicle Structures, Tri-State Offset Co., Cincinnati, Ohio, 1965, pp. C.61, C6.3-C6.6, and C9.1.

A49.   Roark, Formulas for Stress and Strain, McGraw-Hill Book Company, 1965, pp. 349-351.

A50.   C. H. Whitlock and R. J. Bendura, Inflation and Performance of Three Parachute Configurations for Supersonic Flight Test in a Low-Density Environment, NASA TN D-5296, July 1969.

A51.   C. W. Eckstrom, Flight Test of a 40-foot Nominal Diameter Disk-Gap Band Parachute Deployed at a Mach Number of 3.31 and a Dynamic Pressure of 10.6 Pounds per Square Foot, NASA TM-X-1924, February 1970.

A52.   P. J. Bobbitt and R. J. Mayhue, Supersonic and Subsonic Wind-Tunnel Tests of Reefed and Unreefed Disk-Gap-Band Parachutes, AIAA, Dayton, Ohio, Paper 70-1172, 1970.

LIST OF REFERENCES (Cont)

A53.   C. V. Eckstrom, High-Altitude Flight Test of a 40-Foot Diameter Ringsail Parachute at a
        Deployment Mach Number of 2.95, NASA, TN D-5796, June 1970.

A54.   C. V. Eckstrom and D. R. Branscome, High Altitude Test of a Disk-Gap-Band Parachute
        Deployed Behind a Bluff Body at a Mach Number of 2.69, NASA TM X-2671, December 1972.

APPENDIX B

TERRADYNAMICS

Introduction

The Mars penetrator is based on earth penetration technology developed at Sandia Laboratories during 14 years of analytical and experimental effort. This technology has led to the deployment of more than 30 earth penetration and earth implant systems, in both military and peaceful applications.

In the Sandia program, more than 10,000 projectiles from 2.5 to 76 cm in diameter and weighing from 4.5 to 2700 kg have been used. Tests with impact velocities from 60 to 840 meters per second have been conducted, and penetrations of up to 67 meters have been achieved.

The Sandia studies have been carried out in both soil and rock materials. Projectiles have successfully penetrated natural deposits of loose to dense moist sands, dense cemented sands, and gravels, soft estuarine muds, stiff moist to saturated clays, hard dry silty clays, loessial permafrost, glacial ice, dense gypsite, and salt water; projectiles have also penetrated significantly into intact bedrock such as dense sandstone, granite, welded tuff, and dacite.

The Earth-Penetration Event

The essential elements of a simple earth-penetrator are shown in Figure B-1. The device, whose afterbody is hollow to accommodate the instrument package and to provide a forward center of gravity, is structured of solid metal. The aerodynamic fins on the tail provide stability while the projectile is falling through the air. These fins are made of a frangible material so that they shatter when they hit the ground. The base of the aerodynamic fin is usually metal which protrudes perhaps 1.25 cm above the body; though small, the terradynamic fin seems to aid in maintaining the stable underground trajectory. In addition, the ratio of vehicle length to diameter must be large, of the order of 8 to 10, for a stable underground trajectory.

The instrumentation normally includes a high-frequency accelerometer which is doubly integrated to give the "rest" depth of penetration. In many applications, the accelerometer output is telemetered by a trailing antenna during the earth penetration, although onboard memories capable of operating through the landing shock environment have been developed. These memories can store the deceleration record for later recovery.
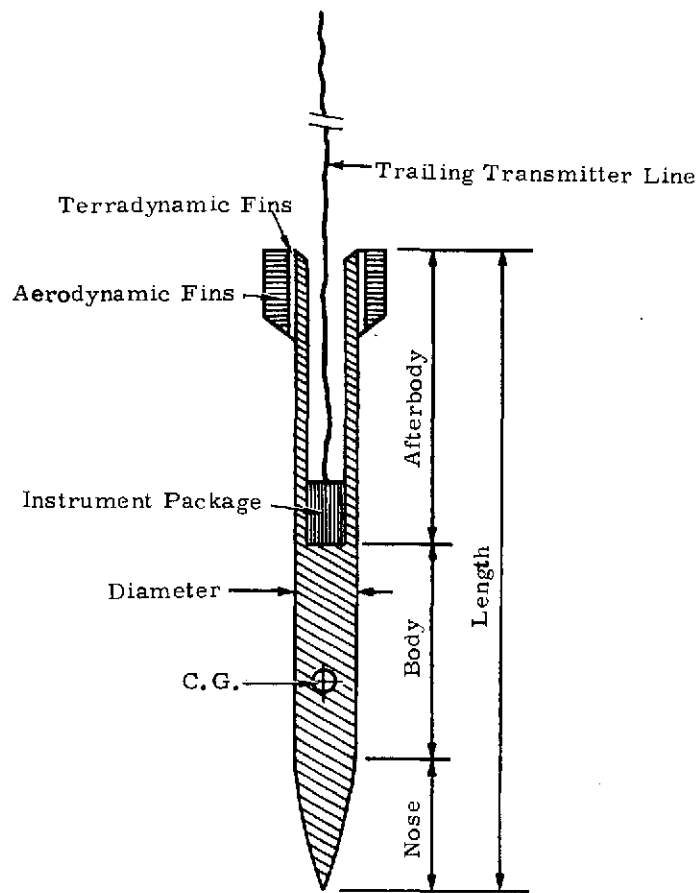
Figure B-1.   Details of Earth-Penetrating Projectile

When the free-falling projectile initially impacts the ground, the nose slices the soil, Figure B-2(a), so that a small crater with a minor amount of ejecta is formed. At this time, the projectile has its maximum velocity, and the deceleration shown by point (W) on Figure B-2(d) is usually a rather high value. As the projectile continues to penetrate, the aerodynamic fins shear off, and this event can sometimes be seen as a small deceleration impulse.

When the projectile is well into the earth but still traveling at a substantial velocity, the penetration takes place mostly by the slicing action of the nose, interval (X) on Figure B-2(e). The slicing action shears and compresses a thin zone of soil around the projectile and pushes the soil particles away from the passing nose with considerable lateral velocity. During the intermediate part of the penetration event, this imparted lateral velocity moves the soil particles away from the projectile body; at all but the lowest of velocities, the body has moved past before the soil particles have commenced to rebound. As a result, only mild skin friction acts on the projectile body during the major part of the penetration event: usually, the paint on the penetrator afterbody is only slightly scratched during the entire penetration sequence. The soil particles do, however, rebound somewhat after the projectile has passed and the resulting trajectory hole is typically smaller than the projectile which made it. During the terminal portion of the penetration event, the penetration velocity is low enough that the rebounding soil grips the penetrator as it comes to rest. In some cases, this gripping action causes the highest decelerations, (Y) on Figure B-2(e).

Minor Ejecta

Small Crater

(a) Initial Impact

Aerodynamic Fins
at Surface

Usually Soil Not
in Contact with
Projectile

(b) During Penetration

Hole open, or
partially filled
with dust; closed
only in softest
soils.

Usually soil
tightly gripping
projectile

(c) At Rest

(W) Nose in Ground

Fins Shear

(X)

(Y) Terminal
Deceleration

(2) Terminal
Oscillation
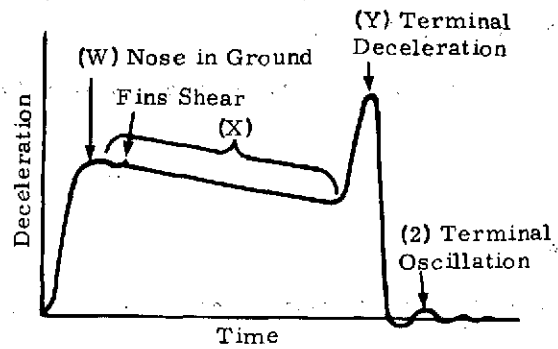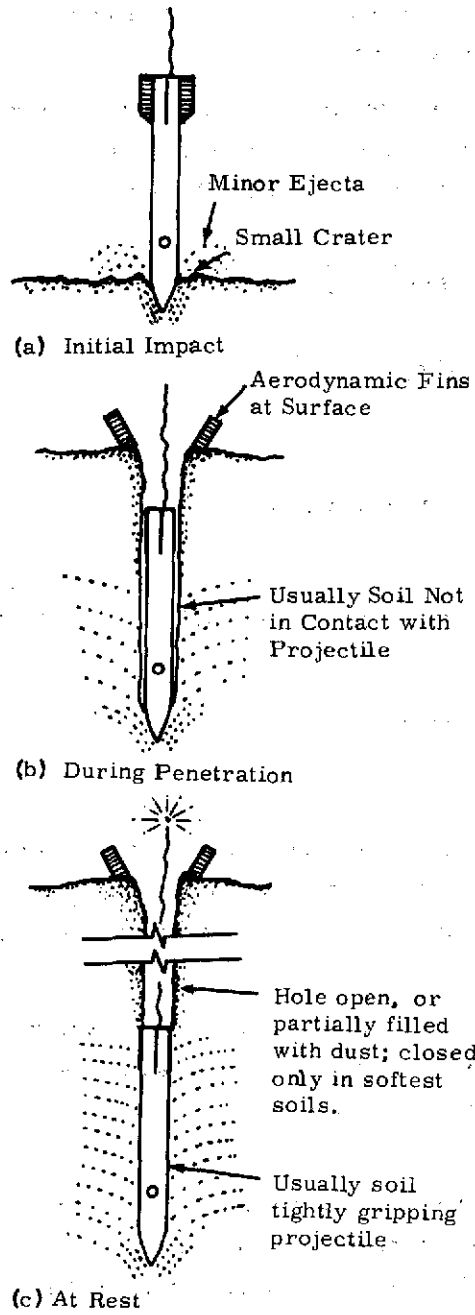
Time

(d) Raw Data
Plotted Against Time

(W)

(X)

(Y)
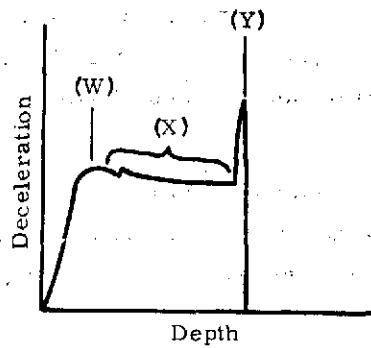
Depth

(e) Data in Useful Form
Plotted Against Depth

Figure B-2.   The Earth-Penetration Event
(sketches, no scale)

Earth penetration analysis is complicated by the fact that typical target materials are nonhomogeneous and nonlinear in their response to penetration. Penetration is so difficult to describe that no satisfactory analytical solutions to the problem yet exist, although extensive test experience has led to the formulation of empirical equations which allow prediction of both deceleration and depth of penetration for typical terradynamic vehicles with reasonable accuracy.

Development of the Sandia depth-of-penetration equations begins with an assumed form of the depth-prediction equation and an assumption as to which parameters affect penetration. The equations are strictly empirical, but sufficient high-quality penetration data were available to permit the good fitting of the equation to data.

The total depth of penetration was assumed to be of the form

$$D = f_1(N)f_2(A)f_3(W)f_4(V)f_5(S) \, , \qquad \text{(B-1)}$$

where

D = depth of penetration, measured along the penetration path, meters

V = velocity, meters per second

S = constant, dependent only upon soil properties averaged over the depth of penetration

W = total vehicle weight, kilograms

A = cross-sectional or frontal area, square centimeters

N = constant, vehicle nose-performance coefficient.

In Equation (B-1) all test and vehicle parameters were assumed to be included in the first four functions and all the soil properties in the fifth function. (Because some soil properties are rate-dependent, this is perhaps an oversimplification of the problem.) Two additional vehicle parameters should be mentioned:

1. The probe diameter is important but is, in effect, included in the area. However, in that this equation is not intended to encompass any scaling laws, it should be noted that, to be termed a full-scale test, the vehicle diameter should be at least 7.6 cm.

2. The second vehicle parameter to consider is the total length. As yet, no experimental test program has been conducted to determine the effect of fineness ratio (length of vehicle divided by diameter) on depth of penetration, but it appears that a minimum fineness ratio of 10 is necessary to assure stability during penetration. Also, a fineness ratio of greater than 20 should be avoided because of the increased side-wall friction during penetration.

Details of the development of the equations are given in Reference B1. The final equations are

$$D = 0.0117 \ SN\sqrt{W/A} \ (V-30.5) \quad V \geq 61 \ m/s \tag{B-2}$$

and

$$D = 2 \ SN\sqrt{W/A} \ \ln (1 + 2V^2 10^{-5}), \quad V < 61 \ m/s \tag{B-3}$$

The "break" in the velocity term at 61 m/s should not be construed as a change in the mechanism of penetration. The equations are simply fits to the penetration data; therefore, two simple equations, rather than a single more complex equation, were used. Depth of penetration can be predicted with Equations (B-2) or (B-3) with an accuracy of ± 20 percent; most of the inaccuracy derives from the necessity to estimate the soil constant. Table B-I gives typical soil constants for some natural earth materials. The soil constant (S-number) can be predicted and the above accuracy can be achieved on the basis of existing data.

TABLE B-I

Typical Soil Constants for Natural Earth Materials

Soil Constants	Materials
0.2 - 1	Massive medium- to high-strength rock, with few fractures. Concrete, 2000 to 5000 psi, reinforced.
1 - 2	Frozen silt or clay, saturated, very hard. Rock, weathered, low strength, fractured. Sea or fresh-water ice more than 10 feet thick. Basaltic lava flows.
2 - 3	Massive gypsite deposits (WSMR). Well-cemented coarse sand and gravel. Caliche, dry. Frozen moist silt or clay.
4 - 6	Sea or fresh-water ice from 1 to 3 feet thick. Medium dense, medium to coarse sand, no cementation, wet or dry. Hard, dry dense silt or clay (TTR dry lake playas). Desert alluvium.
8 - 12	Very loose fine sand, excluding topsoil. Moist stiff clay or silt, medium dense, less than about 50 percent sand.
10 - 15	Moist topsoil, loose, with some clay or silt. Moist medium stiff clay, medium dense, with some sand.
20 - 30	Loose moist topsoil with humus material, mostly sand and silt. Moist to wet clay, soft, low shear strength.
40 - 50	Very loose dry sandy topsoil (Eglin AFB). Saturated very soft clay and silts, with very low shear strengths and high plasticity (Great Salt Lake Desert and bay mud at Skaggs Island). Wet lateritic clays.
> 50	Massive sediments.

The nose performance coefficient (N) is another experimentally determined constant. In general, the more pointed nose shapes have higher values of N as can be seen in Table B-II and Figure B-3. (The nose caliber is the nose length divided by its base diameter.)

TABLE B-II

Nose Performance Coefficient

Nose Shape	Nose Caliber	N
Flat	0	0.56
Hemisphere	0.5	0.65[1]
Cone	1	0.82[1]
Tangent ogive	1.4	0.82
Tangent ogive	2	0.92
Tangent ogive	2.4	1.0
Cone	2	1.08
Tangent ogive	3	1.11
Tangent ogive	3.5	1.19
Cone	3	1.33

[1]Estimated
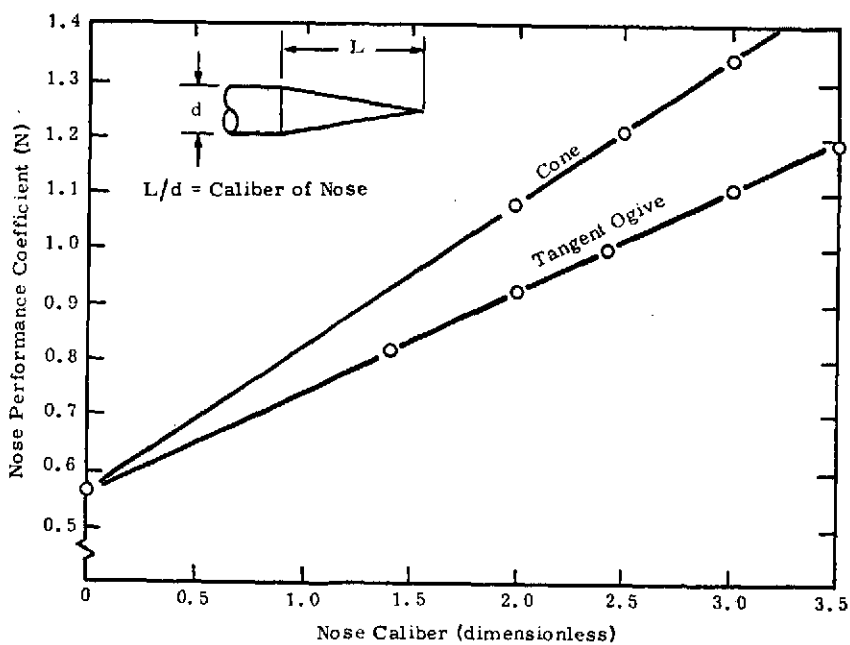
Figure B-3. Effect of Nose Length on Nose Performance Coefficient

For many terradynamic applications, the penetration environment must be controlled so that the penetrator reaches some desired depth in hard soil but does not overpenetrate in soft soil. At the same time, the deceleration level must be controlled within certain limits. The most common method of controlling penetration depth and deceleration is to add terrabrakes to the penetrator. These terrabrakes, which are normally designed to bend and thus absorb energy on contact with hard soil, still remain effective in soft soil. Other terradynamic applications call for a penetrator that is fully buried in hard soil for concealment; further, even if the soil is soft, an antenna must be left at or near the soil surface. Often electronic components are sensitive to the deceleration loads, and it is not practical to attempt to stop the complete vehicle near the soil surface. The detachable afterbody (DAFT) concept in vehicle design may be used to meet all of the system requirements. Figure B-4 shows a schematic of a typical DAFT penetrator. The DAFT vehicle is the one which has been adopted for the Mars penetrator.

Flat Plate (terrabrake)

Detach

Afterbody
Separation

Rest Position

Soil Contact

Umbilical
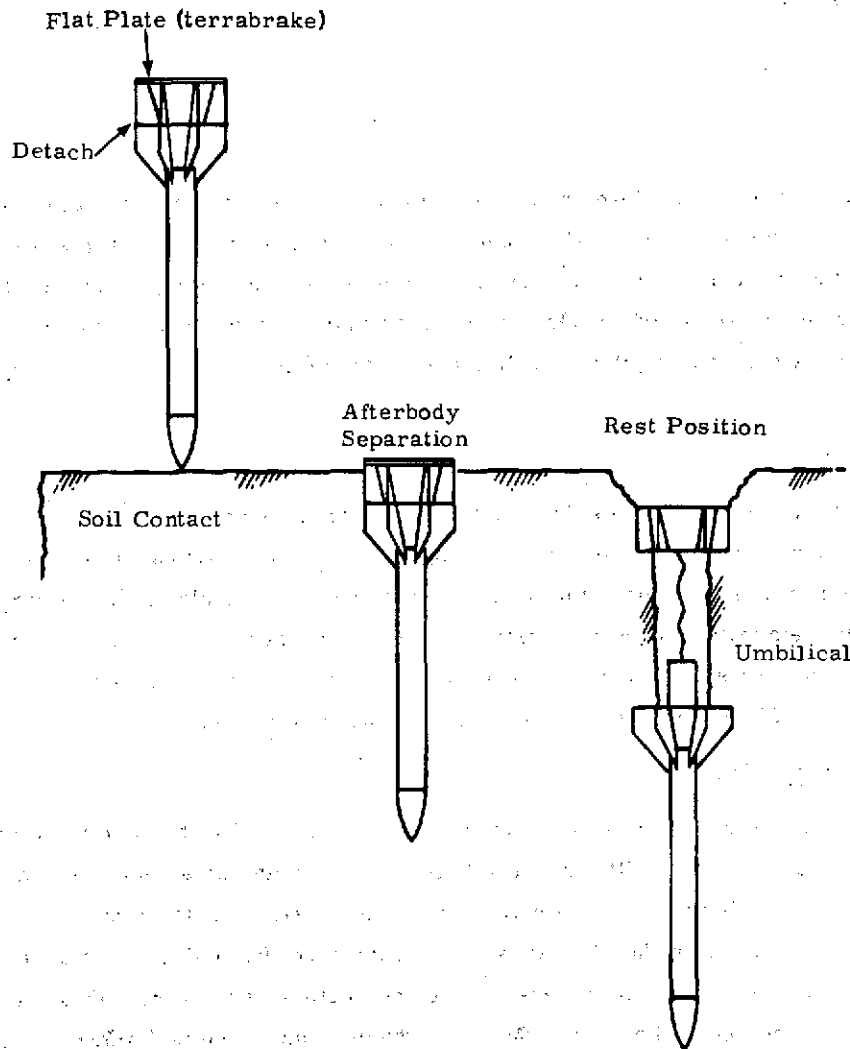
Figure B-4. Detachable Afterbody Concept of Penetrator Design

To predict the performance of a DAFT vehicle, the total vehicle and then, after separation occurs, the forward and aft sections must be considered independently. Reference B2 discusses the use of the equations in predicting penetration performance of complex penetrator shapes and includes sample calculations for both terrabrake and DAFT penetrators.

The penetration equations published by Young in 1967 which remain unchanged for the penetration of homogeneous soils, are the basic equations used in the empirical technique for predicting the penetration performance of complex penetrator configurations and of simple penetrators in layered soils.

When Equations (B-2) and (B-3) are used to predict the depth of penetration of a simple penetrator in a homogeneous target material, the predictions are accurate within approximately +20 percent. For the penetration of a layered soil by a simple penetrator, the depth and the average deceleration may be predicted within approximately +25 percent. For a complex penetrator configuration in a homogeneous soil, the depth of penetration and average deceleration profile may be predicted within +40 percent.

Applications

Earth penetrators were developed as a weapon delivery technique in connection with various DOD and AEC programs; however, the technology has since been used in support of missions in geophysics, marine studies, acoustic and seismic sensing, vulcanology, etc. In that these applications have involved a variety of sensors and because many of the penetrators have been similar to the proposed Mars penetrator (size, etc.), a brief description of some of these applications is included below.

Sensor Vehicles

In support of the "McNamara line," a family of earth penetrators which implanted acoustic or seismic sensors near the surface was developed. In that an antenna had to remain operable on the surface even though the penetrator impacted in surface materials of widely varying penetrability, terrabrakes and detachable afterbodies were essential. In fact, most of the investigation of those concepts was made in connection with this program. Figure B-5, shows a family of these penetrators. Over 10,000 of these vehicles were successfully deployed.

Sea Ice Penetrators (SIP)

A penetrator (Reference B3) was developed for the U. S. Coast Guard to remotely measure the thickness of sea ice. The SIP, shown in Figure B-6, contained an accelerometer which measured the deceleration during ice penetration and transmitted the data from the detachable afterbody to a receiving station in the aircraft which had dropped the device. The deceleration record was integrated twice to give velocity versus time and depth versus time. By noting the depth at the time the deceleration approached zero, the ice thickness could be determined within +7.6 cm. The SIP was designed to penetrate up to 3 m of sea ice.
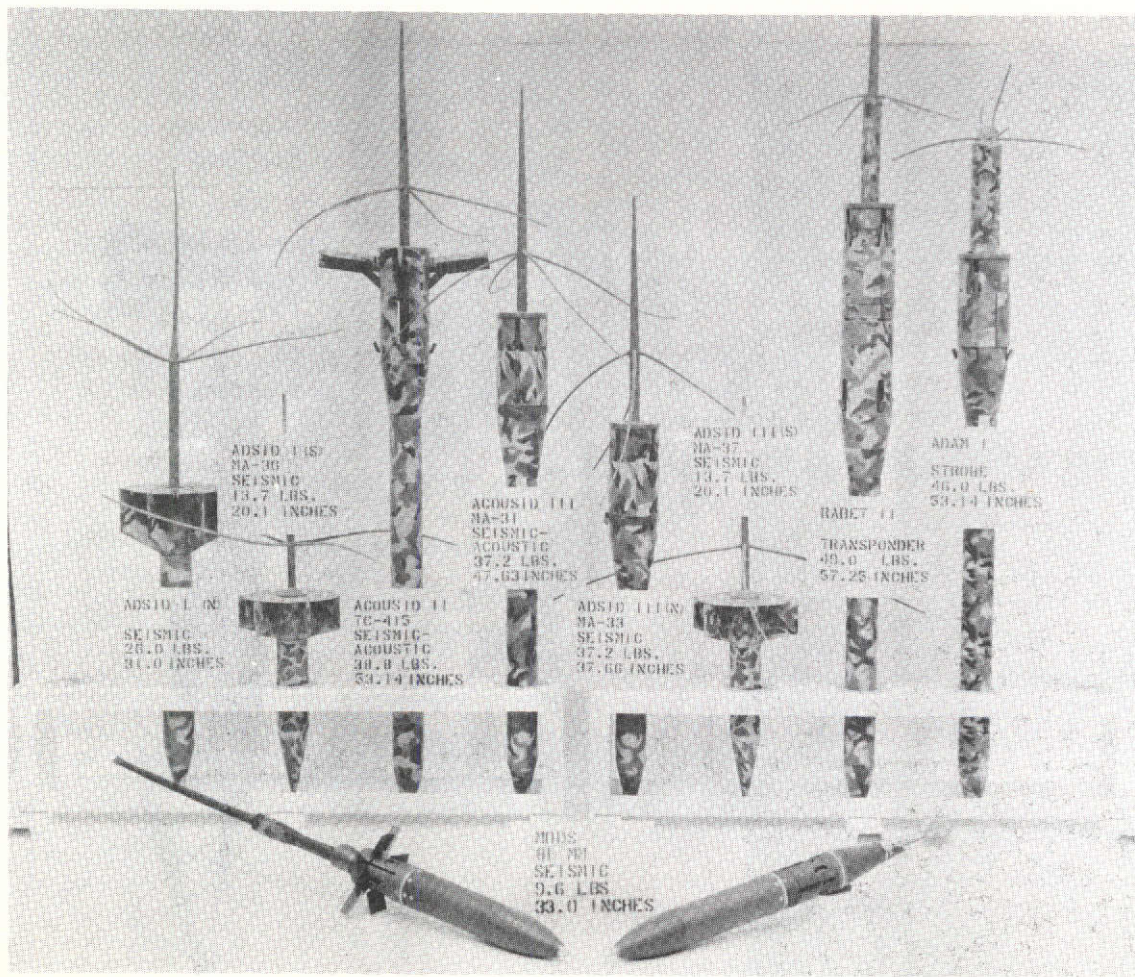
Figure B-5. Sensor Vehicle
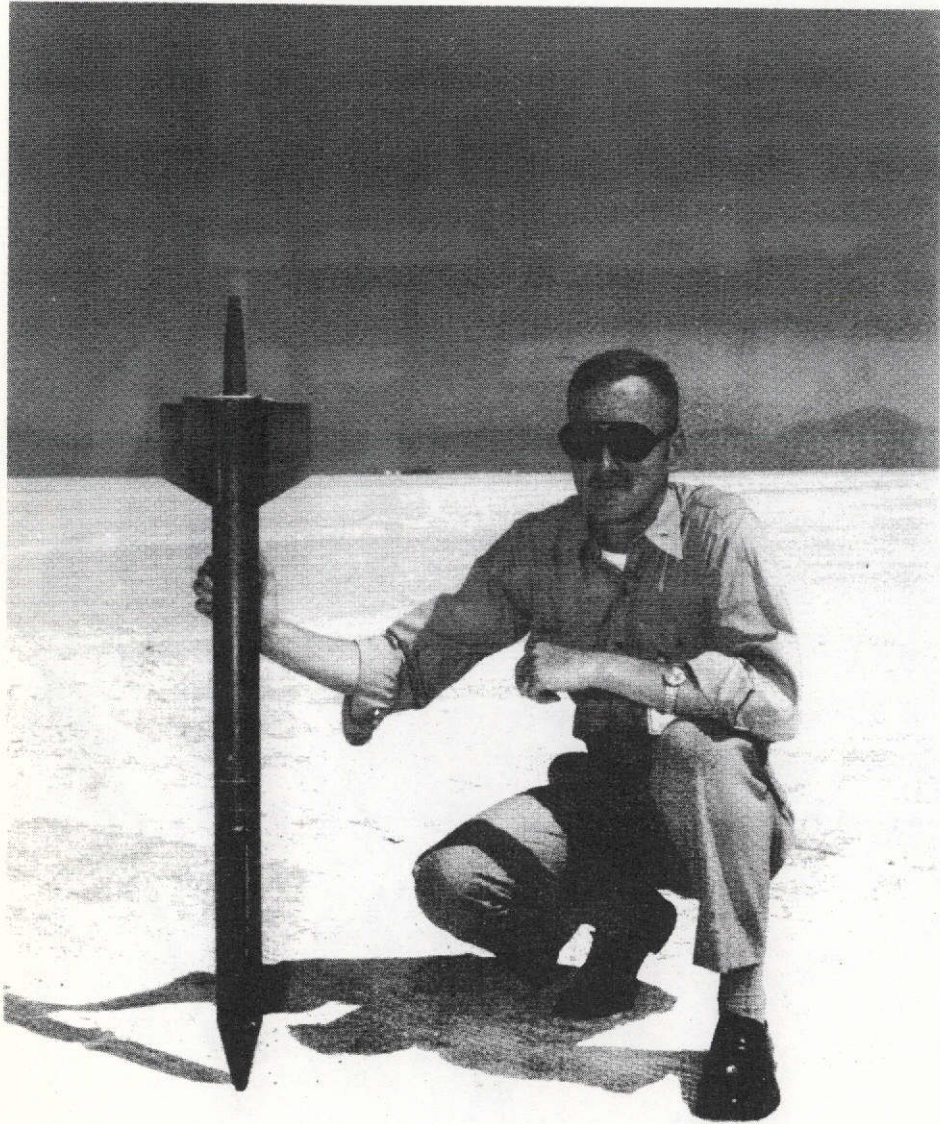
Figure B-6. SIP

Terradynamic Electrode

In support of a geothermal energy program, the University of Hawaii is exploring the island of Hawaii for subsurface concentrations of hot brine by measuring the electrical resistivity. One of the practical problems is the difficulty of obtaining a good electrical contact between an electrode and the dry lava. A penetrator was developed at Sandia to serve as a terradynamic-electrode. The penetrator, which weighed 68 kg and had a detachable afterbody, was dropped from an altitude of 1524 m. Depths of penetration in the lava varied from 1.5 m to 5.6 m. An umbilical line connected the penetrator to the detached afterbody. The contact resistance between the penetrator and the lava was found to be far less than that encountered with conventional electrodes buried in trenches. These penetrators were uninstrumented, but the same vehicle is being modified to measure the heat flow in ash deposits on Mt. Augustine in Alaska.

Marine Sediment Penetrator

The penetrator shown in Figure B-7 was developed to measure the penetrability (and therefore make an indirect measurement of strength) of sediments on the ocean floor. The system has been tested in the Gulf of Mexico. The penetrator is designed for a terminal sink rate velocity of 30 m/s; up to 15.2 m of penetration into soft sediments could be achieved.
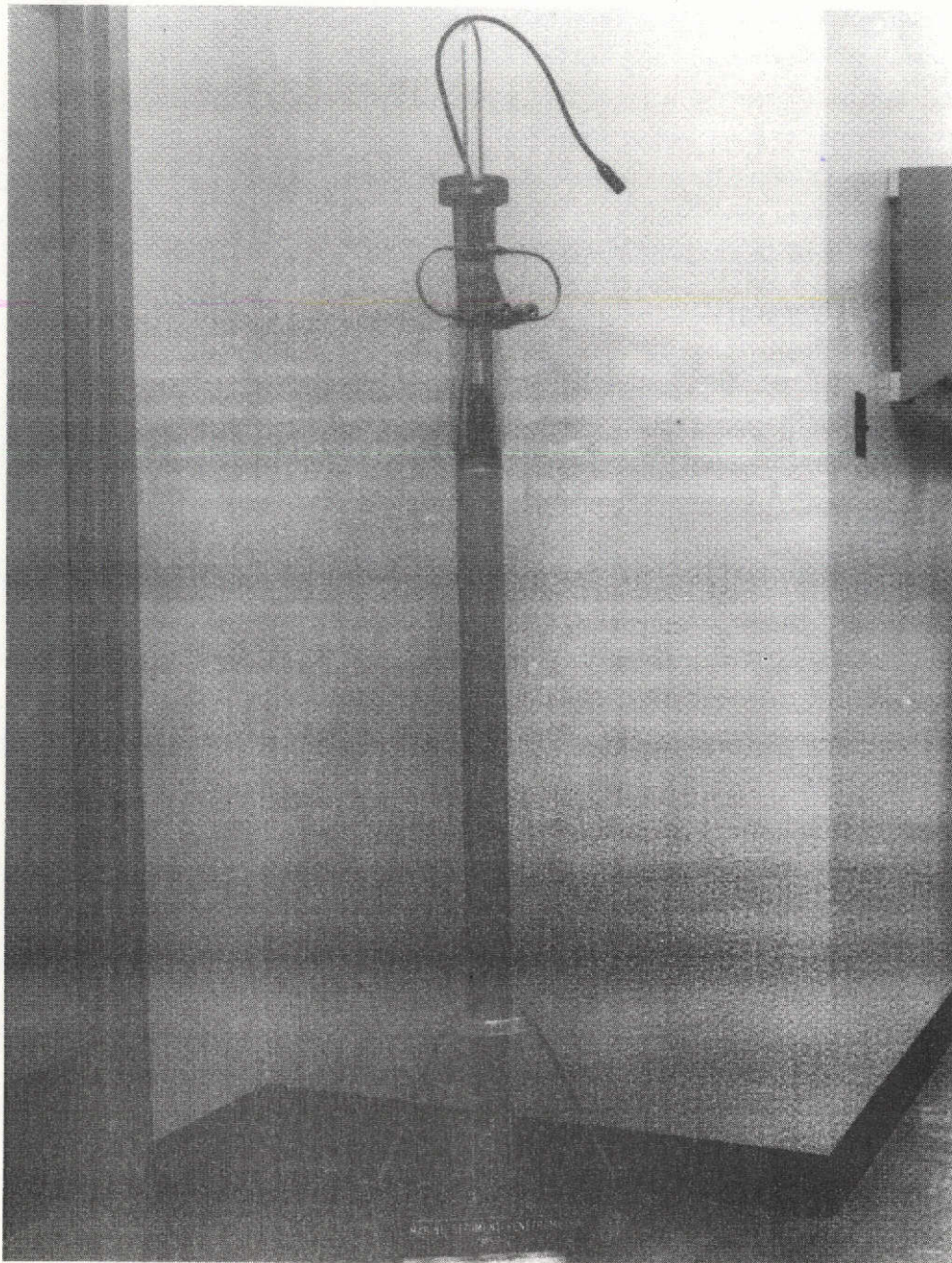
Figure B-7. Marine Sediment Penetrator

References

B1. C. W. Young, The Development of Empirical Equations for Predicting Depth of an Earth-Penetrating Projectile, Sandia Laboratories, Albuquerque, N. M., SC-DR-67-60, May 1967.

B2. C. W. Young, Empirical Equations for Predicting Penetration Performance in Layered Earth Materials for Complex Penetrator Configurations, Sandia Laboratories, Albuquerque, N. M., SC-DR-72 0523, December 1972.

B3. C. W. Young and L. J. Keck, An Air Dropped Sea Ice Penetrometer, Sandia Laboratories, Albuquerque, N. M., SC-DR-71-0729, December 1971.

APPENDIX C

MARS PENETRATOR

Introduction

The Mars penetrator must implant a scientific payload into the broadest possible range of surface materials and terrains without exceeding the deceleration limits of the onboard science and electronics and maintain communication with the orbiting spacecraft after implantation. This appendix summarizes a systems study of the competing demands of terradynamics, terminal aero-dynamics, electronics and science, and Martian physical environments which determined the physical penetrator design as proposed for the Mars mission.

Two types of constraints were placed on the penetrator: those constraints imposed by space-craft and launch vehicle capabilities and those imposed by the scientific payload. The spacecraft and launch vehicle capabilities (1) dictate that the weight of the penetrator be kept as low as possible and (2) limit the Δv which can be imparted to the penetrator to deorbit it. The capability of the payload to withstand deceleration loading during penetration and the maximum tolerable rest inclina-tion to the local vertical dictate the penetrator sectional density and the attitude and velocity of the penetrator at impact.

The penetrator design in Figure C-1 will be shown to meet the performance requirements while remaining within the mission constraints. This penetrator employs the detachable afterbody design concept (discussed in Appendix B) as illustrated in Figure C-2. The detachable afterbody permits an antenna to be left on the surface and the main body to penetrate sufficiently deep in the broadest possible range of surface materials to limit the deceleration to safe limits for the onboard science and electronics. As described in the applications section of Appendix B, over 10,000 seismic and acoustic sensors were successfully deployed in Southeast Asia on the McNamara line with the detachable afterbody design.

In the Mars penetrator, the antenna, transmitter, and receiver are located in the afterbody. The principal scientific payload, power supply, and data handling electronics are all located in the forebody probe. The probe will be made of HY 180 steel which combines high-yield strength and superior fracture toughness. The afterbody will be made of 7075 T7351 aluminum for minimum weight and adequate strength.

The physical characteristics of the Mars penetrator are shown in Table C-I.

For reasons to be discussed in detail later, a nominal impact velocity of 150 m/s is used. Calculations indicate that this vehicle, under these conditions, will perform as follows:

1. Penetrate to a depth of 1 meter in a basaltic lava with a 2500 N/cm^2 unconfined compressive strength, a bulk density of 2 gm/cm^3, and a porosity of 30 percent.

All Dimensions in cm

Figure C-1. Penetrator Configuration
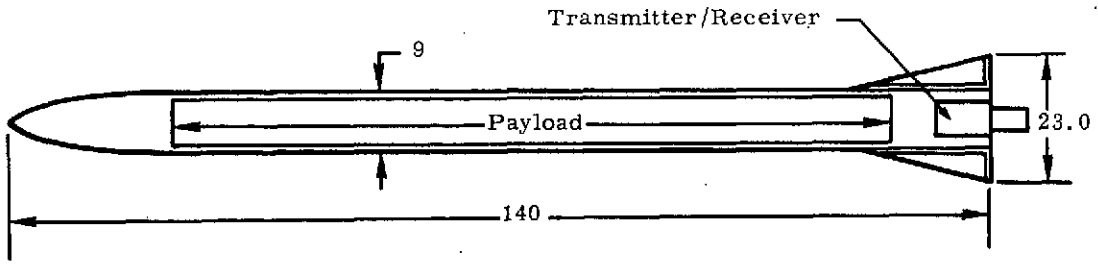
Mass - 31 kg
Payload Volume - 4500 cm^3
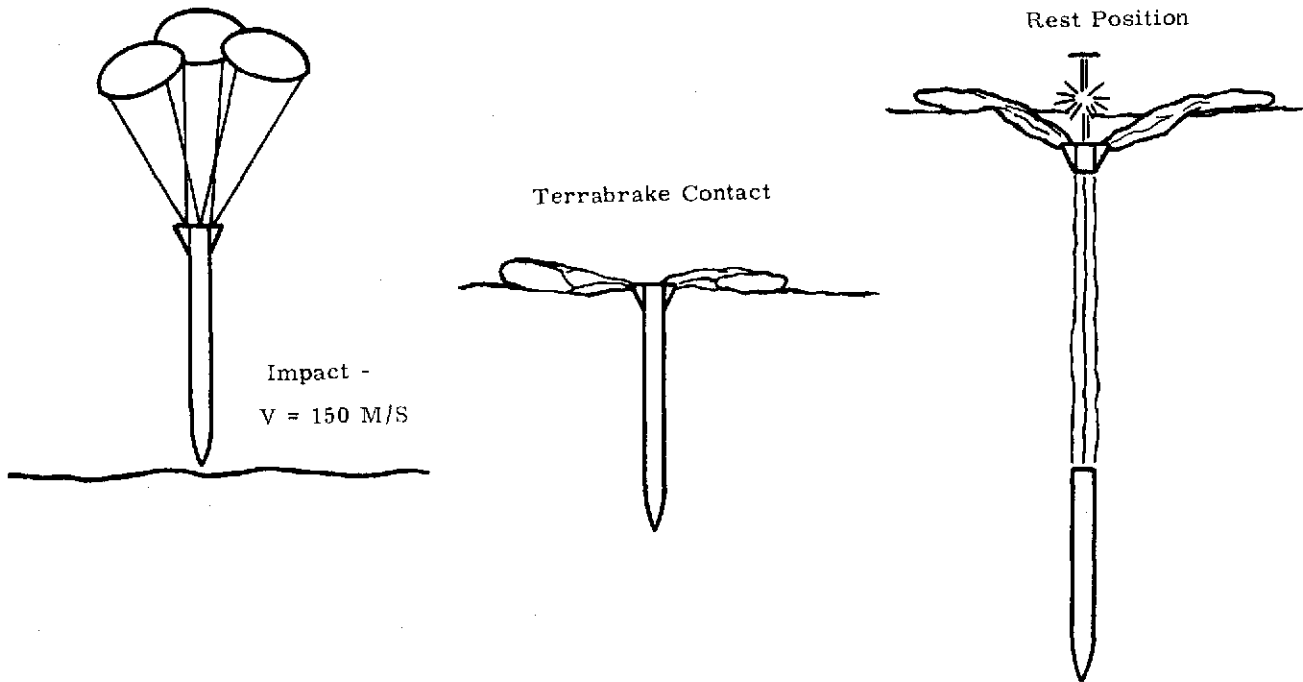
Figure C-2. Implant Sequence

2. The forebody probe will penetrate to a maximum depth of 15 meters.

3. The payload will experience maximum average decelerations of 1200 Earth g's for 15 to 20 msec and maximum peak decelerations of 1800 Earth g's for 5 msec.

4. The detachable afterbody will experience peak decelerations of 18,000 Earth g's for 2 to 3 msec.

TABLE C-I

Physical Characteristics of Mars Penetrator

Complete Penetrator

Weight	31 kg
Principal diameter	9.0 cm
Frontal area	63.6 cm^2
Sectional density	0.49 kg/cm^2
Length	140 cm

Forebody Probe

Weight	28.7 kg
Principal diameter	9.0 cm
Frontal area	63.6 cm^2
Sectional density	0.45 kg/cm^2
Length	123 cm

Detachable Afterbody

Weight	2.3 kg
Principal diameter	23.0 cm
Frontal area	348 cm^2
Sectional density	0.007 kg/cm^2
Length	28 cm

The remainder of this appendix details the systems analysis leading to the penetrator configuration shown in Figure C-1.

Penetrator Design

Equation (B-2) of Appendix B,

$$D = 0.0117 \ SNK \ (W/A)^{1/2} \ (V - 30.5),$$

where

D = depth, meters

S = material penetrability, dimensionless

N = nose coefficient, dimensionless

K = mass scale factor, dimensionless

W = weight, kg

A = sectional area, cm^2

V = velocity, m/s,

was used to determine the values of the design parameters N, W/A, and V which would give the desired depth of implantation over the broadest range of penetrability of surface materials.

A tangent ogive nose with a length-to-diameter ratio of 2.4 was chosen because test experience (References C1 through C3) has shown this nose shape to have satisfactory performance characteristics over a wide range of surface materials. The nose shape has a nose coefficient value of 1.0.

The impact velocity and sectional density were determined by

1. A minimum penetration of one meter in the hardest anticipated material: $S = 1.0$

2. A maximum allowable payload deceleration of ≤ 1800 Earth g's.

Figure C-3 shows penetration depth as a function of impact velocity for various values of sectional density. For a depth of 1 meter (Figure C-3), the required impact velocity for the various values of section density is determined. These values of impact velocity determine the deceleration environment the penetrator will experience. The average deceleration is

$$\bar{a} = \frac{V^2}{2Dg} \quad , \quad \text{Earth g's}$$

and peak deceleration is

$$\hat{a} \cong 1.5 \, \bar{a} \quad .$$
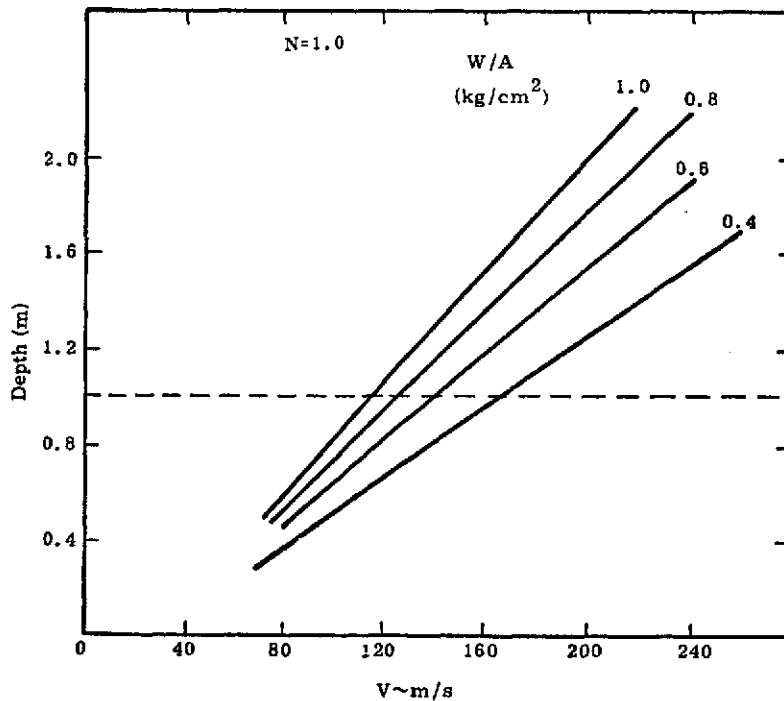
Figure C-3. Depth versus Impact Velocity

Figure C-4 shows deceleration as a function of sectional density for a 1-meter penetration into a material with penetrability of 1.0. If the payload peak deceleration loading is limited to 1800 Earth g's, the sectional density (W/A) is 0.49 kg/cm^2. This sectional density requires an impact velocity of 150 m/s to achieve the required 1-meter depth in material with penetrability of 1.0.
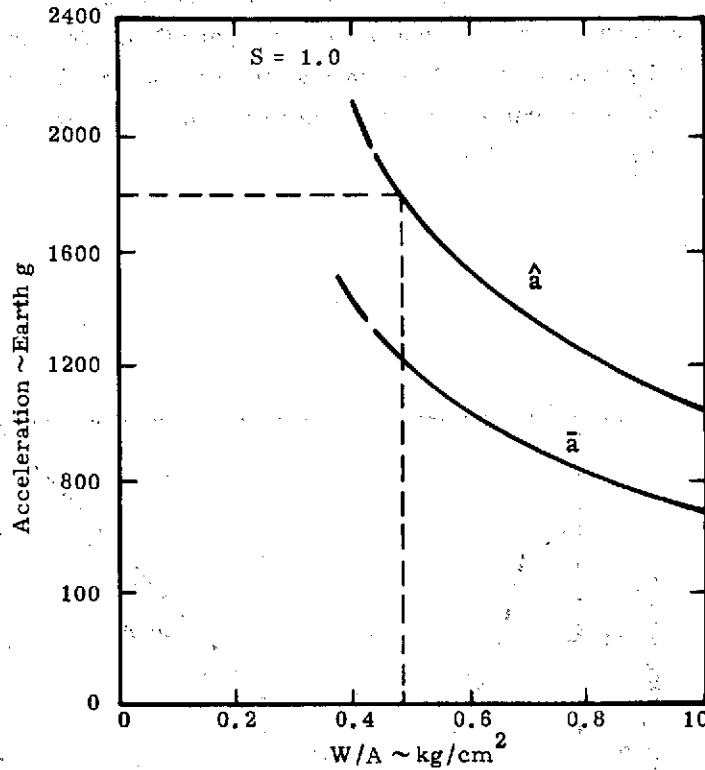
Figure C-4. Acceleration versus Sectional Density

The penetrator diameter and the weight are determined by the payload diameter and the penetrator case wall thickness. A payload diameter of 7.6 cm and a case wall thickness of 0.70 cm were selected as being consistent with the science requirements and the launch limitations for the Mars penetrator. The resulting principal diameter of the penetrator is 9 cm and penetrator weight is 31 kg.

The forebody probe length is determined by the payload volume. The nominal design has a payload volume of 4500 cm^3; therefore, the resulting payload length is 102 cm. When the nose length is added, the length of the probe becomes 123 cm. The weight of the probe is 21.4 kg, exclusive of the payload. The payload is estimated to weigh 7.3 kg, which brings the total probe weight to 28.7 kg. The detachable afterbody is estimated to weigh 2.3 kg including aluminum structure, antenna, transmitter, and receiver.

Penetration Performance

The penetration performance of the Mars penetrator has been estimated from Equation (B-2) of Appendix B. In that the surface penetrability of Mars is unknown, the performance has been estimated as a function of surface penetrability (S). The depth and average deceleration of the afterbody are shown as a function of surface penetrability in Figure C-5. The deceleration curve is terminated at a penetrability value of 2.0. For penetrability values less than 2.0, separation does not occur, and the afterbody experiences the same deceleration as the probe. The probe deceleration and depth are shown in Figure C-6.
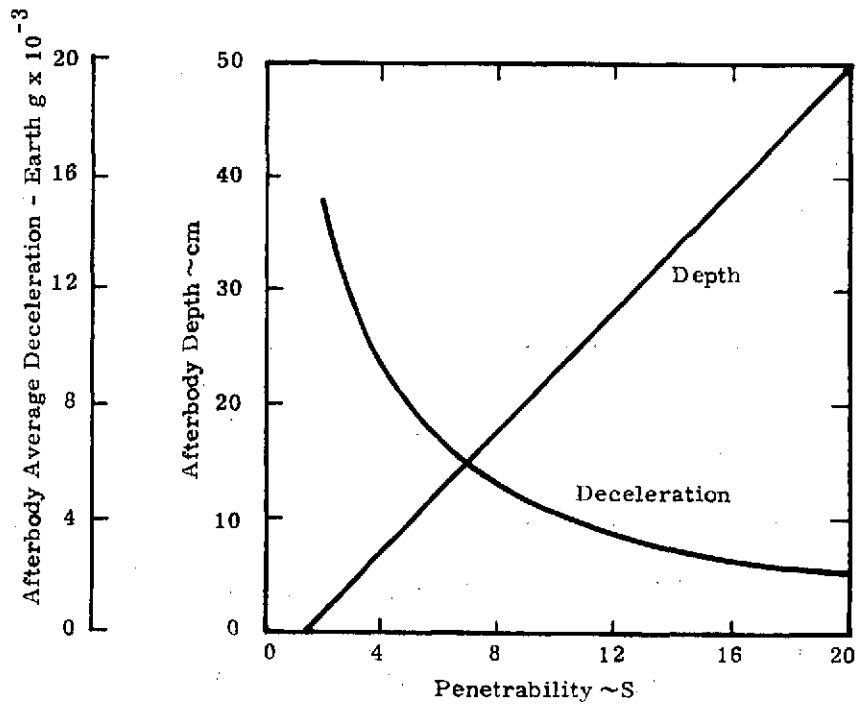
Figure C-5. Afterbody Performance

Surface Materials

Four surface materials have been considered for Mars: rock, lag gravel, dune sand, and loess (Reference C4). A range of expected penetrability values has been estimated for these models based on experience with similar Earth materials.
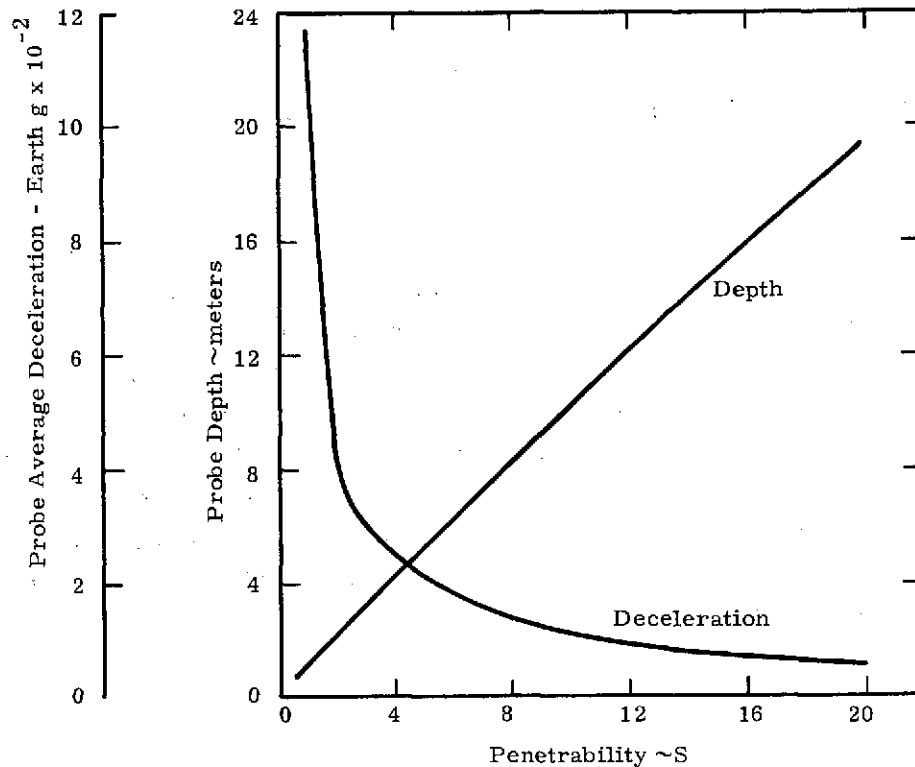
Figure C-6. Probe Performance

The rock is expected to have a penetrability ranging from S = 0.2 to S = 1.5. The Mars pene-trator is designed to satisfactorily implant in fairly porous (porosity $\geq$ 30 percent) lava rock, which from previous test data has a penetrability of 1.0. A penetrator capable of penetrating in a massive, very hard rock formation would be too heavy for the Pioneer/Mars mission, and the payload would experience excessive decelerations. Reference C4 states that a surface of hard rock " ... seems improbable."

Lag gravel is defined by Reference C4 as being ". . . coarse particulate materials too large to be removed by wind." The effect of such blocks on penetrator performance is dependent on block size and the probability of hitting a block large enough to adversely affect penetrator performance. A block diameter of the order of 5 times the penetrator diameter is considered tolerable. Data from Surveyor sites, shown in Reference C4, indicate that the cumulative frequency of blocks per square meter larger than 0.5 meter in diameter is of the order of 10^{-2} and that the cumulative fraction of the area covered by blocks larger than 0.5 meter is also of the order of 10^{-2}. Consequently, it is assumed that the lag gravel will have no effect on the penetrator performance, and no penetrability value has been assigned for this case.

Dune sand and loess are wind-deposited materials differing primarily in grain size; loess is the finer grained material. Experience with similar Earth materials indicates that the penetrability of dune sand should range between S = 10 and S = 12 and that the penetrability of loess should range between S = 10 and S = 15.

The maximum depths for the probe and afterbody (Figures C-5 and C-6) are 15 meters and 36 cm, respectively, for the range of penetrabilities anticipated.

Wind Effects

Surface winds affect penetrator performance. In the presence of a surface wind, the velocity vector of the penetrator with respect to the ground is not aligned with the longitudinal axis of the penetrator at impact. As the penetrator enters the surface, lateral forces are experienced as the longitudinal axis of the penetrator aligns itself with the resultant velocity vector. The magnitude of the resulting lateral forces is a function of the ratio of the wind velocity to the impact velocity and of the penetrability of the material: the larger the velocity ratio and the harder the surface material, the greater the lateral forces. The effect of lateral forces ranges from slight changes in penetrator rest angle, with respect to the local vertical, to failure to implant. However, to date, the effects of winds on penetration performance have not been predictable. Experience has led to an empirical rule: for all soils (not rock), a velocity ratio of

$$\frac{\text{wind velocity}}{\text{impact velocity}} \leq 0.2$$

is tolerable. For the Mars penetrator, this corresponds to a wind velocity of 30 m/s. Probability distributions for near-surface winds for both north and south latitudes are given in Reference C4 and are summarized in Appendix G. These data indicate that tolerable wind conditions can be expected in the north 95 percent of the time; in the south, the probability drops to 80 percent.

It should not be concluded that a penetrator necessarily fails if the wind exceeds 30 m/s at impact. In cases where the material impacted is fairly penetrable (such as loess), the result of somewhat higher winds would be larger rest angles (with respect to the local vertical) than anticipated. In such cases, only that science, such as the nonrighting seismometer, dependent on close alignment with the local vertical would be affected.

References

1. C. W. Young, The Development of Empirical Equations for Predicting Depth of an Earth Penetrating Projectile, Sandia Laboratories, Albuquerque, New Mexico, SC-DR-67-60, May 1967.

2. C. W. Young, Empirical Equations for Predicting Penetration Performance in Layered Materials for Complex Penetrator Configurations, Sandia Laboratories, Albuquerque, New Mexico, SC-DR-72-0523, December 1972.

3. W. J. Patterson, Projectile Penetration of In Situ Rock, Sandia Laboratories, Albuquerque, New Mexico, SLA-73-0831, November 1973.

4. J. S. Martin, Mars Engineering Model, NASA Langley Research Center, Viking Project Office, Hampton, Virginia, M75-125-3, January 1974.

APPENDIX D

ELECTRONICS

The most notable characteristic of the electronics designed for use in the Mars penetrator is the technique of maximizing the usefulness of the limited memory available (50 kbits). This maximizing will be accomplished by means of the analytical abilities of the command and control logic and the wide variety of the sequences stored in the read-only-memory (ROM) as those two capabilities are exercised through the command receiver. As an example, if it is discovered that the seismic level on Mars is lower than has been anticipated, a command to the appropriate set of instructions in the ROM could lower the threshold above which seismic events are recorded. One could even perform analyses such as spectral analysis, and thereby lower the amount of data necessary to be stored and transmitted.

An additional consequence of the above technique is that if a portion of the random-access-memory should fail, the appropriate ROM instruction could be initiated to bypass the failed portion so that the random access memory could continue to function.

Thus, the entire operation of the penetrator is based on two unusual features of the electronics package: the analytical capability of the command and control logic plus the large number of sequences stored in the read-only-memory, as those features are utilized through the command link from the orbiter.

Objectives

To fulfill the requirements of the Mars penetrator and the scientific experiments, the following design objectives were established:

1. To support the scientific experiments with appropriate command and control, data gathering, data analysis, data storage, data transmission, and power.

2. To provide housekeeping information so that the states of health may be assessed for the scientific experiments and the electronics package itself.

3. To provide enough options in the command and control hardware to allow for a variety of situations.

4. To provide flexibility in the implementation of the command and control hardware. This flexibility is needed to make possible the inclusion of new aspects of the various scientific experiments as those experiments evolve toward their final designs.

5. To perform the above tasks during the variety of environments which the electronics package can be expected to experience.

6. To perform the above tasks for a long enough time to provide a scientifically useful mission lifetime.

7. To perform the above tasks with enough reliability to provide a probability of success sufficient to justify the mission.

Command and Control

The command and control scheme for the electronics package has been designed specifically to address the first four points in the statement of objectives above.

First, in order to provide for the maximum flexibility in command, a command receiver has been included in the electronics package. This receiver allows an experimenter on earth to change the operations of the scientific experiments through appropriate commands relayed to the penetrator via the orbiter. In order to insure that the proper command is executed, the penetrator retransmits the command it receives and then waits for a specified time before continuing. This delay allows for any necessary correction (from the orbiter) of an incorrectly received command. In the case of the failure of the command link, the command and control logic on the penetrator will still step the scientific experiments through a preassigned sequence of operations. This facet of the command and control hardware thus provides a fail-safe operation in case the command link is somehow interrupted.

Data-gathering will be done digitally: analog signals will be digitized by an analog-to-digital converter which will be time-shared through a commandable multiplexer.

Data analysis, if such is desired by the experimenters, will be accomplished by the command and control logic, again with commands for analysis which will have been stored in the ROM.

Data storage will be accomplished through use of a 50-kilobit solid-state Random-Access-Memory (RAM). Use of such a memory allows storage of enough data to be compatible with the scientific missions which have thus far been designed, without using an inordinate amount of the necessarily limited power available in the penetrator. The random-access nature of the memory allows for great flexibility in data storage and allows for such possibilities as the easy addition of counts from the various frequency windows of the alpha-backscatter experiment as those counts are accumulated during successive time intervals.

Data transmission will be accomplished under command from the orbiter. The bit rate, time of transmission, and resetting of the penetrator clock from the orbiter master clock will be accomplished automatically. The data stored in the RAM will then be shifted out in sequence to the transmitter for transmission to the orbiter which will then store the data for retransmission to the earth at a lower rate.

Housekeeping information will be taken either under command from the earth or at preassigned points in the operation of the scientific experiments, or both.

The third and fourth points in the statement of objectives are met by the fundamental principle of operation of the command and control portions of the penetrator: all commands are stored in a ROM. The appropriate sequence of commands is initiated from the ROM by having the command from the orbiter contain the address in the ROM in which the first command in the sequence is stored. By use of subroutines in the ROM, joined together by the actual routine in the ROM which is specified by the command from the orbiter, an almost limitless number of different sequences can be initiated. Another virtue of the ROM is that the commands which actually control the commands to the experiments can be easily altered as the experiments themselves evolve toward their final designs. (This "easy alteration" would be provided by using a programmable ROM until the final design.) Also, by altering the commands in the ROM, the operation of the whole system can be easily checked. After the final design of the system is complete, the storage of the commands in the ROM will make them secure by the nature of the virtual indestructibility of data stored in a ROM.

The command word which will be sent down from the orbiter to the penetrator (and retransmitted back up to the orbiter for confirmation) is shown in Figure D-1, along with some typical possible commands. The 200-bit preamble is to allow synchronization of the receiver system, including addressing a particular penetrator. The ROM address actually specifies the new command. The data portion of the command word is used for those instructions which require specific data, such as the new bit rate for the command "change bit rate."

DOWN | 200 BITS | CODED ROM ADDR. | CODED DATA

UP   (SAME)

COMMANDS

1. UPDATE CLOCK.
2. CHANGE BIT RATE.
3. CHANGE TRANSMISSION TIME.
4. TRANSMIT DATA.
5. RETRANSMIT DATA.
6. TAKE NEW DATA.
7. DON'T AUTOMATICALLY TRANSMIT (KEEP DATA).
8. CALIBRATE CHEMISTRY EXPERIMENT.
9. RUN CHEMISTRY EXPERIMENT.
10. CHANGE SEISMIC CRITERIA.
11. READ HUMIDITY, TEMPERATURE, LIGHT, HOUSEKEEPING.
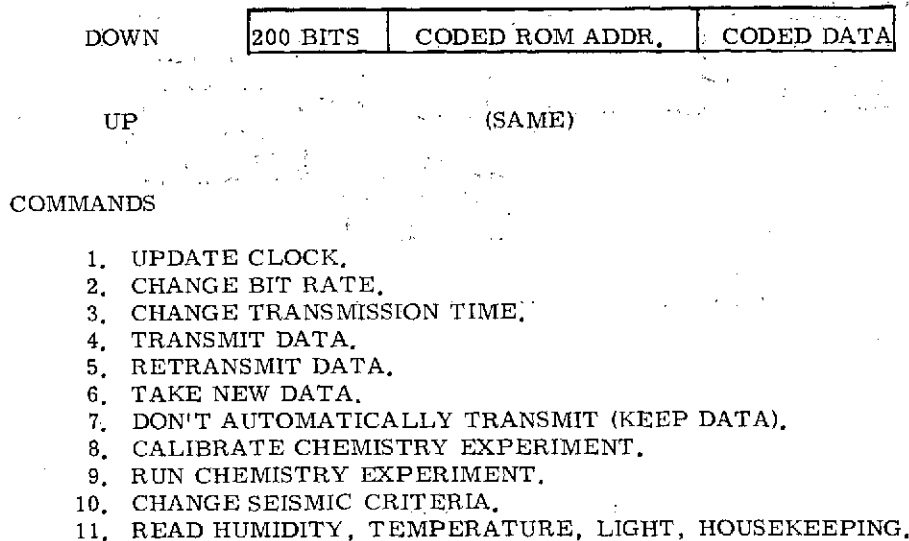
Figure D-1. Penetrator Command and Control

The command/memory organization is shown in Figure D-2. The command receiver, bit synchronizer, and format synchronizer deliver the command word (the ROM address) to the command decoder, which places the word in the program counter. The program counter gives

the next address for the memory address register. As is indicated in the diagram, the memory address is loaded into the memory address register which then uses that address to address the proper sequence in the ROM. The memory address register also can control the address to be used in the RAM. The commands from the ROM are read into the memory buffer register. The instruction portion of the command word from the ROM is read into the instruction register, which actually does the commanding of the rest of the logic. The memory buffer register can also use the information stored in itself to load the next address into the program counter and can read into and out of the RAM. All commands to the external devices (experiments, the clock, the bit-rate control circuitry, the various switches for power, and the analog multiplexer) as well as all returns from the various external devices go through the accumulator. All external devices are treated as peripheral devices to the command and control system, and all such external devices are addressed as such, individually.
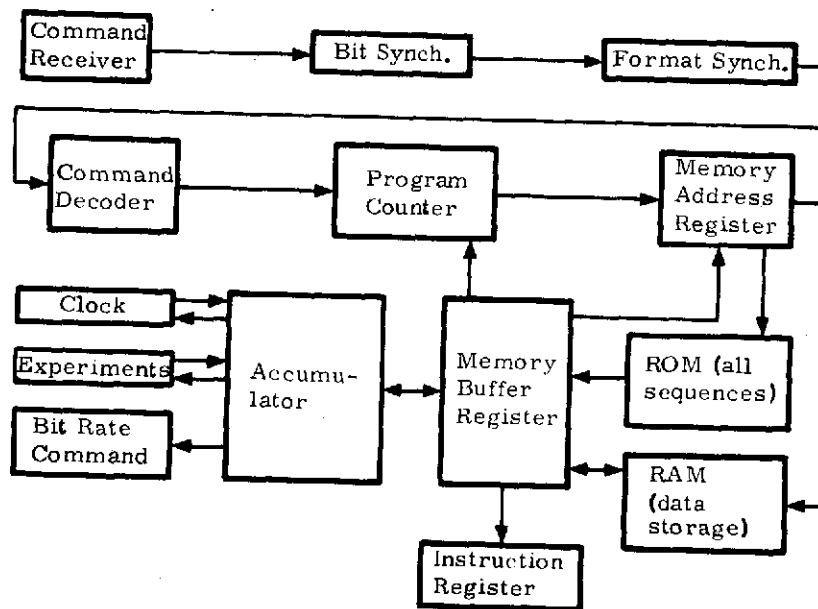
Figure D-2. Command/Memory Organization

Electronics Description

The block diagram for the electronics is shown in Figure D-3. The block diagram shows the division between the forebody, which penetrates below the surface, and the afterbody, which remains near the surface. The lines shown between the forebody and the afterbody constitute the umbilical which must be payed out between the two bodies.

AFTERBODY

FOREBODY
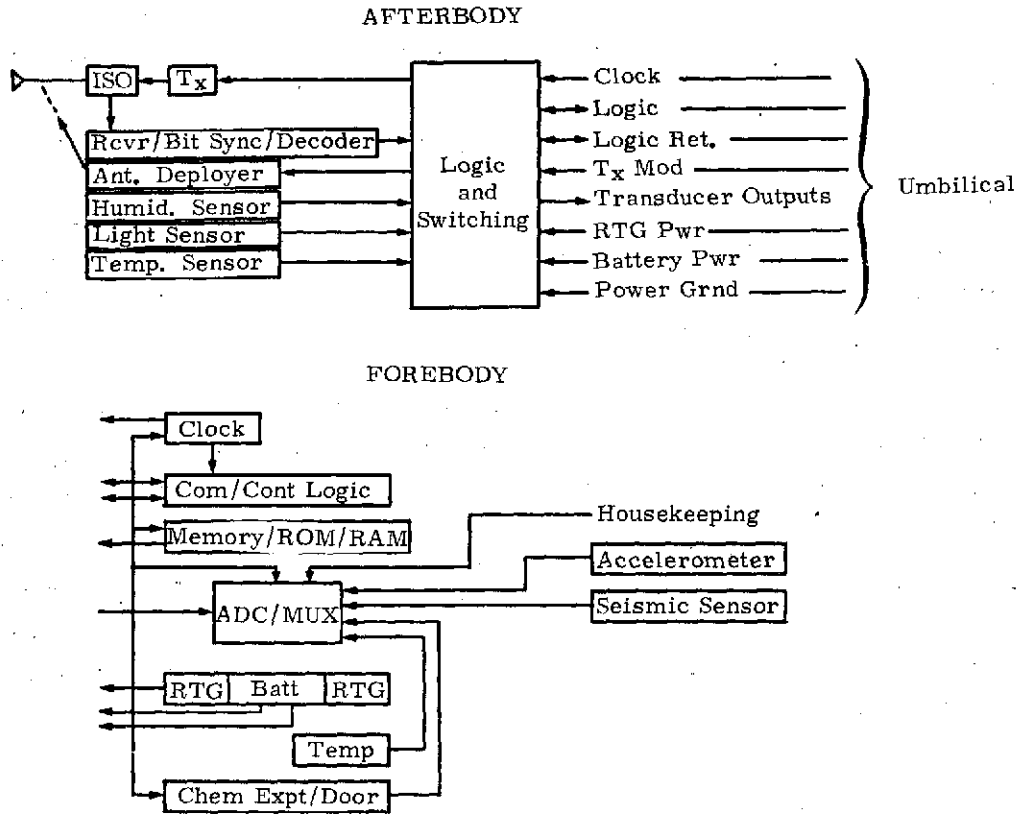
Figure D-3. Penetrator Electronics Block Diagram

The afterbody contains the transmitter and the receiver (necessary because the losses associated with carying the radio-frequency signals down the long umbilical would be too great), the antenna and antenna deployer, some experiments, and the necessary logic to specify the experiment to be run and to control it.

The forebody contains the command and control system, including the memories, the analog-to-digital converter (ADC) and the programmable multiplexer which feeds it, the power supplies, and more experiments.

System Operation

A typical sequence of operation would begin with the emplacement of the penetrator in the ground. During this emplacement the accelerometer would generate the deceleration signal which would be digitized and stored in the RAM. Next the antenna would be erected, which must be done soon after the penetrator lands before the extreme cold makes the antenna deployment more difficult. Housekeeping data would then be read. The penetrator would then transmit the acceleration and housekeeping data to the orbiter, which would analyze the Doppler shift in the signal from the penetrator to discover the penetrator location. Once the location of the penetrator has been determined, the orbiter can choose the optimum times for penetrator transmission. After the first transmission (barring command link failure), subsequent transmissions will be commanded from the orbiter at those optimum times. Also after the first automatic penetrator

activities (erecting the antenna, reading the housekeeping information, transmission), the orbiter will command the specific operations to be performed by the penetrator. If the command link should fail, a "fail-safe" sequence of instructions stored in the ROM would be initiated. The "fail-safe" sequence would insure that at least some functions would be performed, but mission lifetime would be shortened in such an event. Mission lifetime would be shorter because the transmission period would have to be longer to insure that the orbiter be able to receive the signal from the penetrator, because the best times for transmission would not then be available. These longer transmission periods would use up the energy stored in the battery more quickly.

Environmental Requirements

The environmental requirements for the Mars penetrator are characterized by two significantly strenuous conditions. The components must survive the high shock environment of penetrator impact and entry and they must survive high temperatures for a significant time for planetary quarantine.

The various environmental requirements for the Mars penetrator electronic components are presented in Table D-I. The specification in each category reflects the worst-case condition for each category in the various regimes (planetary quarantine, launch, transit to Mars, descent to Mars, impact on Mars, operation on/under the surface of Mars).

Electronic Components

The Mars penetrator electronic components are all state-of-the-art devices based on components which have long and successful histories of use in similar environments. Past experience has indicated that an electronic package which can meet the requirements of the Mars penetrator mission can be produced.

Integrated Circuits

Pulse code modulation (PCM) systems with data storage have been utilized in both air-dropped and gun-fired penetrators. The 50,000-bit memories that store and output data upon command from an inflight aircraft have been developed for the Marine Corps for use with implanted sensors. The major difference is the lifetime requirement for the penetrator components; this requirement is much greater than that for the systems now being utilized. However, through proper evaluation programs, the lifetime requirements can be met.

In that one of the primary requirements is that the system consume minimum power, all the digital logic will be implemented with C-MOS integrated circuits. Sandia has been utilizing C-MOS integrated circuits in similar type systems since 1969. The qualifications of most C-MOS devices for deep-space application have been completed; therefore, these devices can now be manufactured and tested to MIL-M-38510. The production facilities have been certified by the Defense Electric Supply Center and by NASA. C-MOS integrated circuits are now being used in space vehicles such as Nimbus, Helios, Apollo-15, Earth Resources Technical satellites, and many others. The memory devices, both ROM's and RAM's, will be C-MOS semiconductor memories.

TABLE D-I

Acoustical Noise Levels

Octave Band Center Frequency (Hz)	Sound Pressure Level (dB Ref. 0.0002 microbar)	Duration
15.8	115	1 minute for complete exposure
31.5	124	
63	130	
125	134	
250	137	
500	134	
1000	128	
2000	127	
4000	125	
8000	122	

Translational Vibrations

Input Direction	Frequency (Hz)	Acceleration/Displacement
Longitudinal axis	5-8.5	0.4 in. (1.02 cm) (double amplitude)
	8.5-200	±1.50 g (0-to-peak)
Lateral axes	5-8	0.3 in. (0.76 cm) (double amplitude)
	8-200	±1.00 g (0-to-peak)

Random Vibration

Frequency (Hz)	Power Spectral Density Level (g^2/Hz)	Acceleration g (rms)	Duration
20-150	0.00036 to 0.02, increasing between 20 Hz and 150 Hz at 6 dB/octave to 0.02 g^2/Hz at 150 Hz	6.2 overall level	2 minutes each axis

Other Environments

Shock: Forebody - 2000 g's peak for 5 ms
1300 g's average for 15 ms

Afterbody - 20,000 g's for 2 ms

Acceleration (deployment from orbiter): 203 g's for 40 ms

Temperature: Battery - 0°C to 60°C ⎫ Except for sterilization for planetary quarantine
Otherwise - -25°C to 60°C ⎭

Planetary Quarantine - 10 hours at 125°C

Life: 600 days nonoperational, followed by 400 days operational

Pressure: Extremely low

Humidity: Extremely low

The ROM's will be the primary control elements of the system. In that past experience has indicated a need for a very flexible control circuit during the initial phases of development during which experiments change and data requirements are altered, the system will be implemented with programmable read-only memories. This would provide the capability of fast response to required control changes. However, it is felt that for the flight system memories programmed by the manufacturer should be utilized to insure reliability.

NASA-qualified C-MOS integrated circuits and low-power analog devices will be used in the design of the A/D converter so that the reliability of the converter can be assured by Sandia. The ROM-controlled multiplexer would also be designed with NASA-qualified C-MOS integrated circuits for reliability.

It is apparent that by using qualified components that have been utilized in several similar programs at Sandia with success and by including redundancy of circuits, a highly reliable sophisticated data acquisition system can be developed for this program.

Battery System For the Mars Penetrator

The three battery systems which appear to be the most likely candidates for fulfilling the requirements of the Mars penetrator are the lithium-organic, the mercury-cadmium, and the nickel-cadmium. The Mars penetrator power requirement, which poses a unique battery design challenge, is that of meeting the COMBINED conditions of high-energy density (2.8 watt-hours/in^3), high-temperature environments (0 to 125°C), long battery life (~1000 days), and high shock resistance (2,000 g's). Of the above electrochemical systems, only the lithium organic is ideally suited to fulfill all the above requirements. In this section, the lithium organic battery specifically designed by Sandia Laboratories for the Mars penetrator is discussed, and the reasons why the other systems are not suitable are reviewed.

An extensive test program, in which the storage and discharge capabilities of Honeywell's lithium-organic "Double D" cells will be determined as a function of temperature and discharge rate, is under way. Test data now available from Honeywell indicate that performance is relatively constant over the temperature range of -10° to +120°F (~-25° to ~+50°C) at low discharge rates. Cells stored at 140°F (60°C) for 60 days delivered 85 percent of the capacity of the unstored cells, and 180 days' storage at 32°F (0°C) had no effect on performance.

High temperature is the most detrimental condition for these batteries. In recent sterilization tests of Honeywell's system, cells survived at 125°C for 6 hours, and at 100°C one cell survived 40 hours. It appears that the sterilization problem might be solved by switching to a less conductive, more stable electrolyte. This electrolyte should be satisfactory for the low-current drain required in the Mars penetrator. Under the assumption that this new electrolyte will solve the sterilization and high-temperature-storage problems, the lithium-organic battery will meet all the other requirements for the Mars penetrator.

The mercury-cadmium, 600 HC, Ray-O-Vac button cells cannot meet requirements for a Mars penetrator because of (1) excessive increase of cell resistance at temperatures above 30°C for 920 days and (2) the low voltage per cell (about 0.9) requires a battery length of 7.5 inches.

The recently designed high-rate HC cells might alleviate the time-temperature problem; but no solution is apparent for the excessive battery length except to lower the power and voltage requirements. If a storage and operating temperature of 25°C could be provided and a battery length of 7.5 inches were acceptable, a battery of six paralleled cell stacks, each with 30 Model 600 HC cells in series, could possibly meet all of the other penetrator requirements, including the sterilization for which these cells have been tested (23 hours at 125°C). This battery would weigh 7 pounds.

Nickel-cadmium batteries, which have performed reliably in many space programs, are capable of providing up to 0.5 watthour per cubic inch (0.03 watthour/cm^3) in an operating temperature range of 20 to 30°C. The output of the radioisotopic thermoelectric generators (RTG) could be used to maintain a high state of charge, and the low impedance of the battery would provide good pulse or peak power conditions. Sealed nickel-cadmium batteries, as with most battery systems, are degraded by exposure to high temperatures. The result of high-temperature exposure (25 to 65°C) is decreased cell voltage and loss of capacity. The magnitude of this degradation is a function of exposure time and temperature. Nickel-cadmium batteries are being used as the rechargeable secondary power source for the Mars Viking program and experience gained there would be directly transferable to the Penetrator.

RTG for Mars Penetrator

The radioisotopic thermoelectric generator (RTG) is designed to meet the Mars penetrator requirements of continuous operation for up to 400 days, of providing the heat required for battery operation, and of withstanding the severe environmental conditions of impact and penetration. All penetrator power requirements except that for the transmitter are fulfilled by the RTG. The power levels required of the RTG for the Mars mission fall between the typical SNAP system levels of 10 to 200 watts and the submilliwatt level of heart pacemakers. The technology for a 150-mW RTG is significantly different from that required for either of these extremes. For instance, semiconductor thermopile elements with small cross sections, which make thermopile fabrication and intraconnection more difficult, must be used. The heat source, which can be unvented, unlike some SNAP heat sources, is small enough so that temperature gradients within the source are not significant. However, to provide a reduced size unit, the helium pressures must be higher than those in pacemakers.

Sandia has expended a large effort in developing materials and processes for a long-life (15 years), high-reliability 50 mW RTG* (the MC2730) for use in weapons applications. Forty-seven of those units have been built. The first ones, assembled in late 1971, are still operating. The RTG proposed for the Mars penetrator mission would draw almost entirely on technology developed in support of that project.

The proposed RTG will look much like that shown in Figure D-4, except for small heat-source and thermopile dimensional changes and possibly a different output connector. It is 5 cm in diameter and 8 cm in length. The short-lifetime requirement will allow higher conversion efficiencies in the Mars unit, and time schedules will permit complete reliability verification before flight. Cutaway RTG identifying the elements is shown in Figure D-5.

---

* This work is summarized in SLA 74-0046.
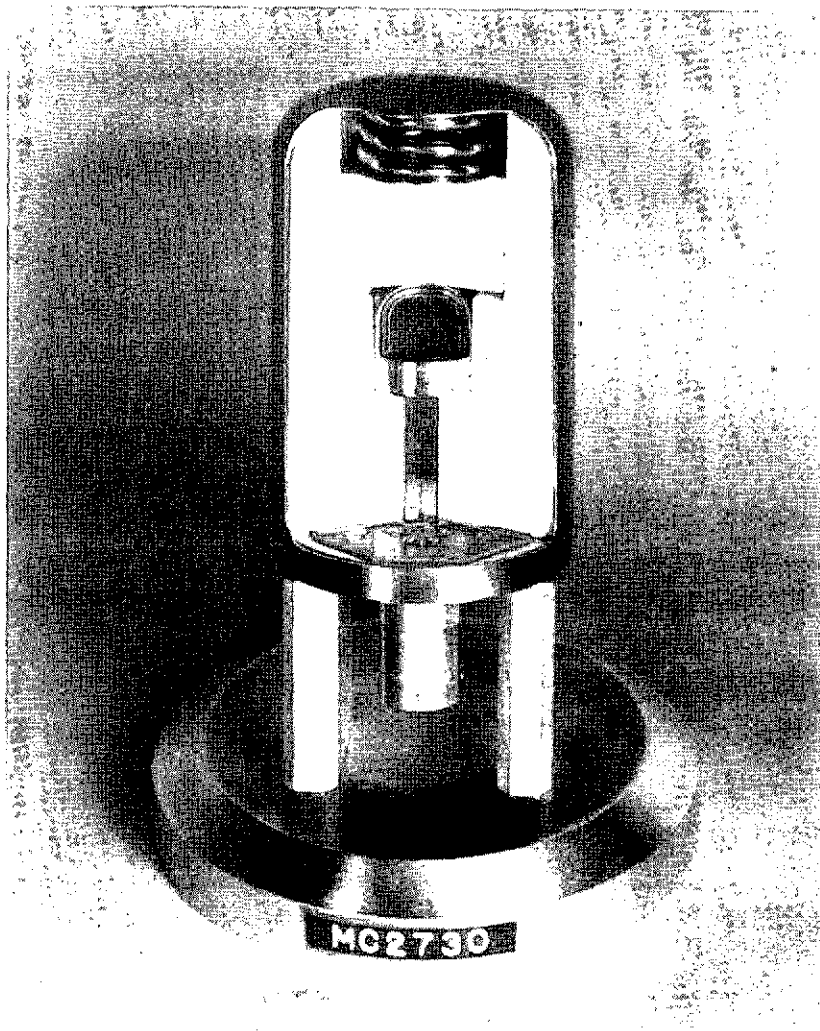
Figure D-4. Radioisotopic Thermoelectric Generator (RTG)
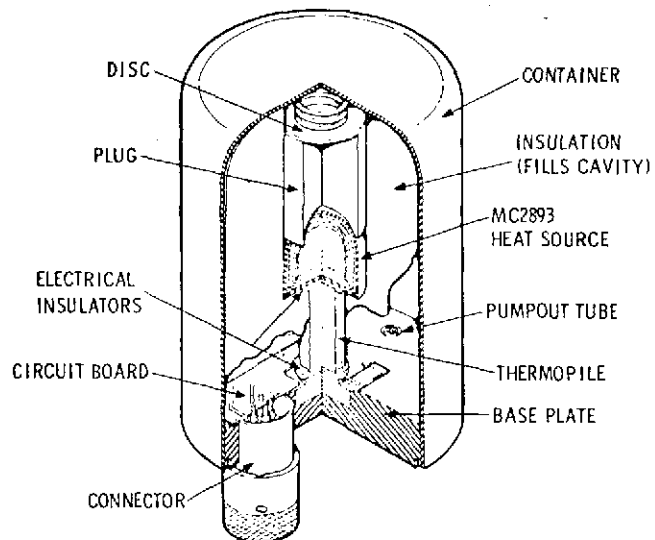
Figure D-5. Schematic Showing Elements of RTG

Thermopile -- The 150-mW, 10-volt power requirement for the proposed RTG requires some changes from thermopiles previously fabricated at Sandia, although the same materials would be used (SiGe thermoelectrics, glassed together to form a monolithic structure). An SiGe thermopile can withstand the shock loadings required; other thermoelectrics would have to be proven. The voltage requirement can be met by using about 70 pairs of elements of about the same size as those in thermopiles previously fabricated. Because thermopile fabricability is a function of element size, fabrication should be no more difficult than in previous designs. The shorter required life would allow use of intraconnections consisting of a platinum-rhodium alloy, reaction bonded to the SiGe elements. This, in turn, makes possible the use of hot junction temperatures of 825 K to maximize RTG efficiency. Thus, 150-mW electrical output could be generated with 10-W thermal input. Samples of the proposed intraconnections have already aged for about two years; therefore, data which will require no extrapolation will be available to determine safe operating temperatures for the intraconnections in a Mars RTG.

Heat Source -- The proposed RTG employs an unvented heat source consisting of doubly encapsulated plutonia shards, 53 μm to 500 μm in diameter. The fuel, which is 80 percent $^{238}PuO_2$, and most of the remainder $^{239}PuO_2$, is oxygen-16 exchanged to reduce the neutron flux caused by alpha-neutron reactions. The neutron spectrum is shown in Figure D-6. Note that the scale here is per thermal watt so that for a 150-mW generator, which requires about 10 thermal watts, the total neutron flux is obtained by simply raising the ordinate by an order of magnitude. In terms of radiation levels, neutrons from a 10-watt heat source should produce less than 95 mrem/hr at the generator surface (r = 3 cm). The γ-spectrum is considerably more complicated with energies ranging from 43.5 keV to 1085 keV. The radiation level produced by γ's will remain approximately constant during the generator lifetime at about 57 mrad/hr at the generator surface. This number and that for neutrons approximately obey the inverse square law.

Because of the apparent absence of any severe accident environment involving an unprotected heat source, the size of the capsule for the Mars mission will be controlled only by the packing density of the fuel. In the case of a 10-watt unit this leads to an outer diameter of 2.2 cm for an aspect ratio of 1.

Finally, as far as materials compatibility is concerned, data already indicate no detrimental effects to the encapsulation after aging with PuO_2 for 240 days at temperatures up to 1173 K. Two-year data for these temperatures should be available by January 1975.

Quarantine/Environmental Requirements -- Sandia milliwatt RTG's have been tested at 423 K for hundreds of hours with no significant degradation. An RTG is easily designed to survive any planetary quarantine requirement (10 hrs at 398 K).

The ambient temperature requirement is less severe than that currently required on Sandia RTG's.

No acoustic tests have been performed, but no problems are foreseen in meeting these requirements.

Sandia milliwatt RTG's are vibration tested at 10 g's zero to peak sinusoidal not exceeding 0.2 inch double amplitude, from 10 to 2000 Hz, along all three axes. The penetrator requirements are not the same, but there should be no problem meeting them.

All Sandia milliwatt RTG's are shock tested to 275 g's, 0.7 ms in six directions, while two units have been tested to 900 g's without failure; the Mars RTG need survive shock in only one direction and therefore should experience no difficulty with this environment. Sandia has tested a thermopile with a heat-source mass mockup on one end to a 2500-g, 5-ms half-sine shock with no failure. In that this is the most fragile part of an RTG, the shock requirement appears attainable.

It should be re-emphasized that the proposed RTG's use the same materials and processes as milliwatt RTG's already highly developed at Sandia.
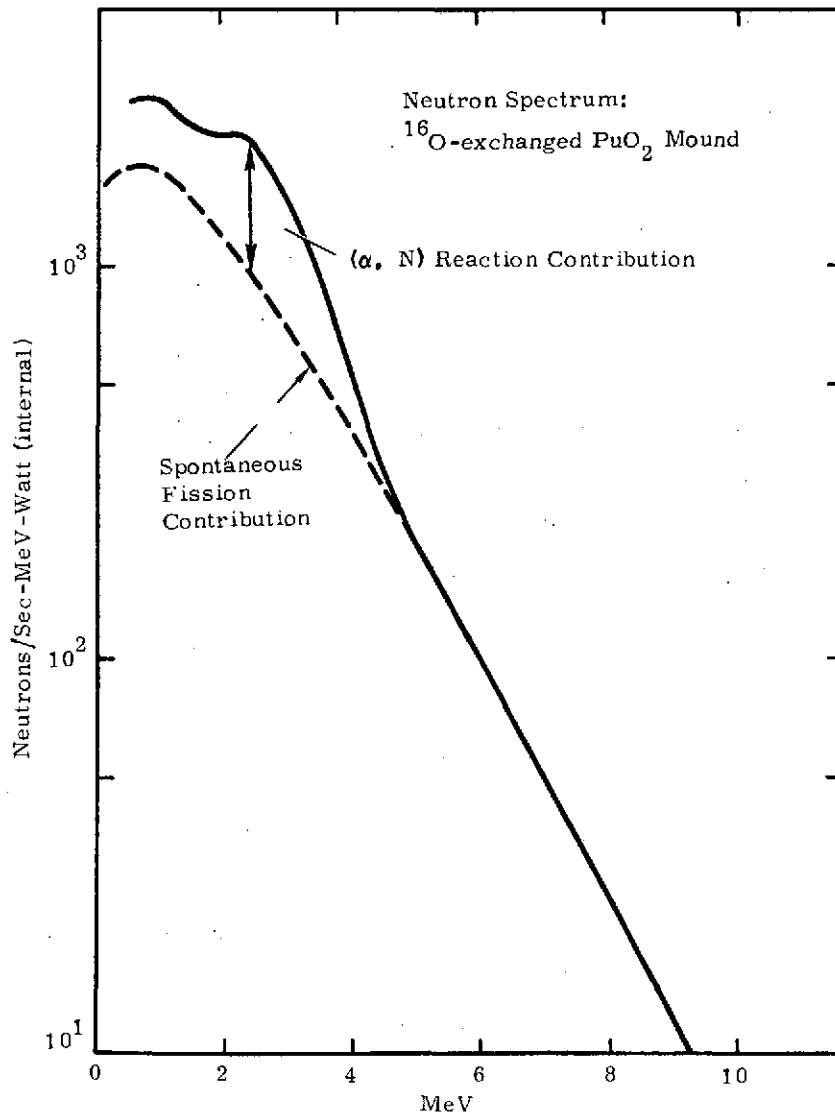
Figure D-6. Neutron Spectrum

Transmitter

The 400-MHz telemetry transmitter proposed is an all-solid-state transmitter capable of 0.5 watt of RF output. State-of-the-art techniques will be used in the design of equipment which will satisfy severe requirements on size, frequency stability, and dissipation over a temperature range from -25 to +60 °C. A block diagram of the transmitter is shown in Figure D-7. The diagram shows typical operating frequencies, nominal power gains, and power levels.

VCXO -- The oscillator-modulator function of the transmitter is performed by a voltage-controlled crystal oscillator. The frequency of the oscillator is approximately 22 MHz. The modulation network of the VCXO is comprised of a capacitive-resistive input circuit and voltage variable capacitor. This arrangement provides the necessary modulation characteristic, i.e., DC-100 kHz.

The multipliers used in the transmitter utilize transistors rather than varicaps. The multiplications are limited to X2 and X3 for circuit simplicity, space saving, and efficiency. Power at 0 dbm, in the range of 22 MHz, is supplied to the first tripler. Here, the frequency is multiplied up to 66 MHz, and the level is increased to +6 dbm. Filtering at this point removes, to a level of 60 dbm, any ±2 MHz signal. This signal, applied to the second tripler, is multiplied up to approximately 200 MHz, and the level is increased to 16 mW. Filtering at this point removes any ±66-MHz component. This signal is further multiplied by a doubler. This stage places the signal at a frequency of 400 MHz and a power level of 50 mW. Filtering at this point eliminates any ±200-MHz component from the output signal. The last two stages in the transmitter are straight-through amplifiers. The gain total required for the two is 13 db. This level, which allows for variation over temperature, enables the system to maintain greater than one-half watt of output power. The output stage is operated at very low gain to enhance overall efficiency and allow for this stage to be impervious to VSWR changes at the antenna terminal.

Finally, all the stages in the transmitter are fed B+ voltage from a series line voltage regulator. This provides transmitter isolation from external voltage variation.

Efficiency Analysis -- The following stage-by-stage analysis illustrates compliance with the need for greater than 20-percent efficiency:

Stage	Current (ma)
VCXO	3
X3 (No. 1)	3
X3 (No. 2)	6
X2	10
Amp No. 1	55
Amp No. 2	90
Line Regulator	10
	177

$$\text{Efficiency} = \frac{\text{Power out}}{\text{Power in}} \times 100$$

Power in = 177 ma x regulator voltage
= 0.177 x 22 volts

Power in = 3.894 W

$$\text{Power out} = \frac{3.9 \times 25}{100} = 0.97 \text{ W}$$

1 mW

66 MHz

```
┌─────────────┐        ┌─────────────┐        ┌─────────────┐
│             │        │             │        │             │
│   VCXO      │───────▶│    X3       │───────▶│   Filter    │
│    22       │        │   6 db      │        │             │
│   MHz       │        │             │        │             │
└─────────────┘        └─────────────┘        └─────────────┘
                                                     │
┌─────────────┐  ┌─────────────┐  ┌─────────────┐  ┌─────────────┐
│             │  │             │  │             │  │             │
│   Filter    │◀─│    X2       │◀─│   Filter    │◀─│    X3       │
│             │  │             │  │             │  │             │
│             │  │      6 db    │  │             │  │      6 db    │
└─────────────┘  └─────────────┘  └─────────────┘  └─────────────┘
       │              50 mW            198 MHz         16 mW
┌─────────────┐        ┌─────────────┐        ┌─────────────┐
│             │        │             │        │             │
│   Amp       │───────▶│   Amp       │───────▶│  Low Pass   │───▶ ◎
│  10 db      │        │   3 db      │        │   Filter    │    ⏚
│             │        │             │        │             │
└─────────────┘        └─────────────┘        └─────────────┘
    500 mW                  1 W
                         400 MHz

┌─────────────┐
│             │
│   Line      │
│  Regulator  │
│             │
└─────────────┘
```
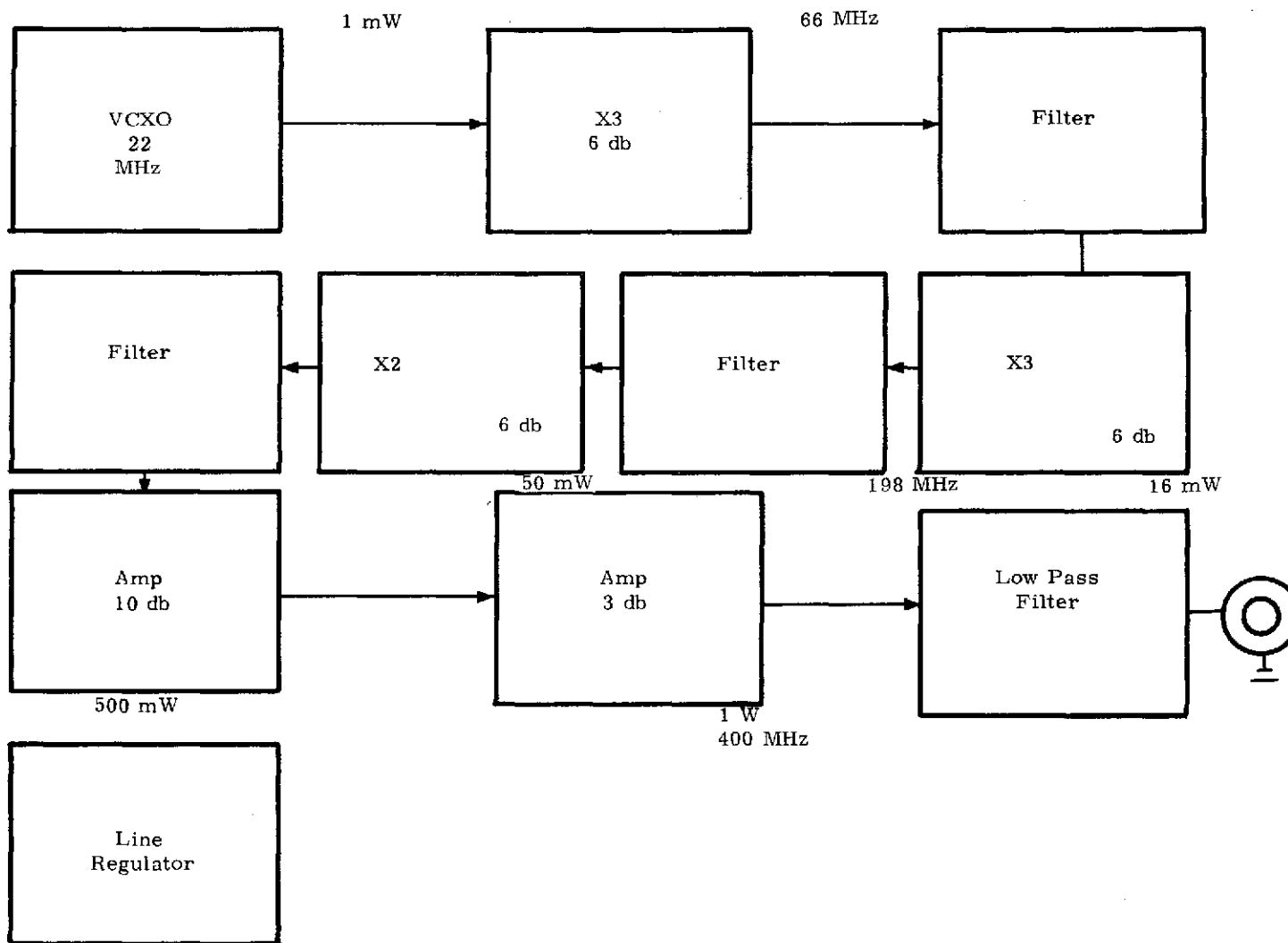
Figure D-7. 400-mHz 1-W Transmitter Block Diagram

The efficiency, which will therefore be a nominal 25 percent, can easily be kept above the 20-percent minimum specification.

Shock Consideration -- Sandia's experience in qualifying and fielding VHF and UHF transmitters in the area of 15,000- to 20,000-g shock environments has established the capability for the transmitters to survive the penetrator environments. Transmitter characteristics especially suited to the proposed design are as follows:

1. A high shock crystal capable of survival up to 30,000 g's.

2. Mechanical design for shock.

3. Use of types of resistors and capacitors that are known to survive this environment.

4. Total encapsulation of all components with a previously proven encapsulant.

5. Use of semiconductors whose survival is probable, given experience with previous shock hardened transmitters.

Examples of previously developed equipment which Sandia has had successful experience with and which meets the above criteria would be the Vector model T-102 and T-202 FM transmitters and the Microcom Model T-49.

Reliability -- The development of this transmitter would be accomplished in a manner similar to that employed by Sandia on Joint Test Assembly (JTA) programs. In these programs, Sandia works with an approved commercial supplier to develop a documented and controlled product which is thoroughly qualified to all specification parameters. All components used are of either JAN-TX or 883 Method B quality or better. Sandia-designed product testers are supplied to these approved vendors to insure proper product testing at the vendor level.

Command Receiver/Demodulator

The command receiver/demodulator which will be used in the Mars penetrator will be commercially available equipment. Such equipment has been used with great success in similar programs with similar environments.

The command receiver/demodulator will be used to receive command signals from the orbiter, decode them, and present the command to the logic in the penetrator.

The receiver will be a single-conversion superheterodyne receiver with a biphase detector for detection of the phase-shift-keyed carrier which is sent from the orbiter. A buffer stage holds the output from the receiver for entry into the demodulator portion of the system.

The demodulator performs the functions of orbiter transmission clock regeneration, bit synchronization, and the decision as to when the actual command begins (as opposed to the preamble and synchronization code) so that the command may be gated to the logic in the penetrator.

Command Receiver/Demodulator Specifications --

Center Frequency:	400 MHz, nominal
Sensitivity:	-114 dbm for bit error rate of 1×10^{-6}
Modulation Type:	Biphase
Bit Rate:	400 bps
IF Bandwidth (3 db):	35 kHz
Outputs:	Serial data 1's and 0's; clock
Input Voltage:	10 Vdc, regulated
Input Power:	40 mW
Operating Temperature:	-25 to +60 °C
Shock, Nonoperating:	20,000 g for 2 ms
Acceleration:	200 g 40 ms
Vibration:	6 g rms
Size:	2.5 in. dia. x 1.75 in. high

Antenna for Mars Penetrator

The antenna design (Figure D-8), based on an antenna used with seismic detector penetrators (Figure D-9) in Southeast Asia, differs primarily in the addition of a horizontal dipole which provides greater overhead antenna gain. The shock environment projected for the Mars mission is comparable to that successfully survived by the seismic penetrator antenna.

Antenna deployment is powered by a coiled spring, called a STACER, which is a patented product of Hunter Spring Co., Hatfield, Pennsylvania. When released, by either an electrical or mechanical latch, the spring will uncoil and drive the antenna assembly out of the storage tube. Once the spring/mast has driven the antenna clear of the tube, the rigid, spring-loaded dipole arms will unfold, and the flexible ground plane arms will deploy. The ground plane arms, which are wrapped around the dipole base, are made of a steel spring material very similar to that of an ordinary steel tape measure. The proposed antenna design will have a ground plane height of about 18 inches above the mounting surface. The complete antenna, which would be packaged in a tube 2 inches (5 cm) in diameter and 10 inches (25 cm) in length, would weight about 1.8 pounds (750 gm).
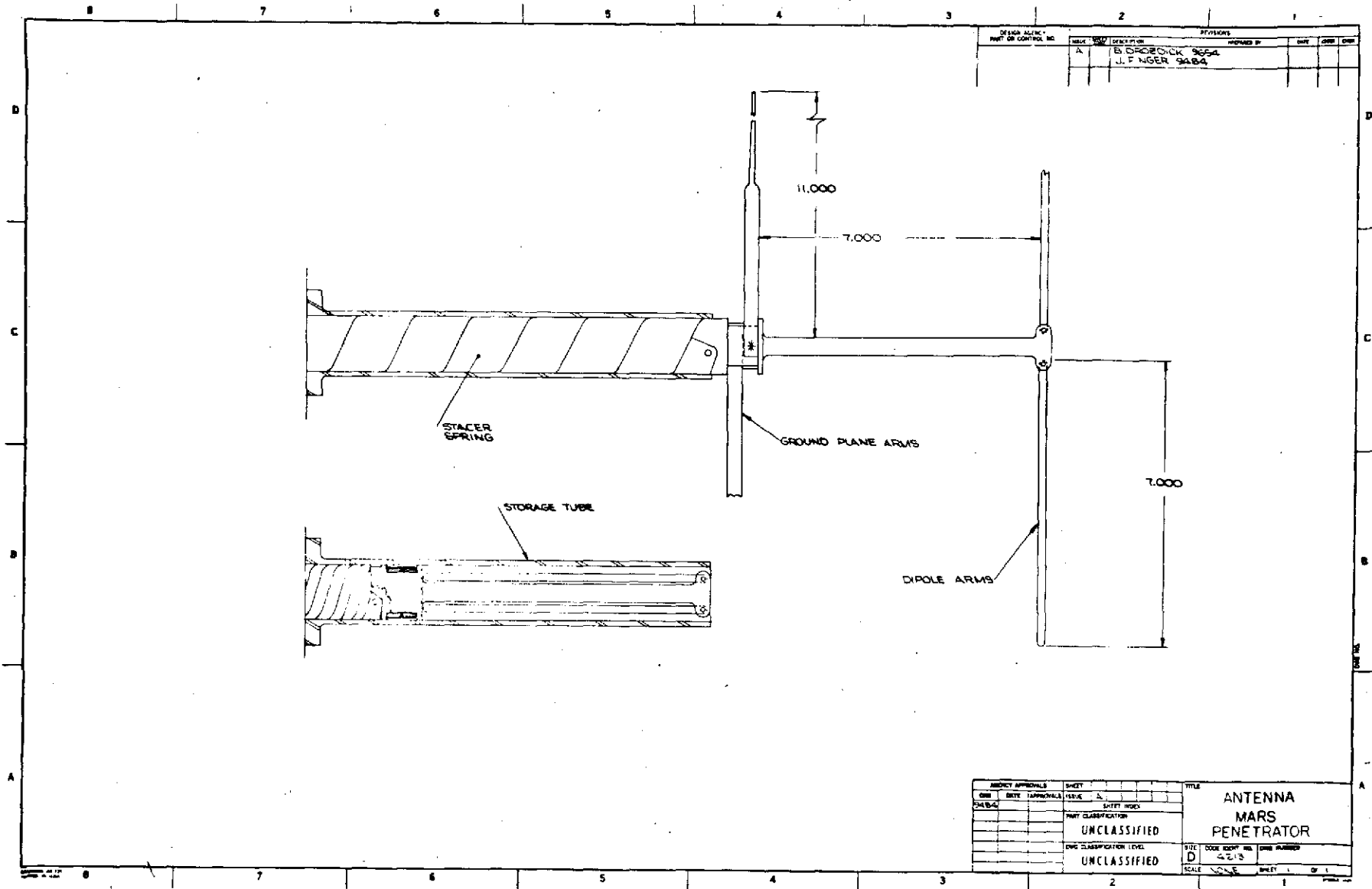
Figure D-8. Mars Penetrator Antenna
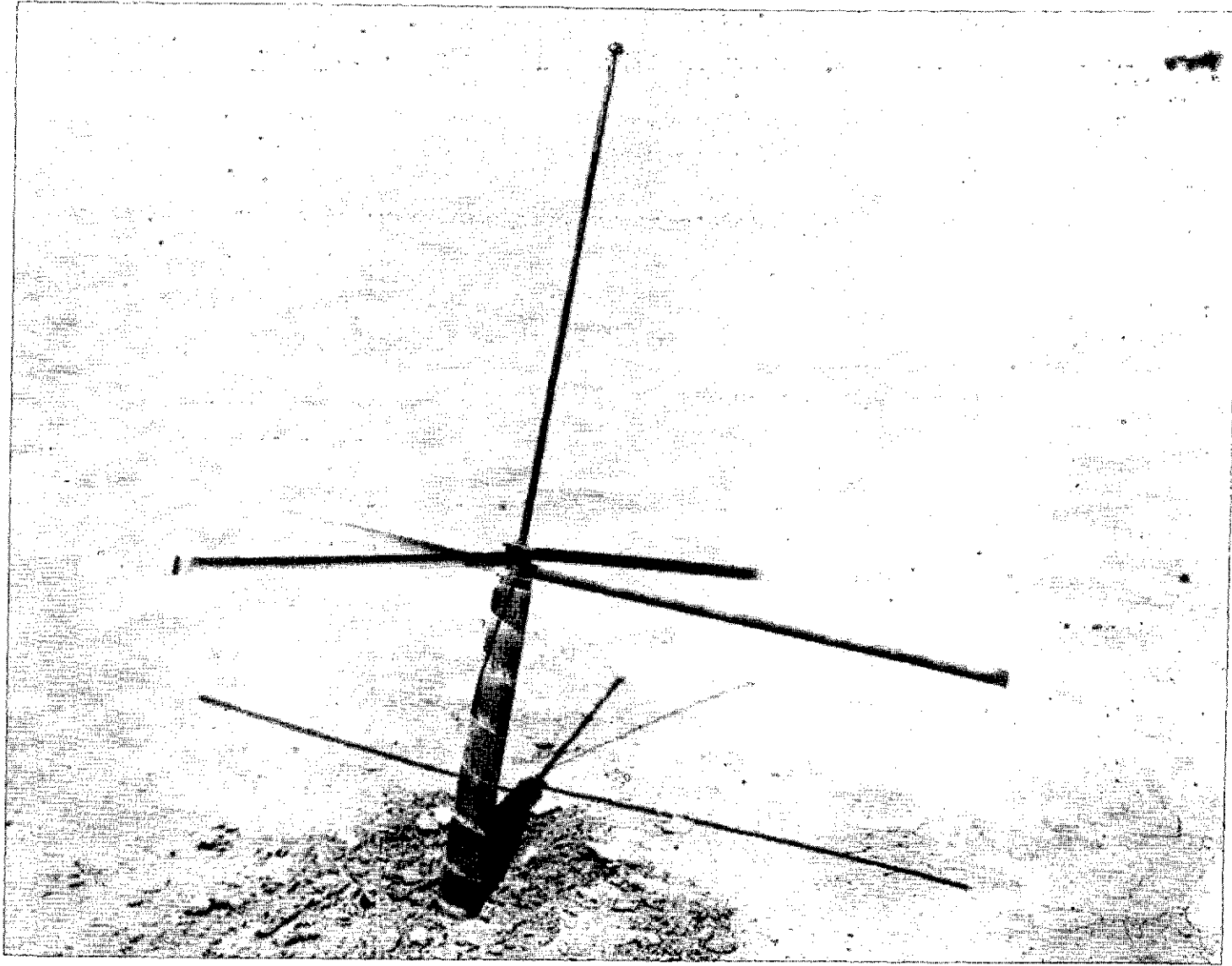
Figure D-9. Seismic Penetrator Antenna

APPENDIX E

THERMAL MANAGEMENT

Introduction

The results of this analysis of penetrator-thermal management, which involved the Mars flight (300 to 700 days), Martian entry (1 day), and penetrator burial (< 400 days), indicate that the thermal requirements can be satisfied for all three of these phases of the mission.

For the analysis, the thermal control requirements set by the temperature limits for the chemical batteries are

1. Battery temperature less than 333K during the Mars flight and planetary entry

2. Battery temperature between 273K and 333K during penetrator burial.

The penetrator design was idealized to be

1. A chemical battery - RTG package which is assumed to be uniform in temperature

2. A mounting shell which centers the above package in the penetrator shell

3. A penetrator shell.

Interior Thermal Analysis

A calculation common to all three mission phases is the temperature difference between the battery package and the penetrator shell. Two different mounting shells are assumed:

1. Asbestos

2. Aluminum alloy.

If perfect thermal contact is assumed, the temperature drop between the battery package and the penetrator shell is defined as follows:[E1]

$$\Delta T = Q \, \frac{\ell n \, (d_o/d_i)}{2 \pi k \ell} \quad ,$$
(E-1)

where

Q — total RTG power – 20 W

d_o, d_i — outer, inner diameters of mounting cylinder, 7.6 cm, 6.1 cm

k — thermal conductivity of mounting shell; asbestos – 0.0021 W/cm-K, aluminum alloy – 1.4 W/cm-K

ℓ — package length – 28 cm.

For these parameters,

ΔT = 12K for asbestos

0.02K for aluminum alloy.

The effect of thermal contact resistance at the battery package/mounting shell/penetrator shell interfaces was estimated by using a 0.005-cm airgap as a worst case. The temperature difference across the gap is given by

$$\Delta T = \frac{Q \, \Delta r}{kA} \quad , \tag{E-2}$$

where

k — thermal conductivity of air at 273K is 0.00023 W/cm-K

A — cylindrical contact area, $\pi d\ell$.

The temperature differences ranged between 1 and 2K at the various radial locations.

Mars Trip

For the Mars trip, the thermal output of the RTG's must be transmitted to the space radiator. One end of a beryllium plug is attached to the space radiator and held at 260K. The other end is a spherical cup which is loaded against the penetrator support structure. The support structure consists of a cylinder-cone portion which mates to the penetrator just behind the nose and a double truncated cone-cylinder portion which mates to the penetrator over the region 28 cm to 38 cm behind the nose. These portions will be made of aluminum, magnesium, or beryllium alloys.

Beryllium Plug

The plug is approximated as a cylinder 5 cm long x 5 cm diameter. The thermal conductivity is assumed to be 0.8 W/cm-K. The resistance to heat flow is

$$R = \frac{L}{kA} = 0.31 \text{ K/W} \tag{E-3}$$

Contact Cup

The contact cup is assumed to be a spherical segment with a 45-degree half-angle and a spherical radius of 3.4 cm. The assumed contact coefficient was 0.17 W/cm^2-K, which is at the low end of the range for metal to metal contact.[E2] The resistance to heat flow is

$$R = \frac{1}{hA} = 0.28 \text{ K/W} \tag{E-4}$$

Support Structure

The support structure provides two parallel paths to conduct the heat to the contact cup: a path through the nose/ballast region of the penetrator and the cylinder-cone member and a path through the double-truncated cone-cylinder member. The resistance for each path was calculated from

$$R = \int_S \frac{ds}{k A(s)} \tag{E-5}$$

where S is the path length and A(s) is the cross section at s.

If the members have approximately half of their cross-sectional area drilled out to minimize weight, the resistances for an aluminum alloy structure are

Cylinder-cone nose path - 4.5 K/W

Double-truncated cone-cylinder path - 3.1 K/W

Total resistance for the parallel paths is $\frac{4.5 \times 3.1}{4.5 + 3.1} \simeq 1.83$ K/W

If the structure is made from magnesium alloys or beryllium alloys (k $\sim$ 0.8 W/cm-K), the resistances are

Cylinder-cone-nose path - 4.9 K/W

Double-truncated cone-cylinder path - 5.4 K/W

Total resistance for the parallel paths is $\frac{4.9 \times 5.4}{4.9 + 5.4} \simeq 2.57$ K/W

Contact resistance between the penetrator and the support structure is neglected because of the large metal-to-metal contact areas.

The total resistance from the penetrator surface to the space radiator is

R = 0.28 + 0.31 + 1.83 = 2.42 K/W for an aluminum alloy structure

= 0.28 + 0.31 + 2.57 = 3.16 K/W for a magnesium alloy or beryllium alloy structure

Thus for a 20-W output from the RTG's, the temperature difference between the penetrator surface and the space radiator is in the range of 48K to 63K.

A combination of worst cases (i.e., asbestos battery support shell, maximum contact resistances, and magnesium or beryllium alloy support structure, would lead to a battery temperature of 260 + 78 = 338K, which is outside the allowable range. With reasonable care, the batteries can be kept in the range 273K to 333K, in that the above calculations neglect the heat loss path via radiation to the penetrator container can.

Entry - Exoatmospheric

During the exoatmospheric portion of the Martian entry phase, the thermal output of the RTG's must be dissipated to space through the reentry canister. The reentry canister is assumed to be a three-layer composite with a 0.025-cm rubber inner layer, an aluminum or beryllium center layer, and a 0.13-cm layer of Dow Corning - 325 ablative material. The canister is 28 cm in diameter and 380 cm long. The penetrator is assumed to be centered in the canister.

Steady-state calculations for the penetrator surface temperature were made to determine whether the temperature would remain in the allowable band. Starting temperature is assumed to be near 330K.

To determine the canister temperature, it is assumed that the canister continuously absorbs solar energy over an area equal to its projected area side-on. In that the canister will be spinning and its central layer is a high-conductivity metal, it is assumed that the solar heating is uniform over the surface and that the canister surfaces are at uniform temperatures.

The incident solar radiation at Mars is approximately 460 W/m.^{2} The projected area of the canister is 1.06 m.^{2} The DC-325 coating has a solar absorptivity of 0.31 and a room temperature emissivity at 294K of 0.9.^{E4} The total solar energy absorbed is

$$Q = 460 \text{ W/m}^2 \times 1.06 \text{ m}^2 \times 0.31$$

$$= 151 \text{ W}$$

The canister surface temperature is given by

$$T = \left(\frac{Q + 20}{\sigma \epsilon A} \right)^{1/4} \tag{E-6}$$

where

σ - Stefan-Boltzmann constant $5.67 \times 10^{-8} \dfrac{W}{m^2 K^4}$

ϵ - surface emissivity

A - cylindrical area = 3.35 m^2

For these parameters, T is ~180K.

To determine the penetrator temperature, the ΔT across the canister wall must be determined. This ΔT can be used with the outer skin temperature to define the inner wall temperature which will be used with the gray-body radiation heat transfer equation to calculate the penetrator surface temperature.

The temperature drop across the canister skin is calculated on the basis of zero temperature drop in the metal layer and zero contact resistance at the two interfaces. The thermal conductivity of the rubber is assumed to be 0.087 W/cm-K and that of the DC-325 ablative coating is 0.00015 W/cm-K.[E4] For both layers, the temperature difference is determined from

$$\Delta T = \frac{Q \Delta X}{kA} \qquad . \qquad (E-7)$$

For a 20 W(th) RTG and the above parameters for the canister skin, the ΔT across the canister skin is less than 1K.

The heat transfer across the gap between the penetrator shell and the canister is assumed to occur only by radiation. The heat transfer is defined as follows:[E1]

$$Q = \sigma A_1 \mathscr{F}_{1-2} (T_1^4 - T_2^4) \qquad , \qquad (E-8)$$

where

A_1 = the penetrator surface area

$\mathscr{F}_{1-2}$ = the gray-body shape factor

T_1, T_2 = temperatures of penetrator shell and inner surface of canister

The gray-body shape factor is assumed to be that for two concentric spheres.[E1]

$$\mathscr{F}_{1-2} = \frac{1}{\dfrac{\rho_1}{A_1 \epsilon_1} + \dfrac{1}{A_1} + \dfrac{\rho_2}{A_2 \epsilon_2}} \qquad (E-9)$$

where

$A_{1,2}$ = surface area, penetrator, $0.43 m^2$; canister, $3.35 m^2$

$\rho_{1,2}$ = reflectivity, 0.65, 0.1

$\epsilon_{1,2}$ = emissivity, 0.35, 0.9

For the above parameters,

$A_1 \mathscr{F}_{1-2}$ = $0.064 m^2$.

For a 20W(th) RTG and assuming the inner canister surface temperature to be 180K, the previous expression for the heat transfer across the gap can be solved to give T_1 = 284K.

Note that the penetrator temperature was higher than 284K during the Mars flight; thus, the penetrator shell temperature will approach the steady-state temperature of 284K from above.

Burial

The calculations for the burial phase are divided into two parts: an estimation of steady-state temperatures and estimates of the times required to reach steady state.

Steady-State Temperatures

The steady-state temperature was calculated from the thermal resistance factor for a finite cylinder in an infinite medium and from a newly developed set of equations for steady-state heat transfer in the prolate spheroidal coordinate system. For both cases, the soil conductivity was assumed to be 4.6×10^{-4} W/cm-K, which is in the middle of the recommended range,[E3] and the thermal resistance at the penetrator-soil interface was assumed to be zero.

The thermal resistance for a finite cylinder in an infinite medium is[E5]

$$R = \frac{1}{2\pi k \ell} \ell n \, (2\ell/d) \tag{E-10}$$

where

ℓ, d = cylinder length (152 cm), diameter (8.9 cm)

k = soil thermal conductivity

For the above parameters, the value of R is 8.04 K/W; thus, for a 20W(th) RTG, the temperature of the penetrator above the ambient soil temperature is

$$\Delta T = QR = 161K \quad .$$

The equation for steady-state heat flow in the prolate spheroidal coordinate can be shown to be

$$T(\xi_2) - T(\xi_1) = \frac{Q}{2\pi ka} \left[\coth^{-1}(\xi_2) - \coth^{-1}(\xi_1) \right] \tag{E-11}$$

where

a = interfocal distance

ξ = radial parameter

The surface area of the penetrator is well approximated by a prolate spheroid with a radial parameter value of 1.003 and an interfocal distance of 152 cm. If these values are used in the above equation and $\xi_1 \to \infty$ (i.e., $T_1 \to 0$, the undisturbed temperature), the temperature of the penetrator above the ambient soil temperature is $T(1.003) = 148K$.

The steady-state temperature results indicate that if the soil temperature is assumed to be 150K,[E3] the steady-state penetrator surface temperature will be between 300K and 310K and the batteries will be up to 15K hotter. This is within the acceptable range.

Transient Heating

To obtain estimates on the time required to reach steady-state conditions, two existing solutions of the heat diffusion equation were utilized. The effect of a penetrator arriving at a temperature higher than the ambient soil temperature was estimated by using a solution of the diffusion equation for a perfectly conducting sphere embedded in an infinite medium. The effect of the thermal output of the RTG's was estimated by using a solution for the temperature in an infinite region bounded internally by a sphere with a constant heat flux at the surface of the sphere.

The size of the sphere used for these calculations was such that the surface area of the sphere equaled that of the penetrator. For a penetrator which is 8.9 cm in diameter by 152 cm long, the equivalent surface area sphere has a radius of 18.4 cm.

The equation describing the decay of the temperature difference for a sphere with no internal heat generation is[E6]

$$T = T_o \left[\frac{R^3}{2K\pi^{1/2}(\alpha t)^{3/2}} + \frac{3R^4(2 + RH(2 - K))}{4HK^2\pi^{1/2}(\alpha t)^{5/2}} + \cdots \right] \text{ for } \frac{\alpha t}{R^2} > 1 \qquad \text{(E-12)}$$

where

T_o = initial temperature difference

R = sphere radius, 18.4 cm

α = soil thermal diffusivity, 5.8×10^{-4} cm^2/s

t = time

$K = 3 \times \left[\dfrac{\text{(density * specific heat) soil}}{\text{(density * specific heat) sphere}} \right]$

$H = \left[\dfrac{\text{thermal contact resistance at sphere soil interface}}{\text{thermal conductivity of the soil}} \right]$

The sphere was assumed to have a density-specific heat product which is one-sixth that of a solid sphere; this value is based on the product for the penetrator being one-half that of an equivalent size solid-steel cylinder, and the volume of the sphere is approximately three times that of the cylinder. The value of K is 3.75. The value of the contact resistance at the sphere-soil interface was chosen so that the value of H is 200; this will give results close to those for perfect contact. The thermophysical properties of the soil taken in the middle of their recommended ranges[E3] are

Density specific heat product = 0.8 J/cm^3 K

Thermal conductivity $\approx$ 4.6 x 10^{-4} W/cm K

When these parameters are used in the above equation, the calculation shows that the temperature difference will have dropped to less than 5 percent of the initial difference within 10 days. This calculation will be mentioned again later in regard to the penetrator configuration proposed for the planetary heat-flow experiment.

The equation describing the temperature increase resulting from the thermal output of the RTG's is[E6]

$$T = \Delta T_{\substack{Steady \\ State}} \left[1 - \exp\left(\frac{\alpha t}{R^2}\right) \; \text{erfc} \; \left(\sqrt{\frac{\alpha t}{R^2}}\right) \right] \qquad . \qquad \text{(E-13)}$$

When the parameters listed earlier are used, evaluation of the above equation shows that approximately 50 percent of the steady-state temperature increase will be obtained in 4.5 days and approximately 80 percent within 50 days.

On the basis of the steady-state calculations and the above transient calculations, the battery temperature will possibly fall 10K to 15K below the recommended range in the period 5 to 15 days after emplacement. After that period, it will again be in the operational range.

Penetrator Heat-Flow Experiment: Preliminary Analysis

The previous calculations have dealt with penetrators which have internal batteries and RTG's. A second type of penetrator is that for the Mars heat-flow experiment; this penetrator would have the batteries and a radioisotopic heat source in the penetrator afterbody which remains at the surface. The heat source would probably be in the range of 1 to 3 watts.

Preliminary calculations indicate that the batteries could be maintained in the allowable temperature range by radiation cooling if the afterbody can temperature is in the range 150K to 260K; this covers the expected range of surface temperatures.[E3]

Determination of the planetary heat flow requires that the temperature difference over a known distance and the thermal conductivity of the soil be measured. Two possible methods for obtaining the temperature gradient are (1) making temperature measurement at the extreme ends of the penetrator body or (2) making the measurement with sensors spread over the length of the umbilical cable.

If the temperature is measured on the penetrator, preliminary calculations for a prolate spheroid buried in an infinite' medium with a linear temperature gradient indicate that the tempera-ture gradient in the penetrator will be 10 to 15 percent of that in the soil far from the penetrator.[E6] To measure the temperature on the umbilical would require near thermal equilibrium between the cable and the walls of the penetrator bore hole.

In the previous section on transient heat transfer during burial, it was indicated that the penetrator would have cooled off to within 5 percent of the initial temperature difference between the soil and the penetrator within 10 days. It should be within 1 percent after 30 days. By moni-toring the temperature history (cool down), an estimate of the soil thermal conductivity can be made. Monitoring the cooldown will allow determination of when measurements can begin for the temperature gradient.

REFERENCES

E1. F. Kreith, Principles of Heat Transfer, International Textbook Co., 1963, pp. 26, 204, 206.

E2. M. L. Mingles, Thermal Contact Resistance - Vol. I, Air Force Materials Laboratory, Wright-Patterson AFB, Ohio, AMFL-TR-65-375.

E3. R. E. Hutton, Mars Surface Models, Final Report, TRW Systems, Contract No. NAS8-29605, May 1974.

E4. Information About Aerospace Materials, Dow-Corning Corp., Bulletin 61-051b, October 1973.

E5. H. Gröber, S. Erk, and R. Grigull, Fundamentals of Heat Transfer, McGraw-Hill Book Co., 1961, p. 120.

E6. H. S. Carslaw, and J. C. Jaeger, Conduction of Heat in Solids, 2nd Ed., Oxford University Press, 1959, pp 248, 350, 427.

APPENDIX F

SCIENCE INSTRUMENTS

Introduction

Because the limitations of survivability or of operation of the science are a principal factor
in deciding on penetrator characteristics, the key parameters for the baseline instruments, such as
deceleration levels, temperatures, inclination to local vertical, and radiation sensitivity, are dis-
cussed in detail to vindicate the choices made for penetrator impact velocities and attitudes and size
and placement of RTG power supplies. A secondary function of the appendix is to present a discus-
sion in lesser detail of instruments which have been proposed or used on other space missions for
science objectives identified in the main body of this report as having unique advantages when em-
placed subsurface but which are of questionable compatibility with some aspect of the penetrator
environment.

Baseline instruments such as the high frequency accelerometer and thermocouples for moni-
toring the internal temperatures of the battery stack, etc., are not discussed because there is no
reason to believe they will affect the penetrator design.

α-Particle - Geochemistry

In this section, an adaptation to the Mars penetrator of an α-particle geochemistry experiment
used successfully on the 1967-68 Surveyor missions and in a preprototype evaluation for the Mars
Viking mission is described. The modifications include a substantial reduction in size and weight
and a closer spacing of the α-sources-sample-detectors to minimize the effects of the Martian
atmosphere. The limitations of this instrument in doing such surface geochemistry, both as to
elemental analysis, $Z \leq 12$, and accuracies, are summarized from actual test data. Related en-
vironmental test results, showing that the instrument can be expected to survive both the required
sterilization dry-heat cycles and the impact deceleration on Mars, are presented. Finally, it is
shown that the induced environment--radiation from the RTG power supplies and exhaust heat from
the electronics and nuclear capsules--will not interfere with the measurements.

The experiment is based on two types of interactions of α particles with matter: (1) elastic
scattering by nuclei, in which an α detector is used, and (2) (α, p) nuclear reactions with light ele-
ments, where a proton detector is used. A door must be opened in the hull of the penetrator for
this experiment.

Figure F-1 shows the expected layout of a detector assembly without showing details for the door mechanism. Recent penetrator drop tests have shown that the slapback forces resulting from the void closing on the penetrator as the vehicle comes to rest are negligible; therefore, no difficulty is expected in providing and opening doors in the hull.
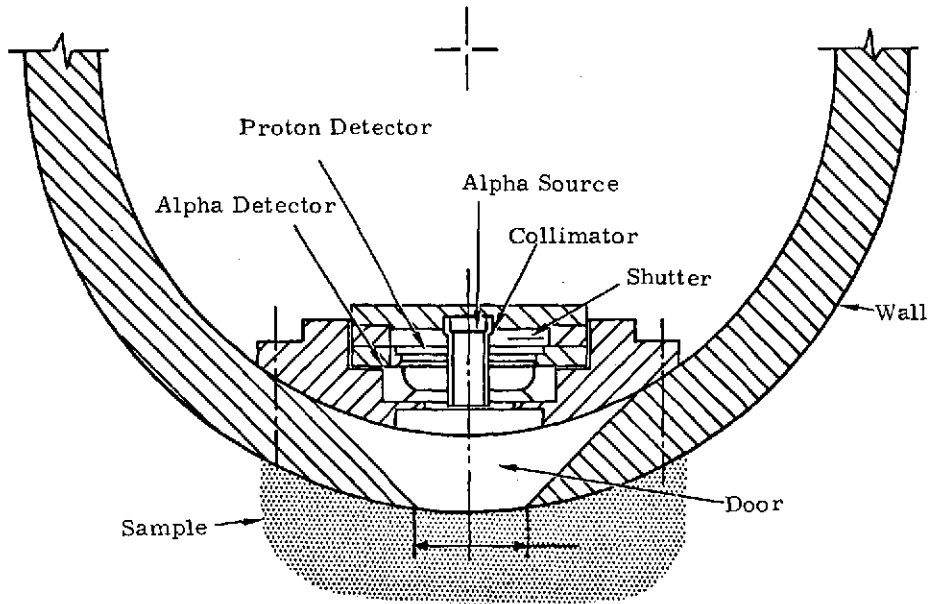

Figure F-1. Micro-Alpha Detector Assembly

Figure F-2 is a functional block diagram of the electronics required for the α-particle experiment. Much of this is in redundant usage by other experiments and is not dedicated to this experiment.
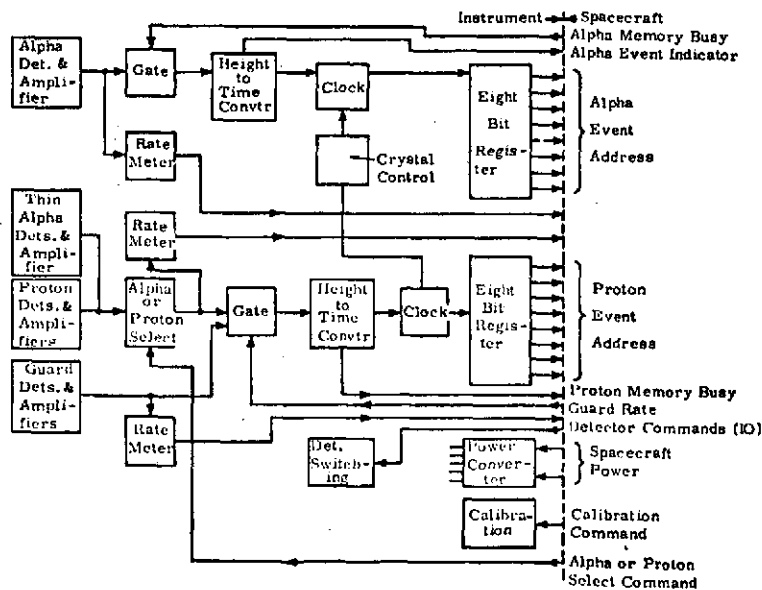

Figure F-2. Block Diagram of Electronics for α-Particle Instrument

Table F-I summarizes the capabilities of the instrument for elemental analysis as determined from laboratory studies for the preprototype Viking mission and the Surveyor mission. Figure F-3 shows the detailed comparisons of the analyses of returned lunar samples with the on-site Surveyor measurements.

Four stages of operation are expected for the α-particle experiment on Mars. In the first stage, the background in the Martian environment will be measured with the shutter over the sources closed. This background is expected to result from solar and cosmic ray particles and secondaries produced by them in the Martian atmosphere and in the instrument. Next, with the source shutter open, the α and proton spectra resulting from α particle interaction with the Martian atmosphere will be measured. From these data, some indication of the density and the composition of the Martian atmosphere will be available.

In the third stage, a sample of known composition will be examined under the same conditions that will prevail in the analysis of the Martian sample. This analysis will provide assurance that the instrument is capable of correct chemical analysis under conditions that may not be completely foreseeable.

Finally, in the last stage, a Martian sample will be analyzed.

Throughout all these stages, periodical calibrations of the instrument will be made with an electronic pulser, so that the gain of the system is known at all times.

TABLE F-I

90-Percent Confidence Limits on Weight Percent Analyses

Martin Marietta Experiment Laboratory Studies[*] (1973)		Alpha Scattering on Surveyor Missions[**] (1967-1968)	
		C	(+0.3)[***]
		O	+0.9
(H+Li+..+O+F±Na)	+2.8	F	+0.08
		Na	+0.2
Mg	+2.8	Mg	+1.7
Al	+2.8	Al	+0.5
Si	+2.1	Si	+1.6
K	+0.7	(K + Ca)	+1.3
Ca	+0.6		
Ti	+0.2	"Ti"	+1.2
Fe	+0.7	"Fe"	+1.2

[*]B. C. Clark and A. K. Baird, Earth and Planetary Science Letters 19, 359 (1973). Their quoted numbers at the 75-percent confidence level have been converted to 90-percent confidence limits by multiplying by 1.4. The data of Toulmin et al. (Icarus 20, 153-176 (1973)), based on analyses of four samples, do not lead to significantly lower estimates of 90-percent confidence limits for the analysis of an unknown sample.

[**]Average 90-percent confidence errors for each element from results on six samples on three Surveyor lunar missions (Turkevich, Accounts of Chemical Research 6, 81-89 (1973)).

[***]Carbon was not found on the Surveyor missions. Later work (J.G.R. 78, 781 (1973)) has indicated that carbon can be determined with the indicated accuracy even in the presence of a simulated Martian atmosphere.

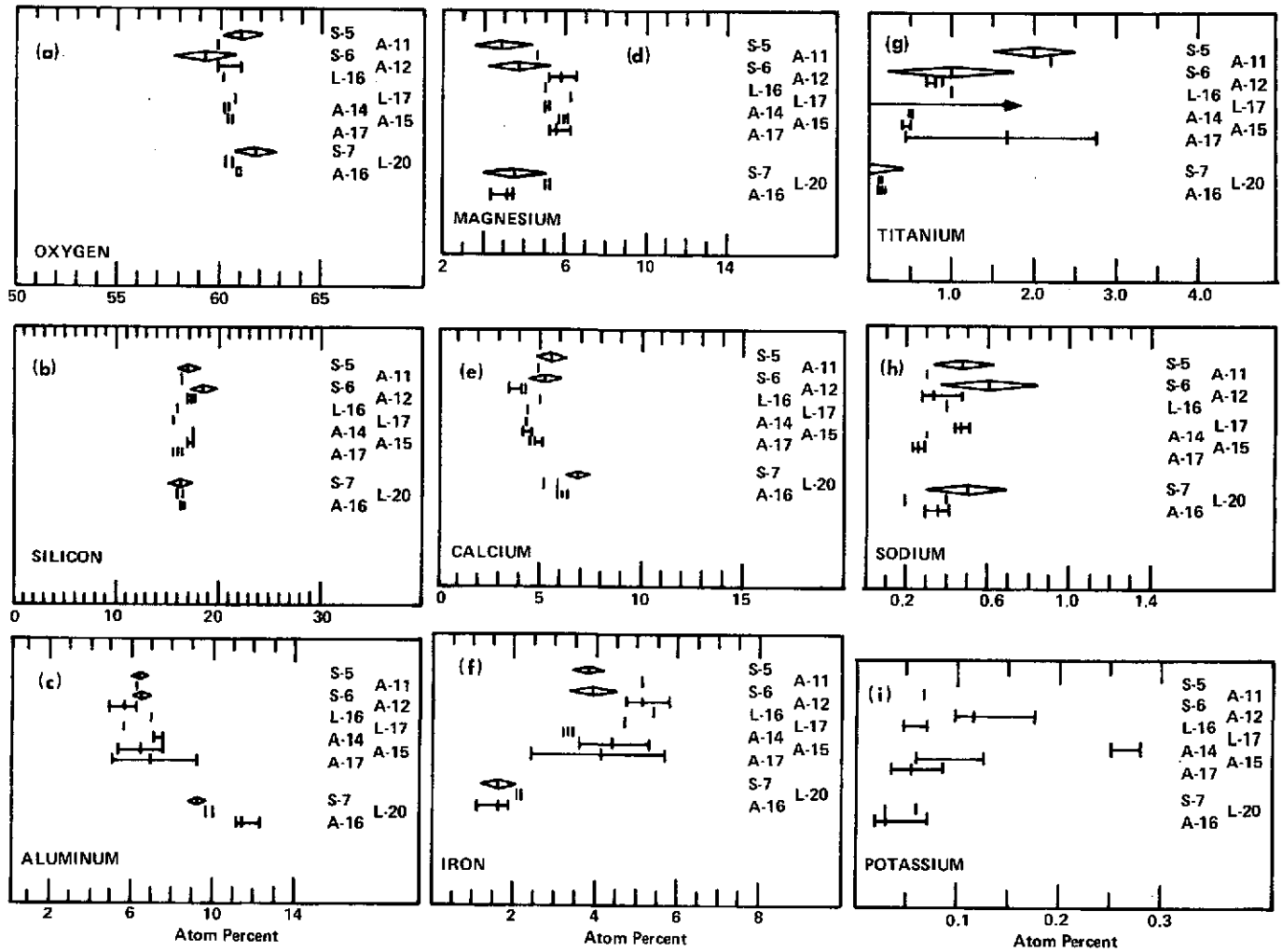S Indicates Surveyor, A Indicates Apollo, L Indicates Lunik

Figure F-3. Lunar Sample Analyses Results Compared With Surveyor Measurements

It is planned to store the spectra from the α-particle instrument in two 256-channel by 12-bit memories. The stored data will be transmitted to the orbiter once each day for transmission at an appropriate time to earth. The total α-particle experiment data requirement is about 3×10^4 bits for a mission involving the analysis of one sample.

This sequence of events and typical times required for their execution is shown in Table F-II.

TABLE F-II

Nominal Experiment Sequence

1.	Turn instrument on.	
2.	Accumulate background data.	10 minutes
3.	Perform pulser calibration.	2 minutes
4.	Open shutter in front of source.	
5.	Make standard sample and local atmosphere measurements.	60 minutes
6.	Open the wall door.	
7.	Make sample measurement.	300 minutes
8.	Perform pulser calibration.	2 minutes
9.	Turn instrument off.	
	Total time for a Standard Sequence	375 minutes

In order to compensate for uncertainties in sample placement, atmospheric density, and composition or aging of the ^{242}Cm source (since not all penetrators need be deployed simultaneously), these events need to be commanded from the orbiter as the experiment is conducted.

In order to provide information about more than one sample of Martian soil, as well as to provide redundancy in case of detector failure, three separate alpha-backscatter detector assemblies are included in the penetrator. These three assemblies are dispersed 120 degrees apart around the penetrator body, as far apart as possible longitudinally.

One of the obvious questions concerning the α-particle experiment is whether the $\approx 10^5$ neutrons/sec flux from the 20-watt radioisotope heat source, Appendix D, will interfere with the measurements. The ^{242}Cm α source emits 10^3 neutrons/sec at a distance of only 1 cm from the sample, so that if the RTG heat capsule were positioned 10 cm away from the sample the neutron flux would be the same from each source. Neither presents a problem, however, because $\approx 10^9$ neutrons/cm^2/sec can be tolerated at the sample before a degradation of the data is observed.

The Martian atmosphere has been proven not to interfere with the operation of the α instrument. Table F-III summarizes the results of several such experiments in which analyses were made of representative geological samples in a 5 mm of Hg CO_2 simulated Martian atmosphere.

The dry-heat sterilization cycles to satisfy the planetary quarantine requirements are especially severe for most science instruments. In the α-particle instrument, the most sensitive components are the solid-state particle detectors and the thin films used to prevent the spread of radioactivity from the sources.

Summary of Results on Analysis of Nine Rocks in 5 mm CO_2 Atmosphere

Mass Range	Symbol	Average Bias	Scatter
12	C	-0.09	0.22
16	O	+0.15	0.46
19	F	+0.03	0.05
23	Na	+0.15	0.46
24-26	Mg	-0.17	0.55
27	Al	+0.28	0.34
28-34	Si	-0.11	0.90
35-44	"Ca"	+0.24	0.46
45-51	"Ti"	+0.01	0.15
52-69	"Fe"	-0.30	0.23
70-∞	"Ba"	+0.009	0.010

. The above data are in atom percent.

In the case of the solid-state detectors, existing data on the detectors used for proton registration and on the thin absorber detectors indicate that these detectors can survive the sterilization condition with no appreciable deterioration in their characteristics. Figure F-4 shows that changes are caused in a thin Ortec detector by a severe 143°C 20-hour sterilization test; however, these changes are insignificant. Additional work is still required to increase confidence in the detector's performance after the heat sterilization treatment.

The thin films used on the Surveyor missions (VYNS-Al_2O_3) do not survive high temperatures reliably. An apparently satisfactory replacement has been found in a parylene film made by the Union Carbide Company. Several films of this type have been tested at temperatures of $> 150°$ C, and no deterioration of their mechanical properties has been observed. The effect of radiation after the heating remains to be determined, and tests are under way to estimate critical parameters of radiation damage. However, in that the shutter between the radioactive sources and the films will protect these films during the long transit period to Mars, the accumulated radiation doses during actual measurements on Mars are not expected to be significant.

Shock tests have been performed on three Surveyor-type detector assemblies (proton and guard) at 500, 930, and 1860 Earth g's to determine whether this instrument is compatible with penetrator application. All detectors survived the shock test physically and no degradation in resolution was observed.

It is believed that the solid-state detectors of this type can survive much higher decelerations, but actual tests will have to be performed to determine the upper limits. The present tested limit is compatible with the Mars penetrator landing environment.

The detectors tested were somewhat larger than the ones planned for the Martian mission.

Example of some data on shock test at 1860 g's

Proton Detector No. Li-493 }
Guard Detector No. Li-457 } in Surveyor assembly

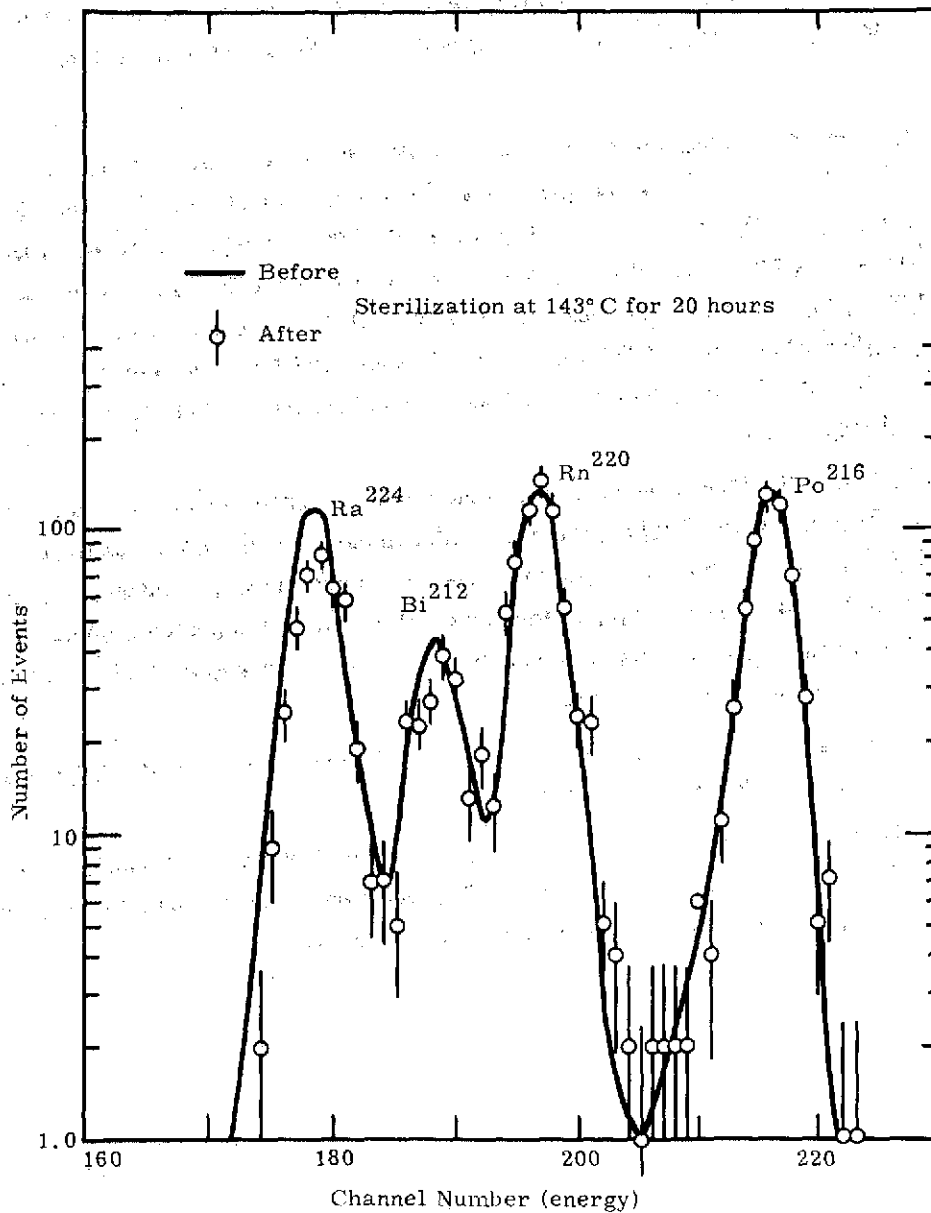|	Before Test	After Test
Applied bias	15 V	15 V
Leakage current	0.80 μA	0.43 μA
Charge collection	99.7 %	100.0 %
Noise at low energy	None	None
Resolution	No change in resolution	

Figure F-4. Sterlization Test of a Thin Ortec Detector

Seismic Instrument

The instrument described in this section is an adaptation of a three-axis seismometer designed by D. Anderson and F. Lehner for use in the Viking mission. The primary constraints have been the physical dimensions of the penetrator, the landing shock environment, the onboard data storage, and/or the limited capacity of the data link with the orbiter.

In recognition of these constraints, a three-axis seismic system which makes possible the coverage of 17 "interesting" seismic events per Martian day (this compares with a capacity for 20 such events with twice the time coverage planned for Viking) is proposed. This system employs threshold signal detection, limited time coverage for a particular seismic event, and a data compression scheme based on Anderson's[F1] recommendation for the Viking Lander system.

Seismometers

The vehicle diameter of 7.6 cm constrains the size of the seismic spring-mass system and its attendant natural period. The instrument proposed by F. Lehner of Cal Tech for the Viking Lander could be adapted to fit into this diameter; however, the "boom"-type seismometer employs relatively fragile flexures as springs and would require substantial caging system design to survive impact. The horizontal instruments appear particularly vulnerable in this respect. The Viking instrument, which was designed with a 0.22-second natural period and a 10,000-ohm coil, gives usable output below 1 Hz. It will also operate with the instrument axis displaced from vertical (or horizontal) by as much as 15 degrees.

Adaptation of more conventional geophone instruments or a modification of the Lunar Ranger seismometer also appears possible. Again, the question of impact survival is of paramount importance, and considerable design and testing effort to assure operation after impact would be required. It is not clear what angle off vertical (or horizontal) could be tolerated by instruments of this type. The 4.5-Hz Geo Space or Mandrel instruments could be adapted to the size of the penetrator--not considering caging mechanisms.

Figure F5 illustrates how the Viking instruments could be contained in the 3-inch penetrator. Figure F6 is a similar sketch for 4.5-Hz geophones.

The constant-amplitude response versus frequency of the 10,000-ohm Viking seismometer and two commercial geophones is shown in Figure F7. If a geophone is employed for this mission, its number of turns should be increased to give a higher output signal.
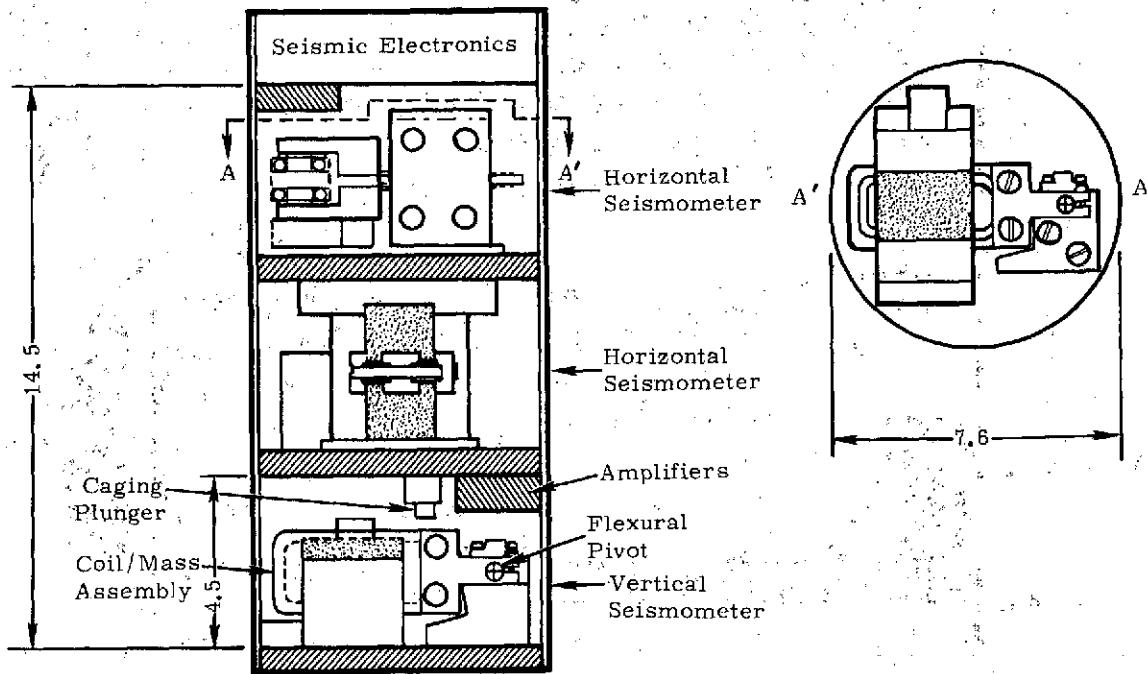
Note: Caging plunger mounted over center of percussion.

Figure F-5. Viking Triaxial Seismometer Mounted in Penetrator
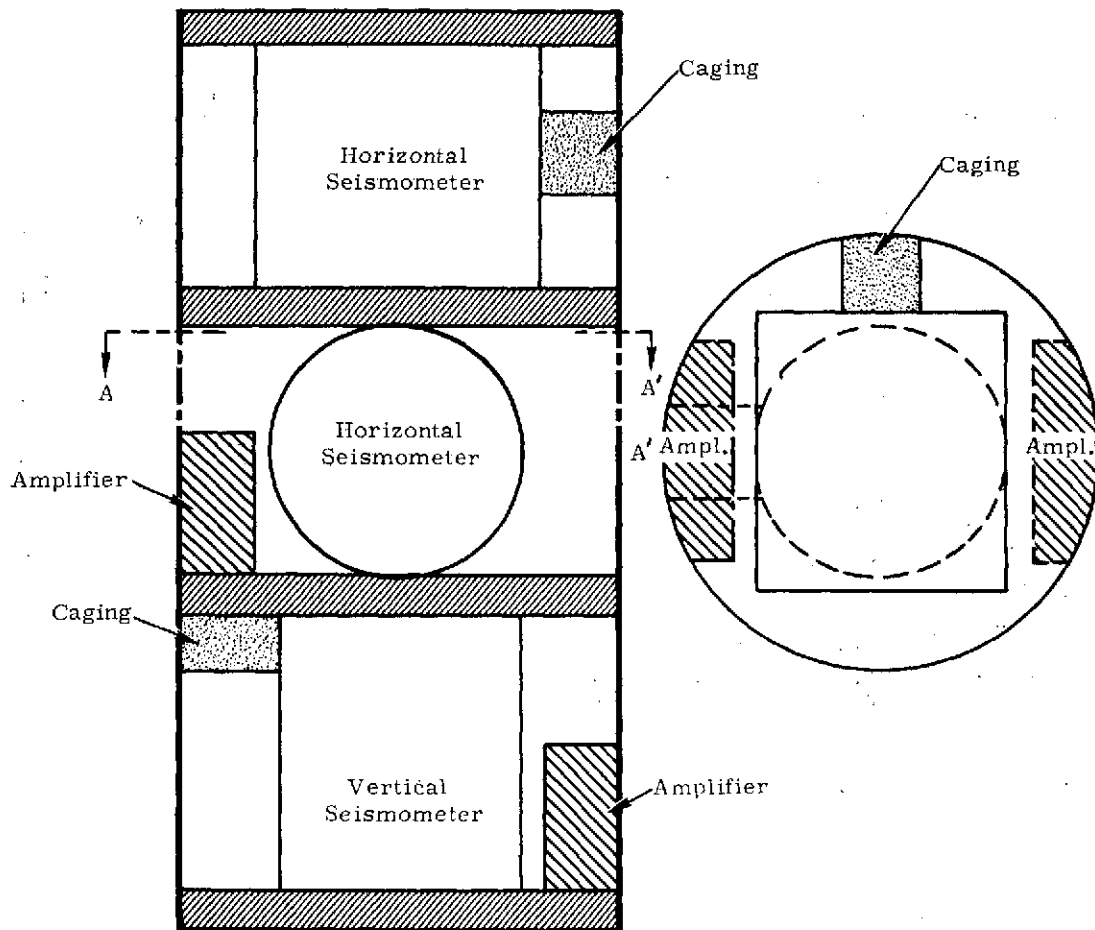
Figure F-6. Triaxial Seismometer Section with 4.5-Hz Geophones - Mars Penetrator

The chart shows "Output (volts)" on the vertical axis versus "Frequency (Hz)" on the horizontal axis.

Constant-Displacement
Response for 3
instruments.

$(50 \times 10^{-9}$ m p-p)

1. Cal. Tech. 4.5 Hz
    Viking Seismometer
    $(10,000 \; \Omega, \; 0.5 \; \text{cr.})$

2. Mandrel EVS-8
    4.5 Hz Detector
    $(800 \; \Omega, \; 0.6 \; \text{cr.})$

3. Geo Space HS-1
    4.5 Hz Geophone
    $(215 \; \Omega, \; 0.52 \; \text{cr.})$

Figure 7. Comparative Sensitivities of the Viking Seismometer
and Two Commercial Geophones with the Same
Resonant Frequency

Seismic Data Compression System

The size of the penetrator determines the amount of primary power available for data processing and data transmission. The Mars orbiter is not in a synchronous orbit in view of the penetrator impact area. In order to accumulate statistics on Mars seismic activity, a system which monitors the seismometers continuously and stores the data for transmission to the orbiter once per 24-hour period is envisioned. Ideally, one would sample the data at least 20 times per second on each of the three axes with 16- or 17-bit resolution, time-tag the data to within 1/10 second, store the data, and retransmit the data at a very high data rate when the orbiter is in view. However, it is expected that only 300 milliwatts of continuous power will be available. Furthermore, the data storage capacity (in keeping with memory size constraints) will average 37,000 bits per transmission. Because of capabilities, a system similar to the Viking "moderate data rate" system is proposed.

The seismic data (Figure F-8) are amplified and low-pass filtered to a 10-Hz upper limit. The filtered signals are then sent to an envelope detector/filter, an axis-crossing detector, and to an event detector.

The envelope detector full-wave rectifies the seismic signal and passes it through a 0.5-Hz low-pass filter to the commutator and A/D converter where the envelope amplitude is sampled once per second and converted to an 8-bit digital signal.

The axis-crossing detector detects positive-going axis crossings above the second bit level of the A/D system and forwards a pulse to a 4-bit counter which is reset once per second. At the time of an A/D conversion of the e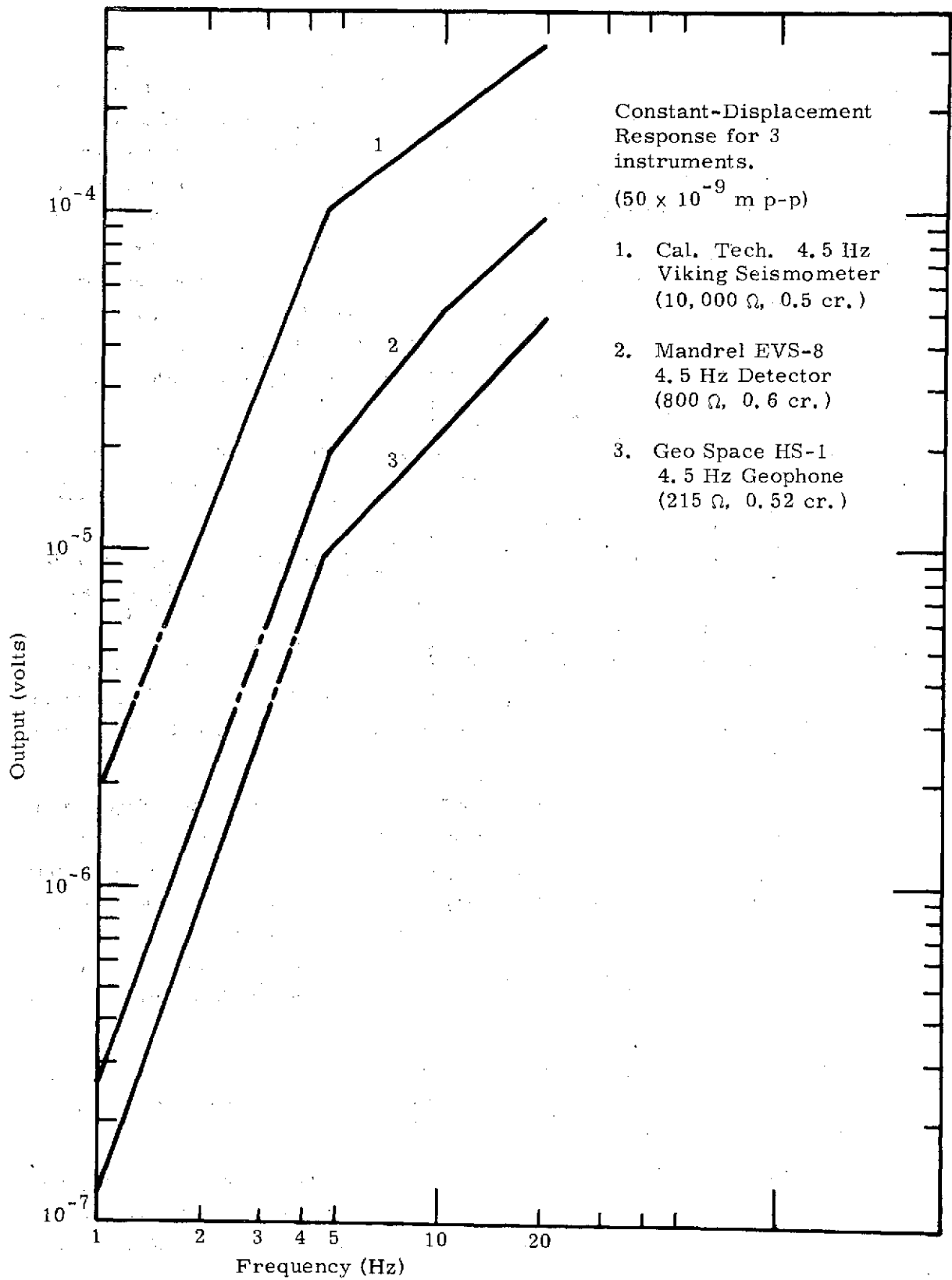nvelope signal, the corresponding 4 bits of axis-crossing information are assembled and forwarded to the data sequencer.

The event detector, which keeps a running average of the seismic background, triggers when the seismic signal exceeds the background by a preselected factor. When triggered, the event detector initiates a sampling sequence which reads out the amplitude and axis-crossing information of the three channels at least twice at a 1-sample-per-second rate. If the "event" is no longer above threshold, the sampling is shut off after 2 seconds. If the signal persists above threshold, the sequence is continued for a predetermined time, such as 60 or 64 seconds, after which the system returns to standby for a fixed interval of time. At the beginning of each sequence, a timing word is stored to indicate when the trigger was received.

With the above scheme, at least 17 1-minute seismic events could be stored during each 24-hour period. Tradeoffs between number of events and event length could also be made to employ the fixed data storage to the best advantage.

To reconstruct the received seismic data, the amplitude samples would be passed (computationally) through inverse filters; then, the resultant would be convolved with signals of the period indicated by the axis-crossing detector output to give an approximate reconstruction of the seismic event.
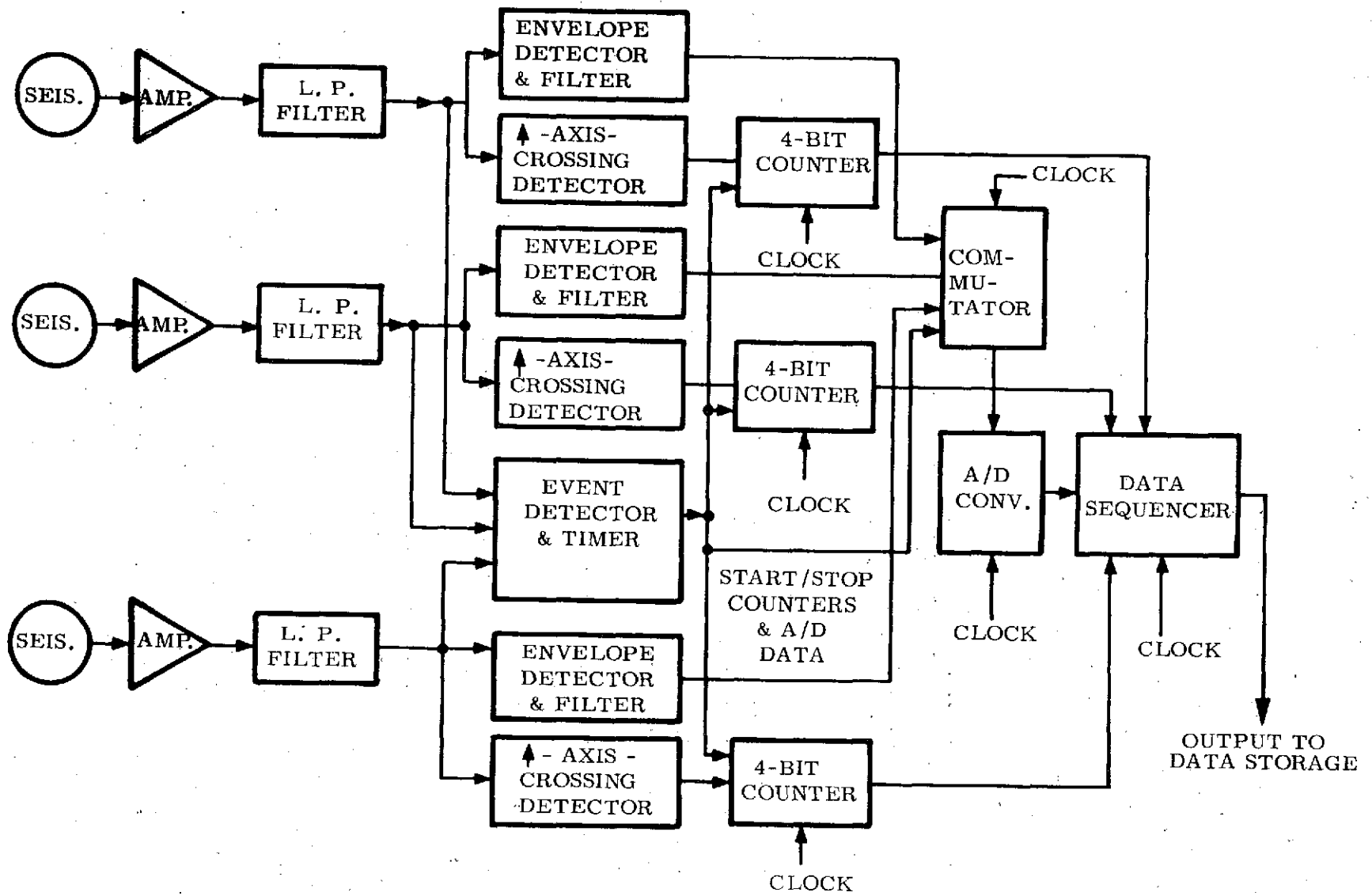
Figure F-8. 3-Axis Seismometer and Data Compression System Block Diagram

Thermal Conductivity (Temperature)

As a part of the lunar heat flow experiment developed for the Apollo ALSEP program,[F2] thermal conductivity had to be measured. The method used was to measure the soil temperature as a function of time when a precisely known electrical heater source was switched on. The same technique is applicable to a penetrator, although provision must be made for bringing the sensor into intimate contact with the Martian soil surrounding the vehicle. The lunar instrument used platinum resistance thermometers which have the advantage of an extremely wide range of temperature operation and millidegree resolutions but the disadvantage of being essentially a strain gage and hence sensitive to mechanical shock. Basically the lunar instrument consisted of a 4-active-arm resistance bridge with two pairs of platinum resistor elements (gradient sensors) separated by approximately 50 cm as shown in Figure F-9.
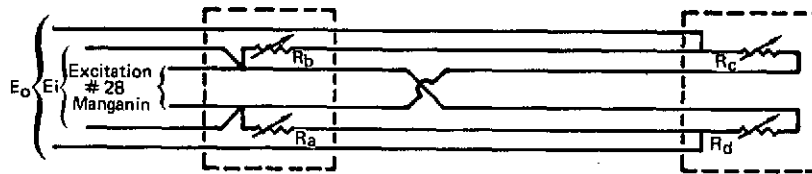
Figure F-9. Lunar Four-Active-Arm Resistance Bridge

and another pair of similar, less precise sensors (ring sensors) separated by 28.7 cm located symmetrically between the first pair of sensors.

An electrical heater wound over each gradient sensor is used for measuring the thermal conductivity of the lunar soil. For low conductivity values (below ~0.05 $W_m^{-1}K^{-1}$), the heater is energized with 2-mW power, and the temperature rise of the gradient sensor under the heater is measured relative to the other (unheated) sensor. If the conductivity is greater than this, an alternate method employing the pair of ring sensors is used. These are connected in the same sort of bridge as the gradient sensors. The heater power is increased to 0.5 W, and the temperature versus time relation of one ring sensor (located 9.4 cm from the heater) relative to the other ring sensor (located 38 cm from the heater) provides a measurement of the thermal conductivity.

There is also the possibility of monitoring the temperature rise of the soil/penetrator as a function of time for a period of weeks and of using the precisely known heat output of the radio-isotope heat capsule in the RTG's to compute the thermal conductivity of the surrounding material; Equation (E-13) provides a basis for these computations. This measurement could be used only if the penetrator were fully buried in a homogeneous material whose thermal conductivity remained constant through the time of the experiment. Significant sublimation of CO_2 frost, phase change of water in melting permafrost, etc., could completely obscure the thermal conductivity, although other independent measurements would indicate whether these conditions had been satisfied.

The measurement techniques, which depend only on temperature measurements, are hence not restricted to platinum resistance thermometers. Three other temperature sensors might also be used for these measurements: solid-state sensors, thermistors, and thermocouples.

The sensitivity of a commercial solid-state (extrinsic silicon resistance) sensor which is representative of this class of device characteristics is about 0.7%/°C (Reference F3). A sensor of this type generally deviates from the computed characteristics at higher temperatures. The material becomes intrinsic and the resistance varies with the total number of carriers. This results in a resistance somewhat below that predicted. This effect serves to linearize the silicon resistance sensor. A monitor circuit similar to that used with platinum resistance sensors can be used with the silicon resistance sensor; however, the required amplifier gain will be much lower.

Thermistors have the advantage of having high sensitivity, which implies narrow temperature range; low thermal mass, which makes fast measurements possible; and high shock insensitivity. This latter property is the result of thermistors being constructed by sintering mixtures of various metallic oxides to form a hard material which resembles ceramic. Because they are formed by sintering, thermistors can be made in almost any size or shape. In the past, thermistors have earned a reputation for being relatively unstable devices; aging of the exposed sintered material caused large resitance shifts. However, hermetic sealing of the element and restricting the maximum temperature to which the thermistor is exposed seems to have alleviated most of the problem. Commercial oceanographic thermistors are now available with annual drifts of less than 0.05°C and long-term accuracies of 0.1°C, which is just adequate to make them adaptable to thermal conductivity measurements.

The thermocouple is another type of temperature sensor which has been used in space applications. For example, in the lunar heat flow experiment, the downhole probe had a chromel wire in the cable with constantan leads attached at several points to provide a rough indication of thermal diffusitivity and the time variation of upper surface soil temperature. Ordinarily, thermocouples are best suited to high-temperature measurements, although by choosing materials of widely different thermoelectric potential (Table F-IV), low-temperature couples are possible.

TABLE F-IV

Thermoelectric Series

100°C	
Antimony	Palladium
Chromel[*]	Cobalt
Iron	Alumel[*]
Nichrome	Nickel
Copper	Constantan (Adams)
Silver	
$Pt_{90}Rh_{10}$	Copel[*]
Platinum	Bismuth

[*]Registered Trademarks of Hoskins Mfg. Co.

Thermocouples are subject to a gradual drift (aging) over a long period of time. Also, slight impurities can cause gross sensitivity changes. These considerations generally limit noble metal thermocouple accuracy to $\pm .1°C$.

For higher precision measurements, resistance thermometers, which are very sensitive to shock, must be used. However, several temperature sensors offer long-term accuracies of $\leq 0.1°C$ combined with shock insensitivity.

Water Measurements

The best quantitative instrument for water vapor measurements is an adaptation of a commercial phosphoric acid detector (Ref. F4). Phosphorous pentoxide is a highly hygroscopic material. If a gas sample containing water vapor is passed over a ceramic bed laden with P_2O_5, phosphoric acid is formed which is electrically conducting. In a known geometry, i.e., for a specific detector, this change in conductivity could probably be interpreted directly as water in the sample; however, it is possible to electrolyze the phosphoric acid to evolve hydrogen and oxygen and regenerate the anhydrous oxide. The integrated electrolysis current is proportional to the amount of water present in the hygroscopic bed. To use this concept for a remote soil water measurement, "... a 0.1 milliliter sample of surface material which has been screened to less than 400 microns is introduced into a small metal cup. A lid with a small vent hole is sealed to the cup which is then inserted into one of a pair of thermally matched ovens. An oven shroud cover is sealed over the oven and a flow of purge gas established. The ovens are heated at a constant rate of temperature rise and the difference in heater power required by the control oven and the sample oven is measured. This power difference is equivalent to the energy of phase changes occurring in the sample. It is desired to begin the temperature ramp from as low a temperature as possible in order to define the state of any water present. A temperature of -10°C is considered desirable in order to be able to measure the melting of any ice present in the sample."

The purge gas is passed through the detector cell, and the water content is measured as described above.

The difficulties of adopting this technique to the penetrator are primarily twofold: a sample, seived, must be gathered, although it need be only a very small quantity of material and the gas chemistry/oven system must be miniaturized and adapted to the vehicle. Both problems appear to be solvable with a development program.

Another soil water measurement technique would use an aluminum oxide hygrometer element. Sandia Laboratories pioneered* the development of these hygrometer elements (References F5 through F9). Basically, the aluminum oxide humidity element consists of a base of

---

*USAEC Patent No. 3075385 by Sandia Corporation, dated January 29, 1963 (inventor, C. M. Stover).

aluminum, an oxide made by anodizing the base material, and an evaporated coating of metal (normally gold) (Figure F-10). The base metal acts as one electrode, and the evaporated metal as the other, or outer electrode. A change in relative humidity causes an impedance change (resistive and capacitive) between the electrodes, and the resulting complex impedance is measured by balancing the element in an AC (Wein) bridge circuit.
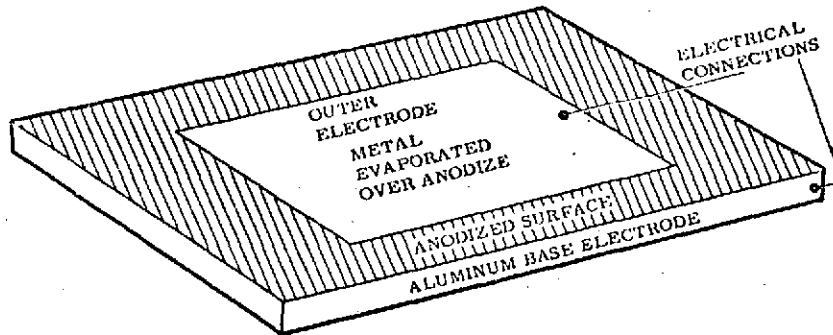

Figure F-10. Aluminum Oxide Hygrometer Element

The sensors are affected by temperature, they fail to distinguish between ammonia or various amines and water vapor, and they age in a manner dependent on the humidity of the environment in which they are stored. The first of these difficulties is met by mating a very low thermal mass thermistor with the hygrometer element so that the temperature at which the measurement is made will be known. The second is not anticipated to be a problem on Mars. Laboratory tests in a low-pressure carbonic acid environment have indicated that it is the partial pressure of water vapor which is measured. The last problem would be avoided by sealing the element in a vial of low-humidity gas. Sealed in this way, elements have survived the high-temperature sterilization environment specified by NASA. The probe must be kept in a known humidity gas during the temperature cycling to preserve the presterilization calibration. In the penetrator, the sensors would be kept in this stable environment during preflight, launch, and interplanetary flight to insure their calibration on arrival at Mars. One of the prime advantages of the element is its small size. Outer electrodes have been made with an active surface area as small as 0.004 square inch. These small outer electrodes have been deposited on aluminum foil as thin as 0.0005 inch. The anodized layer (the oxide) is less than 0.000075 inch thick. An average sized production element on 0.003-inch foil is 3/16 inch wide by 5/8 inch long and contains a 1/16-inch by 3/8-inch outer electrode. This element weighs about 12 milligrams. This small mass results in an extremely small alteration in the humidity and temperature of the environment being measured and at the same time allows a rapid response.

Elements have been successfully calibrated over the temperature range -80°F to +135°F which represents the limits of Sandia's humidity testing apparatus. The temperature-cycled response of one temperature-cycled element is shown in Figure F-11.
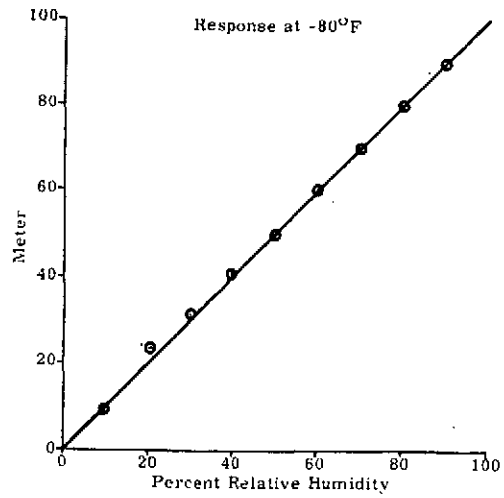
Figure F-11.   Aluminum Oxide Hygrometer Response

In conclusion, the aluminum oxide hygrometer element is a simple low-mass sensor which at worst will give a yes/no indication of the presence of water over a range of temperatures and relative humidities (10-100% RH at -84°F) and at best could give some quantitative measurements of water vapor content of the gas in the void formed by the penetrator flight.

References

F1. Final Report: Development of Performance Criteria and Functional Specifications for a Passive Seismic Experiment on Mars, California Institute of Technology, December 1969.

F2. Instrument Society of America, Pittsburgh, Pa., Temperature Its Measurement and Control in Science and Industry, "Unique Platinum Resistance Temperature Sensors for Lunar Heat Flow Measurements," by Lowell Kleven and Lyle Lofgren, Vol. IV, 1972.

F3. Instrument Society of America, Pittsburgh, Pa., Temperature Its Measurement and Control in Science and Industry, "Comparison of Temperature Sensors for Space Instrumentation," by Earl E. Swartlander, Jr., Vol. IV, 1972.

F4. Exploration of Mars After 1976, Draft Document, April 1974.

F5. C. M. Stover, "Aluminum Oxide Humidity Element for Radiosonde Weather Measuring Use," Review of Scientific Instruments, Vol. 34, 1963, pp. 632-635.

F6. C. M. Stover, New Aluminum Oxide Humidity Element, Sandia Laboratories, Albuquerque, New Mexico, SC-4667 (RR) 1962.

F7. C. M. Stover, Humidity Indicator, Sandia Laboratories, Albuquerque, New Mexico, SCTM-123-61(72), November 1961.

F8. C. M. Stover, AMT-4 Radiosonde Transmitter Modification Assembly, Sandia Laboratories, Albuquerque, New Mexico, SCTM 151-61(72), September 1961.

F9. C. M. Stover, Preliminary Report - New Aluminum Oxide Humidity Element, Sandia Laboratories, Albuquerque, New Mexico, SCTM 222A-60(52), July 1960.

APPENDIX G

MARS MODEL

Introduction

This appendix collects summaries of present knowledge about key Mars parameters that are vital to the material in other appendices or in the body of this report. Thus, the reader can satisfy himself that the values selected throughout the report are reasonable; and, furthermore, he can appreciate how uncertainties concerning these parameters affect the design and/or analysis.

A good example of the function which this appendix serves can be seen in Appendix E: Thermal Management. Once the penetrator is buried on Mars, the only mechanism available for the dispersion of the 20 thermal watts exhaust from the RTG power supplies is conduction into the surrounding Martian soil. The specific rate at which this occurs (thermal conductivity, k) determines the equilibrium temperature of the penetrator. If k is very small, i.e., the soil a good insulator, the penetrator temperatures will become so high that the electronics, science, and power supply will fail; on the other hand, if k is too large, the penetrator will become so cold that the main chemical power supply cannot deliver the rated power for the transmitter or indeed may fail altogether if the temperature is sufficiently low. Obviously, the estimation of k is vital to the systems analysis. Unfortunately, k can only be inferred by indirect measurements made from orbit; therefore, a discussion of the various values which have been estimated and of the arguments as to their validity is included in this appendix to support the choice of $k = 4.6 \times 10^{-4}$ W/cm-K as the most likely value and also to indicate the range of estimates which have been inferred by different investigation from the data.

The same usage is intended for each parameter group summarized here: winds, topography, soil models, temperatures (surface and subsurface), and bulk thermal.

Atmosphere (Density)

The model for the Martian atmosphere used in entry calculations was adopted from the Mars Engineering Model.[G1] The atmosphere for the near-Mars environment (300 km to 35,000 km) has been taken from Section II-A of the above document (pages II-1 and II-2). The model for the lower atmosphere (-10 km to 300 km) was taken from Table III-A-3 of the above document, the mean equatorial model. This model was chosen because the Viking office at NASA Langley regards it as the best mean model and also because it is in closest agreement with the results from the single Russian lander which successfully telemetered aeronomy data during descent.

The model for the winds in the Martian atmosphere was also taken from the Mars Engineering Model. Consideration was given to various factors in this model, among them transient surface winds (dust devils), vertical variations of wind velocity, gusts in the free stream (wind shear), and surface gusts. Discussions of these factors can be found in pages III-A-13 through III-A-16 in the referenced document. The most important factor taken from the model, however, is the one of steady winds (the general circulation) which is discussed in Pages III-A-8 through III-A-11 of the Mars Engineering Model. A summary of the expected wind velocities in the northern and southern hemispheres is found in Figures III-A-4 and III-A-5, reproduced here as Figures G-1 and G-2. The following discussion of surface winds is extracted from Reference G2. References, which are to the bibliography of that document, have not been repeated because the concern is with the summary discussion as reported by Hutton.

"Theoretical wind velocity estimates are generally made based on observations of cloud movements. Blumsack (Ref. 57) developed a theoretical model to study steady winds as influenced by large-scale topography and the associated large-scale atmospheric circulation caused by thermal and dynamic effects. He quotes other investigators who indicate the average velocity of clouds to be in the range 8 to 45 m/s. In Reference 58, Gifford (1964) presents results from a study of yellow cloud motions along with a discussion of Bagnold's theory (Ref. 59) governing wind induced sand motion. Gifford estimates the average drift velocity of the yellow clouds to be about 8 m/s which he concludes has associated winds having velocities large enough to initiate soil particle movement. He concludes that the yellow clouds are most likely composed of wind-driven sand grains moving by saltation within a few meters of the Martian surface, accompanied by an overlying dust cloud of much smaller particles, extending to many thousands of meters.

"Steady wind velocity estimates presented in Reference 62 indicate the maximum steady wind velocity above the boundary layer is 70 m/s and that the maximum steady wind within the boundary layer about 1 m above the surface is 40 m/s. These velocities are a little lower than the earlier values recommended in Reference 63 which indicated maximum velocities in the range 100 to 145 m/s. These estimates were deduced from theoretical computations made by Leovy and Mintz. Reference 62 recommends surface gusts should be assumed to have a 3σ value equal to one-half the maximum free stream velocity, i.e., 35 m/s. The reference further recommends that combined steady wind and gusts should not be considered to exceed 70 m/s."
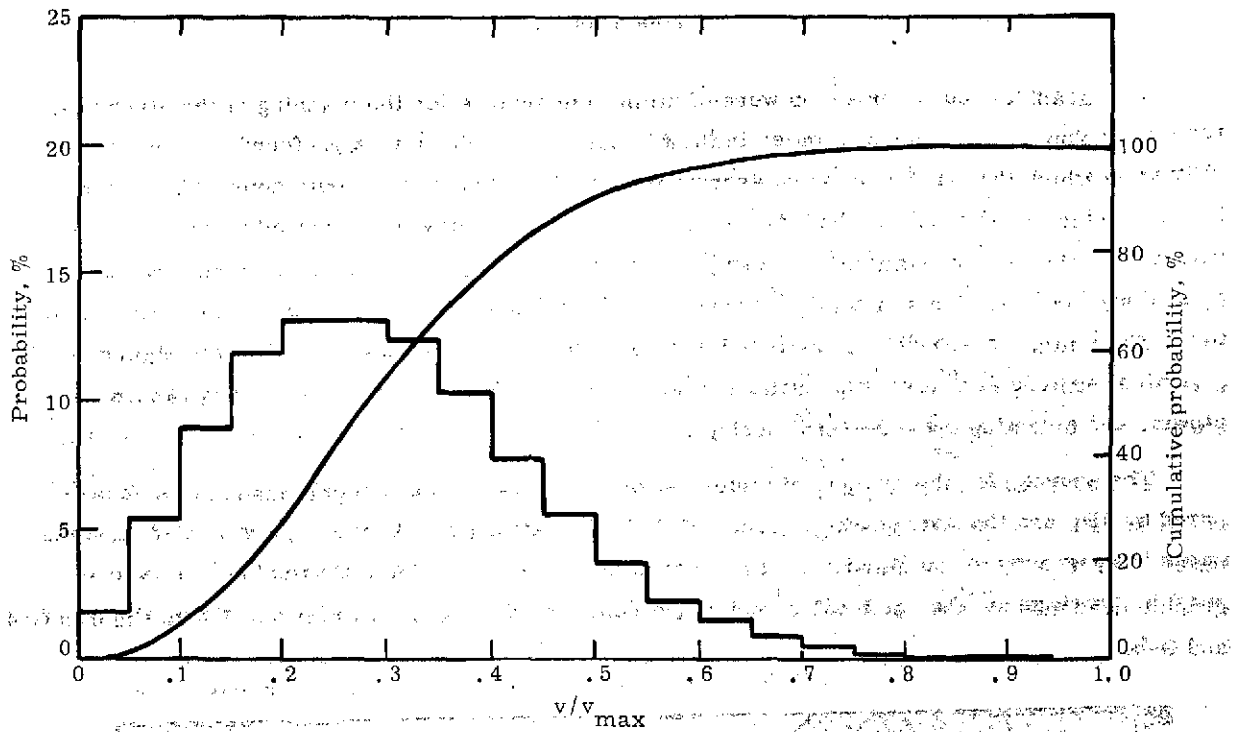
Figure G-1. Probability Distribution of Near-Surface Wind Speed on Mars Between 10°N and 42°S Latitude Near the Summer Solstice in the Northern Hemisphere. For source of data, see text. v_{max} is specified to be 70 meters per second.
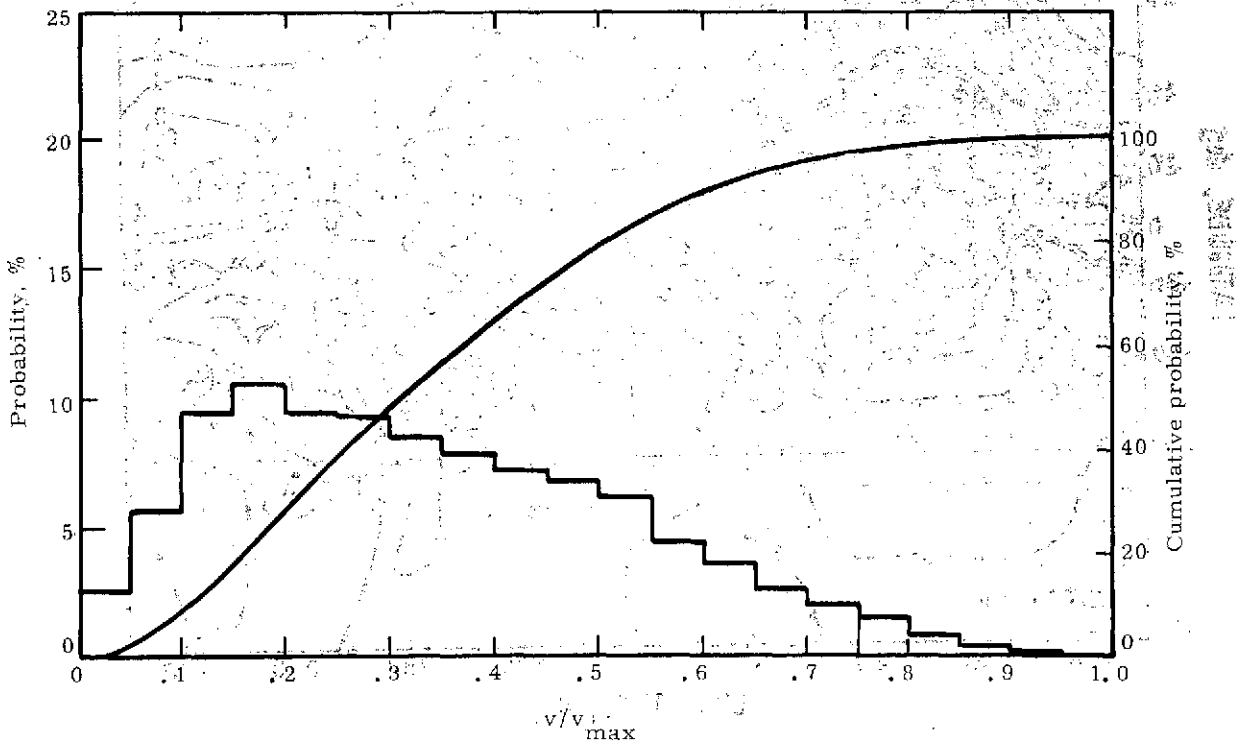
Figure G-2. Probability Distribution of Near-Surface Wind Speed on Mars Between 42°N and 10°N Latitude Near the Summer Solstice in the Northern Hemisphere. For source of data, see text. v_{max} is specified to be 40 meters per second.

Topographical considerations were of utmost importance for the planning of the Mars pene-
trator mission, because uncertainties in the Martian topography have a profound influence on the
altitude at which the penetrator must assume an attitude and be at a velocity appropriate for pene-
tration. This means that the whole problem of atmospheric entry is influenced by the topographic
predictions and the uncertainties in those predictions. Clearly, the penetrator must have assumed
an attitude for penetration (a nearly vertical attitude) at an altitude above the highest terrain fea-
tures which might reasonably be expected to be encountered. This necessity for the attainment of
a vertical attitude at a fairly high altitude also has clear implications on the method chosen for
slowing and orienting the penetrator during reentry.

The sources for the topographic information were interim topographic maps of Mars pre-
pared by JPL and the Astrogeology branch of USGS for latitudes ≤ 80°N or S, Figure G-3, and the
paper "Topography of the Martian Polar Layered Deposits[G3] for Polar Estimates." Two topo-
graphic drawings for the south polar region are reproduced here from Reference G3 as Figures G-4
and G-5.

Figure G-3. Global Topographic Map (interim map prepared by JPL based on combined
Radar, Occultation and Iris data referred to the 6.1 mb areoid)

Figure G-4. Low-Resolution Topography of the Martian South Polar Region Layered Terrain)

Figure G-5.   High-Resolution Topography of the South Polar Region
(Blank area in Figure G-4)

Soil Models - Penetrability

Information about soil models was taken from two sources--the Mars Engineering Model and Mars Surface Models. The soil models considered in the former reference (pp. III-C-31 through III-C-39) used the lunar surface as a no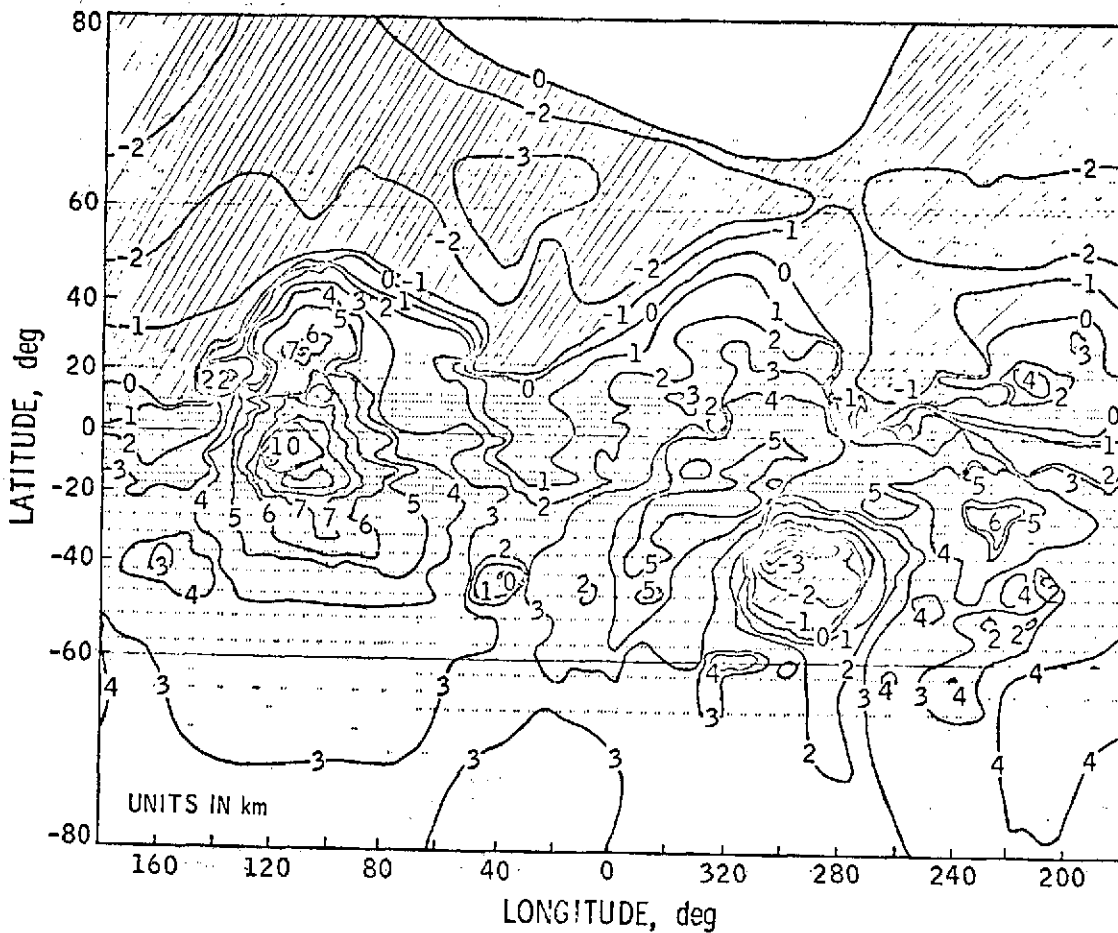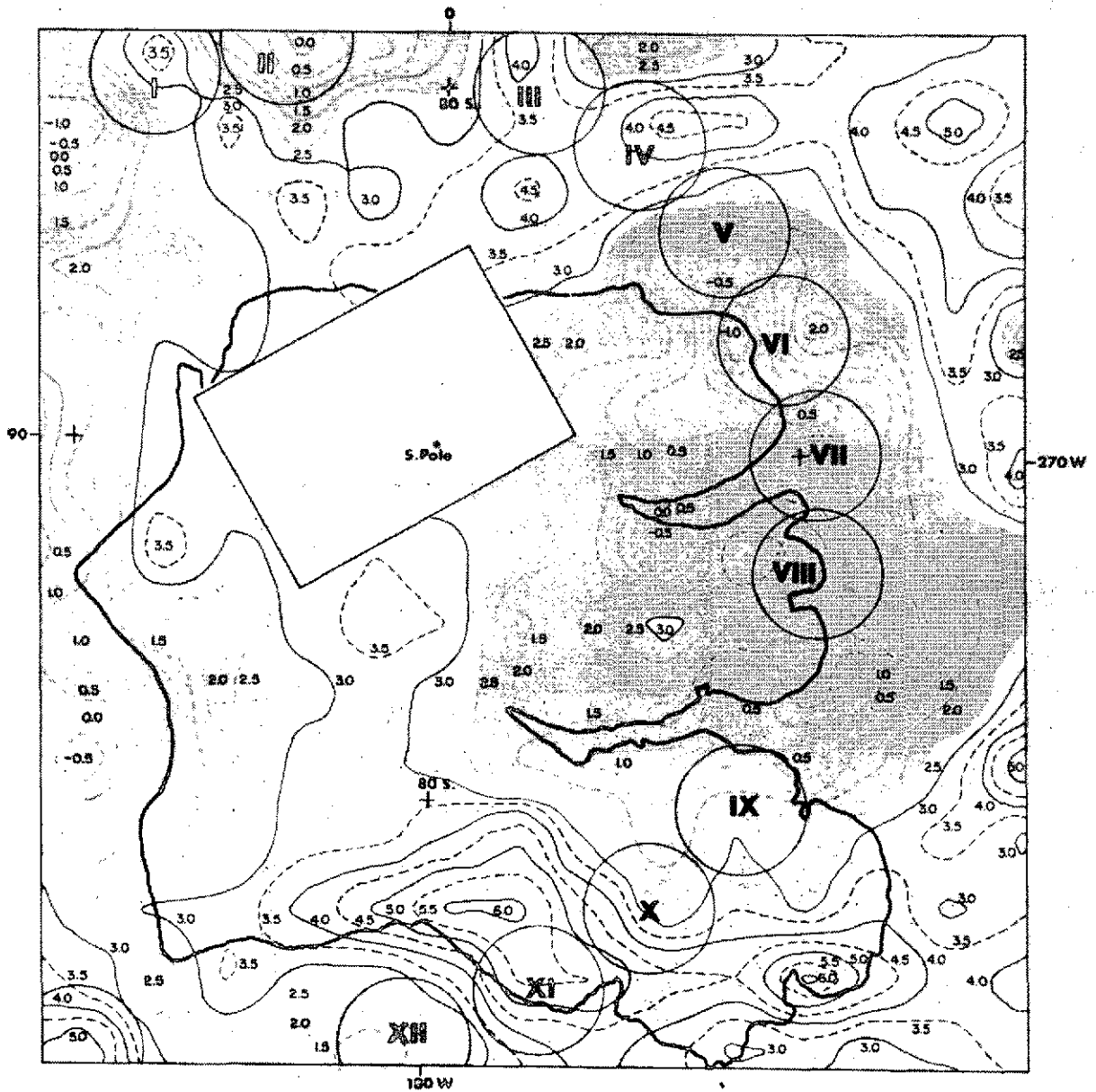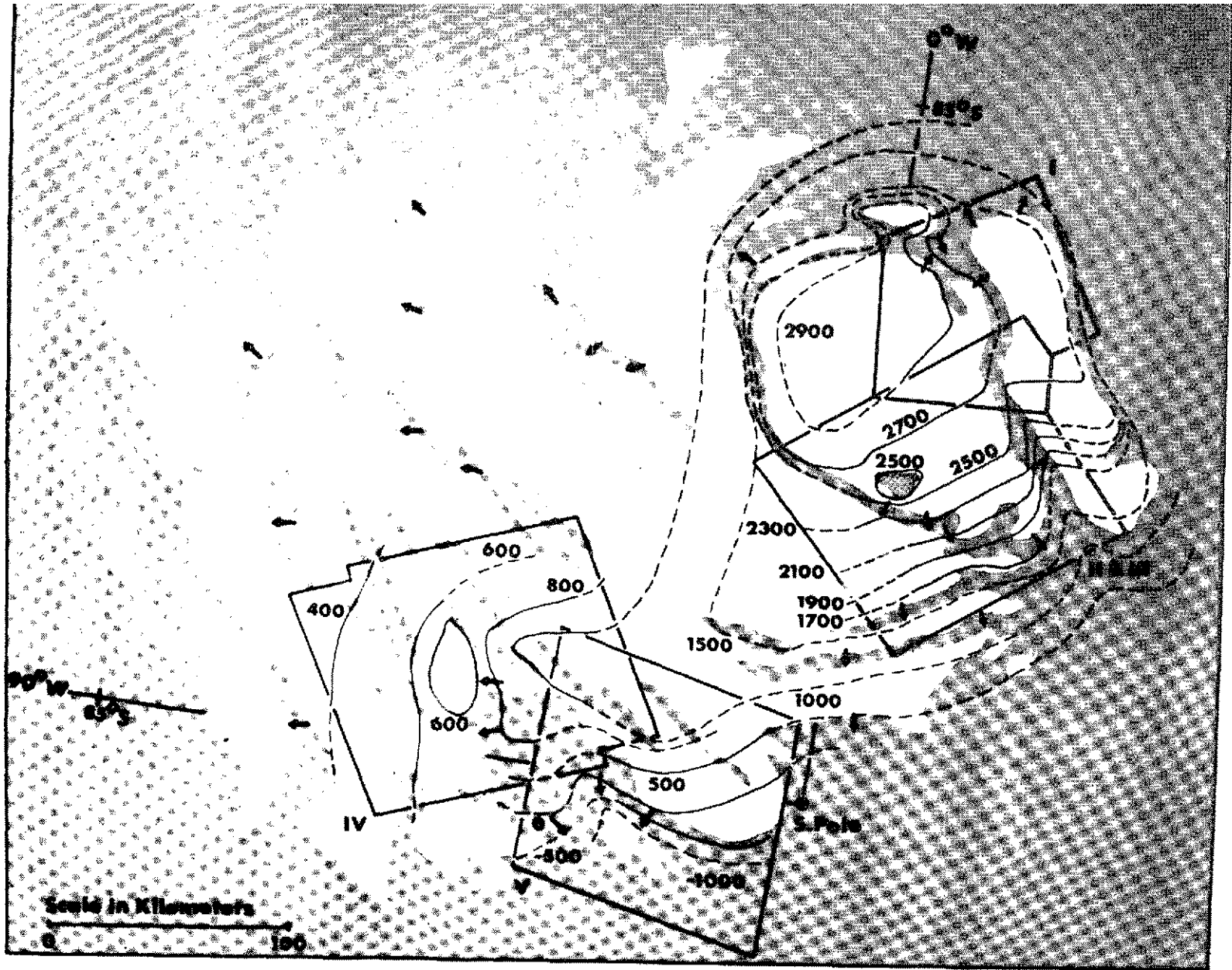minal representation of the Martian surface. In addition, four other likely component materials for the Martian surface, including rocks, lag gravel, dune sand, loess, and combinations of those materials, were considered. The important results are summarized in Table III-C-2 (Reference G2), included here as Table G-I.

The latter reference considered the same constituent materials for the Martian surface as did the former reference, adding also (pp. 59 and 60) that "The near-surface materials of Mars can be considered to be basaltic in composition with 60 ± 10 percent SiO_2, except where there are extensive deposits of carbon dioxide. Reflectivity data have been interpreted to conclude the surface contains varying amounts of limonite, hematite, geothite, montmorillonite, and other impurities, as a result of chemical weathering and oxidation of the basalt."

The latter reference also gives the penetration resistance of the lunar nominal soil as from about 1 to 6 $N/cm^2/cm$.

A summary table is also included from the latter reference as Table G-II.

Surface and Subsurface Temperatures

An extensive discussion of methods for estimating the Martian surface temperature is reproduced in Mars Surface Models (pp. 28 through 33). Graphical summaries of these estimates are given in Figures G-6 and G-7, as well as an estimate for equatorial subsurface temperature reproduced as Figure G-8.

Thermal Conductivity

A discussion of possible thermal conductivities of the Martian surface appears in Mars Surface Models (pp. 34, 35, 64). Because of the extreme importance of the thermal conductivity to the viability of the Mars penetrator mission, the discussion is reproduced here in its entirety.

"Reference 98 presents results from thermal conductivity measurements made on 37- to 62-μm-diameter basalt powders in lunar and Martian simulated environments. The samples were tested at packing densities ranging from 0.79 to 1.50 g/cm^3 in simulated Martian atmospheres; CO_2 at 7 mb pressure and temperatures ranging from about 200 to 300 K were used in the tests. The thermal conductivity was found to be essentially independent of packing density and temperature. Evidently, the interstitial CO_2 tends to negate the effects of temperature and density. The thermal conductivity measurements in the Martian environment ranged from about 0.23×10^{-4} to 0.29×10^{-4} cal/cm sec K. In the simulated lunar vacuum and temperature regime, the thermal conductivity

TABLE G-I

Martian Soil Models

	Lunar (nominal)	Lag Gravel	Dune Sand	Loess	Rock
Grain size 100% Distribution 75% 50% 25% 0	$1\,\mu$ (63) $15\,\mu$ $40\,\mu$ $300\,\mu$	$1,0\times\mu$ (64) $1,000\mu$ $20,\times0\mu$ $1,860\mu$ $150\,(00\mu$ $4,120\mu$ $530,(00\mu$ $16,000\mu$ large large	$50\,\mu$ (67) $50\,\mu$ (66) $150\,\mu$ $400\,\mu$ $190\,\mu$ $500\,\mu$ $230\,\mu$ $600\,\mu$ $1000\,\mu$ $1600\,\mu$	$3\,\mu$ (70) $1\,\mu$ $20\,\mu$ $9\,\mu$ $37\,\mu$ $20\,\mu$ $60\,\mu$ $30\,\mu$ $1000\,\mu$ $149\,\mu$	Rock Surface
Bulk Density (ρ) g/cm^3	$1.35-1.8$ (63) 1.5 (60)	$1.4-1.7$	$1.4-1.7$	(70) $1.0-1.6$	$2.7-3.2$ 3.0
Porosity %	48 ± 8	49 ± 5	49 ± 5	56 ± 10	very low $3\pm$
Cohesion dynes/cm^2	10^3-10^4 (29) $3.5\times10^3-7\times10^3$ (60)	0	$0-10^3$	$0-10^6$ (70)	10^8 to 5×10^8
Angle of internal friction	$30-40$ (29) $35-37$ (60)	35 ± 5	35 ± 5	(70) 33 ± 8	45 ± 5
Permeability cm^2	$10^{-7}-10^{-8}$ (62)	$10^{-5}-10^{-1}$ (62)	$10^{-3}-10^{-6}$ (62)	$10^{-6}-10^{-8}$ (62)	$<10^{-10}$
Thermal inertia $(k\rho c)^{-1/2}$ cgs units	500 to 800 (74) (in lunar vacuum)	100	165 (42)	220 (42)	50
Dielectric con- stant cgs	3.0 (2, 18, 46 & 47) $2.5-3.8$	3.5 Mars Av. (12) (18) $3-4$	3.5 Mars Av. (2) (18) $3-4$	3.5 Mars Av. (2) (18) $2.3-4$	$8-9$ (18 & 46)
Pore pressures	probably impor- tant when $\rho=1.0$, c is small, and near surface	unimportant	unimportant	probably impor- tant when $\rho=1.0$, cohesion is small, and near surface	unimportant
Composition	(60 & 63) Basaltic	(73) Basaltic	(73) Basaltic	(73) Basaltic	(73) Basaltic

Reference numbers in parentheses.

TABLE G-II

Soil Parameters

PARAMETER	SOIL MODEL				
	Nominal	Loess	Dune Sand	Lag Gravel	Rock
Bulk Density, ρ (g/cm^3)	1.35 to 1.8	0.7 to 1.6	1.4 to 1.7	1.4 to 1.7	2.7 to 3.2
Porosity (percent)	48 ± 8	56 ± 10	49 ± 5	49 ± 5	0 to 3
Cohesion (N/cm^2)	0.003 to 0.21	0 to 10	0 to 0.01	0	1000 to 5000
Angle of Internal Friction (deg)	35 to 45	25 to 41	30 to 40	30 to 40	40 to 50
Permeability (cm^2)	10^{-8} to 10^{-7}	10^{-8} to 10^{-6}	10^{-6} to 10^{-3}	10^{-3} to 10^{-1}	10^{-10}
Thermal Inertia, I (10^{-3} cal/cm^2 s$^{1/2}$ K	1.2 to 2.0	4.5	6.0	10	20
Dielectric Constant	2.5 to 3.8	2.3 to 4	3 to 4	3 to 4	8 to 9

Figure G-6. Annual Variation of Minimum Global Surface Temperature in Degrees K (from Kieffer for I = 0.0065 cal/cm^2 s$^{1/2}$ K, A_{bol} = 0.25, ϵ = 1.00)
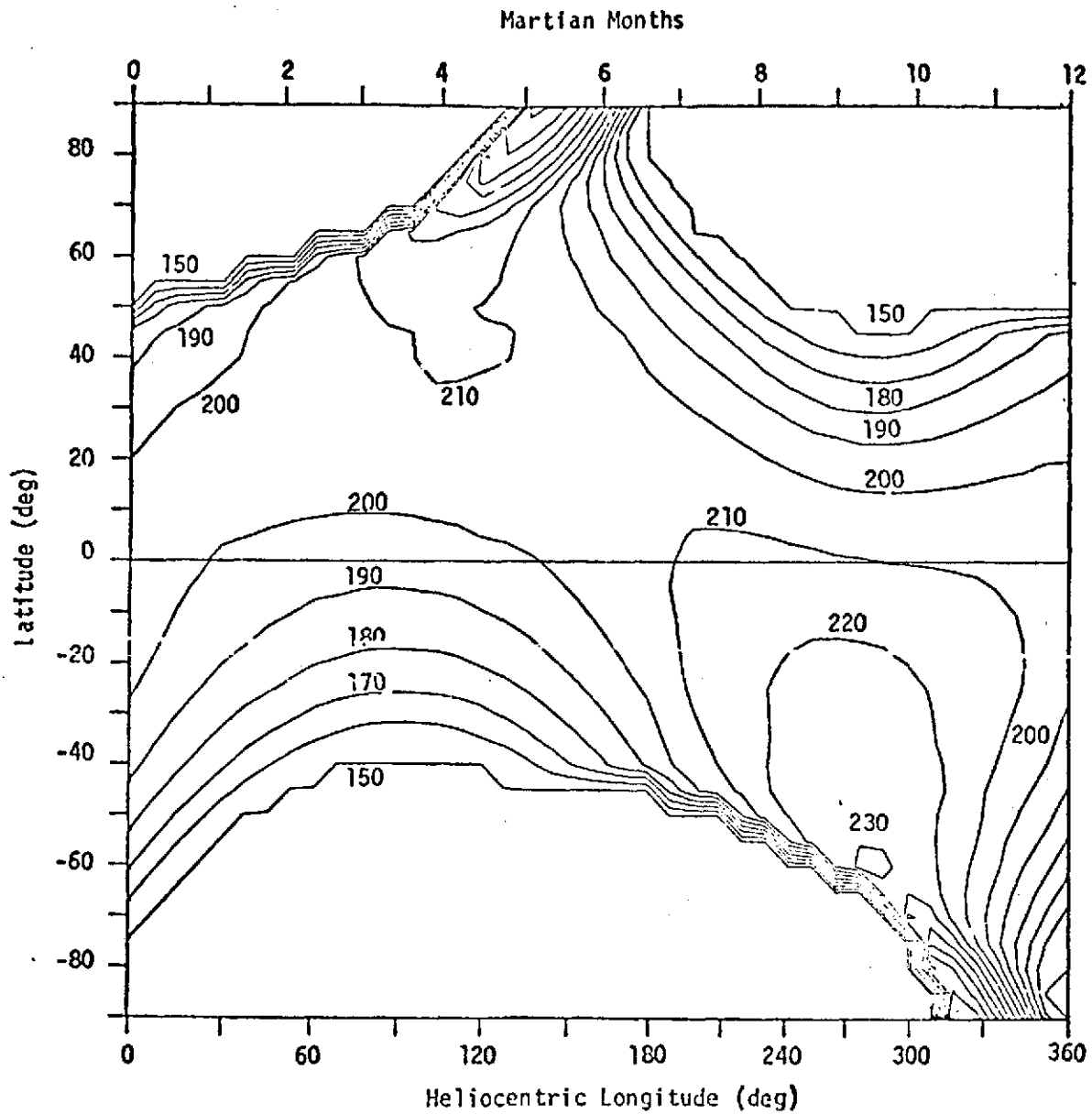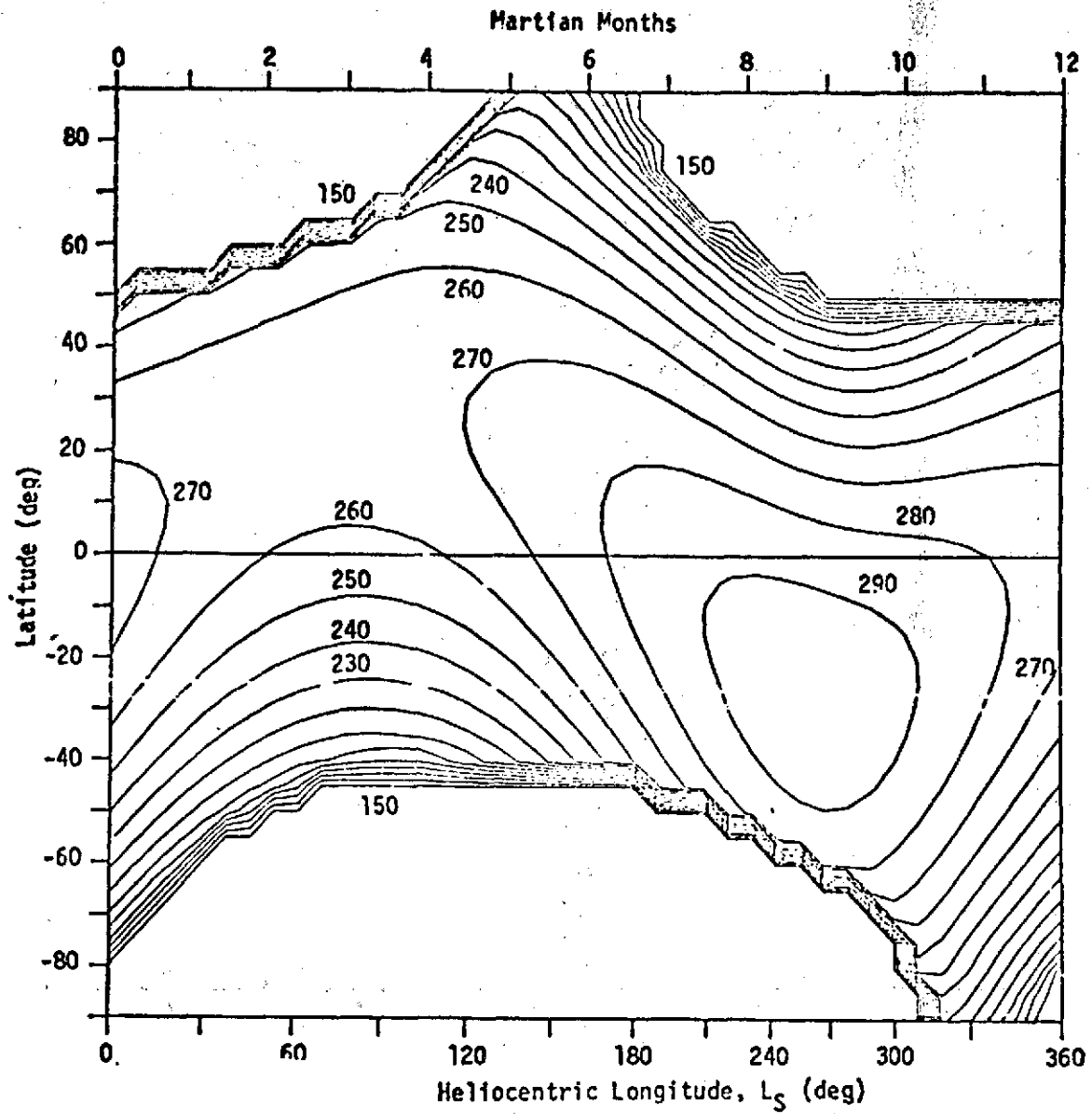
Figure G-7. Annual Variation of Maximum Global Surface
Temperature in Degrees K (from Kieffer for
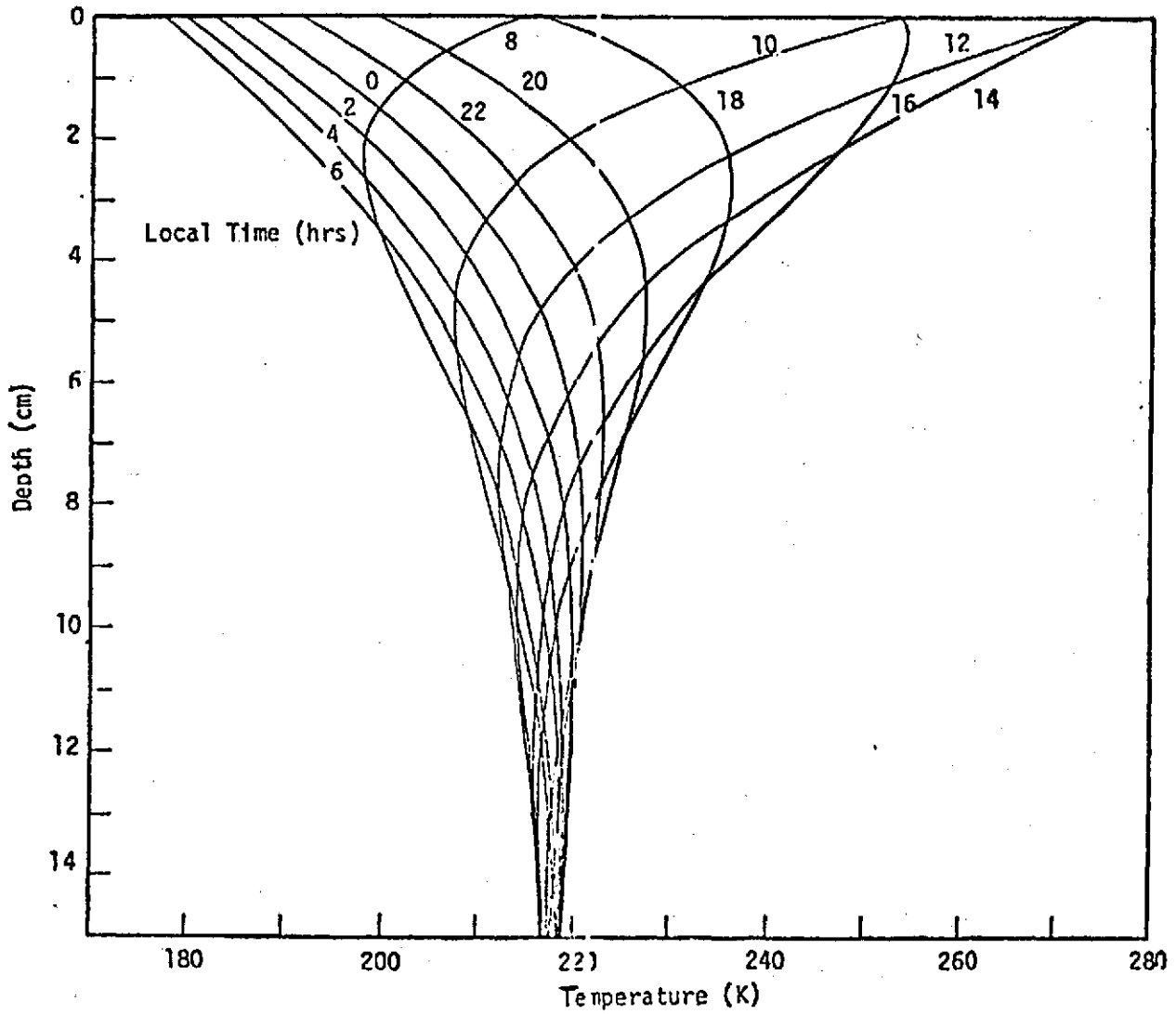$I = 0.0065 \ cal/cm^2 \ s^{1/2} \ K$, $A_{bol} = 0.25$,
$\epsilon = 1.00$)

Figure G-8.   Equatorial Subsurface Temperature (from Kieffer
for the beginning of northern spring, $I = 0.0065$
$cal/cm^2 s^{1/2}$ K, $A_{bol} = 0.25$, $\epsilon = 1.00$)

was found to increase with density. It also increased with temperature approximately according to the law $k = A + BT^3$. In that the Martian temperature is lower than the lunar temperature, some investigators believe the BT^3 term is small compared with the A term; therefore the thermal conductivity of the Martian surface material can be considered to be independent of temperature.

"Direct measurements of thermal conductivity for the Martian surface material are not presently available. Current conductivity estimates are made from the measured thermal inertia by adopting representative values for the specific heat and density of the Martian surface material. Data compiled by Winter and Sarri (Ref. 99) for most common geologic materials suggest that the specific heat lies in the range 0.10 to 0.18 cal/g K over the Martian temperature range (150 to 300 K). From these data, Kieffer concluded that 0.16 is a representative average value for the specific heat and 0.3 cal/cm^3 K is a representative value for the product of soil density and specific heat. Thus, for example, if the thermal inertia is measured to be 6×10^{-3} cal/cm^2 s$^{1/2}$ K, the thermal conductivity would be 1.2×10^{-5} cal/cm s K, which corresponds to the value $\rho c = 0.3$ cal/cm^3 K. Typical thermal conductivities k used by investigators during analyses of Martian data in units of cal/cm s K were: 1.0×10^{-4} and 1.6×10^{-4} by Leovy (Ref. 93); $(7\pm3) \times 10^{-5}$ and $(12\pm4) \times 10^{-5}$ by Morrison, et al. (Ref. 92); and 1×10^{-4} to 7×10^{-4} by Troitskii (Ref. 100). Kieffer, et al. in Reference 16 used the values 10^{-5} to 10^{-3} cal/cm s K measured on powdered rocks having diameters ranging from 40 to 800 μm. The thermal conductivity measured in situ on the lunar soil was 0.33×10^{-4} cal/cm^2 s K at a 49-cm depth and 0.60×10^{-4} cal/cm s K at a 138-cm depth (Ref. 97)."

References

G1. Mars Engineering Model, M75-125-3, prepared by the National Aeronautics and Space
     Administration, Langley Research Center, Viking Project Office, Hampton, Virginia,
     January 1974.

G2. Mars Surface Models, prepared by R. E. Hutton, TRW Systems Group, Redondo Beach,
     California, for Aero-Space Environment Division, NASA/George C. Marshall Space
     Flight Center, Alabama, May 1974 (Contract No. NAS8-29605).

G3. Topography of the Martian Polar Layered Deposits, by D. Dzurisin and Karl B. Blasius,
     based on data from C. W. Hurd, University of Colorado, and Kevin Pang, JPL, 1974
     (in preparation).

APPENDIX H

PRELIMINARY RELIABILITY ANALYSIS

Introduction

The preliminary reliability analysis indicates that the penetrator system design concept is sound, is based upon proven or achievable technology, and has a potential for high to very high penetrator as well as penetrator-system reliability. The analysis in this appendix critically studies the penetrator system design concept to determine the potential for a successful mission and to highlight areas where reliability may be improved rather than attempting to arrive at a specific numerical reliability prediction which would not be adequately substantiated by applicable test data.

Recommendations

The following recommendations are felt to offer an increased potential for achieving very high penetrator reliability or for otherwise improving the system capabilities of the penetrators:

1. In that two RTG's are to be used, it would be desirable to have adequate power from each RTG so that the system could operate if either failed. Operation may have to be at a reduced level.

2. It would be desirable to eliminate the use of the limited-life power supply (the Li battery). If some rechargeable transmitter power source having long life could be used, the penetrator system would have the potential for several years of operation.

3. The command and control logic and clock could be made redundant.

4. Feasibility of a redundant analog-to-digital converter should be investigated.

5. General - If all of the recommendations could be incorporated, the penetrator would be essentially redundant for all critical functions except the antenna, antenna deployment system, and the transmitter; furthermore, the penetrator would have a capability of extended-life operation.

Whether or not incorporation of these recommendations is desirable depends upon constraints such as increased cost, weight, thermal loads, size, etc.

Overall System Insensitivity to Penetrator Reliability

One inherent advantage of the penetrator mission is that from four to six independently targeted penetrators will be used on each mission. Independent targeting combined with the uncertainty of aiming almost ensures a variety of impact terrains which increases the independence of penetrator impact survivability. Conditions other than impact that influence penetrator reliability should be reasonably independent in any case. Figure H-1 shows the effect of number of penetrators and penetrator reliability on overall system success, given that a minimum of three penetrators is necessary for overall system success.* This figure, which is conditioned upon independence between penetrators (see analysis for equations), clearly indicates that a high system reliability can be obtained even if penetrator reliabilities were modest.
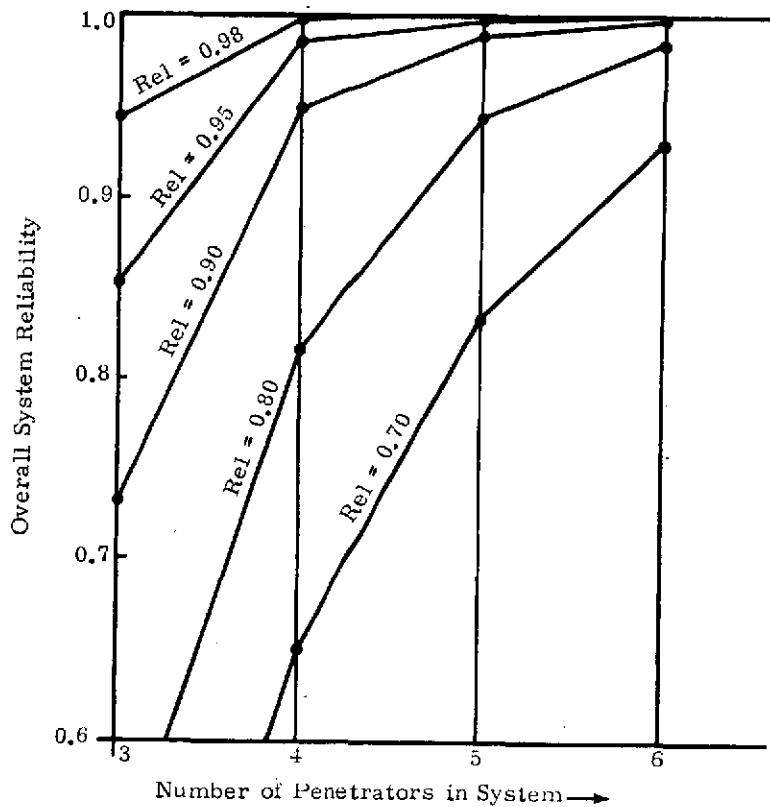
Penetrator Reliability	Number of Penetrators in System		
	4	5	6
0.8	0.82	0.94	0.983
0.9	0.948	0.991	0.999
0.95	0.986	0.999	0.9999
0.98	0.998	0.9999	0.99999

Figure H-1. Overall System Reliability Potential

* Based upon an implied need of three seismometer systems for proper seismic data analysis.

Penetrator Potential Reliability

The penetrators have a potential for a high to very high reliability (≥ 0.9). This potential results from a variety of reasons: the simplicity of the system, use of generally proven technology, ability to have an extensive test program at costs comparable with minimal test programs for other space systems, penetrator component redundancy, and selection and control of high-quality hardware.

Penetrator Simplicity

A simple system design usually has a higher reliability than a complex design. The penetrators are simple compared with most planetary lander systems. All components are stationary within their housings except for antenna deployment, forebody separation from afterbody with umbilical deployment, and door or window opening for the chemical experiment package. Mechanical systems for these functions can be designed to be simple, rugged, and reliable. The stationary components consist of transmitter/receiver system, power supplies, command and control logic system, experiment packages, and associated multiplexer and analog/digital converter. The system functional block diagram is shown in Figure H-2. Modern technology for the command and control logic system, multiplexers, and analog-to-digital converter[*] allows for a reduction of piece parts and simplification of hardware from older designs.

Proven Technology

Much of the proposed penetrator system is based upon demonstrated technology from various other programs at Sandia Laboratories and elsewhere. The basic penetrator concept has been demonstrated many times under a variety of impact conditions and with various penetrator weights and designs. The electronics packages are considered to be state-of-the-art and generally supported by similar hardware from other programs. The experimental packages are envisioned to employ piece parts of generally demonstrated high reliability. The RTG design is nearly identical, except for scaling, to an existing design being developed for a nuclear weapon application. This application has an RTG reliability goal of 0.999 that required power will be delivered over a 15-year service life. Thirty-three complete prototype RTG units containing the radioisotopic fuel capsule are presently under test. The oldest unit built in December 1971 has shown no degradation other than that resulting from fuel decay.

Test Programs

In that the penetrator system consists of four to six identical penetrators of moderate cost, a large number of systems can be tested to verify the necessary reliability models. Additionally useful reliability statements can be made directly from the system test data. The test schedule summary given in Table H-I depicts the various system tests and test sequences for a typical development program. The test program was for a continuously operating electronics system which contains many peripheral sensors (mechanical and electronic) and other features similar to those of

---

[*]Reference: Uncl. Sandia Laboratories memo, J. W. McKiernan, 1642, to R. D. Robinett, 9485, subject, Reliability Analysis of PCM Encoder SA2257, dtd 5/18/73.
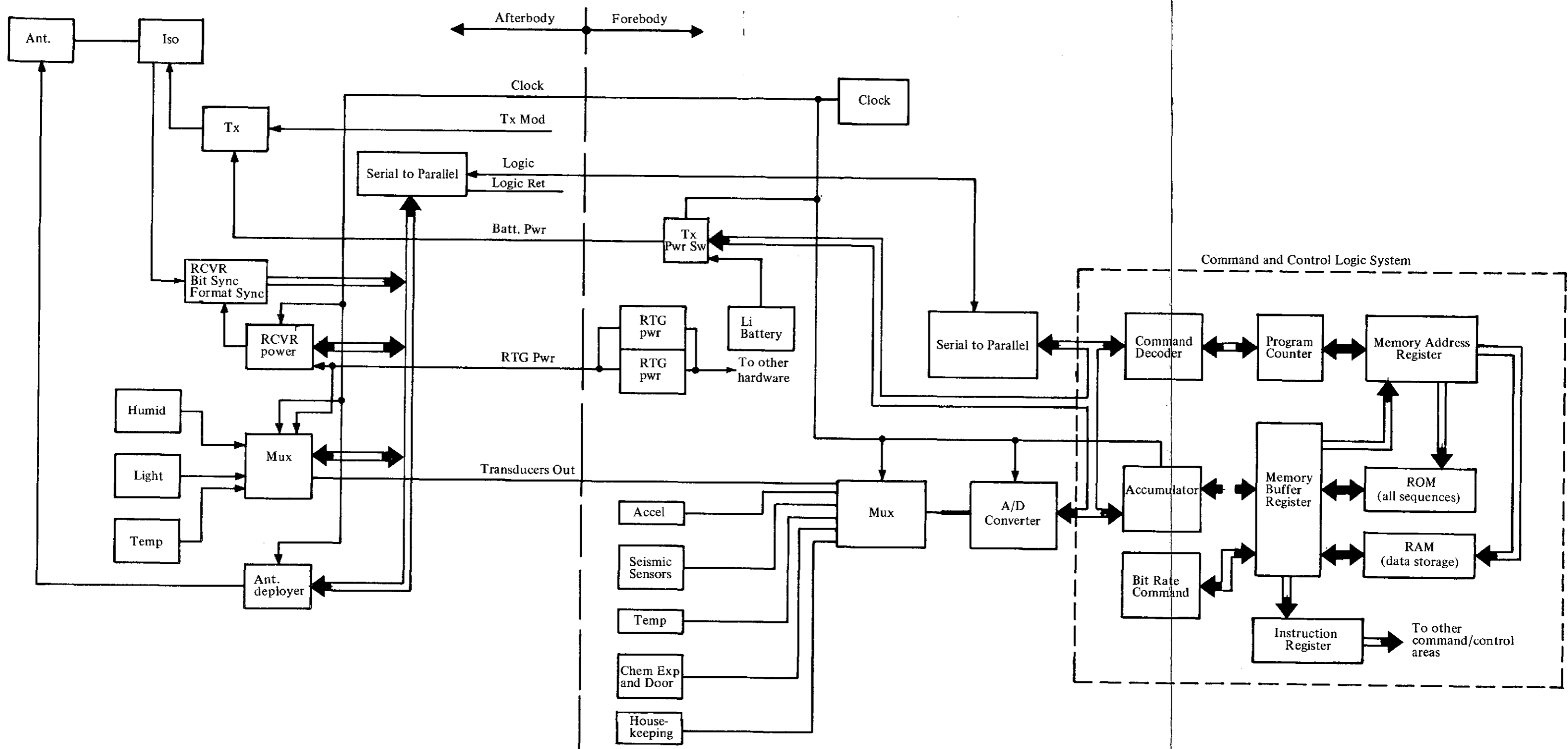
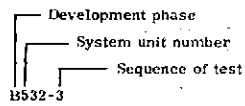Figure H-2. System Functional Block Diagram

TABLE H-1

Typical System Test Program Plan for a Continuously Operating Electronics System

Test Type	1974 4	5	6	7	8	9	10	11	12	1975 1	2	3	4	5	6	7	8	9	10	11	12	1976 1	2	3	4	5	Premature Monitor Continuous	Dud Check Before and After	Dud Check Periodically
Thermal	B532-1								C10-1	C13-1	C6-3	C16									D6-3	D7-3					X	X	X
Vibration		B532-2						C6-1			C16	C13-2						D6-1	D7-1								X	X	
Shock			B532-3							C6-2	C16		C13-3						D6-2	D7-2								X	
EMR					B532-5					C10-2												D25-2					X	X	
Nuclear Radiation													C10-3											D25-3			X	X[1]	X
Acceleration											C11-2																X	X	
Radiant Heat																					D25-1							X	
Flyaround				B532-4																				D28-1			X	X	
Long-Term Storage						B532-6			C12		C17		C23						D16	D17	D18	D19	D20	D21	D22	D23	X[2]		X
Disable																				D27								X[1]	
Laydown																					D6-4								
Premature Only								C8				C11-3	C6-4	C13-4			D8 D9	D10 D11	D12 D13	D14 D15		D7-4 D33		D28-2 D36	D37			X[1]	
Lab Experimental	B594						C2										D3												
Vulnerability													C22								D24						X	X	

(1) Before only-destructive test

(2) Periodic

```
 ┌─── Development phase
 │ ┌─── System unit number
 │ │ ┌─── Sequence of test
 B532-3
```

Number of Tested Systems, Phase B = 2   (prototype development)
Phase C = 11 (preliminary development)
Phase D = 25 (final development)

the penetrator. This test program which employs 38 complete systems and extends over a 2-year period, is envisioned to be of comparable complexity to that planned for the penetrator system. Additionally, a significant number of component and subsystem tests on critical hardware, such as RTG's, antenna deployment system, transmitter, and command and control logic, will also be conducted.

These extensive test data provide a capability of demonstrating high penetrator reliability.

Penetrator Redundancy

The present penetrator system has some inherent design features that provide hardware and software redundancy. Closely related to redundancy is the fact that failure of individual experiment packages will not cause a failure of other parts of the system.

Redundancy is possible in the computer ROM (Read Only Memory) and in the RAM (Random Access Memory). Experiment instruction subroutines can be made redundant in the ROM. System operational instructions that sequence the order and type of experiments to be performed may be made redundant or multiply redundant by calling some experiments in many different operational instructions. The data from the experiments can be stored in various RAM locations as directed by the system operational instructions. This provides for a RAM storage redundancy. Redundancy in both the ROM and RAM can be both logical and physical in that the redundancy can be associated with different memory IC's.

A hardware-software redundancy exists for the receiver. If command link fails, a preprogrammed sequence is initiated from the ROM. Additional redundancy may be possible with the RTG's in that one RTG could be designed to provide for a reduced experimentation capability or equivalent power could be supplied from the Li battery if both RTG's failed.

The present system design could be modified so that the whole command and control logic system would be redundant. It may even be possible to design a system that is essentially redundant except for some experiment packages and the antenna and transmitter.

High-Quality Hardware

Sandia Laboratories has had extensive experience with the design, development, and manufacture and use of high-quality hardware in satellite systems such as those in the Vela series. In some instances, the hardware quality requirements exceeded those specified for Mil Standard high-quality hardware. Many of the techniques previously employed by Sandia, such as batch processing for similar characteristics; extensive component testing, both 100 percent and at environmental extremes; and a meaningful quality assurance effort will be used on the penetrator program.

Analysis

The penetrator system logic as given in Figure H-2 was studied from a reliability point of view as to design logic adequacy, potential hardware problems, etc. Preliminary system probability

equations are given for various system definitions and system concepts. Major failure event probabilities are given in equations for the system definitions. These failure events are listed in Tables H-II and H-III. Table H-II lists major events that can cause a total penetrator failure, given the present penetrator design. Table H-III lists those events that cause a partial system failure or that are redundant.

Although the penetrator design is in the proposal stages, a preliminary analysis indicates that the achievable penetrator reliability should be in the low to high 0.9's.

TABLE H-II

Events That Cause Total System Failure

Event Symbol	Description
Ant	Antenna
Ant_D	Antenna deployer system
Iso	Isolator common
IT	Isolator-transmitter components
Tx	Transmitter
T_{sw}	Transmitter power switch
Li	Li battery power supply
RTG	RTG milliwatt power supply
SP	Serial to parallel register
Um	Umbilical cable common
Mux	Multiplexer in forebody-common failure
AD	Analog-to-digital converter system
Acc	Accumulator
Buf	Memory buffer register
In	Instruction register
ROM	Read-only-memory common
RAM	Random-access-memory common
Add	Memory address register
CD	Command decoder
Co	Program counter
BRC	Bit rate command
Cl	Clock

Redundant Events or Events That Cause Partial System Failure

Event Symbol	Description
IR	Isolator-receiver components
Rec	Receiver
R_{sw}	Receiver power switch
M_a	Multiplexer in afterbody common
Hu	Humidity transducer
Li	Light transducer
Te	Temperature transducer in afterbody
A_c	Accelerometer
SS_1	Seismic sensor longitudinal
SS_a	Seismic sensor axial
Te	Temperature transducers in forebody
Ch	Chemical experiment package
C_{ROM}	I. C. 's of read only memory
C_{RAM}	I. C. 's of random access memory
R_{ROM}	Preprogrammed sequence for receiver failure
Mux_{sw}	Multiplexer in forebody: single experiment failure
M_{sw}	Multiplexer in afterbody: single experiment failure

Baseline Design System Probability Equations

R_{sys} = probability of at least 3 out of η penetrators providing all output functions for the required mission time given proper deployment from the orbiter.

$$= \sum_{i=0}^{\eta-3} \binom{\eta}{i} R_1^{\eta-i} Q_1^{\eta} \quad ,$$

where

R_1 = probability of a penetrator providing all output functions for the required mission time given proper deployment from the orbiter.

$= 1.0 - Q_1$

Q_1 = probability of a penetrator failing to provide all output functions for the required mission time given proper deployment from the orbiter.

$$\cong \text{Aft} + \text{Fore} + \text{Red.} + \text{Um}$$

Aft = occurrence of failure events in the afterbody that cause total system failure.

$$\cong \text{Ant} + \text{Ant}_D + \text{Iso} + \text{IT} + \text{Tx} + \text{SP}$$

Fore = occurrence of failure events in the forebody that cause total system failure.

$$\cong \text{T}_{sw} + \text{Li} + \text{RTG} + \text{SP} + \text{Mux} + \text{AD} + \text{Com} + \text{Cl}$$

Com = occurrence of failure events in the command and control.

$$= \text{Acc} + \text{Buf} + \text{In} + \text{ROM} + \text{RAM} + \text{Co} + \text{CD} + \text{BRC}$$

Red. = occurrence of redundant failure events or events that partially degrade the penetrator capabilities.

$$\cong C^2_{ROM} + C^2_{RAM} + (\text{IR} + \text{Rec} + R_{sw}) R_{ROM} + (H_u + \text{Li} + \text{Te} + M_A)$$

$$+ (A_c + 2SS_1 + SS_a + \text{Te} + \text{Ch}) + 3M_{sw} + 7\text{Mux}_{sw}$$

Modified System Probability Equations

Q_2 = probability of a penetrator failing to provide a reduced output given proper deployment from the orbiter. Reduced output is loss of no more than three experiments or transducers, or reduced system operational life.

$$\cong Q_2 - \text{Red.}$$

Q_3 = probability of a penetrator failing to provide all output functions for the required mission time given command and control logic, analog-digital, RTG, and clock redundancy, and given proper deployment from the orbiter.

$$= \text{Aft} + T_{sw} + \text{Li} + \text{SP} + \text{Red.} + \text{Um}$$

Q_4 = probability of a penetrator failing to provide all output functions for the required mission time given Q_2 and Q_3 options are used.

$$\cong \text{Aft} + T_{sw} + \text{Li} + \text{SP} + \text{Um}$$

APPENDIX I

PLANETARY QUARANTINE

Introduction

This appendix collects the present standards for the quarantine of Mars and, in those cases where a mission-by-mission decision must be made by NASA, cites the values for related missions, and then estimates the impact of these requirements on the systems design for the Mars penetrator. A sterilization procedure and schedule are presented; this approach should satisfy the most stringent of those requirements and should allow an estimate to be made of the effect which sterilization will have on the system reliability.

The sterilization sequence for the Mars penetrator involves seven distinct stages as the impacting-system and decelerator are first assembled into an entry canister which is also a biobarrier; this subsystem is then mated with a retromotor and heat sink which are finally assembled inside a second biobarrier. The total sterilization requirement for the landed system is found to be 10 hours at 125° C if only dry heat is used for the sterilization cycles.

By international agreement, the probability that Mars shall become "contaminated" from space probes must not exceed 10^{-3} during the period 1968 through 1988. It is possible to derive specific mission requirements consistent with this value. For example, the probability that any flight in the Mariner/Mars mission contaminate Mars may not exceed 7.2×10^{-5}, while no Viking flight may present a probability of contaminating Mars greater than 10^{-4}. For the purposes of this report, the Viking value of 10^{-4} is assumed for the probability of a penetrator since it is also a landed mission.

Basic Parameters

By definition, for Mars to be contaminated, a terrestrial organism must be deposited directly into the Martian environment (and not merely reside on a spacecraft in that environment) and subsequently undergo division (growth). Thus, in theory, for each organism on the spacecraft at launch one must assess the probability that it has survived to (is viable at) launch, $P_S(L)$, the probability that it will survive a space voyage to the Martian environment, $P_S(S)$, the probability that it will be released (in a still viable condition) from the spacecraft into the Martian environment, P_R, and the probability that it will subsequently grow, P_G. Not all organisms on a spacecraft at launch will have the same $P_S(L)$, $P_S(S)$, P_R, and P_G values. Specific values depend not only on the type of organism involved but also upon its location on the spacecraft and in some instances upon the technical success of the flight. The Martian environment itself must also be considered in assigning

values to these parameters. By using weighted average parameter values for the contaminating organisms, the basic planetary quarantine expression can be given in the form

$$P_C = E(n_L) \cdot P_S(S) \cdot P_R \cdot P_G \quad , \tag{I-1}$$

where $E(n_L)$ denotes the expected number of viable organisms on the spacecraft at launch.

A Mars probe can be regarded as composed of two classes of hardware: that which is intended to impact the planet (or intersect its atmosphere) and that which is not. For a normal mission, the probability of contamination, (P_{CI} and P_{CNI}), is simply the sum of the probabilities for each class:

$$P_C = P_{CI} + P_{CNI} \quad . \tag{I-2}$$

If one requires that $P_C \leq \epsilon$, then

$$P_{CI} \leq \epsilon_I \quad \text{and} \quad P_{CNI} \leq \epsilon_{NI} \tag{I-3}$$

where $\epsilon_I + \epsilon_{NI} \leq \epsilon$.

In restricting the value of P_{CNI} so that it satisfies Equation (I-3), the dominating factor is the probability of impact with Mars because, if the hardware does not intersect the Martian environment, it is assumed that no contamination takes place. If the probability of impact, P_I, is sufficiently small, no other action is required. This is easily seen by letting

$$P_{CNI} = E(n_L) \cdot P_S(S) \cdot P_R \cdot P_G \leq \epsilon_{NI} \tag{I-4}$$

and assuming

$$P_R = P_I \cdot P(R|I), \tag{I-5}$$

where $E(n_L)$ is the number of viable organisms on the nonimpacting hardware at launch and $P(R|I)$ is the probability of release given impact. If

$$P_I \leq \frac{\epsilon_{NI}}{E(n_L) \cdot P_S(S) \cdot P(R|I) \cdot P_G} \quad . \tag{I-6}$$

Equation I-4 is automatically satisfied. If Equation (I-6) is not satisfied, $E(n_L)$ becomes the control parameter, as in the case of impacting hardware.

For hardware designed to intersect the Martian environment,

$$P_{CI} = E(n_L) \cdot P_S(S) \cdot P_R \cdot P_G \leq \epsilon_I \quad ,$$

wgere $E(n_L)$ is the basic parameter to be controlled. If

$$E(n_L) \leq \frac{\epsilon_I}{P_S(S) \cdot P_R \cdot P_G} \quad , \tag{I-7}$$

then $P_{CI} \leq \epsilon_I$ as required. For this case, P_R depends on whether the hardware impacts the planet in the design mode. An entry failure is generally assumed to increase the likelihood of release, so that

$$P_R = P_{NL} \cdot P(R|NL) + P_{NNL} \cdot P(R|NNL) \tag{I-8}$$

where P_{NL} and P_{NNL} are the probability of a normal and nonnormal landing, respectively, and $P(R|X)$ denotes the probability of release under the condition $X = NL$ or NNL.

Before penetrator mission calculations can be performed, one further level of complication must be introduced in these expressions. The parameter values $P_S(S)$ and P_R, as well as sterilization parameters (described below), depend on whether an organism is

an <u>encapsulated organism</u> - embedded in nonmetallic materials,

a <u>surface organism</u> - exposed directly to the surrounding environment, or

a <u>mated surface organism</u> - neither of the above (e.g., between mated surfaces or on interior surfaces of closed boxes, tubes, etc.).

These three categories are designated E, S, M, respectively. With this nomenclature, expressions (I-4), I-5), and (I-6) become

$$P_{CNI} = \left[\sum_{x=S,M,E} E\left(n_L^{(x)} \right) \cdot P_S^{(x)}(S) \cdot P_R^{(x)} \right] \cdot P_G \leq \epsilon_{NI} \tag{I-9}$$

$$P_R^{(x)} = P_I \cdot P\left(R^{(x)}|I \right) \tag{I-10}$$

and

$$P_I \leq \frac{\epsilon_{NI}}{\left[\sum_{x=S,M,E} E\left(n_L^{(x)} \right) \cdot P_S^{(x)}(S) \cdot P\left(R^{(x)}|I \right) \right] \cdot P_G} \tag{I-11}$$

while Equation (I-7) and (I-8) become, for $x = S, M, E$;

$$E\left(n_L^{(x)} \right) \leq \frac{\epsilon_I^{(x)}}{P_S^{(x)}(S) \cdot P_R^{(x)} \cdot P_G} \qquad \text{with} \qquad \sum_{x=S,M,E} \epsilon_I^{(x)} \leq \epsilon_I \tag{I-12}$$

and

$$P_R^{(x)} = P_{NL} \cdot P\left(R^{(x)}|NL \right) + P_{NNL} \cdot P\left(R^{(x)}|NNL \right) . \tag{I-13}$$

In all cases,

$$P_S^{(x)}(S) = P_S^{(x)}(uv) \cdot P_S^{(x)}(vt) \cdot P_S^{(x)}(e) , \tag{I-14}$$

where $P_S(uv)$ denotes the probability of surviving ultraviolet radiation in space; $P_S(vt)$, the probability of surviving vacuum and temperature changes at launch; and $P_S(e)$, the probability of surviving Martian entry.

NASA planetary quarantine requirements are based upon dry heat sterilization. Exceptions are permitted, but the biological efficacy of any alternate procedure must be demonstrated and the effect upon reliability must be assessed. For dry heat, the sterilization model is:

$$E(n(t)) = E(n(0)) \, 10^{-t/D_T} \qquad (I-15)$$

where $n(t)$ is the bioburden being subjected to dry heat at time t during the sterilization process, E denotes expectation, and D_T is the decimal reduction time at a temperature of T. The parameter D_T is a function of not only the temperature but also of the nature of the bioburden (surface, mated surface, or encapsulated); for example,

$$D_{125°C} = \begin{cases} 1/2 \text{ hour, surface} \\ 1 \text{ hour, mated surface} \\ 5 \text{ hours, encapsulated} \end{cases} \qquad (I-16)$$

and

$$D_T = D_{125°C} \cdot 10^{(125-T)/21} \qquad (I-17)$$

for temperatures other than 125°C. Temperatures below 100°C may not be used according to NASA standards, and approval to use temperatures below 110°C probably would be difficult to obtain. From expressions (I-15) and I-16), one can see that 10 encapsulated organisms take as long to sterilize as 10^5 mated surface organisms or 10^{10} surface organisms. To minimize sterilization time, encapsulated and mated surface burdens should obviously be minimized.

The goal of sterilization is that each $E\left(n_L^{(x)}\right)$, $x = S, M, E$, be sufficiently small that P_{CI} be within its prescribed limits. To this end, there must be a terminal sterilization cycle which takes place with all components requiring sterilization inside of a biobarrier. The final values of $E(n(t))$ after this cycle becomes the $E\left(n_L^{(x)}\right)$ to be used in Equations (I-9) through (I-11), provided the biological integrity of the biobarrier is not violated prior to launch. This may be insured by maintaining a positive pressure (5 inches of water) in the biobarrier until launch.

Prior to the final sterilization cycle, many individual sterilization cycles of piece parts, subcomponents, components, subassemblies, and assemblies may take place to reduce mated surface and encapsulated burdens in order to minimize final sterilization trauma to the most sensitive items.

The calculations in this section are based on the Viking mission values of $P_C = 10^{-4}$ and $P_G = 10^{-6}$. As mentioned earlier, these values must be decided on a mission-by-mission basis; however, the similarity of loaded missions makes these assumptions reliable. Standard values for $P(R^{(x)}|NL)$, $x = S$, M, E, have also been given for soft landers:

$$P(R^{(S)}|NL) = 1 \quad , \quad P(R^{(S)}|NNL) = 1$$

$$P(R^{(M)}|NL) = 10^{-3} , \quad P(R^{(M)}|NNL) = 10^{-1}$$

$$P(R^{(E)}|NL) = 10^{-4} , \quad P(R^{(E)}|NNL) = 10^{-4} \quad . \tag{I-18}$$

Other parameter values that will be assumed, consistent with NASA standards, are:

$P_S(uv) = 1$ (for surface organisms exposed to ultraviolet for at least one hour, a value of 10^{-4} may be used)

$P_S(vt) = 1$

$P_S(e) = 1$

$P(R^{(x)}|I) = P(R^{(x)}|NNL)$

$\bar{d}_v(o) = 130/cc$ (This is the average density of spores buried in nonmetallic spacecraft material; lower values may be used at a subassembly level if they are justified.)

$b_s(o) = 0.5/cm^2$ - Class 100 laminar flow, controlled

$\qquad 10/cm^2$ - Nominal clean room, uncontrolled

$\qquad 100/cm^2$ - Uncontrolled manufacturing

(This is the surface burden per unit area; lower values may be used, but must be justified.)

It will be assumed for purposes of these preliminary computations that

$$\epsilon_I = 6 \times 10^{-5} \quad \text{and} \quad \epsilon_{NI} = 4 \times 10^{-5} \quad .$$

With the above parameter values, expression (I-11) becomes

$$P_I \leq \frac{4 \times 10^{-5}}{10^{-6}\left[E\left(n_L^{(S)}\right) + E\left(n_L^{(M)}\right) \cdot 10^{-1} + E\left(n_L^{(E)}\right) \cdot 10^{-4}\right]}$$

The spacecraft and penetrator design result in the major burden being $E\left(n_L^{(S)}\right)$. Assuming a conservative value of $E\left(n_L^{(S)}\right) = 10^8$,

$$P_I \leq 4 \times 10^{-7} \quad .$$

Actually, two factors will make the requirement on P_I less severe. An extensive prelaunch cleaning program is envisioned. Under these circumstances one might anticipate $E\left(n_L^{(S)}\right) \leq 10^6$ consistent with previous Lunar Orbitor and Surveyor missions. Additionally, some of the burden $E\left(n_L^{(S)}\right)$ will be exposed to ultraviolet during flight. One might, therefore, expect a requirement of the order of

$$P_I \leq 10^{-4} \quad .$$

Additionally, assurance will be given that the probability of deorbit of the Pioneer vehicle during the period 1988-2018 will not exceed 0.05.

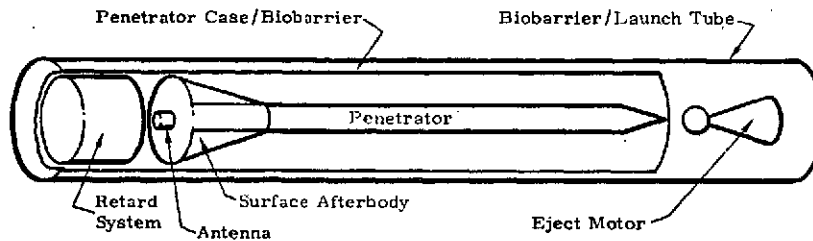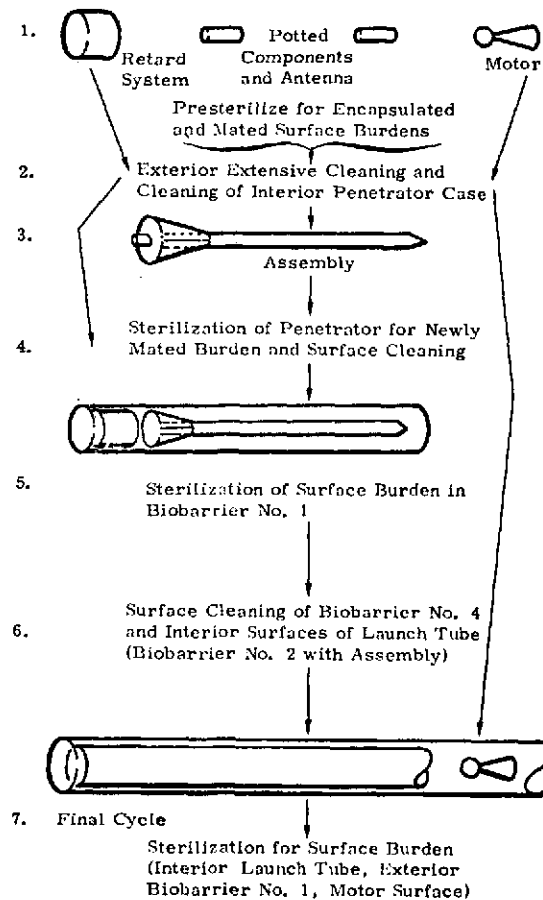The following block design of the penetrator system is used to estimate sterilization requirements.

Figure I-1.

A tentative sterilization sequence is outlined below.

The penetrator is approximated to be 6600 cc volume containing the average encapsulated burden of 130 organism/cc at stage 1 above; i.e.,

$$E(n^{(E)}(0)) \approx 9 \times 10^5 / \text{penetrator}$$

or

$$E(n^{(E)}(0)) \approx 6 \times 10^6 / \text{flight} \ .$$

A maximum mated burden at stage 4 is estimate to be

$$E(n^{(M)}(0)) = 2000 \text{ in.}^2 \cdot 10 \text{ organisms/cm}^2 \cdot (6.45) \frac{\text{cm}^2}{\text{m}^2}$$

$$= 1.3 \times 10^5 \text{ penetrator}$$

$$E(n^{(M)}(0)) = 7.8 \times 10^5 / \text{flight} \ .$$

A maximum surface burden at stage 5 is estimated to be

$$E_1(n^{(S)}(0)) = 4000 \cdot (64.5) = 2.5 \times 10^5 / \text{penetrator}$$

$$E_1(n^{(S)}(0)) = 1.6 \times 10^6 / \text{flight} \ .$$

A similar estimate for surface burden at the terminal sterilization cycle would be conservative also, so that

$$E_2(n^{(S)}(0)) = 1.6 \times 10^6 / \text{flight} \ .$$

The sterilization times can be approximated by letting

$$\epsilon_I^{(E)} = 2.9 \times 10^{-5}$$

$$\epsilon_I^{(M)} = 2.9 \times 10^{-5}$$

$$\epsilon_I^{(S)} = 0.2 \times 10^{-5} \tag{I-19}$$

so that Equation (I-12) becomes

$$E\left(n_L^{(E)}\right) \leq \frac{2.9 \times 10^{-5}}{10^{-10}} = 2.9 \times 10^5$$

$$E\left(n_L^{(M)}\right) \leq \frac{2.9 \times 10^{-5}}{10^{-9}} = 2.9 \times 10^4 \quad (\text{assuming } P_{NNL} \text{ very small}), \text{ and}$$

$$E\left(n_L^{(S)}\right) \leq \frac{0.2 \times 10^{-5}}{10^{-6}} = 2 \tag{I-20}$$

which yields the following values for sterilization time at 125°C.

Stage 1: t_s = 6.6 hours at 125°C

Stage 4: t_s = 1.5 hours at 125°C

Stages 5 and 7: t_s = 3 hours at 125°C

The cleaning program and the use of Class 100 laminar flow should reduce some of these figures appreciably; hence, the worst-case current hardware design specifications call for an ability to withstand 10 hours of dry heat at 125°C.

It should be pointed out that the current philosophy is to complete sterilization of as much of the hardware as possible prior to final testing and to maintain the inside biobarrier at a positive overpressure during the testing period. This may eliminate the need for a sterilization cycle after final spacecraft assembly.

If, after terminal sterilization, the outside biobarrier fails, the inside biobarrier should remain intact so that only a terminal sterilization cycle for surface contamination of less than 1.5 hours at 125°C would have to be repeated. The spacecraft design permits the replacement of any penetrator canister by another sterilized canister at any time during the final testing of the spacecraft.

DISTRIBUTION:
U. S. Atomic Energy Commission
Division of Military Applications
Col. W. B. Haidler
Assistant Director for Research and Development
Washington, D. C. 20545

D. K. Nowlin, Director
Special Programs Division
U. S. Atomic Energy Commission
Albuquerque, New Mexico 87115

National Aeronautics and Space Administration
Washington, D. C. 20546
Attn: D. H. Herman

Ames Research Center
National Aeronautics and Space Administration
Moffett Field, California 94035
Director: Dr. Hans M. Mark
           For: R. W. Jackson (50)

Langley Research Center
National Aeronautics and Space Administration
Langley Station
Hampton, Virginia 23665
Director: Mr. Edgar M. Cortright

Goodard Space Flight Center
National Aeronautics and Space Administration
Greenbelt, Maryland 20771
Director: Dr. John F. Clark

Jet Propulsion Laboratory
4800 Oak Grove Dr.
Pasadena, California 91103
Director: Dr. William H. Pickering
           For: D. G. Rea

Goodard Institute For Space Studies
National Aeronautics and Space Administration
2880 Broadway
New York, New York 10025
Director: Dr. Robert Jastrow

1	Morgan Sparks
2	W. J. Howard
1000	G. A. Fowler
1500	R. L. Peurifoy
1600	H. E. Lenander
2000	K. D. Bowers
2400	R. S. Claassen
4010	C. Winter
4700	D. B. Shuster
4730	R. G. Clem
5000	A. Narath
5100	J. K. Galt
5120	G. J. Simmons (200)
5250	H. D. Sivinski
5600	A. Y. Pope
5620	R. C. Maydew

DISTRIBUTION: (cont)
5626 D. F. McVey, Attn: W. D. Sundberg
                        D. F. Wolf
5628 S. McAlees, Jr., Attn: S. G. Beard
                        D. D. McBride
                        G. F. Wright
5700 J. A. Scott
5710 G. E. Brandvold
5716 W. N. Caudle
5716 E. W. Reece
8000 T. B. Cook, Jr.
9000 R. A. Bice
9420 T. L. Pace
9426 A. B. Campbell
9480 J. E. Stiegler
3151 C. K. Lumpkin
3151 W. F. Carstens (3)
      For AEC/TIC (Unlimited Release)
3141 A. M. Torneby (5)
8266 E. A. Aas (2)